Methods and computational techniques for investigating and monitoring seismic velocities in the Earth's Crust

Adrian Shelley

A DISSERTATION

in

GEOPHYSICS

Presented to the Faculty of Science of Victoria University of Wellington
Fulfillment of the Requirements for the Degree of Doctor of Philosophy

2015

Dr. Martha Savage and Dr. Charles Williams
Dissertation Supervisors

Acknowledgments

I express the following statements of gratitude to those that have enabled in producing this thesis:

To Martha Savage, my supervisor, for her immeasurable tutelage, support and patience over the years. To Katrina Jacobs and Sapthala Karalliyadda, my long-term office cohabitants, for their tireless and unlimited help in my endeavours both in and outside the office. To Charles Williams, my co-supervisor, for his guidance and collaboration, and for being my French window out onto the patio of computational modelling and stress. To Jess Johnson, for her supreme introduction to the ins and outs of studying and processing seismic anisotropy, and for her script legacy. To Selwyn Jones and Pegah Lashgary for being wonderful, friendly office mates and conversationalists. To Sam McQuilkan, Ben Kepka and Patrick Walsh for keeping me sane and chaperoning me through Kiwi life. To Yosuke Aoki for his helpful correspondence and contribution to my work in Japan, and to the University of Tokyo, Japan, for accommodating me during my visit in 2012. To GNS, ERI, and especially to Rob Holt, for providing me with essential data. To Sarah Bogle, for her support and sublime grasp of the English language during the completion of my thesis. To Boris Gurevich for his correspondence and help with understanding empirical stress-anisotropy laws. And finally, to Victoria University, for hosting me in Wellington and making their bureaucracy neither insurmountably Byzantine nor insignificant enough to insulate me from the stresses of the real world.

ABSTRACT

Methods and computational techniques for investigating and monitoring seismic velocities in the Earth's Crust

Adrian Shelley

Dr Martha Savage and Dr Charles Williams

This thesis is concerned with scrutinising the source, distribution and detectability of seismic velocity phenomena that may be used as proxies to study conditions in the crust. Specifically, we develop modelling techniques in order to analyse the directional variation of seismic wave speed in the crust and test them at Mt. Asama in Japan and Canterbury, New Zealand. We also implement both active source and noise interferometry to identify velocity variations at Mt. Ruapehu, New Zealand.

Observations of temporal variation of anisotropic seismic velocity parameters at Asama volcano in Japan indicate that there is some process (or processes) affecting anisotropy, attributed to closure of microcracks in the rock as it is subjected to volcanic stress in the crust. To test this assertion, a 3D numerical model is created incorporating volcanic stress, ray tracing and estimation of the anisotropy to produce synthetic shear wave splitting results using a dyke stress model. Anisotropy is calculated in two ways; by considering a basic scenario where crack density is uniform and a case where the strength of anisotropy is related

to dry crack closure from deviatoric stress. We find that the approach is sensitive to crack density, crack compliance, and the regional stress field. In the case of dry crack closure, modelled stress conditions produce a much smaller degree of anisotropy than indicated by measurements. We propose that the source of anisotropy changes at Asama is tied to more complex processes that may precipitate from stress changes or other volcanic processes, such as the movement of pore fluid.

We develop a generalised anisotropy inversion model based on the linearised, iterative least-squares inversion technique of Abt and Fischer [2008]. The model is streamlined for use with results from the MFAST automatic shear wave splitting software [Savage et al., 2010]. The method iteratively solves for the best fitting magnitude and orientation of anisotropy in each element of the model space using numerically calculated partial derivatives. The inversion is applied to the Canterbury plains in the region surrounding the Greendale fault, using shear-wave splitting data from the 2010 Darfield earthquake sequence. Crustal anisotropy is resolved down to a depth of 20 km at a spatial resolution of 5 km, with good resolution near the Greendale fault. We identify a lateral variation in anisotropy strength across the Greendale fault, possibly associated with post-seismic stress changes.

We perform active source and noise interferometry at Ruapehu in order to investigate potential seismic velocity changes and assess their use as a possible eruption forecasting method. Six co-located 100 kg ammonium nitrate fuel oil explosives were set off serially at Lake Moawhango, situated approximately 20 km south-east of Mount Ruapehu. Two

methods of interferometry, using moving window cross correlation in the time and frequency domains, respectively, were applied to the recorded signal from each explosion pair in order to determine velocity changes from the signal coda waves. We identify possible diurnal velocity variations of $\sim 0.7\%$ associated with strain caused by the solid Earth tide. Synthetic testing of velocity variation recoverability was also performed using both methods. Interferometry of noise cross-correlations during the period was also performed using moving window cross correlation in the frequency domain. Analysis of velocity variations in the ZZ, RR and TT component pairs show little coherency. This, combined with results from synthetic testing that show that the frequency domain interferometry technique employed is unstable above velocity variations of 0.1%, indicate that the method may not be suitable for determining velocity variations at Ruapehu.

Preface

This thesis aims to strengthen our understanding of dynamic volcanic and seismic processes in the crust that can be detected with seismic waves. In the modern era, populations and economies have spread, diversified and globalised, simultaneously exposing more people to natural hazards and providing us with the tools and means to mitigate against, and speed recovery from, their effects. Running parallel to this is the drive to develop understanding of Earth processes to the point where accurate and reliable predictions about future Earth processes that may pose a risk to human interests are possible. Although not unique amongst scientific disciplines, geophysical research into the nature of the Earth is often (and conveniently) touted as a step towards better hazard prediction. While this helps to bring in line the interests of geophysicists, who generally strive to understand the unseen Earth, and the general public, who generally strive to live in safety and without fear of Earth hazards, caution and diligence are essential when bridging the gap between theory and reality. As an aside, this is not only required when theories are incomplete or incorrect, but also in how theories and ideas are communicated to others, as was tragically demonstrated during and after the 2009 L'Aquila earthquake, which caused the deaths of 309 people and resulted in the conviction of six scientists and a government official of involuntary manslaughter after their risk assessment prior to the earthquake was determined to have contributed to the loss of life (the conviction was overturned by appeal). This thesis, therefore, seeks to investigate two areas of seismology in which the word 'forecast' is used frequently; seismic anisotropy and seismic interferometry, in the hope that their nuances may be accounted for in any application to hazard prediction. This is my main motivation for taking the research presented here in the direction it has gone in, but there is also an element of pursuing understanding for the sake of understanding.

Contents

Chapter 1

Introduction

This thesis is not a linear thesis, as one that concerns the development of one theory, the application of one method to different scenarios, or the detailed analysis of one phenomenon would be. Instead it is branching; the second chapter explores parameters that are thought to contribute towards seismic anisotropy changes at volcanoes and from the results presented there the topic forks in two, focusing on seismic anisotropy in the third chapter, and varying seismic properties in the fourth chapter. The two themes of the thesis are seismic anisotropy and velocity variation (either anisotropic or isotropic), which come packaged together in the second chapter before being separated out in the following chapters. Ideally, each of the aforementioned chapters can be read intelligibly as independent studies, so anybody reading the thesis as a whole should bear this in mind.

The first chapter of the thesis is an introductory chapter, in which I aim to present an elementary review of the concepts and ideas used in the subsequent chapters. As each chapter has a somewhat different focus to the others, each will contain its own preamble to introduce the reader to the specific problem, leaving this chapter with concepts and explanations which are generally suited for the broader themes of the subsequent chapters.

The second chapter focuses on the study of the evolution of seismic anisotropy at Mount Asama, Japan, before and during its eruption in 2004. The study consists of using novel forward modelling techniques to investigate data measured by Savage et al. [2010b]. The approach seeks to evaluate the source of an observed co-eruptive variation in anisotropy that coincided with continuous GPS measurements that indicate a stress/strain relationship with anisotropy. In order to do this, we combine stress modelling of the volcanic system with forward modelling of shear wave splitting, testing several different possible relationships between the volcanic stress conditions and anisotropy. The content of this paper was published in 2014 in the *Journal of Geophysical Research* [Shelley et al., 2014]. Co–author Dr. Martha Savage provided data and supervision for the project. Co–author Dr. Charles Williams provided expertise on stress modelling. Co–author Dr. Yosuke Aoki provided geodetic data concerning the volcanic plumbing system at Mount Asama, and co–author Boris Gurevich provided the three-component analytic relationship between stress and anisotropy used in the modelling. The paper is reproduced in this thesis with minor revisions from its published counterpart.

The third chapter describes a modelling inversion technique that seeks to solve for a model of anisotropy, given a dataset of shear wave splitting parameters. The method is a development of that introduced by Abt and Fischer [2008], using an iterative, linearised least-squares technique. We refine the technique for crustal anisotropy, applying it to the comprehensive Canterbury shear wave splitting dataset of Holt et al. [2013] which encompasses several months of aftershocks related to the September 2010 Darfield earthquake, a sequence that caused significant damage to the region. The other aim of this chapter is to present a method that can be used flexibly with shear wave splitting data, specifically data obtained using the automatic MFAST program [Savage et al., 2010a].

The fourth chapter is an investigation of seismic velocities around Mount Ruapehu, New Zealand, which combines results from an active source experiment in nearby Lake Moawhango with velocity variation results determined from the ambient seismic noise field recorded in the area using both permanent GeoNet sensors (http://www.geonet.org.nz, last accessed 23 October 2014) and a temporary deployment. The study was performed during a period of ostensible volcanic quiescence and results were directly compared to those from an eruptive period in 2006, which was studied by Mordret et al. [2010].

Finally, a summary of the thesis and its conclusions is presented, with a discussion about what future avenues of research in the respective areas may be.

1.1 The Theory of Elasticity

The theory of elasticity is the mathematical description that is used to describe the deformation response of materials to an applied force. In a purely elastic system all deformation, or strain, applied to a material is fully recoverable upon removal of the acting force. In rock physics, materials are often described to behave in a viscoelastic manner, where a component of the strain applied is not elastically recoverable. A wide range of behaviour for solids and fluids can be defined within the mathematical framework of elasticity and viscoelasticity.

Stress is the physical quantity, defined as force per unit area, that quantifies the forces exerted by neighbouring particles in a material. Deformation causes a rearrangement of the molecules in a body, moving their structure out of thermomechanical equilibrium. The forces arising that tend to return the body to equilibrium after such elastic deformation are therefore considered internal stresses.

For any body, the total force applied to a point within it can be written as a volume integral $\int F \mathrm{d}V$, where F is the force per unit volume. In three dimensions, this integral over an arbitrary volume can be transformed into a surface integral in three components with the force F_i being the divergence of a tensor of rank two [Marsden and Hughes, 1994], i.e.:

$$F_i = \frac{\partial \sigma_{ij}}{\partial x_j} \tag{1.1.1}$$

Thus the volume integral is expressed as a surface integral using Gauss's divergence theorem:

$$\int F \mathrm{d}V = \int \frac{\partial \sigma_{ij}}{\partial x_j} \mathrm{d}V = \oint \sigma_{ij} \mathrm{d}f_j \tag{1.1.2}$$

The tensor σ_{ij} is known as the stress tensor. Its nine components describe the normal and tangential (i.e. shear) forces acting on the surface element $\mathrm{d}f_j$. For instance, σ_{zz} is

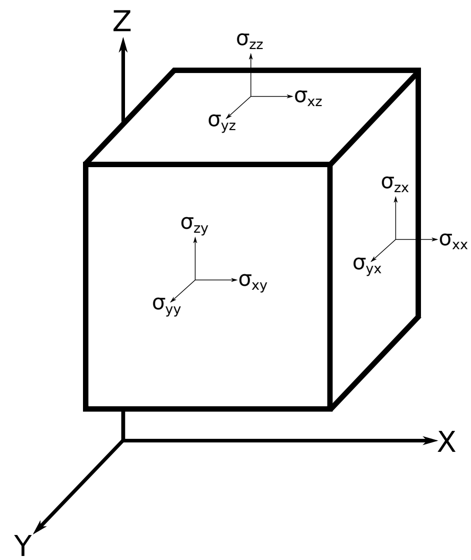

Figure 1.1: Visualisation of the stress tensor σ_{ij} as it acts on a volume element within a solid body.

the force per unit area acting normal to the area perpendicular to the z-axis, and σ_{yz} is the tangential force per unit area acting parallel to the y-axis on the area perpendicular to the z-axis (see Figure 1.1).

For an elastic material, there is a relationship between stress and strain defined by the properties of the material itself. Hooke's law defines this relationship for a linearly elastic solid:

$$\sigma_{ij} = C_{ijkl}\eta_{kl} \tag{1.1.3}$$

Where η_{kl} is the infinitesimal strain tensor, and C_{ijkl} is the fourth order stiffness tensor that transforms between the strain and stress tensor. The stiffness tensor, C_{ijkl}, has the following symmetries [Babuska and Cara, 1991]- due to the symmetry in σ_{ij} imparted by the conservation of angular momentum:

$$C_{ijkl} = C_{jikl} \tag{1.1.4}$$

and due to symmetry in η_{kl},

$$C_{ijkl} = C_{ijlk} \tag{1.1.5}$$

The final symmetry arises from consideration of thermodynamic equilibria, giving:

$$C_{ijkl} = C_{klij} \tag{1.1.6}$$

These symmetries mean that there are only 21 possible independent elements to the C_{ijkl} tensor. Thus, it is common and convenient to express the stiffness tensor as the following 6×6 matrix:

$$C_{ij} = \begin{bmatrix} C_{1111} & C_{1122} & C_{1133} & C_{1123} & C_{1113} & C_{1112} \\ C_{2211} & C_{2222} & C_{2233} & C_{2223} & C_{2213} & C_{2212} \\ C_{3311} & C_{3322} & C_{3333} & C_{3323} & C_{3313} & C_{3312} \\ C_{2311} & C_{2322} & C_{2333} & C_{2323} & C_{2313} & C_{2312} \\ C_{1311} & C_{1322} & C_{1333} & C_{1323} & C_{1313} & C_{1312} \\ C_{1211} & C_{1222} & C_{1233} & C_{1223} & C_{1213} & C_{1212} \end{bmatrix} \tag{1.1.7}$$

where the indices relate to each C_{ij} matrix element's position in the C_{ijkl} tensor. Due to the condition $C_{ijkl} = C_{klij}$, the C_{ij} matrix is symmetric (i.e. $C_{ij} = C_{ij}^T$), leaving just

$36 - 15 = 21$ independent coefficients. Due to further, material specific symmetry in the stress and strain tensors, the number of independent elements can be significantly reduced. For example, fluids have only one independent C_{ijkl} coefficient, otherwise known as it's bulk modulus. The C_{ijkl} tensor of an isotropic solid can be fully described with just two independent coefficients, λ and μ, known as Lamé's coefficients. Further symmetries in the stiffness tensor are commonplace amongst various minerals and elastic regimes in the Earth, and taking these into consideration is important when investigating anisotropic wave propagation. We will look at these types of symmetries later on. An in depth discussion of the derivations of the various fundamental equations in the theory of elasticity can be found in Marsden and Hughes [1994].

Principal Stresses and notation

As we have seen, the condition of stress that defines strain alongside the elastic tensor is fully described as a symmetric 3×3 matrix (see Figure 1.1). It is common to express the elements of the stress tensor in terms of orthogonal normal stresses and orthogonal shear stresses, which are notated as σ and τ, respectively. For instance, σ_{xx}, or the force normal to the x-axis, can be written simply as σ_x, and σ_{xy}, or the tangential force acting parallel to the x-axis on the area perpendicular to the y-axis, is written as τ_{xy}. Thus, taking symmetry into account, the stress tensor can be written as:

$$\begin{bmatrix} \sigma_x & \tau_{xy} & \tau_{xz} \\ \tau_{xy} & \sigma_y & \tau_{yz} \\ \tau_{xz} & \tau_{yz} & \sigma_z \end{bmatrix} \tag{1.1.8}$$

As the stress tensor is symmetric, there exist three mutually orthogonal eigenvectors, e_1, e_2, and e_3, and associated real eigenvalues, λ_1, λ_2, and λ_3, that satisfy the eigenvalue problem $\boldsymbol{\sigma} e_i - \lambda_i e_i = 0$ [Zoback, 2010]. Rotation of the stress tensor into a coordinate system where the axes are the eigenvectors will give a diagonal matrix with elements λ_1, λ_2, and λ_3. Therefore for any particular stress tensor there exists a frame of reference in which all shear stresses are equal to zero, leaving only three mutually orthogonal matrix elements with which to describe the stress state. These three elements are known as the principal stresses.

This result is useful in geophysics as it allows for a simpler way to characterise the state of stress in a medium. Generally, the three principal stresses are denoted as σ_1, σ_2, and σ_3, where $\sigma_1 > \sigma_2 > \sigma_3$. Alternatively, it is common to see principal stresses denoted as s_1, s_2, and s_3, with the equivalent magnitude relationship. The reason why principal stresses are so commonly used in geophysics is that very often, especially in the crust, one principal stress axis is parallel or near-parallel to vertical [Zoback, 2010]. Which of the principal stresses are vertically aligned forms the basis of the Andersonian theory of faulting [Anderson, 1951], in which normal faulting regimes are characterised by a vertical σ_3, strike-slip faulting regimes by a vertical σ_2 and reverse faulting regimes by a vertical σ_1 (see Figure 1.2).

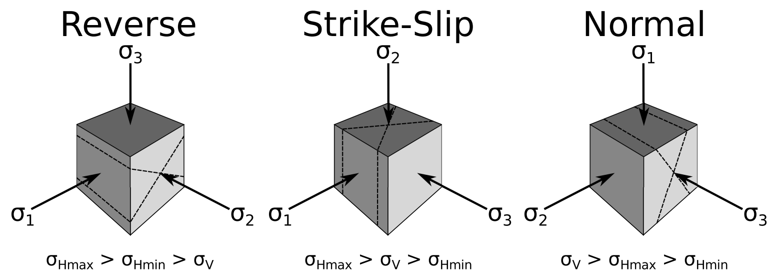

Figure 1.2: The three end-members of the Andersonian theory of faulting and how the principal stresses are oriented in each. Also given are the relative magnitudes of σ_V, σ_{Hmax} and σ_{Hmin} based on the assumption that one of the principal stresses is vertically aligned.

Since one of the principal stresses is generally expected to be vertically aligned, they are regularly referred to as σ_V, for the vertical component, and σ_{Hmax} and σ_{Hmin} for the two horizontal components. As shown in Figure 1.2, the relative magnitude of σ_V and the horizontal principal stresses determines the faulting regime of the stressed medium. Therefore knowledge of the faulting regime and orientation of σ_{Hmax}, determined through means that will be discussed later in this thesis, provides information on the relative magnitudes and orientation of the entire stress tensor.

1.2 Seismic Anisotropy

Seismic anisotropy is the term used to describe the directional dependence of seismic velocities, and is virtually ubiquitous amongst materials in the Earth [Teanby et al., 2004]. In the context of geophysics it is an emergent phenomenon of anisotropic elastic properties in the Earth's rock, and can be caused by effects ranging in scale from microscopic structures to large scale extrinsic features. Seismic anisotropy in rock masses have five general known causes with varying degrees of influence [see Crampin 1987, Crampin and Lovell 1991, Savage 1999, Crampin and Peacock 2008]. In the crust, microcracks and pore space in rocks can also produce anisotropy if they exhibit preferential alignment, which can be induced through the application of a deviatoric stress condition that deforms and closes microcracks preferentially the more the associated crack normals align parallel to the direction of σ_1 (often assumed to be σ_{Hmax} in the crust) [Crampin, 1994]. Also in the Earth's crust, macroscopic fractures and faulting will affect the anisotropy of a region, despite the regional stress fields [Boness and Zoback 2006, Mueller 1991].

Mineral fabrics also induce seismic anisotropy, as different mineral axes exhibit varying elastic properties, producing an emergent crystal lattice preferred orientation (LPO) [e.g. Christensen and Crosson 1968]. Fabric alignment and orientation are linked to the nature and maturity of past strain, as well as the mineral type, and is the prevalent cause of anisotropy in the upper mantle where rocks deform plastically. Finally, a small but perceptible velocity anisotropy can be induced in an inherently isotropic medium with the application of a deviatoric stress field [Dahlen, 1972].

Seismic anisotropy is expressed in all compressional and transverse seismic waves. The first observations of large-scale anisotropy were made in seismic refraction measurements in oceanic mantle lithosphere by Hess [1964]. The authors of this study found mantle lithosphere P-wave velocities were consistently higher when travelling perpendicularly to the axis of a mid ocean ridge, attributed to the inherent elastic anisotropy of olivine crystals aligned by mantle flow in the tectonic spreading regime. This represents an example of azimuthal anisotropy, in which differences in seismic velocity are dependent on the azimuth at which they arrive at the seismic recording device used. Analysis of transverse seismic waves allows for the measurement of polarisation anisotropy, predominately through shear-wave splitting (SWS) [e.g. Crampin 1985], in which the strength and orientation of anisotropy is determined from the properties of the incoming S-wave, having been 'split' by propagating through anisotropic media. Shear-wave splitting constitutes the sole type of anisotropy analysis in this thesis, and the technical details of this are discussed in section 1.2.3.

Since the early work of Hess [1964], various aspects of anisotropy in the Earth have been widely studied using a multitude of methods. In particular, mantle anisotropy measurements and laboratory experiments have been used to determine and constrain mantle kinematics and structure [e.g. Schlue and Knopoff 1977, Montagner and Anderson 1989, Karato and Wu 1993, Ekström and Dziewonski 1998, Long and Becker 2010]. In the crust, the source and distribution of anisotropy is somewhat more enigmatic, however there have been numerous studies that look at the relationship of crustal anisotropy to long- and short-term deformation events, metamorphic phenomenon, and petrology [e.g. Crampin 1994, Okaya et al. 1995, Levin and Park 1997, Shapiro et al. 2004, Gerst and Savage 2004, Savage et al. 2010a]. Anisotropy at a range of depths has been characterised using earthquake surface waves [e.g. Montagner and Nataf 1986, Nishimura and Forsyth 1989, Debayle et al. 2000]. In addition to using more traditional seismological techniques, the development of ambient noise tomography has provided the opportunity to use surface waves to study radial and azimuthal anisotropy at various depths [e.g. Bensen et al. 2009 , Lin et al. 2011, Xie et al.

2013, Fry et al. 2014].

1.2.1 Wave equations

The work in this thesis focuses on studying shear wave splitting, which is the manifestation of elastic anisotropy in seismic plane waves. By considering Newton's laws of motion with respect to the dynamic equilibrium of a cubic element of a continuum [Lay and Wallace 1995, Shearer 2009], we can define the equation of motion thus:

$$\rho\frac{\partial^2 u_i}{\partial t^2} = f_i + \frac{\partial \sigma_{ij}}{\partial x_j} \tag{1.2.1}$$

where ρ is density, u_i is the component of displacement, t is time, x_j is position and f_i is any external or body force. Having the value of f_i set to zero is a special case known as the homogeneous equation of motion:

$$\rho\frac{\partial^2 u_i}{\partial t^2} = \frac{\partial \sigma_{ij}}{\partial x_j} \tag{1.2.2}$$

In three dimensions, the equation for plane wave displacement, u, at time t and location **x** is:

$$u(\mathbf{x}, t) = Ae^{i(\omega t - \mathbf{n}_c \cdot \mathbf{x})} \tag{1.2.3}$$

where A denotes the wave amplitude and polarity, and ω is angular frequency. $\mathbf{n}_c$ is the wavenumber vector that defines the direction of ray propagation and satisfies $|\mathbf{n}_c| = \omega/c$, where c is the phase velocity of the medium. Taking the derivative function of u with respect to time (t) and space ($\mathbf{x}$), respectively, gives:

$$\frac{\partial^2 u_i}{\partial t^2} = A_i(i\omega)^2 e^{i\omega(t-\mathbf{n}_c\cdot\mathbf{x})} \tag{1.2.4}$$

$$\frac{\partial^2 u_l}{\partial x_j x_k} = A_l \mathbf{n}_{cj}\mathbf{n}_{cl}(i\omega)^2 e^{i\omega(t-\mathbf{n}_c\cdot\mathbf{x})} \tag{1.2.5}$$

The second-order strain tensor is related to displacement thus:

$$\eta_{kl} = \frac{1}{2}(\frac{\partial u_k}{\partial x_l} + \frac{\partial u_l}{\partial x_k}) \tag{1.2.6}$$

Recall the inherent symmetry of the strain tensor, η_{kl}, of which the effects on the elastic tensor are described in equation 1.2.5. This allows us to rewrite Hooke's law (equation 1.2.3) as:

$$\sigma ij = C_{ijkl}\frac{\partial u_k}{\partial x_l} \tag{1.2.7}$$

This can be substituted into equation 1.2.2 to give:

$$\rho\frac{\partial^2 u_i}{\partial t^2} = C_{ijkl}\frac{\partial}{\partial x_j}\cdot\frac{\partial^2 u_k}{\partial x_l} \tag{1.2.8}$$

Substituting the derivatives in equations 1.2.4 and 1.2.5 into this equation and dividing by common terms, we find:

$$\rho A_i = C_{ijkl}A_k\mathbf{n}_{cj}\mathbf{n}_{cl} \tag{1.2.9}$$

or:

$$(C_{ijkl}\mathbf{n}_{cj}\mathbf{n}_{cl} - \rho\delta_{ik})A_k = 0 \tag{1.2.10}$$

where δ_{ik} is the Kronecker delta (equal to 1 if i = k, otherwise equal to 0). Now we rearrange the equation to put it in terms of phase velocity, c, and ray propagation, $\vec{n}$, given that $|\mathbf{n}_c| = \omega/c$:

$$(\frac{1}{\rho}C_{ijkl}n_j n_l - c^2\delta_{ik})A_k = 0 \tag{1.2.11}$$

We now define what's known as the Christoffel Tensor:

$$m_{ik} = \frac{1}{\rho}C_{ijkl}n_j n_l \tag{1.2.12}$$

allowing us to write equation 1.2.11 as:

$$(m_{ik} - c^2\delta_{ik})A_k = 0 \tag{1.2.13}$$

As can be seen from this equation, the square of the shear wave phase velocity is the eigenvalue of the Christoffel matrix, with the vectors A being the associated eigenvectors. These eigenvectors are mutually perpendicular, as the Christoffel matrix inherits the symmetrical property of the C_{ijkl} tensor. Solving for the three eigenvalues and their associated eigenvectors gives the value and orientation of the resultant quasi-*P*-wave (P_1), fast *S*-wave (S_1) and slow *S*-wave (S_2). The degree of difficulty in solving the eigenvalue problem

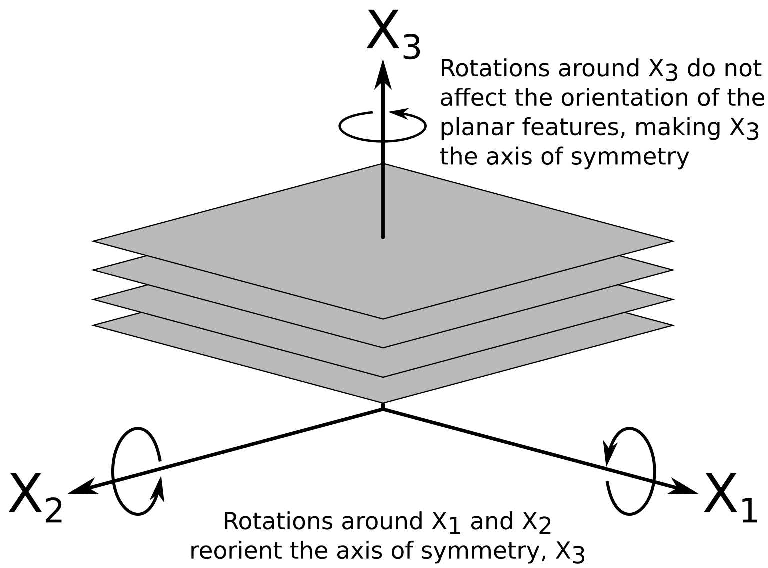

Figure 1.3: Schematic diagram illustrating how media with layers or planar features that contribute to anisotropy exhibit hexagonal symmetry. Any rotations around the symmetry axis, X_3, will not affect the material's elastic properties. Planar features found in the Earth's rocks include sedimentary layering, rock fabrics, fractures and microcracks.

depends on the overall symmetry of the C_{ijkl} matrix, which will be discussed in the next section.

1.2.2 Anisotropy in Earth Materials

As mentioned earlier, rocks that seismic waves propagate through can exhibit anisotropy produced from a number of different sources. The characteristic expression of the anisotropy varies depending on what is causing it. These characteristics are determined by the theory of elastic anisotropy of solid materials, developed in works such as Love [1927] and Biot [1955], and comprehensively described in Babuska and Cara [1991].

First we will revisit the form that the elastic tensor takes when describing anisotropic solids. Crystallographic structures are used as directly analogous terms describing types of anisotropic elastic tensors, since those structures are directly responsible for anisotropic elastic properties of crystals. More complex crystal systems require more independent C_{ijkl} coefficients to fully describe their behaviour. For example, crystals with triclinic structures have 21 independent elastic coefficients, and cubic structures require 3 (see table 1.1). This system of describing anisotropic materials based on symmetry extends beyond individual minerals and can be used to approximate structural conditions and lithology (e.g. sedimentary layers, fractures, schistosity, etc.) in the Earth. Any anisotropic system that exhibits invariant properties when rotating around one of its axes can be described by an elastic tensor with hexagonal symmetry (see Figure 1.3). This is significant, as layered, cracked and fractured media, which tend to dominate anisotropic regimes at shallow crustal depths, fall broadly into this category. These systems, with a plane of rotation which is invariant to the axis of symmetry, are referred to as transversely isotropic bodies [Love, 1927] and are often categorised further into systems with a vertical axis of symmetry, or vertical transverse isotropy (e.g. sedimentary layers, this is sometimes known as radial anisotropy), and systems with a horizontal axis of symmetry, or horizontal transverse isotropy (e.g. stress-aligned microcracks in certain stress regimes). There are various ways of formulating the independent elastic coefficients for such media, using Love coefficeints A, C, F, L and N, for example [Love, 1927]. Each of these formulations have various degrees of suitability for a specific problem. In this thesis, specific formulations are explained in further detail when they are employed. C_{ij} matrices with hexagonal symmetry take the form:

$$C_{ij} = \begin{bmatrix} C_{1111} & C_{1122} & C_{1133} & 0 & 0 & 0 \\ C_{2211} & C_{2222} & C_{2233} & 0 & 0 & 0 \\ C_{3311} & C_{3322} & C_{3333} & 0 & 0 & 0 \\ 0 & 0 & 0 & C_{2323} & 0 & 0 \\ 0 & 0 & 0 & 0 & C_{1313} & 0 \\ 0 & 0 & 0 & 0 & 0 & C_{1212} \end{bmatrix} \tag{1.2.14}$$

for an axis of symmetry parallel to x_3 (i.e. vertical transverse isotropy). As there are only five independent coefficients, we can also express the following equivalencies:

$$C_{1111} = C_{2222} \tag{1.2.15}$$

$$C_{1122} = C_{2211} \tag{1.2.16}$$

$$C_{1133} = C_{2233} = C_{3311} = C_{3322} \tag{1.2.17}$$

$$C_{2323} = C_{1313} \tag{1.2.18}$$

In anisotropy studies, orthorhombic systems are widely employed due to the fact that mantle peridotite, the most common rock in the upper mantle, is mostly comprised of olivine and orthopyroxene, which both have orthorhombic symmetry [Savage, 1999].

Crystal systems	Number of independent elastic coefficients	Typical minerals
triclinic	21	plagioclase, microcline
monoclinic	13	hornblende, muscovite
orthorhombic	9	olivine
tetragonal	6	stishovite, zircon
trigonal I	7	ilmenite
trigonal II	6	quartz
hexagonal	5	ice
cubic	3	garnet
isotropic solid	2	volcanic glass

Table 1.1: Number of independent elastic coefficients for the various crystal systems found in Earth's minerals. This table has been reproduced from Babuska and Cara [1991].

1.2.3 Shear Wave Splitting Parameter Determination

Now that we have a basic framework in which to describe elastic anisotropy and its effect on seismic waves, we go into more detail about shear wave splitting (SWS). SWS, or seismic birefringence, is broadly analogous to birefringence of electro-magnetic waves, however its cause is due to anisotropic velocity properties rather than anisotropic refractive properties. Split shear waves measured at a sensor consist of two sequentially arriving orthogonally polarised waves. The condition of SWS for a particular wave is described in terms of the first arrival's polarisation, known as the fast polarisation direction (ϕ), and the elapsed time

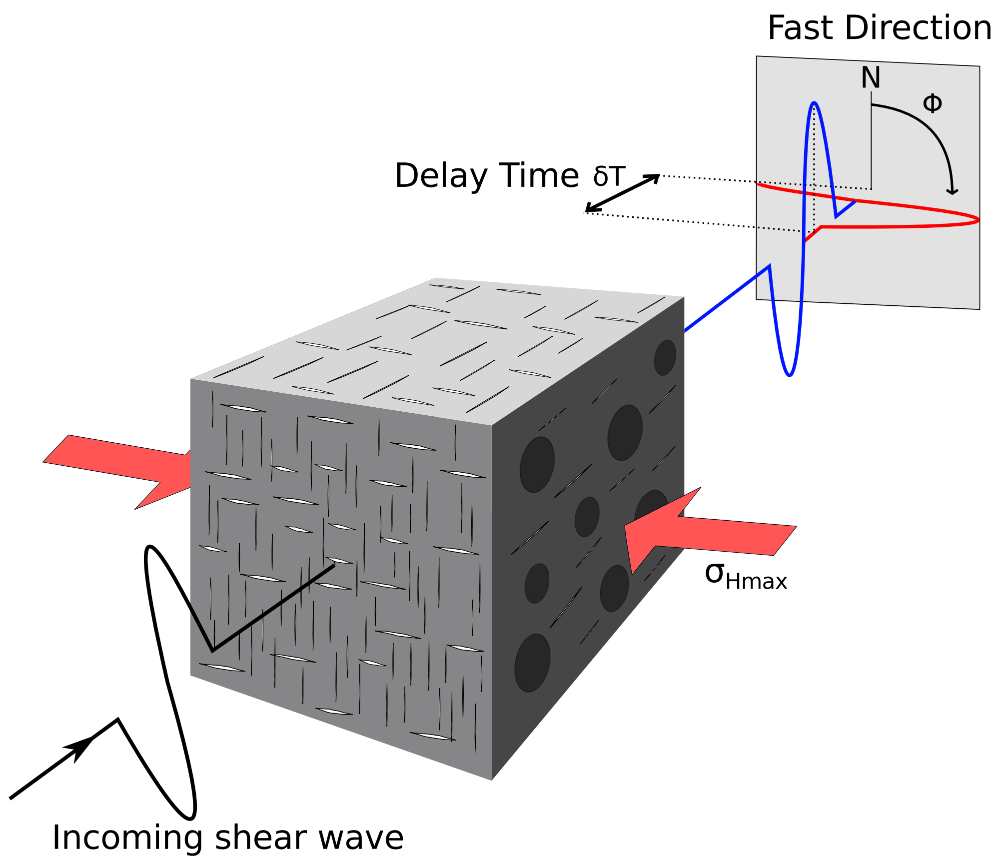

Figure 1.4: Diagram showing shear wave splitting in a cracked anisotropic medium. The incoming shear wave is split into fast (red) and slow (blue) components. δt is the time delay between the split waves, and ϕ is the polarisation angle of the fast split wave (projected to the horizontal plane). In the case of stress-induced anisotropy in a cracked medium, ϕ is parallel to the maximum horizontal compressive stress direction, σ_{Hmax}.

between the two arrivals, or the delay time (δt) (see Figure 1.4). As was shown in section 1.2.1, the velocity difference and orientation of the fast and slow component of an S-wave passing through an anisotropic medium is a function of the medium's elastic properties, density and the wave's propagation vector. The final measured splitting parameters are therefore the integration of these parameters over the length of the entire raypath from source to receiver.

A widely used method for determining ϕ and δt for a split shear wave is that of Silver and Chan [1991], an approach which has been subsequently modified and corrected by Walsh et al. [2013]. This approach defines a splitting operator, Γ, which produces a split shear wave when applied to a shear wave, as the following:

$$\Gamma \equiv e^{-i\omega\delta t/2}\hat{\boldsymbol{f}}\hat{\boldsymbol{f}}^T + e^{i\omega\delta t/2}\hat{\boldsymbol{s}}\hat{\boldsymbol{s}}^T \tag{1.2.19}$$

where $\hat{\boldsymbol{f}}$ and $\hat{\boldsymbol{s}}$ are the fast and slow S-wave vectors, determined from the eigenvalue problem in equation 1.2.13. The value for δt in this formulation is found using the associated eigenvalues of $\hat{\boldsymbol{f}}$ and $\hat{\boldsymbol{s}}$, V_{sf}^2 and V_{ss}^2, which correspond to the square of the fast and slow shear velocities, respectively. For small anisotropy this value is expressed in terms of a relative perturbation in shear velocity, $\delta\hat{V}_s = V_{s0}^{-1}(\delta V_{sf} - \delta V_{ss})$, as:

$$\delta t = V_{s0}^{-1} L \delta\hat{V}_s \tag{1.2.20}$$

where V_{s0} is the isotropic shear velocity and L is the path length of the shear wave. We can rewrite equation 1.2.3 (the equation for plane wave displacement) as a function of frequency at an arbitrary position:

$$u(\omega) = w(\omega)e^{-i\omega t} \cdot \mathbf{n} \tag{1.2.21}$$

where $w(\omega)$ is a wavelet function and **n** is the ray propagation unit vector such that $A = w(\omega)\mathbf{n}$. Applying the Γ operator to this gives the equation for a split waveform, u_s:

$$u_s(\omega) = w(\omega)e^{-i\omega t}\Gamma(\phi, \delta t) \cdot \mathbf{n} \tag{1.2.22}$$

where ϕ is defined as the angle between $\hat{\boldsymbol{f}}$ and **n**. This equation is the mathematical foundation that is used when forward modelling the effect of anisotropy on a synthetic shear wave. Defining the tensor:

$$\delta T = \frac{\delta t}{2(\hat{\boldsymbol{f}}\hat{\boldsymbol{f}} - \hat{\boldsymbol{s}}\hat{\boldsymbol{s}})} \tag{1.2.23}$$

we can now write Γ as:

$$\Gamma = e^{-i\omega\delta T(\phi,\delta t)} \tag{1.2.24}$$

In order to estimate values for ϕ and δt for a given split waveform, u_s, Silver and Chan [1991] search for the inverse shear operator, Γ^{-1} that will return the unsplit wave in equation 1.2.21. As is evident in 1.2.19, the operator is unitary, meaning that the inverse is also the complex conjugate, Γ^*. To find Γ^{-1}, a search amongst possible ϕ and δt is undertaken in order to find the parameters that return the most linear, and therefore unsplit, particle motion. The linearity of a particle motion function is assessed by calculating the eigenvalues of its two dimensional time-domain covariance matrix. The covariance matrix between two orthogonal components of ground motion, for any pair of splitting parameters ϕ and δt, is defined as:

$$c_{ij}(\phi, \delta t) = \int_{-\infty}^{\infty} u_i(t)u_j(t - \delta t)\mathrm{d}t \qquad i, j = 1, 2 \tag{1.2.25}$$

For a linear shear wave, c will have only one nonzero eigenvalue $\lambda_1 = E_u = \int_{-\infty}^{\infty} w(t)^2\mathrm{d}t$ with a corresponding eigenvector **n**. In the presence of anisotropy, c will have two nonzero eigenvalues, λ_1 and λ_2, unless $\phi = n\pi/2$ $(n = 0, 1, 2, \ldots)$ or δt is zero. The processes of finding the best Γ^{-1} will therefore involve searching for the corrected seismogram $\tilde{u}_s(\omega) = \Gamma^{-1} \cdot u_s(\omega)$ that returns the most singular covariance matrix. For any pair of splitting parameters, the covariance matrix $\tilde{c}(\phi, \delta t)$ for the rotated and shifted seismograms may be expressed in terms of the covariance $c(\delta t)$ of a reference coordinate system (e.g. N-S, E-W) with the components:

$$\begin{aligned} \tilde{c}_{11}(\phi, \delta t) &= \int_{-\infty}^{\infty} \tilde{u}_1^2(t + \delta t/2)\mathrm{d}t = \tilde{c}_{11}(\phi, 0) \\ &= R_{1i}(\phi) c_{ij}(0) R_{1j}(\phi) \end{aligned} \tag{1.2.26}$$

$$\begin{aligned} \tilde{c}_{22}(\phi, \delta t) &= \int_{-\infty}^{\infty} \tilde{u}_2^2(t - \delta t/2)\mathrm{d}t = \tilde{c}_{22}(\phi, 0) \\ &= R_{2i}(\phi) c_{ij}(0) R_{2j}(\phi) \end{aligned} \tag{1.2.27}$$

$$\begin{aligned} \tilde{c}_{11}(\phi, \delta t) &= \int_{-\infty}^{\infty} \tilde{u}_1(t + \delta t/2)\tilde{u}_2(t - \delta t/2)\mathrm{d}t \\ &= R_{1i}(\phi) c_{ij}(\delta t) R_{2j}(\phi) \end{aligned} \tag{1.2.28}$$

$$\tilde{c}_{21}(\phi, \delta t) = \tilde{c}_{12}(\phi, \delta t) \tag{1.2.29}$$

where **R** is a rotation tensor that handles the coordinate change between the reference frame and the orthogonal fast and slow polarization directions that are being tested for. Since there will always be noise when applying this technique to recorded shear waves, the covariance matrix may never actually become singular, so the grid search technique should therefore look for $\tilde{c}$ which is nearest to singular. Silver and Chan [1991] approach this problem by finding the global minimum of the second eigenvalue, λ_2^{min}, within the parameter space being searched over. Error estimation for this method uses the fact that, for an n-point discrete time series, λ_2^{min} is the sum-of-squares of a noise process with an assumed χ^2 distribution. For ν degrees of freedom and k (i.e. 2- ϕ and δt) parameters, we define the confidence region at the α confidence level (e.g. $\alpha = 0.05$ for a 95% confidence level) as:

$$\frac{\lambda_2}{\lambda_2^{min}} \leq 1 + \frac{k}{\nu - k} f_{k,\nu-k}(1-\alpha) \tag{1.2.30}$$

here f is the inverse of the F-distribution. ν is a quantity that depends on the instrument response and noise spectrum, and is usually much smaller than n. Determination of ν uses a function based upon constructing estimators of filter moments from the observed data and is described in Walsh et al. [2013] (NB: the formulation given in Silver and Chan [1991] was found to overestimate the number of degrees of freedom by a factor of approximately 4/3). To summarise, parameter estimation for observed shear waves can be performed using a grid-search of splitting parameters ϕ and δt and finding the conditions in which the covariance of the rotated displacement vector is most singular, in this case by minimising the eigenvalue λ_2.

1.2.4 MFAST

One of the major benefits of applying the method of Silver and Chan [1991] is that its systematic approach reduces problems with subjectivity inherent in other approaches [Teanby et al., 2004]. The method has been ensconced in MFAST [Savage et al., 2010a], an automatic SWS analysis process which has been used to obtain virtually all SWS measurements used in this thesis. Since the steps that MFAST takes are illustrative of some of the limitations faced when determining SWS parameters, a brief overview of them will be presented here.

The main difficulty of the Silver and Chan [1991] method, as identified by [Savage et al., 2010a], is the fact that splitting parameter determination for observed data depends on both the window and filter used while preprocessing the data. Depending on the choice of window, the analysed waveform may have a significant component of the *P*-wave energy that dominates the seismogram before the *S*-wave arrival, or even other unwanted phases arriving after the fast wave arrival. Poor choice of window and filter may lead to cycle-skipping, a phenomenon in which the alignment of fast and slow *S*-waves (and therefore δt) has a factor of $T/2$ ambiguity, for a dominant period of T, due to the oscillatory nature of seismic wave arrivals.

The MFAST technique performs the Silver and Chan [1991] analysis over multiple measurement windows, and cluster analysis is used to determine the best window with the most stable solution to the inverse splitting operator problem. It should be noted that the window position is dependent on having a picked *S*-wave arrival, which is, up to the time of writing, virtually always done by hand and may be considered a likely source of error. For each window, broadband filters are chosen based on the signal-to-noise ratio (SNR) for the filtered data and the length of the window. The SNR is calculated by direct comparison between a window preceding the S arrival (the noise window) and one succeeding the S arrival (the signal window). MFAST discards all windows where the SNR is less than a minimum value. For the remaining windows, cluster analysis is used to search all pairs of ϕ and δt for clusters of measurements with similar values.

Finally, MFAST incorporates a grading criterion that aims to reduce the instance of cycle skipping in the final measurement, or otherwise ambiguous data, by detailed analysis of the frequency and distribution of measurement clusters over the suite of windows used. Also of concern when analysing SWS is the occurrence of null measurements [Silver and Chan 1991, Wüstefeld et al. 2008], which arise when the *S*-wave is polarised along the fast or slow orientation of the anisotropic medium (or if the medium is isotropic). MFAST determines null parameters by using the criterion $20\,\mathrm{deg} \leq |\phi - \alpha| \leq 70\,\mathrm{deg}$, where α is the the initial polarisation as determined after applying the inverse splitting operator. Null measurements are, due to their nature, often discarded when using splitting measurements to characterise anisotropy in the Earth, however they are of interest when modelling anisotropy as they provide a particular constraint on the relative orientation of the anisotropy to the propagation and polarisation of the shear wave. As noted by Savage et al. [2010a], null measurements are often given a poor grade by MFAST since different windows may return wildly varying ϕ or δt measurements. Three examples of MFAST results from analyses at MOVZ, a GeoNet station near Mount Ruapehu, New Zealand, are shown in figures 1.5, 1.6 and 1.7. The processing steps used by MFAST are graphically detailed, and results that are given different grades by the quality control (grades A, B and D) are shown. More details on the grading methodology, and the automatic technique in general, are given in Teanby et al. [2004] and Savage et al. [2010a].

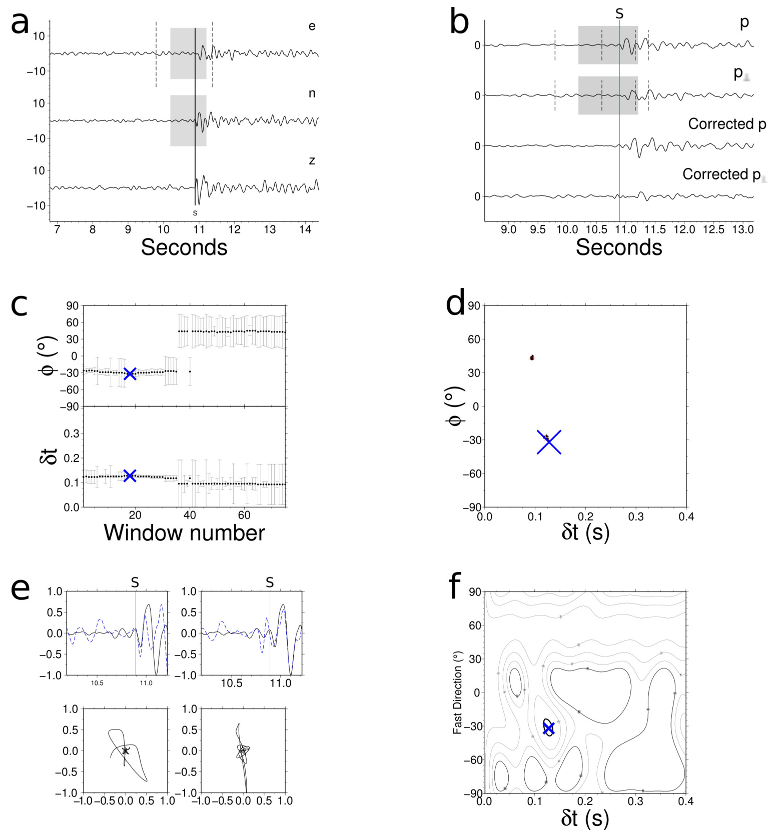

Figure 1.5: Sample high-quality (A grade) MFAST results for a single earthquake. (a) Filtered 3-component waveforms. The solid vertical line shows the S arrival, and the dashed vertical lines show the earliest start times (1) and latest end times for windows (4) used in the processing. (b) The same data rotated into the *S*-wave initial polarisation axis (p) and the axis perpendicular to it (p⊥), as determined by the analysis of Silver and Chan [1991]. Corrected p and corrected p⊥ have been corrected by the value of δt found using the same analysis. Note that there is very little energy on the cor p⊥ component indicating a very linear particle motion. (c) Values of ϕ and δt determined for each measurement window, on which cluster analysis is employed. (d) All clusters of five or more measurements. The large cross indicates the chosen cluster. (e) Waveforms (top) and particle motions (bottom) for the uncorrected (left) and corrected (right) waveform using the final determined splitting parameters. (f) Contour plot showing the smallest eigenvalue of the covariance matrix, λ_2^{min}, for the final chosen window. The black cross shows the position of λ_2^{min} in the parameter space. The thick contour represents the 95% confidence interval.

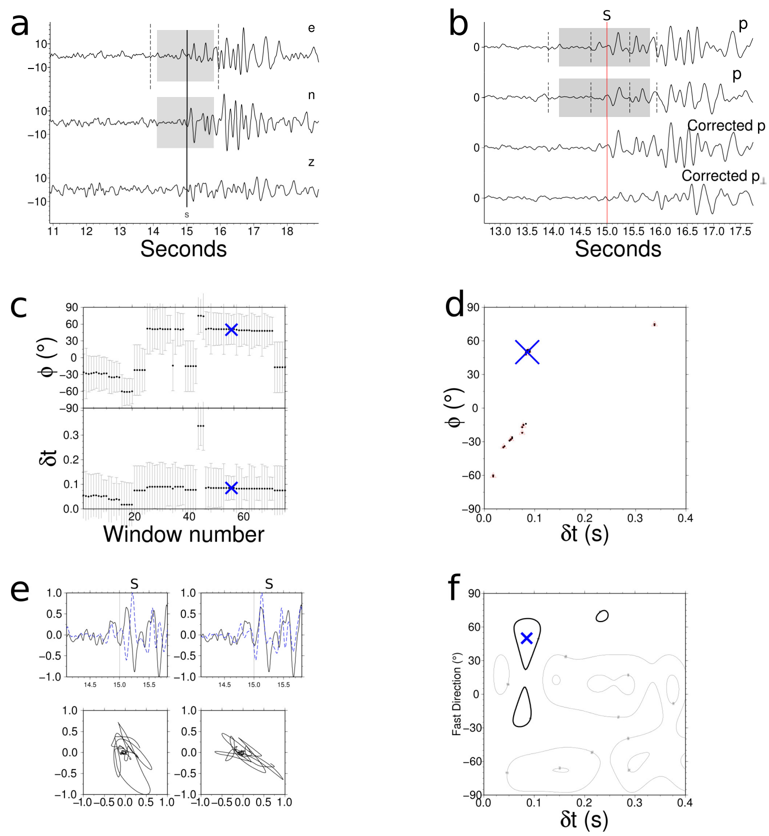

Figure 1.6: Sample mid-range quality (B grade) MFAST results for a single earthquake. (a) Filtered 3-component waveforms. The solid vertical line shows the S arrival, and the dashed vertical lines show the earliest start times (1) and latest end times for windows (4) used in the processing. (b) The same data rotated into the *S*-wave initial polarisation axis (p) and the axis perpendicular to it (p⊥), as determined by the analysis of Silver and Chan [1991]. Corrected p and corrected p⊥ have been corrected by the value of δt found using the same analysis. Note that there is very little energy on the cor p⊥ component indicating a very linear particle motion. (c) Values of ϕ and δt determined for each measurement window, on which cluster analysis is employed. (d) All clusters of five or more measurements. The large cross indicates the chosen cluster. (e) Waveforms (top) and particle motions (bottom) for the uncorrected (left) and corrected (right) waveform using the final determined splitting parameters. (f) Contour plot showing the smallest eigenvalue of the covariance matrix, λ_2^{min}, for the final chosen window. The black cross shows the position of λ_2^{min} in the parameter space.

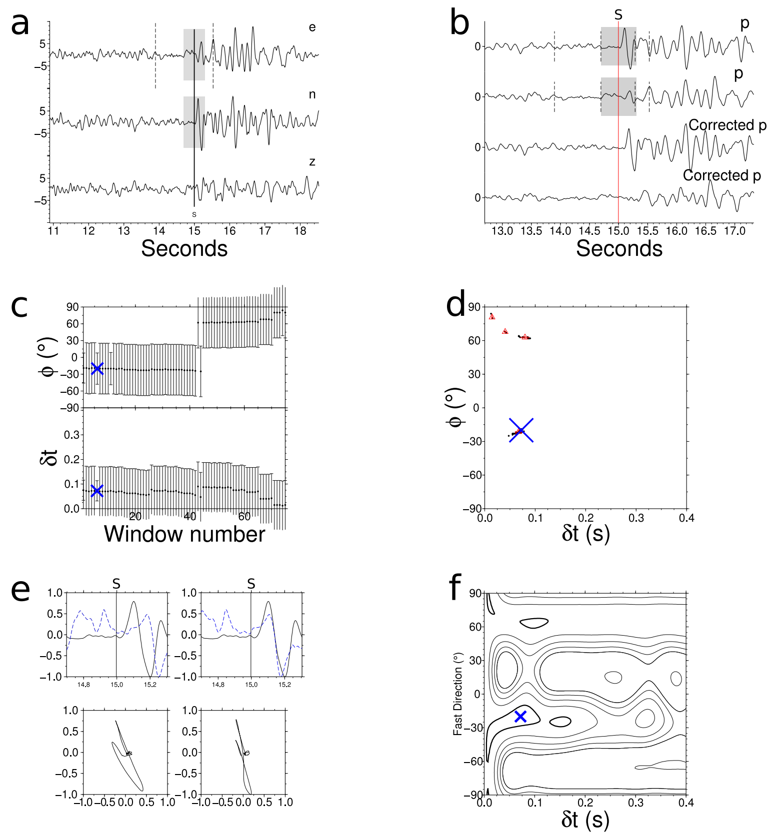

Figure 1.7: Sample low-quality (D grade) MFAST results for a single earthquake. (a) Filtered 3-component waveforms. The solid vertical line shows the S arrival, and the dashed vertical lines show the earliest start times (1) and latest end times for windows (4) used in the processing. (b) The same data rotated into the *S*-wave initial polarisation axis (p) and the axis perpendicular to it (p⊥), as determined by the analysis of Silver and Chan [1991]. Corrected p and corrected p⊥ have been corrected by the value of δt found using the same analysis. Note that there is very little energy on the cor p⊥ component indicating a very linear particle motion. (c) Values of ϕ and δt determined for each measurement window, on which cluster analysis is employed. (d) All clusters of five or more measurements. The large cross indicates the chosen cluster. (e) Waveforms (top) and particle motions (bottom) for the uncorrected (left) and corrected (right) waveform using the final determined splitting parameters. (f) Contour plot showing the smallest eigenvalue of the covariance matrix, λ_2^{min}, for the final chosen window. The black cross shows the position of λ_2^{min} in the parameter space.

1.3 The effects of Stress on Seismic Velocity

Seismic velocities in an isotropic rock are inherent properties that are dependent on its elastic moduli and density with the relationships [Love, 1927]:

$$V_p = \sqrt{\frac{\lambda + 2\mu}{\rho}} \qquad V_s = \sqrt{\frac{K + 4/3\mu}{\rho}} \tag{1.3.1}$$

Early theoretical [e.g. Biot 1955, Biot 1956, Biot 1956] and experimental work [e.g. Birch 1960, Nur and Simmons 1969a, Todd and Simmons 1972, Lockner et al. 1977] found that seismic velocities in porous rocks can change significantly when under confining stress or deformation. Since any external confining pressure will be counteracted by the pressure of the fluid contained within the voids, it is necessary to consider the confining pressure in terms of effective pressure, P_e, defined as the difference between the confining and the pore fluid pressure [Zoback, 2010]. The variation of seismic velocity with effective pressure is attributed to the act of pore or crack 'closure', as the degree of dilatation of the pores directly effect the overall rock mass' elastic stiffness (i.e. its elastic moduli); the rock is said to behave poroelastically. Based on laboratory studies there are a number of empirical relationships between effective pressure and velocity [e.g. Nur and Simmons 1969a] and effective pressure and seismic attenuation [e.g. Johnston et al. 1979]. Changes in seismic velocity due to changing pressure conditions have been observed in the Earth in a variety of situations, such as the periodic effects of the moon's tidal pull on the Earth [Yamamura et al., 2003] and fluid pressure changes associated with large earthquakes [Brenguier et al., 2014]. Depending on lithology and pore pressure, pore space and confining pressure can have an effect on seismic velocities up to a significant depth in the crust [Zatsepin and Crampin, 1997], as even though confining pressure is extreme (e.g. in the order of 150 MPa at a depth of 5 km using the assumption that $P_c = \rho g h$) cracks may still be open due to a low effective pressure.

In addition to isotropic velocity changes, porosity in rocks has a general dispersive effect on seismic waves travelling through them due to the fact that the stiffness of a poroelastic rock is rate dependent [Zoback, 2010]. This manifests as a frequency dependence on velocities and is typically an issue when comparing seismic records, which are between $\sim 0.1 - 20$ Hz for passive and $\sim 10 - 50$ Hz for active source, sonic logs from boreholes, which are typically ~ 10 kHz, and laboratory measurements, which are typically ~ 1 MHz. The dispersive effect that is found in porous rocks arises from pore fluid effects, specifically squirt flow [Dvorkin et al., 1995]. This describes the movement of pore fluid through interconnected pore space due to the conditions imparted on the rock mass by the passing seismic wave, which in turn affects the rock's stiffness. At very high frequencies there is insufficient time for localised fluid flow, meaning local pore fluid pressure increases will not dissipate. Waves travelling at these frequencies will therefore have a higher velocity than lower frequency waves because the increased pore fluid pressure contributes to the overall stiffness of the rock. It is worth noting that observational studies of crustal anisotropy and seismic velocity rarely consider this frequency dependence, since its effects on seismic velocity are minimal for the frequencies generally studied.

Stress-induced anisotropy

From the idea that effective pressure can affect isotropic velocity in poroelastic solids, it naturally follows that deviatoric stress can induce anisotropic velocity in them. As mentioned earlier, this is referred to as stress-induced crack anisotropy. The deviatoric stress field preferentially ‘closes’ pores and cracks which lie close to the plane normal to the maximum compressive stress direction (as in Figure 1.4). The relationship between the deviatoric stress field and induced anisotropy is the focus of Chapter 2, and will be discussed in more detail there. Due to this effect, SWS has been used to attempt to determine the current stress state of the anisotropic medium [e.g. Crampin 1985]. However, there is an issue as it is often impossible to tell whether observed SWS is being affected by the state of stress or the general orientation of existing fractures in the rock [e.g. Zinke and Zoback 2000].

Perhaps the most compelling evidence for stress induced anisotropy is the observation of time varying SWS measurements in conjunction with an expected change in stress conditions (i.e. before and after an earthquake or volcanic eruption), with the reasoning that the variations are happening too quickly for entirely new fracture sets (or indeed rock fabrics or layering, etc.) to develop. The difficulty, however, lies with isolating time-varying changes in anisotropy with spatial variation of anisotropy [Johnson et al., 2011]. Analysis of SWS data has provided evidence of stress changes associated with a number of earthquakes [e.g. Gao and Crampin 2004, Crampin et al. 2008], however the subject is somewhat controversial [e.g. Aster et al. 1990, Liu et al. 2008]. Several SWS studies performed at volcanoes, such as Ruapehu, New Zealand [Gerst and Savage, 2004], Soufrière Hills, Montserrat [Roman et al., 2011], Redoubt, Alaska [Gardine and Roman, 2010] and Asama, Japan [Savage et al., 2010b], identify time-varying anisotropy attributed to the volcanic processes active over the eruptive period. These provide another tantalising opportunity to use SWS to forecast eruptions. However there appears to be no universal technique, based on the current understanding of crustal anisotropy, with truly accurate predictive power.

1.4 Summary

In this chapter we have provided a broad overview of the physical theory of elasticity and the framework within which seismic velocities and anisotropy are considered. As was discussed in the thesis preface, each individual chapter will have an introduction of its own with chapter-specific information relevant to its content. The discussion of anisotropy, particularly the formulations of SWS parameters, is of particular relevance to chapters 2 and 3. Chapter 4, which deals with active source and ambient noise interferometry, contains concepts which are of little relevance to the study and modelling of shear wave splitting, and so the review of those techniques is limited to the chapter itself. However, the underlying concepts governing seismic velocities and their evolution in the Earth are important throughout the thesis.

Chapter 2

Modelling shear wave splitting due to stress-induced anisotropy; with an application to Mount Asama Volcano, Japan

2.1 Abstract

We use numerical modelling to investigate the proposed stress based origin for changing anisotropy at Mount Asama Volcano, Japan. Stress-induced anisotropy occurs when deviatoric stress conditions are applied to rocks which are permeated by microcracks and compliant pore space, leading to an anisotropic distribution of open crack features. Changes

to the local stress field around volcanoes can thus affect the anisotropy of the region. The 2004 eruption of Mount Asama Volcano coincided with time varying shear wave splitting measurements, revealing changes in anisotropy that were attributed to stress changes associated with the eruption. To test this assertion, we create a model that incorporates knowledge of the volcanic stress, ray tracing and estimation of the anisotropy to produce synthetic shear wave splitting results using a dyke stress model. Anisotropy is calculated in two ways, by considering a basic case of having uniform crack density and a case where the strength of anisotropy is related to dry crack closure from deviatoric stress. Our results show that this approach is sensitive to crack density, crack compliance, and the regional stress field, all of which are poorly constrained parameters. In the case of dry crack closure, results show that modelled stress conditions produce a much smaller degree of anisotropy than indicated by measurements. We propose that the source of anisotropy changes at Asama is tied to more complex processes that may precipitate from stress changes or other volcanic processes, such as the movement of pore fluid.

2.2 Introduction

Seismic anisotropy is increasingly being used as a geophysical tool to investigate the Earth's interior. Differential stress in the upper crust can create anisotropy through the closure of aligned cracks and mechanical discontinuities present in the rock mass [Nur and Simmons 1969b, Crampin 1994]. This relationship provides a convenient way to monitor stress orientations in the crust, especially when there is a lack of geodetic observations (GPS, InSAR, etc.) and studies of earthquake focal mechanisms are untenable. Possible changes in seismic anisotropy linked to volcanic activity associated with relatively short term (days to years) magmatic processes [e.g. Jónsson 2009] have been investigated as more complete data sets are collected [Savage et al. 1990, Munson et al. 1995, Bianco et al. 1998, Gerst and Savage 2004, Savage et al. 2010b, Johnson et al. 2010]. However, there have been few quantitative studies on the effect of stress on in situ anisotropy measurements. Understanding of how anisotropy around volcanoes changes over time provides a potential tool for forecasting volcanic activity, and in addition will provide insight into the role of stress-induced anisotropy in the upper crust.

We use computer modelling to investigate how changing stress conditions may affect crack induced anisotropy. To do this, we model shear wave splitting in earthquakes using the interaction between crack induced anisotropy and stress conditions during the 2004 eruptive episode at Mount Asama Volcano, Japan, and compare the results with shear wave splitting measurements made by Savage et al. [2010b]. We also demonstrate the application of the analytical relationship between stress and elastic anisotropy proposed by Gurevich et al. [2011] to the three-dimensional stress and ray path model. Future models can potentially incorporate other analytical or empirical stress-anisotropy relationships. Forward modelling of the effect of anisotropy on shear waves is carried out using a method adapted from that used by Abt and Fischer [2008], described later.

Seismic anisotropy arises from the presence of discontinuities, crystal preferred orientations and material heterogeneities in rocks. These types of features are all present in the brittle upper crust [e.g. Godfrey et al. 2000], however over the relatively short time periods over which volcanic activity occurs we do not expect any significant reorientation of crystal lattices or redistribution of rock material. The mechanical nature of discontinuities, however, has been shown to respond rapidly to the application of a non-uniform stress [Zatsepin and Crampin, 1997]. Small-scale discontinuities, such as cracks and grain contacts (microcracks), preferentially close relative to their alignment normal to the maximum compressive stress direction, so that the distribution of microcracks in terms of their effect on the overall elastic properties of the rock mass becomes anisotropic. This means that, as long as there is a degree of differential stress, particle motion parallel to the direction of maximum compressive stress experiences a higher elastic rigidity (i.e. elastic modulus) than orthogonal particle motion, resulting in higher velocities [Babuška and Cara, 1991]. In the case of shear waves, velocities in an anisotropic medium vary depending on their polarisation. Measuring the direction of the fast polarisation and the delay time from earthquake S-waves provides information on the orientation and strength of anisotropy present in the rock medium that the ray passed through. Microcracks are generally assumed to be randomly oriented and thus isotropically distributed over macroscopic scales, as opposed to large scale discontinuities (fractures) that tend to be in aligned sets. This is due to the nature of the microcracks being created during deposition (in the case of grain contacts in sedimentary rocks) or post-rock formation after initial high temperature and pressure conditions are lifted [Walsh, 1965], rather than large scale fractures which occur due to more consistent tectonic forces.

There is an inherent ambiguity when analysing changes in anisotropy measurements from earthquake generated waves, as it is hard to determine whether changes can be attributed to temporally evolving conditions or to effects dependent on path or source conditions [e.g. Zinke and Zoback 2000, Johnson et al. 2011]. There may only be a relatively short period of time during which magma body inflation or deflation is occurring, limiting the number of available seismic events that sample these transient stress states. This makes distinguishing between temporal and spatial changes in anisotropy vital to attain a robust interpretation of data. In order to predict the spatial component of anisotropy expected to coincide with volcanic activity, Coulomb stress modelling has been used as an aid for comparative interpretation between measurements and the assumed stress field [Savage et al. 2010b, Johnson et al. 2011, Roman et al. 2011]. Two-dimensional tomography [Johnson et al. 2011] has also been implemented, however there is a comparative lack of three-dimensional models looking at stress-induced anisotropy in the crust and around volcanoes. A three-dimensional model will provide the potential to take into account not only the state of stress as it changes vertically and laterally, but also the propagation direction of the ray and the stress contribution from loading. By modelling shear wave splitting caused by stress in three dimensions, the contribution made by stress-induced anisotropy can be further constrained in order to aid future interpretation of splitting measurements.

2.3 Method

The method we use is a combination of finite element method stress modelling and numerical evaluation of ray paths, anisotropy and shear wave splitting. Firstly, we create a number of stress models using *a priori* knowledge about the region and the volcanic source, in this case an inflating dyke. Ray paths are then traced through the model space at which point various models and comparisons are performed. We look at stress-raypath interaction and calculate shear wave splitting along raypaths. The anisotropic elastic properties used to calculate shear wave splitting parameters are set along raypaths using the stress data and two different models from Hudson [1981] and Gurevich et al. [2011].

2.3.1 Stress Modelling

Stress changes are computed using the PyLith finite element code [Aagaard et al. 2007, Aagaard et al. 2013], which was specifically designed for modeling crustal deformation. An important feature for our work is the ability to model faults and/or dykes. We do not include the effect of topography on gravitational stresses because we are only interested in relative changes in the stress state. It is noted, however, that anisotropy due to topographic stress may affect ray propagation, which is not taken into account here. The seismic velocities and densities used to calculate the elastic properties of the model are the same as in the one dimensional model used to trace the seismic ray paths through the model, which will be detailed in the later section on ray tracing. PyLith allows for the modelling of the crustal volume using an elastic rheology, Dirichlet (displacement or velocity) boundary conditions, and kinematic fault interfaces that are applied to model various volcanic features. The dyke opening is modelled using kinematic fault conditions, in which along-strike displacement is set to zero and deformation is controlled using a plane-normal opening parameter. We model a background regional stress in all cases apart from those in which only the dyke stress, rather than the overall stress conditions, is needed. The parameters used for the dyke and for background stresses are outlined in sections 2.2.5 and 2.2.6, respectively. We apply fixed boundary conditions on all model faces other than the topographic surface.

The output is then re-gridded from a tetrahedral mesh to a regular cubic one at the desired resolution for input into the ray tracer and synthetic shear-wave splitting code. We use both 1000 m and 500 m grid sizes for this resampling. The higher resolution 500 m grid size is used for all model results shown here. The stress data are averaged over each new grid element and the principal stress magnitudes ($\sigma_1, \sigma_2,$ and σ_3) and corresponding direction cosines (three for each principal stress) are also calculated.

2.3.2 Seismic Ray Tracing

The model space for the ray tracing and subsequent anisotropy calculation consists of a three-dimensional ordered array of cubes, each of which are assigned uniform material properties. The resolution of the blocks governs the minimum resolvable features in the model. Model coordinates are normalised around the centre of the dyke feature being modelled, with depths being measured relative to sea level.

A one-dimensional subsurface seismic velocity model is used to trace ray paths through the model space. *P*-wave velocities around Asama inferred from an active source seismic experiment [Aoki et al., 2009] are averaged over each depth and then interpolated to the specified model depth increments (see table 2.1). *S*-wave velocities are found assuming a V_p/V_s of 1.7, after Savage et al. [2010b]. This velocity model is also used to constrain elastic data in the stress model. A further constraint about near-surface density at Asama is provided by cosmic-ray muon radiography [Tanaka et al., 2007]. For simplicity, we employ a one-dimensional density model that increases linearly with depth from 2500 kg m^{-3} at the surface to 3000 kg m^{-3} at 30 km below sea level.

Each ray path is traced through the model by finding incidence angles at set depth levels using the 1-D velocity model. This is achieved by iteratively evaluating successively finely spaced ray path angles until the path that has the station as the destination is found (see figure 2.1). A common ray approximation, where each polarised shear wave follows the same ray path, is assumed throughout the model.

Regional events occurring beneath 30 km, outside the model space, are traced using the same technique at a lower resolution using the 1-D velocity/density model, AK135 [Kennett et al., 1995], in order to find the location at which the ray path pierces the stress model boundary.

2.3.3 Stress and Anisotropy Calculations

We approach the subsequent modelling in three successive ways in order to investigate the influence of the magnitude and orientation of volcanic stress on anisotropy. Firstly, we

Table 2.1: The one dimensional S-wave velocity structure, in ms^{-1}, that was used in the model. Z denotes height above sea level. Density followed a simple linear relationship with depth from 2500 to 3000 kg m^{-3} from the top to the bottom of the model space.

Z (km)	V_p	Z (km)	V_p
3	2471	-14	3558
2	2509	-15	3577
1	2661	-16	3588
0	2656	-17	3596
-1	2982	-18	3606
-2	3288	-19	3616
-3	3440	-20	3625
-4	3483	-21	3634
-5	3474	-22	3643
-6	3480	-23	3652
-7	3490	-24	3661
-8	3492	-25	3670
-9	3473	-26	3679
-10	3449	-27	3688
-11	3444	-28	3697
-12	3477	-29	3706
-13	3524	-30	3715

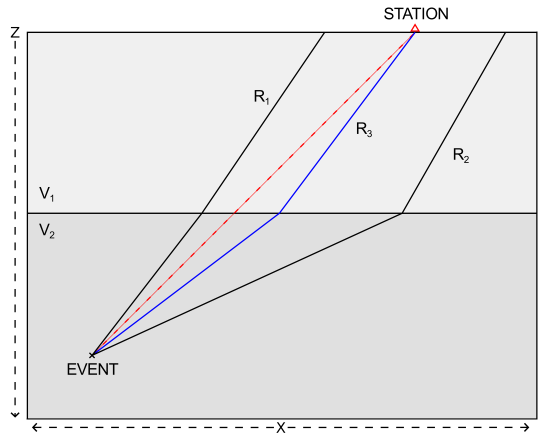

Figure 2.1: The red dashed line shows the earthquake to station distance. Three rays are traced with successively increasing incident angles with respect to the event. R_1 is projected, and the ray destination is closer to the event than the station. The incidence angle is increased, the result being R_2, whose destination is further away than the station. At this point incidence angles in between R_1 and R_2 are projected until ray R_3 is found, whose destination is suitably close to the destination station.

consider stress magnitudes in isolation in order to establish a measure of raypath-stress interaction. Secondly, we consider stress orientation in conjunction with an anisotropic model based on assumed crack densities as a basic approach to investigate the link between modelled stress orientations and measured fast directions, as well as crack density and measured delay times. Lastly, we look at the effect of both stress orientation and magnitude on modelled shear-wave splitting.

Combining stress models and the traced ray paths allows us to quantify, for each ray, the range of stress magnitudes in the raypath vicinity due to dyke inflation. Under the assumption that stress is the source of anisotropy changes in the crust, it is useful to know to what degree the stress field is perturbed by volcanic sources for each raypath. Hypothetically, greater stress magnitudes from the dyke source would result in a more pronounced effect on shear wave splitting. In the simplest case of stress-induced anisotropy arising from crack closure (all else being equal), the magnitude of a stress pertubation in a volume should correlate well with the magnitude of anisotropy change. This analysis gives insight into stress interaction with raypaths which can then be compared with the shear-wave splitting measurements to assess the relationship between the two.

To be able to model anisotropic effects on a shear wave, its medium's elastic properties must be calculated. Hudson [1981] provides first order relationships between crack density (ϵ) and the stiffness tensor (C_{ijkl}) for a rock with an aligned set of circular cracks. These are valid at dilute crack concentrations ($\epsilon \ll 1$). They are characterised by the isotropic stiffness tensor, C^{iso}, defined by the rock's Lamé parameters, modified by some constant, C^{an}, such that:

$$C_{ijkl} = C^{iso} + C^{an} \tag{2.3.1}$$

Due to its symmetry, the fourth order elastic tensor can be defined as a second order matrix (see Appendix A). For dry cracks, the non-zero elements of C^{an} are:

$$C^{an}_{11} = C^{an}_{12} = C^{an}_{21} = C^{an}_{22} = -\frac{4}{3}(\epsilon)\frac{\lambda^2(\lambda+2\mu)}{\mu(\lambda+\mu)} \tag{2.3.2}$$

$$C^{an}_{13} = C^{an}_{31} = C^{an}_{32} = C^{an}_{23} = -\frac{4}{3}(\epsilon)\frac{\lambda(\lambda+2\mu)^2}{\mu(\lambda+\mu)} \tag{2.3.3}$$

$$C^{an}_{33} = -\frac{4}{3}(\epsilon)\frac{(\lambda+2\mu)^3}{\mu(\lambda+\mu)} \tag{2.3.4}$$

$$C^{an}_{44} = C^{an}_{55} = -\frac{32}{3}(\epsilon)\frac{\mu(\lambda+2\mu)}{(3\lambda+4\mu)} \tag{2.3.5}$$

where λ and μ are the Lamé parameters of the medium, and ϵ is crack density, or Na^3, with N being the number density of cracks and a being the mean crack radius. For fluid filled cracks a different formulation for the C^{an} matrix is derived based on a model in which shear traction on the crack is zero and there is only displacement in the transverse direction [Hudson, 1981]. In this case, the non-zero elements of C^{an} are:

$$C_{44}^{an} = C_{55}^{an} = -\frac{32}{3}(\epsilon)\mu\frac{\lambda + 2\mu}{3\lambda + 4\mu} \tag{2.3.6}$$

C_{ijkl} can then be calculated for a given ϵ using Lameé parameters derived from seismic velocity and density data. A number of models are created in which different values of ϵ, which are constant throughout the model space, are used. According to Hudson [1981], errors in the approximation used to produce these relationships propagate as ϵ^2. For example, a basalt with $\lambda = 30$GPa and $\mu = 22$GPa, assuming $\epsilon = 0.05$, has an error of approximately ± 0.19GPa.

Finally, we incorporate stress magnitude and orientation into the determination of the medium's elastic properties using the analytical relationship developed by Gurevich et al. [2011]. This differs from Hudson's method by calculating the perturbation from the isotropic rock state using stress magnitude as a scaling factor. It is assumed that all cracks are identical and can be described by their area and the ratio between their normal and tangential excess crack compliance (which defines the response of the crack to an applied strain). In this case, the underlying framework of determining crack-induced elastic anisotropy is the non-interactive approximation made by Sayers and Kachanov [1995], which is based on the assumption that there are no stress interactions between cracks. The accuracy of this approximation holds only if the positions of the cracks are random, as the presence of cracks in some pattern of alignment will have an overall effect on the average stress field. The change in compliance due to the presence of cracks given by Sayers and Kachanov's approach is:

$$\Delta S_{ijkl} = \frac{1}{4}(\delta_{ik}\alpha_{jl} + \delta_{il}\alpha_{jk} + \delta_{jk}\alpha_{il} + \delta_{jl}\alpha_{ik}) + \beta_{ijkl} \tag{2.3.7}$$

where α_{ij} is a second-order tensor defined as:

$$\alpha_{ij} = \frac{1}{V}\sum_r B_T^r n_i^r n_j^r S_r \tag{2.3.8}$$

And β_{ijkl} is a fourth-order tensor defined as:

$$\beta_{ijkl} = \frac{1}{V}\sum_r (B_N^r - B_T^r) n_i^r n_j^r n_k^r n_l^r S_r \tag{2.3.9}$$

where B_N^r is the normal and B_T^r the shear crack compliance term for the r^{th} crack in volume V, n_i^r is the i^{th} component of the r^{th} crack normal and S_r is the crack area.

Gurevich et al. [2011] express the dependence of tensors α_{ij} and β_{ijkl} as a function of stress using the following relationship between stress and specific crack area, $s = \Sigma A^r/V$, at a given orientation:

$$s = s^0 \exp(\sigma_n/P_c) \tag{2.3.10}$$

where s^0 is the specific area of all cracks before any stress is applied, σ_n is the normal stress traction acting on the crack surface, and P_c is some characteristic pressure at which cracks will close. Substituting this relationship into formulation for tensors α_{ij} and β_{ijkl}

gives solutions that provide the stress-dependant compliance tensor, S_{ijkl}. This tensor, containing 5 independent coefficients and thus having hexagonal symmetry, can be calculated using the isotropic rock compliance, the stress state, and the crack compliances. The corresponding stiffness tensor is the inverse of the compliance tensor.

There are several assumptions that have been made in this analytical approach, discussed by Gurevich et al. [2011]:

1. The rock is assumed be rheologically elastic, an assumption also used by the stress model. This assumption is more problematic when considering volcanic processes, as rocks surrounding magma chambers will undergo a degree of thermomechanical weakening, and studies have found that taking a viscoelastic approach to modelling rheology can significantly reduce the magma chamber pressures needed to match ground deformation when compared to elastic models [e.g Newman et al. 2006, Del Negro et al. 2009]. Stress may also cause failure in rocks, and even in low stress conditions heterogeneities may serve to concentrate stress and produce local cracking. However, since the volcanic source mechanics are previously determined inputs in this model, viscoelastic effects on the rock anisotropy due to thermomechanical weakening will be confined to raypaths that pass nearby the magma source. Otherwise, assuming an elastic rheology is considered applicable to well-consolidated rocks when applied stresses, particularly deviatoric stresses, are small (below 10 to 30 MPa) [Gurevich et al., 2011].

2. The sole cause of anisotropy in the rock is assumed to be stress-aligned micro

cracks, meaning an unstressed rock would be isotropic. This neglects other forms of anisotropy, such as bedding planes, fractures, and mineral fabric. However, the aim of this model is to investigate how volcanic stresses would affect shear wave splitting, so model-observation variations consistent with structural effects will still provide useful data.

3. Due to the use of the non-interactive approximation of Sayers and Kachanov [1995], the cracks are assumed to be sufficiently sparse so that the overall rock compliance is simply a sum of the effects of individual cracks, disregarding any stress-interaction between cracks. The analysis done by Grechka and Kachanov [2006] shows that this is satisfactory for a range of irregular and intersecting approximately flat cracks up to substantial crack densities of at least $\epsilon = 0.15$.

4. The cracks are assumed to be dry, in the sense that there is no hydraulic interconnectivity between them. Changing the compliance ratio of the cracks would effectively simulate having a water, oil or any fluid other than air as crack-fillers, but any interaction between the cracks must be excluded. This is a strong assumption to make in volcanic regions such as Asama, due to a prevalence of hydrothermal systems at volcanoes [Aizawa et al., 2008], and a high water table in the Asama region [Kazama and Okubo, 2009]. This is perhaps the most significant of the assumptions, as microscale fluid flow between cracks is expected to modify the effect of small differential stress on overall anisotropy [Zatsepin and Crampin, 1997].

5. The exponential expression for specific crack area (s, see equation 2.3.10) is simplified to a linear relationship [see Gurevich et al. 2011]. This assumption has the effect of limiting the model accuracy to stresses that are small compared to the crack closing pressure. In our models, we approached this by setting maximum compressive stress to the crack closing pressure in the equations governing rock anisotropy for model blocks where the stress exceeds the closing pressure, in order to avoid a breakdown in the linear approximation.

2.3.4 Determining shear wave splitting parameters

In order to find the shear wave splitting parameters of a ray path, the incremental anisotropic effects on the seismogram for paths through each block that the ray travels through was calculated. Then the method of Silver and Chan [1991] was applied to calculate the splitting parameters from the predicted seismogram at the receiver. We adopted the method of calculating shear phase particle motions used by Fischer et al. [2000] and Abt and Fischer [2008]. For each ray segment, the Christoffel matrix was defined as Babuška and Cara [1991]:

$$m_{il} = \frac{1}{\rho}(C_{ijkl}n_j n_k) \tag{2.3.11}$$

Where ρ is the density, and n_j and n_k are the ray path's directional cosines. The three eigenvalues of the Christoffel matrix are related to the anisotropic velocity and polarisation properties of the wave. Given that $\lambda_1 > \lambda_2 > \lambda_3$, the fast shear wave component velocity has the relation $V_f = (\lambda_2)^{\frac{1}{2}}$, and the slow component velocity has the relation $V_s = (\lambda_3)^{\frac{1}{2}}$, with the corresponding eigenvectors giving the respective polarisation directions. The time shift accrued for each ray segment, δt_n, is equal to $L(V_s^{-1} - V_f^{-1})$, where L is the segment length, and the fast direction, ϕ_n, is the fast polarisation direction eigenvector orthogonal to the raypath. The resulting particle motion, u, for a path with m ray segments is defined by Fischer et al. [2000] as:

$$u(\omega) = \Big[\prod_{n=1}^{m} R^T(\phi_n) D(\delta t_n) R(\phi_n)\Big] u_0(\omega) \tag{2.3.12}$$

where

$$R^T(\phi_n) = \begin{bmatrix} \cos\phi_n & \sin\phi_n \\ -\sin\phi_n & \cos\phi_n \end{bmatrix} \tag{2.3.13}$$

and

$$D(\delta tn) = \begin{bmatrix} e^{i\omega\delta t_n/2} & 0 \\ 0 & e^{-i\omega\delta t_n/2} \end{bmatrix} \tag{2.3.14}$$

The splitting parameters that best fit the ray path are those that, when applied to the split wave, return the most linear motion. This is achieved by finding the ϕ and δt values that produce the most singular covariance matrix (which is attained when the matrix has only one non-zero eigenvalue) [Silver and Chan, 1991].

The initial particle motion that is propagated through the model, u_0, is a simple sine wavelet. The most common frequency window used for the crustal splitting analysis done at Asama by Savage et al. [2010b] had a high pass of 3 Hz for local events (depth < 2.2 km below sea level), and around 1 Hz for regional events (depths between 40 and 156 km). We chose a wavelet with a frequency of 1 Hz to use in the model in order to represent a frequency found in the majority of frequency windows, whilst giving the wavelet an acceptable sample width (1000) for analysis.

Abt and Fischer [2008] performed a comparison between this particle perturbation method of calculating splitting parameters with calculations made using full synthetic waveforms generated using a pseudospectral approach. They considered a vertical boundary between two volumes with different anisotropic properties, finding that in the full-waveform case, interaction of the wave front with the boundary results in an observed difference in splitting measurements from the simple perturbation method, arising from waveform distortion and possible ray bending. These effects are most pronounced with large contrasts in effective velocity. This may present a problem for stress model examples where the volume affected by a significant stress perturbation is comparable to the model element volume, as large changes in stress orientation and, to a lesser degree, magnitude may be expected, however since the modelled stress field expresses incremental spatial variations these effects will diminish with higher block resolutions.

2.3.5 Data

The data used in this study are earthquake and shear wave splitting measurements made by Savage et al. [2010b]. The earthquake data were collected from a total of 17 seismometers monitored by the Asama Volcano Observatory. Earthquakes were catagorised based on their depth as either 'regional' or 'local', with regional events occurring outside the Asama Volcano Observatory network (as determined by the Japan Meteorological Agency) but within 300 km of the volcano, and 'local' events, which occurred inside the network. Overall, 255 high quality shear wave splitting measurements from 97 local events at 17 stations and 1305 high quality shear wave splitting measurements from 276 regional events at 27 stations were analysed in Savage et al. [2010b]. S-wave arrivals for each earthquake were hand picked using expected S-wave arrivals determined using TauP [Crotwell et al., 1999] and the IASP91 arrival time model [Kennett and Engdahl, 1991]. Savage et al. [2010b] indicate that S-wave arrivals at seismometers near the summit of the volcano tend to have poor signal-to-noise ratios. Shear wave splitting measurements were determined using the MFAST algorithm (refer to sections 1.2.3 and 1.2.4). The average filter used for making the shear wave splitting results was a 3 Hz high-pass filter.

As is discussed in the results section, our modelling was performed using various subsets of this overall dataset with respect to the suitability of the data; specifically the 'local' events and regional events recorded at station AVO. The local events have characteristically short raypath lengths, between 0.6 and 5.2 km. As local events have raypaths that travel solely through crust in the vicinity of the volcano they are not influenced by anisotropy in the nearby mantle or lower crust. As these events originate from within the model volume, the anisotropy along the entire raypath can be accounted for without the need for assumptions about the anisotropy along the raypath outside the model. Shear wave splitting data from station AVO is used to perform an investigation into raypath-volcanic stress interaction, as changes in the dataset are strongly correlated with GPS deformation and constitute a strong focus of the discussion in Savage et al. [2010b].

2.3.6 Volcanic Stress at Mount Asama

Mount Asama is an active andesitic volcano situated in central Japan at which numerous vulcanian eruptions occurred at the summit crater during the first half of the 20th century (1910-1960), the frequency of which decreased after 1940. In the second half of last century eruptions were more infrequent, culminating in a moderately large (VEI of 2) eruption in 2004, and minor eruptions in August 2008 and February 2009 [Takeo et al. 2006, Savage et al. 2010b, Murase et al. 2007, Nagaoka et al. 2010]. The 2004 and subsequent eruptions have been well monitored and documented with both seismic and geodetic data, allowing the various magmatic sources to be determined [Takagi et al. 2005, Takeo et al. 2006]. This forms the basis for a first-order constraint on the volcanic stress to be used in the forward model.

In order to model the contribution to the stress field from processes associated with volcanism for input into the forward model, *a priori* knowledge of the magma plumbing system is required. The 2004 eruption at Mount Asama was accompanied by surface deformation and seismicity that has been used to infer a likely magma supply path beneath Asama [Takagi et al. 2005, Takeo et al. 2006]. Using geodetic and seismic data, Takeo et al. [2006] proposed that between June 2004 and March 2005, 6.8×10^6 m^3 of magma was intruded into a near-vertical dyke system trending broadly E-W and extending from 3 km to 5.1 km below sea level. This dyke model has subsequently been imaged as part of a zone of high seismic velocity that signifies repeated past dyke intrusion and cooling [Aoki et al., 2009]. In the final models used in the anisotropy modelling we use the dyke inflation parameters found by Takeo et al. [2006] and later corroborated by Aoki et al. [2013]. It is worth noting that Takagi et al. [2005] and Takeo et al. [2006] both include two small magma reservoirs along the magma ascent path, however we found that their stress contribution had little effect on the regional stress conditions with respect to the dyke stress contribution. Non-inclusion of these reservoirs, located at 1.5 and 2.2 km below sea level [Takagi et al., 2005] means that raypaths travelling close to the caldera of Asama may be poorly modelled.

2.3.7 Regional Stress

Any consideration of stress-induced anisotropy would be incomplete without the inclusion of the effects of the regional stress field. In this paper, the regional stress field will refer to the combined effects of confining pressure and tectonic forces. We assume the regional stress to be constant through time, in contrast to the stress field exerted by the volcano. Interaction between regional stress and local stresses from magma emplacement is a central theme in interpreting seismic anisotropy changes during volcanic eruptions [e.g. Gerst and Savage 2004, Johnson et al. 2011]. Roman and Heron [2007] studied the link between the distribution of volcano-tectonic earthquakes (VT) and Coulomb stress modelling of dyke inflation, finding that VT seismicity patterns are controlled by the regional stress regime and strength. They show that VT seismicity models for a dyke being emplaced in weakly and strongly deviatoric regional stress conditions fit well with VT data for eruptions at Mt. Usu and Miyake-jima volcanoes (both situated in Japan), respectively, as suited by their tectonic setting.

Confining pressures increase with depth due to lithostatic overburden [Turcotte and Schubert, 2002]. Increasing isotropic pressure will influence microcracks equally regardless of the orientation and thus would not be expected to affect the overall rock anisotropy. This notion is consistent with the analytical stress-anisotropy relationship used in this paper. However, increased crack closure at higher lithostatic pressures means that intrinsic lattice preferred orientations (LPO) will begin to dominate the elastic properties of the rock mass [Ji et al., 2013]. At the point at which microcracks and other discontinuities have been closed, seismic anisotropy must be assumed to arise from a rock's LPO. In essence, due to the relationship between depth and lithostatic pressure mentioned above, this means that a maximum depth, below which anisotropy cannot be attributed to the current state of stress, can be estimated. Assuming a crustal density of 2600 kg m^{-3} gives a depth of ~ 1.9 km for crack closing pressures of 50 MPa [Gurevich et al., 2011] and $\sim 3.9 - 7.7$ km for crack closing pressures of 100-200 MPa [Christensen, 1996]. Pressure gradients can be up to two times steeper in regions influenced by horizontal tectonic stresses in the upper lithosphere, or by flexurally-induced vertical loading in the lower lithosphere, resulting in a smaller maximum depth at which these pressures are reached [Petrini and Podladchikov, 2000]. The presence of an incompressible or near-incompressible fluid (such as water) that is confined to the microcracks would significantly increase the pressures at which the cracks would stay open [Zatsepin and Crampin, 1997].

In addition to confining pressure from rock overburden, there will be a component of differential stress exerted by tectonic forces. Folding and thrust belts demonstrate the historic presence of a differential stress field, and the occurrence of earthquakes is evidence of the ongoing existence of differential stresses, the configuration of which determines the mode of failure and faulting in geologic materials [Anderson, 1951]. Following the 'Wallace-Bolt' hypothesis (i.e. fault slip occurs in the direction of maximum resolved shear traction) [McKenzie, 1969], the orientation of the principal stress axes can be retrieved from the earthquake fault plane solutions. Townend and Zoback [2006] calculated principal stress orientations and a measure of their relative magnitudes in central Japan by inverting focal mechanisms for earthquake clusters (see figure 2.2).

Relative principal stress magnitudes were expressed as ϕ, such that:

$$\phi = \frac{\sigma_2 - \sigma_3}{\sigma_1 - \sigma_3} \tag{2.3.15}$$

Where σ_1, σ_2, and σ_3 are the three principal stresses. Values of ϕ approaching zero are indicative of stress conditions where $\sigma_2 = \sigma_3$, and $\sigma_1 \gg \sigma_2, \sigma_3$. As stress becomes isotropic, ϕ will reach unity.

The nearest maximum horizontal stress directions (σ_{Hmax}) calculated near Asama lie to the west of the caldera. Directions lie roughly parallel to the strike of the dyke (N64°W)

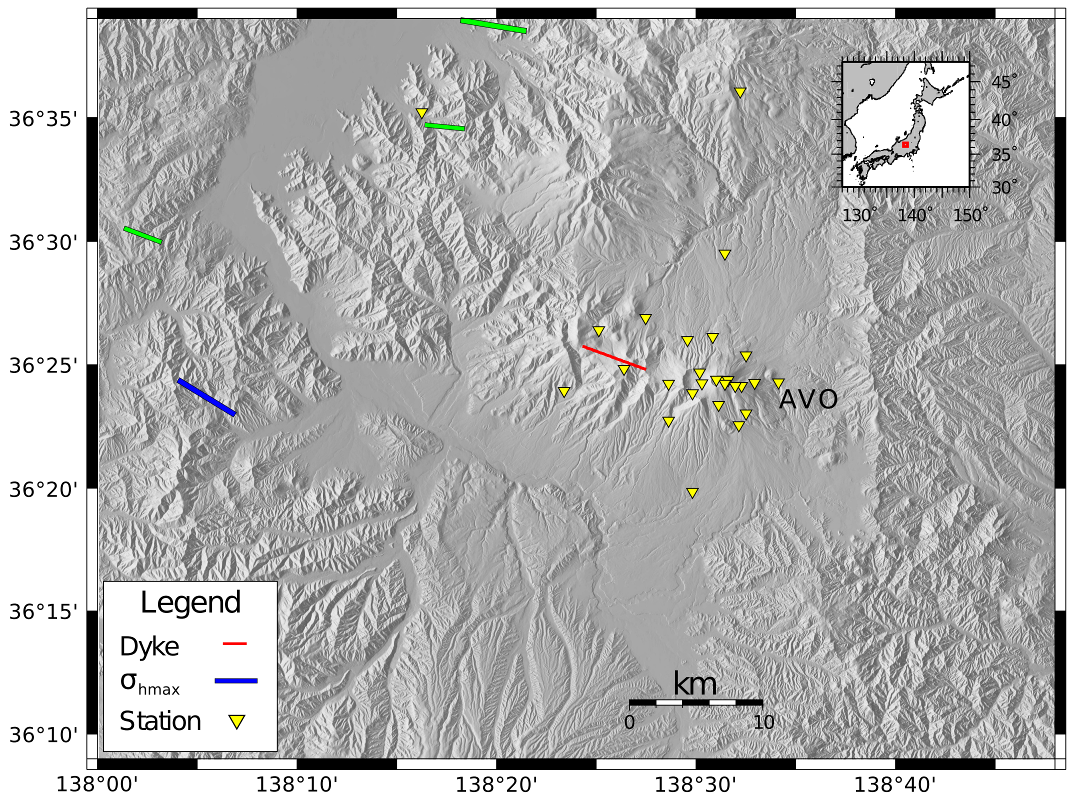

Figure 2.2: The Asama region in central Japan, showing σ_{Hmax} directions determined from earthquake focal mechanisms by Townend and Zoback (2006). Strike-slip and reverse stress states are shown in green and blue, respectively. Large symbols are measurements made from restricting the focal mechanism data to those with strike, dip, and rake uncertainties of $\leq 10°$, whereas small symbols represent measurements whose rake uncertainties are $> 10°$. Also shown is the regional seismic network situated around Asama, with station AVO indicated.

between N58°W and N84°W. Values for σ_{Hmax} calculated from deeper clusters of earthquakes ($\sim$ 8 km), which are all situated northwest of the caldera, trend slightly more east-west than the σ_{Hmax} value calculated from shallower earthquakes, which trends more northwest-southeast. The stress regime in the area is mainly strike-slip, with one measurement exhibiting a reverse stress regime. According to the Andersonian theory of faulting, having strike-slip and reverse stress regimes in proximity could be an indication of σ_2 and σ_3 being roughly equivalent, since the transition between the regimes represents an inversion between the two. The closest measurement to Asama has a ϕ of 0.0779 [Townend and Zoback, 2006], which reinforces this hypothesis. The mean value of ϕ for measurements by Townend and Zoback in the region shown in figure 2.2 is ~ 0.25.

2.4 Results

2.4.1 Anisotropy Model Testing

We tested the forward model by using effective elastic constants for both dry and fluid-filled cracked media given by Crampin [1985] (shown in table 2.2) as a benchmark. To do this, an arbitrary ray path configuration with a range of event-station azimuths and incidence angles was created (see figure 2.3).

In each case, there is a set of cracks dipping vertically, striking east-west. The forward model was configured to assign the same elastic constants to every model block. As can be seen in figure 2.4, the forward model was able to faithfully recreate the results that Crampin

Table 2.2: Elastic properties for rocks with dry and wet-filled cracks given by Crampin [1985]. Values are shown in GPa.

Dry Cracks		
$c_{1111} = 51.546$	$c_{2222} = 83.477$	$c_{3333} = 83.477$
$c_{1122} = 17.175$	$c_{2233} = 25.155$	$c_{3311} = 17.175$
$c_{1212} = 23.240$	$c_{2323} = 29.161$	$c_{3131} = 23.240$
Saturated Cracks		
$c_{1111} = 87.464$	$c_{2222} = 87.464$	$c_{3333} = 87.464$
$c_{1122} = 29.142$	$c_{2233} = 29.142$	$c_{3311} = 29.142$
$c_{1212} = 23.240$	$c_{2323} = 29.161$	$c_{3131} = 23.240$

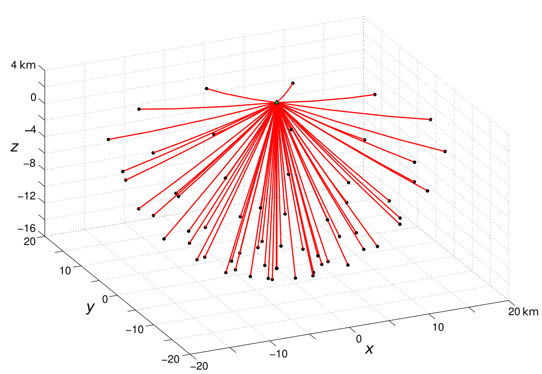

Figure 2.3: Ray path configuration used in the test cases. All ray paths have a length of 20 km, and are positioned to have straight-line surface incidence angles at 15 degree intervals from 0° to 75° at back-azimuths in 30o intervals. The surface of the model is at 4 km.

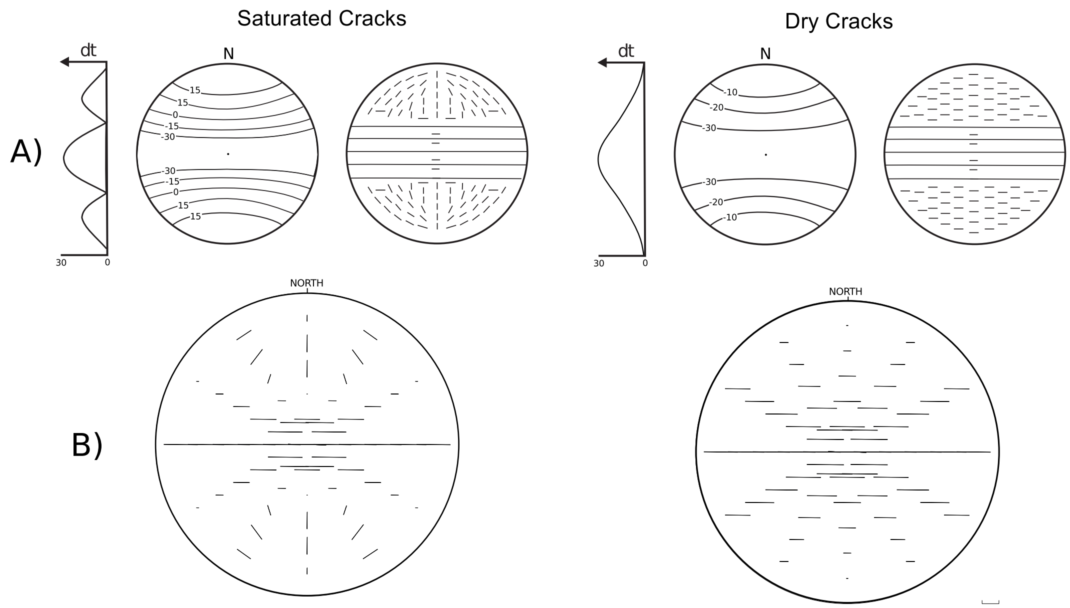

Figure 2.4: Equal-area stereographs showing shear wave polarisations and delay times for dry cracks and cracks saturated with a liquid. A) shows the original results from Crampin (1985), with delay time contours on the left with a north-south section plotted, and horizontal polarisations plotted as solid lines on the right. B) shows results from the model using the same elastic configuration. Fast shear-wave polarisations are plotted, with the size of each line representing the relative delay time.

made in 1985. Similar tests were done with the stiffness matrix, rotated to represent cracks with planes parallel to the horizontal. They display a tangential arrangement of polarisations where delay times increased at larger incidence angles for dry cracks. Saturated cracks display a more complex pattern, showing a polarisation flip between radial directions at low incidence angles and tangential directions for rays that are more steeply inclined to the plane of the cracks. This fast direction flip arises from the elastic properties of the rock and is a reversal of the fast and slow S-wave, with the crack-aligned polarised shear wave arriving later than the complementary polarisation, as opposed to the dry crack case, where the crack-aligned shear wave is always the first arrival.

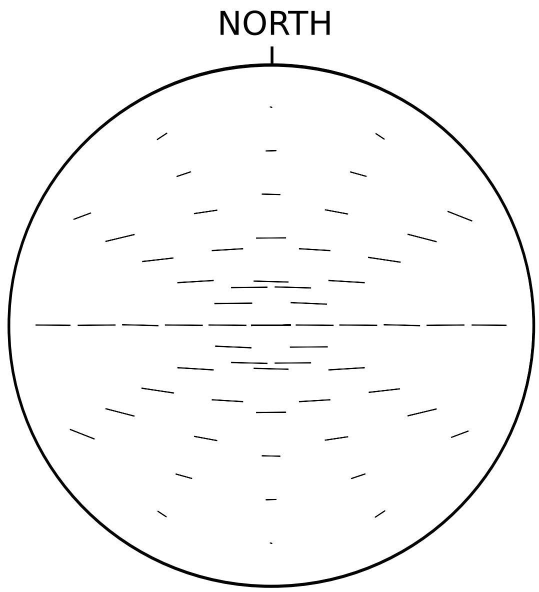

Figure 2.5: Equal-area stereograph showing model results for a model that has had 1 cm of shortening applied in the East-West direction. The parameters used in calculating the elastic properties of the subsurface were; $Z_{to} = 0.024GPa^{-1}, B = 1.76,$ crack closing pressure, $P_c = 19.2MPa, \mu = 20GPa$ and $K = 50GPa.$

In order to produce a comparable forward model using the stress-induced anisotropy calculations, a 50 km by 50 km by 34 km model space was created with a uniaxial stress of 12.5MPa oriented east-west. As before, a range of equidistant event/station pairs were used in order to observe the splitting effects in a range of azimuths and incidence angles. As can be seen in figure 2.5, the results are the same morphologically as the dry cracks shown in figure 2.4, except that fast directions are rotated towards the tangential direction near the north and south poles. As the derivation of the stiffness matrix for figure 2.5 is based on the assumption that the cracks are dry and non-interactive (similarly to the dry crack elastic properties in figure 2.4), the observed similarities in comparative delay times and fast directions for this raypath configuration are expected.

2.4.2 Stress model analysis

In order to investigate any relationship between ray path, dyke stress, and shear-wave splitting, we calculated stress models derived from the known dyke and material properties at Mount Asama and compared the dyke stress along various event raypaths to the respective shear wave splitting measurements. Dyke stresses were considered independently of gravitational and tectonic forces, since in this case we are exclusively assessing the relative change of stress, rather than the absolute degree of shear wave splitting along a ray path. This type of analysis can be done on events occurring deeper than the base of the model without the need for assumptions to be made about shear-wave splitting accrued before the ray's entrance into the model space. Data from Savage et al. [2010b] were analysed in this way. Here we show results from 32 regional events measured at station AVO between January 2004 and December 2005, and 35 local events that occurred between June 2004 and February 2005. In particular, we discuss results from AVO due to the original study observing a high degree of correlation between splitting measurements made there over time and ground deformation over the period spanning the eruption.

Stresses for a dyke opening model alone were unrealisticaly large, as high as 100 MPa at the dyke edges. Such high stresses are an artifact of the application of a uniform opening on the dyke plane in the model. Figure 2.6 shows the extent of the stress magnitudes, which decrease quickly with distance from the dyke face to roughly 10 MPa at less than 1 km from the dyke. Elastic parameters for the stress model were determined from the seismic velocity model of Aoki et al. [2009]. Results for regional events recorded at AVO and local

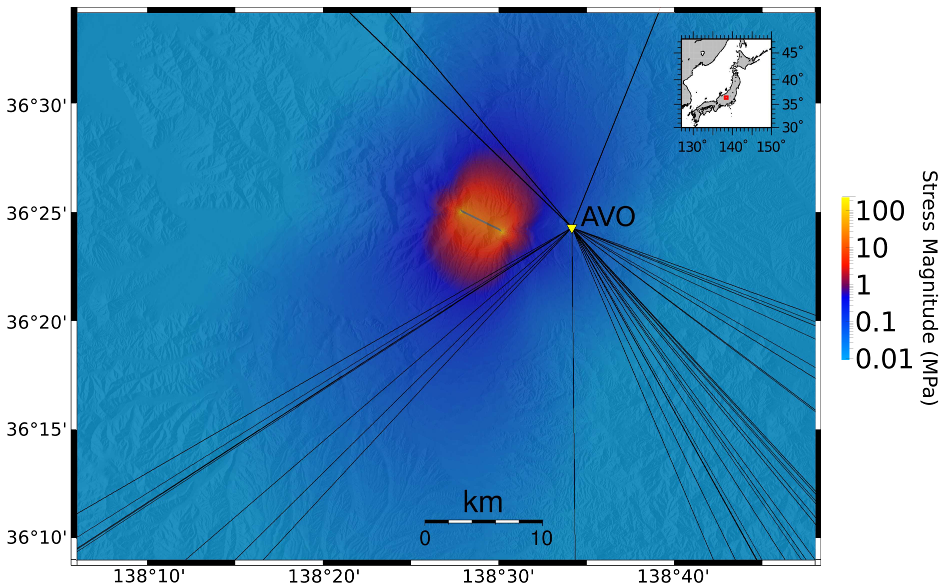

Figure 2.6: Stress model results showing maximum stress magnitudes created by the dyke associated with the 2004 eruption of Mount Asama, Japan, in a horizontal cross section 1km below sea level. Also shown are incoming rays at station AVO for events occurring in 2004. Earthquake depths range from 61 to 366 km.

events show no correlation between the dyke stress felt along the raypath and delay time. At station AVO, the strongest dyke stress conditions for the majority of the raypaths were felt at the depth of the dyke, between 3-5km deep. Results for regional events arriving at AVO (see figure 2.6) experience maximum compressive dyke stresses of 1.0-1.1 MPa, and local raypaths (see figure 2.7) experience similar maximum compressive dyke stresses of 0.9-1.1 MPa.

Dyke stresses were added to regional stress backgrounds during the stress model regridding process. In each case, the regional stress followed a one-dimensional relationship with depth. Isotropic stress increases with depth (where we assumed a constant density of 3000 kg m^{-3} in the relationship), as does deviatoric stresses with σ_1 and σ_3 being 2.5%, 5%,

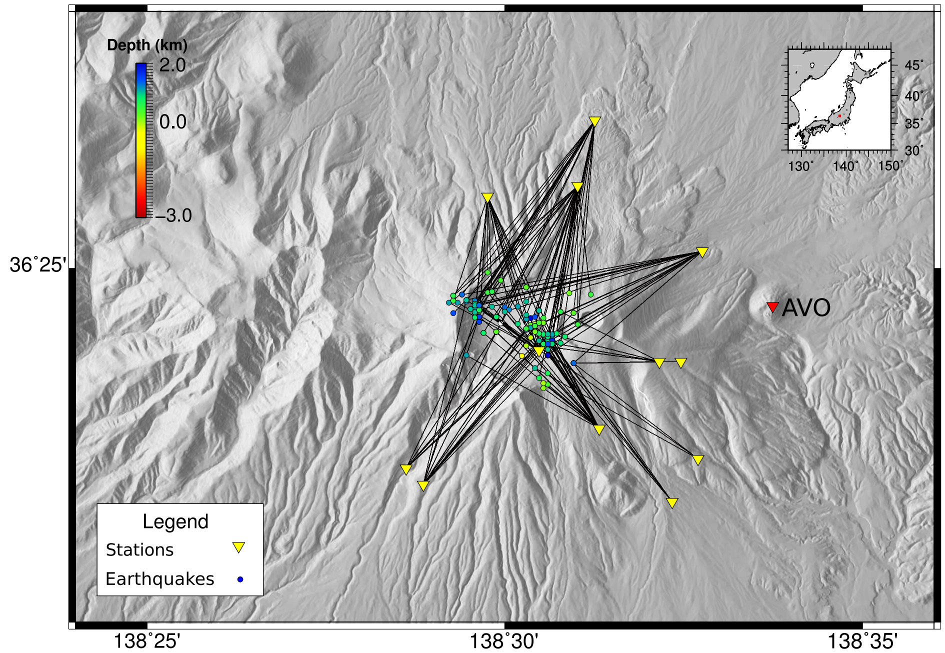

Figure 2.7: Local dataset for shallow earthquakes at Mount Asama. All earthquakes occurred between May 1st, 2004 and February 1st, 2005.

and 10% higher and lower, respectively, than σ_2. In each case, σ_2 was set by the same ρgh relationship as in the isotropic case. Figure 2.8 shows results indicating the ratio between magnitude of the deviatoric stress and the overall stress ($\Delta\sigma/P$). Generally, this was small at all depths apart from cells in close proximity to the dyke edges. For larger deviatoric stresses (20%), $\Delta\sigma/P$ near the dyke face is actually lower than the surrounding region, as the outward pressure directly counteracts the regional stress (see figure 2.8c).

2.4.3 Elastic Tensor

The elastic tensor of each block is the governing parameter for seismic velocity and therefore central to the results taken from this modelling. Taking the calculations from Hudson [1981]

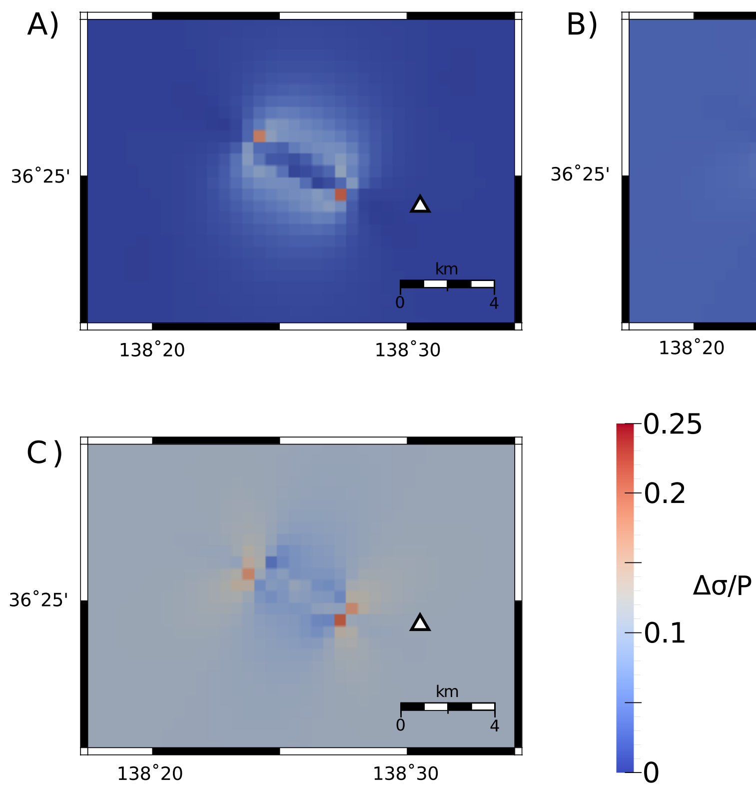

Figure 2.8: Stress model results showing the ratio between deviatoric stress magnitude ($\Delta\sigma$) and pressure (P) 1 km below sea level. The deviatoric stress magnitude is calculated as the difference between the maximum compressive stress magnitude and the average principal stress magnitude. Clockwise from top left, the images show A) the effect of dyke expansion in a lithostatic stress regime B) a strike slip stress regime where σ_1 is 5% greater than σ_3 and C) a strike slip regime where σ_1 is 10% greater than σ_3.

for both dry and fluid-filled cracks, synthetic splitting measurements were calculated for a range of crack densities and stress models. For the stress model, dyke stresses were added to regional stress backgrounds during the stress model regridding process, as discussed in section 2.3.1.

We tested the effects of using various forward models incorporating Hudson's elastic parameters on the data set of 35 local events, comprising 86 individual station-event pairs (see figure 2.7). Results for both dry and fluid-filled crack models show that synthetic fast directions were poorly aligned with measurements regardless of ϵ, with a mean model-measurement misfit of 45-55° (see figure 2.9). Increasing crack density made little impact on the fast direction, as the orientation of anisotropy is consistent whilst using the same stress model. Savage et al. [2010b] found misfits of 38-52° in a simple comparison between the measurements and stress directions found from Coulomb stress modelling of the dyke, as well as the two inflating magma chambers of Takagi et al. [2005]. Here, delay times were best modelled with ϵ values of 0.04-0.08, depending on the stress model used and whether dry or fluid-filled crack equations were employed. For the best fitting models the root mean square error of delay times was around 0.1 seconds, similar to the mean measured delay time for the events (see figure 2.9). As this approach assumes a constant crack density throughout the model, we found that there was a broad correlation between length of raypath and modelled delay times. Such a correlation, however, is not present in the measured data.

Comparison between different models were made by calculating the mean absolute

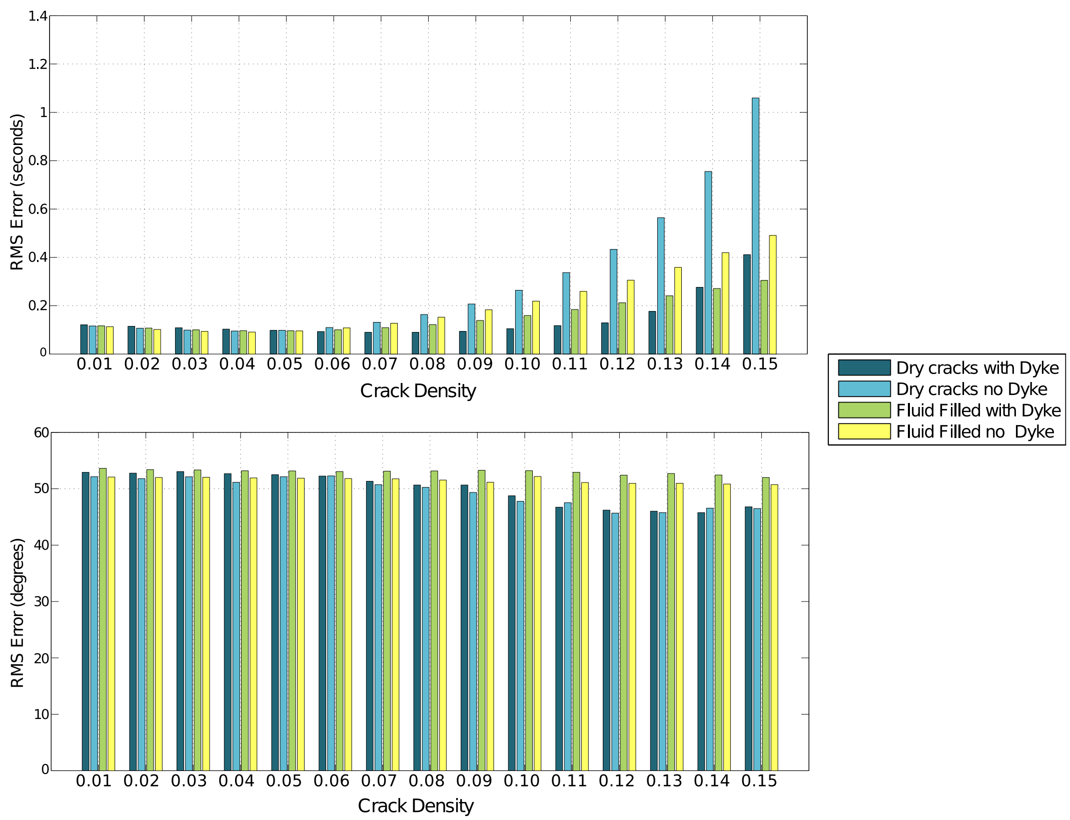

Figure 2.9: *Chart showing root mean square errors between modelled and real shear wave splitting measurements from local events at Mount Asama, comparing solutions at different crack densities (ϵ) for Hudson's fluid filled and dry crack calculations. The stress models used have increasing pressure with depth, according to $\rho g z$, with a regional stress with a differential value of 5% of the background pressure.*

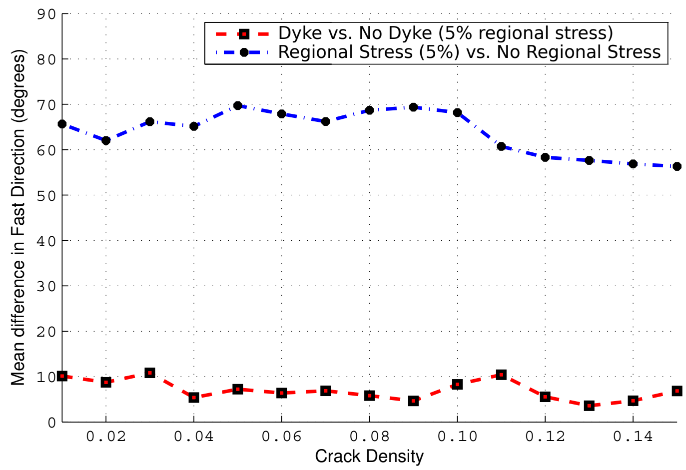

Figure 2.10: *A comparison of mean differences between modelled results. Red squares represent two models with a 5% differential regional stress with and without an inflating dyke and blue circles represent two models with an inflating dyke with and without the background stress. Results show that the presence of the differential regional stress is much more influential on fast directions than the dyke.*

difference between two sets of results, as such:

$$\text{Mean difference} = \frac{\sum_{i=1}^{N} |x_i^1 - x_i^2|}{N} \tag{2.4.1}$$

Where i is each individual measurement. Mean angular differences in fast direction between models having a regional stress where σ_1 was 5% larger than σ_3 (the smallest modelled) with and without the dyke added were between 5-10°, depending on the crack density used. In comparison, mean differences between two models both containing a dyke, with one having the differential regional stress as before and one without were 58-70° (see figure 2.10). This indicates that for these events, the inclusion of the differential regional stresses used is more significant than the dyke itself. For the larger differential regional stress used, at 20%, mean differences between models with and without a dyke were $< 5°$.

We also tested models using the analytical relationship between stress and anisotropy discussed in section 2.3.3, taking into account stress orientation and magnitude. Modelled delay times were invariably significantly smaller than those measured (see figure 2.11). This was due to a combination of short path lengths through a weakly anisotropic medium as well as stresses exceeding the theoretical crack closure pressure at relatively shallow depths. In the case of a non-isotropic background stress, modelled fast directions were dominated by the regional stress direction. Figure 2.12a and 2.12b show comparisons between models with and without dykes. Generally, differences between models were negligible for all regional stress considerations that were modelled. Results are quantised to intervals of 0.001 seconds due to that being the sampling frequency of the synthetic wave. The measured average of the data set was 0.10 seconds, and we consider delays to be significant only if they exceed 0.01 seconds, which is one order of magnitude greater than the model sampling frequency of 0.001 seconds, as well as being double the average standard error for the original. Figure 2.12c shows the model sensitivity to crack compliance; in all results shown in figure 2.12, a normal-to-tangential crack compliance ratio of 1.76 was used and increasing the tangential crack compliance resulted in greater modelled delay times.

The model was unable to account for the degree of anisotropy measured by stations at Asama. Local raypaths are of lengths between 0.6-5.2 km, with measured anisotropy values up to 0.4 seconds, averaging 0.11 seconds. The same raypaths give an average of 0.0012 seconds in models with a tangential crack compliance of 0.024 GPa^{-1} (figure 2.11). The average strength of anisotropy given by Savage et al. [2010b], calculated as

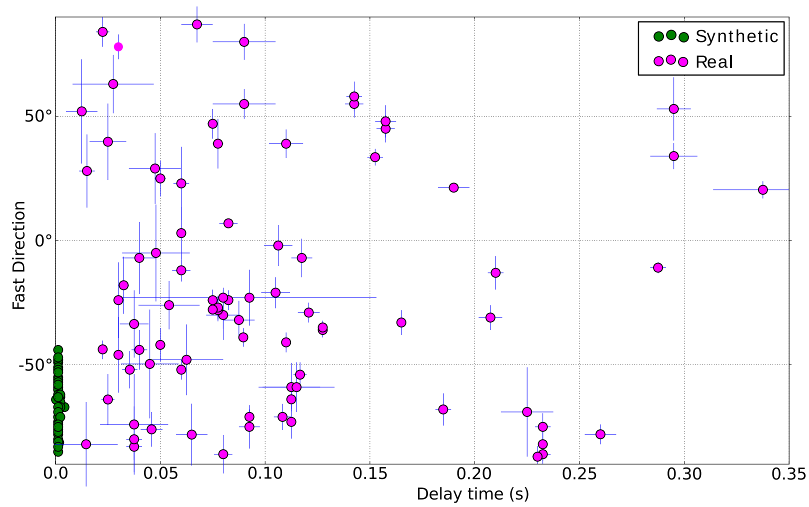

Figure 2.11: *Measured and modelled results from local earthquakes at Mount Asama that occurred around the 2004 eruption. Synthetic results, taken from a model with a tangential crack compliance value of 0.024 GPa^{-1} and a Z_{T0}/Z_{N0} ratio of 1.76 in a model with a dyke situated within a regional stress field where σ_1 is 5% greater than σ_3, were distributed near the regional stress direction (W70N) and had significantly smaller delay times than those measured.*

the fractional velocity ratio ($(v_1 - v_2)/v_1$; v_1 and v_2 being the fast and slow shear wave velocities, respectively), is 6%. Making the cracks significantly less stiff than those modelled by Gurevich et al. [2011] in order to test model sensitivity (using a tangential compliance value of 0.4 GPa^{-1}), results in an increase in delay times. However, no delays exceed 0.015 seconds. With the analytic solution for anisotropy used here, we find that highly deviatoric stress conditions are needed to produce such significant anisotropy. Using the test model parameters used to find the results of figure 2.5 (tangential crack compliance of 0.024 GPa^{-1} and a compliance ratio of 1.76), the maximum velocity ratio for a uniaxial stress of 12.5 MPa is 3.1%, with non-uniaxial stresses being significantly lower.

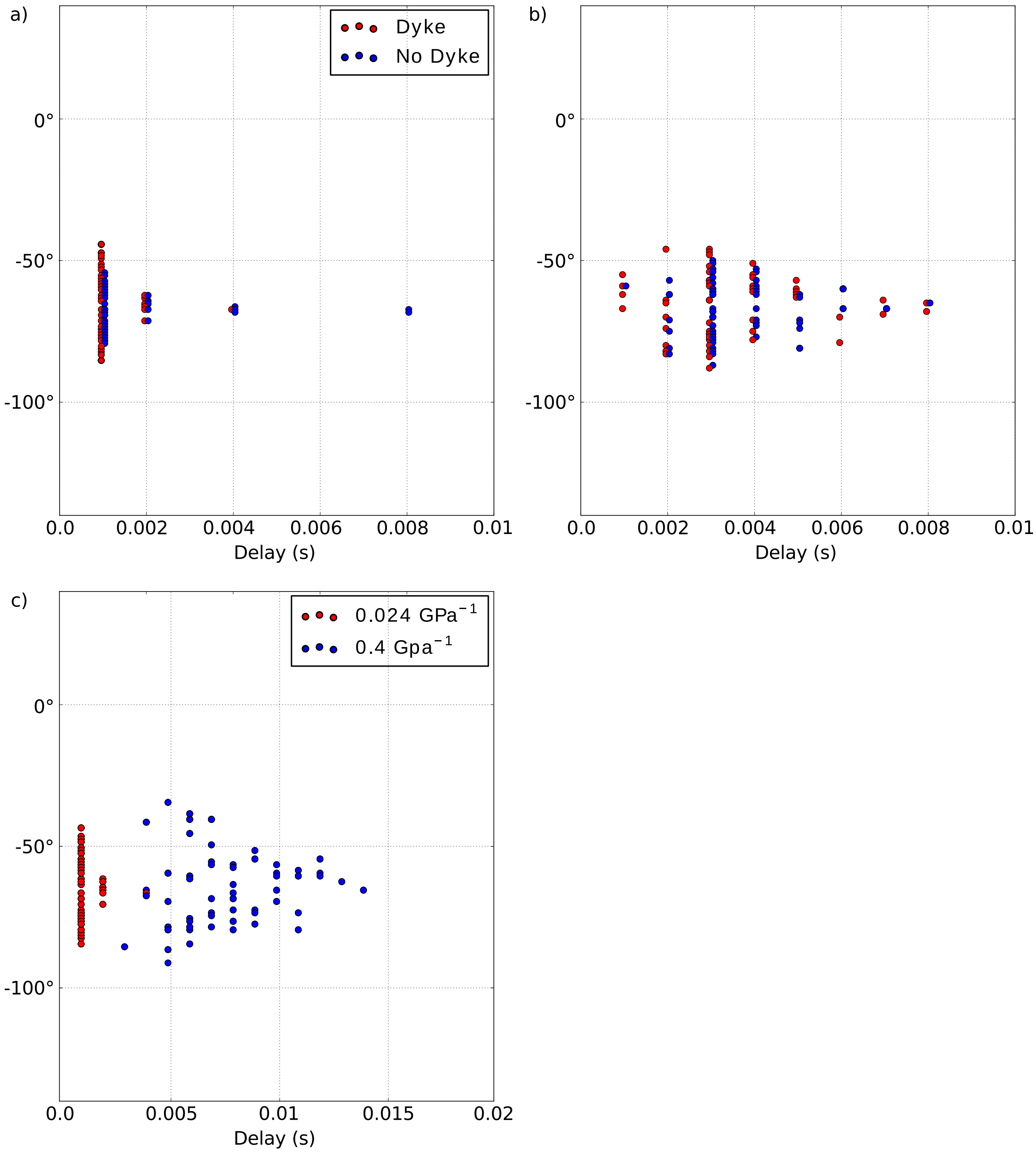

Figure 2.12: Model result comparisons. a) and b) show comparisons of synthetic measurements between models with and without a dyke for regional stress fields where σ_1 is 5% and 20% greater than σ_3, respectively. Tangential crack compliance in both plots is 0.024 GPa^{-1} c) shows the effect of increasing tangential crack compliance from 0.024 GPa^{-1} to 0.4 GPa^{-1}. Results are slightly offset for visual clarity. In each plot, datasets are offset by 0.1 ms for clarity.

2.5 Discussion

Using Hudson's calculations to derive elastic tensors gave the best fitting results at crack densities very similar to those derived from local earthquakes by Savage et al. [2010b] (4.4 x 10^{-2}). Errors between the model and measurements were relatively large, however the mean delay times were similar for models at the above crack density. We observe that the modelled fast direction RMS misfits are in the region of 10° larger than misfits found by the original study using comparisons between Coulomb modelling and fast directions. The same forward models also displayed more sensitivity to regional stresses than to inclusion of the dyke itself. This suggests that accurately defining the background stress conditions is an important step to a more comprehensive understanding of the interaction between volcanic stresses and anisotropy.

In models using the full analytic solution for dry crack anisotropy, modelled delay times were extremely low in comparison to measurements. Using a dry crack model such as this will necessarily underestimate the degree of anisotropy because lower stress conditions are needed to close an air-filled void than to close voids saturated with fluids which are near incompressible (i.e., water). This is because the original formulae for brittle rock anisotropy of Sayers and Kachanov [1995] makes an approximation that assumes a high normal crack compliance. If the cracks are filled with a fluid and there is microscale fluid flow between them this could have strong implications for modelling stress-induced anisotropy. Wave-induced flow between cracks will affect dispersion and attenuation [Chapman et al. 2002, Gurevich et al. 2010], as well as anisotropy [Collet and Gurevich, 2013]. On a longer time scale, this fluid flow may create conditions in which relatively small levels of differential stress can produce significant changes in anisotropy. This was concluded by Zatsepin and Crampin [1997], who posit that hydraulically isolated (in that fluid pressure is maintained at hydrostatic or more) sets of fluid-filled cracks may exist to depths of many kilometres. Our models show that the measured variations in anisotropy occur at distances to Asama where dyke stresses are quickly becoming small compared to expected lithostatic pressure, with or without a regional stress (see figure 2.7). Thus, if stress-induced anisotropy caused the measured changes at Asama [Savage et al., 2010b], then hydraulic interaction between cracks is likely to have occurred. A small differential stress, when applied to such a system, will produce a pressure gradient along which fluid migration can occur from cracks oriented perpendicularly to maximum compressive stress to those aligned parallel. This results in excess pore fluid pressure within the crack that is dependent on differential stress and the relative orientation of the crack [Zatsepin and Crampin, 1997]. If the fluid is near-incompressible, the total crack volume in the medium will not be significantly changed. Fluid under pressure entrained in cracks at depth will also prevent their closure despite increasing lithostatic pressure, provided no upward macroscale fluid diffusion can occur.

The above consideration is approximated by the approach using Hudson's formulations for fluid filled cracks, as strength of anisotropy does not depend on differential stress magnitudes. However it is unlikely that the strength of anisotropy is constant and, as evidenced by the unsatisfactory model fit, that it is entirely controlled by principal stress orientation. Strength of anisotropy may be strongly affected by the lithology, and formation and deformation history of the rock, as well as other features such as other stress sources, fractures, mineral fabrics, and rock unit interfaces. RMS errors for fast direction results shown in figure 2.9 show that, for Hudson models, fast directions are poorly modelled using stress directions. It is unclear whether a stress-oriented model that takes into account fluid-filled microcracks at depth would give a significantly better fit for measured fast directions (although it is considered unlikely given the small range of fast direction measurements found in the Gurevich models compared to the measured data; see figure 2.11). The hypothesised rise in strength of anisotropy would, however, likely make a significant improvement to the model fit for measured delay times. Again, difficulties in fitting observed measurements using models based on a purely stress-induced anisotropy regime arise from not considering other sources of anisotropy experienced by the raypaths. Hence, the focus of interpretation for these models should be on the change of anisotropy that can be brought about by stress changes associated with the volcanic eruption.

Considerations for Future Work

A logical development to this method is to use measurements made outside a volcano's active period to invert for anisotropic structure (using methods such as that of Abt and Fischer 2008, or Wookey 2012) and then applying a model such as Hudson's [1981], the APE model of Zatsepin and Crampin [1997], or a more generic model such as that of Love [1927], to find properties of the rock mass (e.g. crack density) from that. Providing a 'background' model of anisotropy in this way could be key to setting a benchmark from which subsequent measurements can be compared. This would potentially provide not only more robustness in using shear-wave splitting as an eruption forecasting tool, but also help to elucidate the source of temporally changing anisotropy as changes would be relative to what we already believe to be present. This is most important when attempting to interpret changes in measured anisotropy, especially when trying to forecast volcanic activity because data may be sparse.

As volcanic eruptions are often accompanied by changes to the spatial distribution and intensity of the volcanic hydrothermal system, changing fluid properties (both physical and chemical) could be a mechanism for dynamic anisotropy conditions associated with volcanic activity. Fluid flow and gas emission are very much affected by thermal conditions and subsurface permeability, in addition to changing stress properties. Studies on the stress-dependant compliance properties of volcanic rocks would be useful to investigate these effects. Detecting such changes can feasibly be done with seismic methods; V_p/V_s can be a proxy for fluid or gas saturation [Wang et al., 2012]. Johnson and Poland [2013] identified changes in shear wave splitting measurements and V_p/V_s at Mount Kīlauea associated with degassing of SO_2, rather than changes in stress. Angerer et al. [2002], using the APE model of Zatsepin and Crampin [1997] studied the effect of changing fluid pressure on crack content, seismic velocity and anisotropy of a dolomite reservoir, finding *S*-wave anisotropy changes of $\sim 5.8\%$ after injection of high pressure CO_2, as well as a 90° flip in fast polarisation to become stress-perpendicular.

Changes in anisotropy not due to stress changes should also be addressed. Dynamic changes of material filling cracks, and therefore their elastic properties, were not modelled here, although they may have a substantial effect on resultant anisotropy through the influences explained above. The aforementioned analytical solution only considers the bulk and shear moduli of the intact, isotropic rock. Naturally, the effective bulk and shear moduli of the resulting anisotropic material is changed depending on the distribution of open cracks. The solution for the anisotropic term in the stiffness tensor is factored by radial and tangential crack compliances, however the ratio between these compliances is poorly defined. Gurevich et al. [2011] give the ratio, $B_N/B_T = 1.76$ as found from fitting the rock physics model outlined in Angus et al. [2009] to results from tests made on a sample of Barre Granite. The same study by Angus et al. [2009] applied their fitting method to data on sedimentary rocks, finding that compliance ratios range between 0.0 and 2.0 and cluster around 0.6. In addition to microscale fluid flow, the contents of the microcracks are expected to alter B_N/B_T, as the change in compressibility of the fluid or gas in the crack will have a disproportionate effect on the normal compliance over the tangential compliance. Sayers and Han [2002] and especially Angus et al. [2012], while studying sedimentary rocks, find that ratios in dry samples and saturated samples are indeed different. Angus et al. [2012] showed crack saturation had the effect of tightly clustering ratios around 0.5, in comparison to dry samples that showed ratios distributed between 0.4 and 2.0. There is also the issue of the crack compliance value itself, which can significantly affect model results (see figure 2.12). These complications present a challenge when attempting to model complex anisotropic systems.

Finally, we have modelled the dyke emplacement using an elastic finite element method, which offers better control over the model space (i.e. the geometry of the dyke interface and surface topography) than Coulomb stress modelling. As already mentioned, viscoelastic deformation near the magma pathway would likely increase the needed pressure to produce the observed surface deformation. The converse of this is that viscoelastic deformation in an aureole around the dyke will act to reduce the magnitude of the static stress field. Currently it is difficult to quantify the combined effect on anisotropy of both stress and viscoelastic deformation. Furthermore, during the dyke emplacement process the stress state will evolve in a different way to modelling whole-dyke inflation, as has been done in our method. As a dyke is emplaced, magma overpressure is greatest at the edge that is propagating through country rock, producing large, localised stress magnitudes [Taisne et al., 2011], which may significantly alter the stress profile of the region.

2.6 Conclusion

We have developed a method for three dimensional modelling of shear wave splitting in the crust and applied this model to the 2004 eruption at Mount Asama, Japan, in order to investigate the link between the crack closure model of stress-induced anisotropy and observed measurements. Results showed that dyke stresses are small relative to overall stress conditions expected from the rock overburden at depth. We found that applying both a simplistic measure of crack anisotropy and an analytic dry crack anisotropy relationship, taking into account the stress state, produced variations in both strength and orientation of anisotropy smaller than those observed during the eruption. We also observe that for the dyke to have a significant effect on the anisotropy, the deviatoric regional stress must be small with the magnitude of σ_1 being less than 5% greater than σ_3. However, the dynamic rupture process of the dyke during its ascent will concentrate stress at the edge of propagation due to magma accumulation, meaning that we may be underestimating dyke stresses during emplacement. From these findings we conclude that dry crack closure due to dyke-induced stress changes is not a candidate for changing anisotropy conditions. This would suggest a number of possible alternatives, given that the possibility that changes in splitting measurements represent spatial heterogeneity in anisotropy was addressed by Savage et al. [2010b]. The process for creating anisotropy may be different from the one used in the model, for example the APE model of Zatsepin and Crampin [1997], where very small changes in the deviatoric stress component can produce relatively large changes in crack anisotropy, could be applicable. Alternatively there may be a process associated with the volcanism that changes the crack properties themselves, either in terms of their distribution or overall contribution to anisotropy such as changing properties in fluid or gas pressure and saturation.

How stress-induced anisotropy is determined for in situ rocks is important considering that the response of anisotropy to stress is dependent on lithology, crack density and fluid saturation. As the crust is heterogeneous at scales down to a metre or less, building a complete model of how anisotropy is sampled by shear waves is a difficult task. In modelling a dynamic system, however, we can investigate singular processes that changing anisotropic conditions may be attributed to. We suggest this approach should be developed to produce an anisotropic benchmark, with the use of a data inversion technique, on top of which measured changes can be compared and their source better constrained.

Chapter 3

Inversion of Shear Wave Splitting Data: Imaging the subsurface of the Canterbury Plains

3.1 Introduction

A pervasive problem inherent in the analysis of anisotropy data (from shear-wave splitting or other means) is that all the measurements that are made occur at one point on the surface- the seismometer. Shear-wave splitting (SWS) measurements are advantageous in that the same shear wave source provides information on both the orientation and strength of the anisotropic medium that the wave has propagated through. However as a surface measurement this information is abstracted from the medium itself (see e.g. Savage 1999 or this thesis' introduction for more on the nature of anisotropy and SWS). This problem has been addressed in studies utilising SWS with various degrees of complexity, however it is not trivial. What is recorded on the surface, in terms of SWS, is for the most part a convolution of three major factors; the medium that the wave is propagating through, the direction in which the wave is propagating, and how the shear wave particle motion evolves (in a non-commutative manner) as it passes through anisotropic domains.

Most analyses that deal with the measurement and interpretation of SWS pay the greatest attention to the first of these, as it is generally the most important, and it is relatively easy to trace each wavefront from source to receiver in order to reveal how the data are distributed spatially. Wave propagation direction is a more difficult factor to account for. Indeed, earthquake data are commonly filtered to exclude arrivals at incidence angles outside the 'shear wave window' [Nuttli, 1961] (which lies within a critical angle of $\sim 40°$), which also serves to make overall ray propagation more uniform. However, as low velocity surface layers are widespread throughout the Earth, ray paths which are within the shear wave window at the point of measurement are likely to have undergone significant changes in incidence as they propagate through successively lower velocity layers. This is compounded when analysing shallow earthquake data where lateral source-receiver offsets are large relative to source depths. Complications in the way shear waves are split into fast and slow components as they pass from one anisotropic regime into another have been approached by studies [e.g. Silver and Savage 1994, Rümpker and Silver 1998], most of which exploit the fact that most SWS measurements are made from near-vertical propagating waves and the general 1D nature of the Earth by considering a layered medium with different anisotropic properties. Applied studies of SWS data, however, tend to use the splitting parameters (i.e. fast wave polarisation and slow wave delay) in isolation once they are recovered from the data with only a qualitative interpretation of the regime that produced them, sometimes accompanied with forward modelling that does not take into account certain non-unique aspects of SWS.

In this chapter, we expand on the previous chapter's forward modelling to present an inversion method for solving for the state of anisotropy given a set of SWS data, and apply it to the post-Darfield earthquake Canterbury region in New Zealand. Again, the method is based heavily on the framework laid out in Abt and Fischer [2008], however here we specifically approach the application of the inversion to crustal anisotropy rather than mantle anisotropy. The aim is to develop a modelling technique in which 3D spatially-variable anisotropy models can be determined and tested for a given set of anisotropy data. In applying this to Canterbury, we investigate the distribution of anisotropy in the region with respect to its structural and geological elements in order to elucidate what may be the anisotropy's cause.

Anisotropy modelling

Modelling and inversion of seismic data to retrieve the state of anisotropy for a region of interest has previously been approached using various techniques. Models incorporating transverse anisotropy evident in *P*-waves are becoming an entrenched consideration in migration of 3D active source seismic imaging [Gray et al. 2001, Tsvankin et al. 2010]. Inversion of passively acquired shear-wave splitting data was initially performed using genetic algorithms by Horne and MacBeth [1994]. Yang et al. [2003] and Rial et al. [2005] use shear-wave splitting results from passive and induced seismicity in geothermal areas to invert for strike, dip and density parameters of characteristic fracture sets in their study areas. The inversion technique that both studies use is a simple trial-and-error misfit reduction to find one set of fracture parameters. Such an approach is appropriate for study areas in which only one pervasive source of anisotropy (i.e. one fracture set) is responsible for the measured anisotropy.

Verdon et al. [2009] use a grid search algorithm to find the best fitting parameters for splitting in a hydrocarbon reservoir setting. Again, it is assumed that the rock mass in the study area has a homogeneous characteristic anisotropy. This allows for results to be attained using the computationally expensive grid search method and avoids possible issues with underdetermination in the model. However, any significant spatial variation in the study area will render the results inaccurate. Johnson et al. [2011] employ a simple tomography to determine likely spatial distribution of anisotropy strength in 2D. However, in this approach, the relationship between the direction of ray propagation and anisotropy is ignored. Zhang et al. [2007] develop a similar delay time tomography, this time in 3D, and apply it to SWS measurements from Parkfield, California. Again, it assumes that delay accumulates along the whole raypath without taking into account the relative orientation of anisotropy or the direction of ray propagation through it.

Inversion techniques developed by Abt and Fischer [2008] and Wookey [2012] both solve for shear wave anisotropy in 3D. The method of Abt and Fischer [2008] employs a linearised least-squares inversion to solve for anisotropy orientation and an anisotropy strength parameter. This approach is used to investigate mantle anisotropy in the Central American subduction zone and as such uses a Voight-Reuss-Hill averaged olivine-orthopyroxene stiffness tensor that is diluted by a strength parameter, simulating coherency in lattice preferred orientation anisotropy. The method of Wookey [2012] differs from Abt and Fischer [2008] in a number of regards. Significantly, Wookey [2012] uses a neighbourhood algorithm [Sambridge, 1999] to explore parameter space in order to treat the problem as generally non-linear. Also, Wookey [2012] differs from other techniques in that the method attempts to use the seismic data itself to find the splitting parameters that minimise λ_2, the smallest eigenvalue of the covariance matrix between the two data components after an inverse splitting operator is applied, as per the method of Silver and Chan [1991], rather than attempting to reduce misfit in pre-determined splitting parameters. This approach offers certain advantages as null data can be incorporated more easily into the solution and the breadth of parameter space can be reduced. For this study, we elect to integrate the inversion to use results from MFAST [Savage et al., 2010a], an automatic shear-wave splitting code, as it incorporates quality and error assessments that are beneficial within the inversion method.

Solving a linear inverse problem that has the forward problem form $d = \mathbf{Gm}$, relating the data d and the model $\mathbf{m}$, is a computationally easier process than a non-linear inversion, and so we seek to linearise the process to solve for anisotropy. The iterative linear process is strongly dependent on the input, or starting model [Tarantola and Valette, 1982], which is especially true for this application, as the interaction between elastic anisotropy and seismic wave propagation is in fact non-linear over a small portion of parameter space (see section 3.4). The true model that describes the anisotropy in the model space ideally represents a global minimum in the objective function (i.e. the data misfit function) which is sought out in the iterative process. The 'landscape' of this misfit function, however, may exhibit more than one local minimum or a low plateau that makes model convergence to this global minimum difficult. In order to overcome this problem, careful consideration is given to producing an 'average' starting model that is representative of the data. Furthermore, a simple ensemble of models are made with different starting models in order to compare which features of the model can be considered 'robust'. Due to the long computation times involved, this approach is not exhaustive and this must be considered a limitation in the method. However, other techniques [e.g. Johnson et al. 2011] make full use spatial averaging of SWS measurements, and therefore, by inverting from average starting models, this technique approaches this spatial averaging in a more systematic way.

3.2 Data

The shear wave splitting data for the Canterbury region used in this analysis were taken from the Holt et al. [2013] study on stress and anisotropy in the region. A more detailed breakdown of the shear wave splitting data can be found in Holt [2013], the associated

Master's Thesis. The events used comprise aftershocks that occur between the 4 September 2010 main shock and 11 January 2011, just before the large 6.3 M_o aftershock rupture beneath Christchurch on 22 February 2011. Overall, 8374 event-station SWS measurements were obtained using the automated splitting algorithm MFAST [Savage et al., 2010a] (refer to sections 1.2.3 and 1.2.4), providing fast wave polarisation and delay time data along with their determined error (figure 3.1).

The dataset was trimmed to exclude events with straight-line incidence angles greater than a predetermined amount; 60° was found to be a good value for our dataset. The reason for this is twofold; firstly uncertainties are introduced for SWS results with near-surface incidences greater than $\sim 35°$ due to converted *P*-S phase interference [Nuttli 1961, Booth and Crampin 1985]. Holt [2013] (page 38) notes that, for a straight-line incidence angle (i_s) restriction of 60°, all events have a surface incidence (i_c) less than or equal to 37°. Secondly, at greater event-station offsets there is an increasing divergence in the location of the modelled raypath and the true wavefront propagation due to the fact that modelled raypaths may only change their angle of propagation as they pass through a model depth layer. In practice, the second of these reasons is more important as the near-surface low velocity layer ensures near-vertical incidences, as well as the fact that since the publication of Holt et al. [2013], remarkably low $\frac{V_p}{V_s}$ ratios of 1.55-1.60 have been proposed in the near surface region surrounding the Greendale fault [Reyners et al., 2014], having the effect of increasing the size of the 'shear wave window' to incidence angles of $i_c = \sin^{-1}(V_s/V_p) =\sim 41°$. Other data restrictions include a limit of $\delta t = 0.4$ s as an upper bound for delays reflecting expected values for crustal anisotropy and raypaths of $\sim 5-30$ km [Savage et al., 2010b].

Holt [2013] also calculates 2D delay time tomography and fast direction spatial averaging results using the TESSA package [Johnson et al., 2011]. The delay time tomography approach divides the region of interest into a 2D array of square domains, and inverts for strength of anisotropy in each domain based on the simplifying assumption that the delay of each raypath is linearly additive along its length. The fast direction spatial averaging, based on the technique by Audoine et al. [2004], independently estimates prominent fast directions for each domain over the same grid using a weighted average of all the raypaths travelling through the domain. Fast direction weighting of each event can be handled in different ways. It is based on entire-raypath delay relative to the strength of anisotropy found in the delay time tomography and a scaling factor dependent on the distance along the raypath, based on the assumption that splitting measurements are more likely to represent anisotropy properties near the end of the path [Nistala and McMechan, 2005]. The scaling factor is set in terms of distance along the raypath, d, either as a $\frac{1}{d}$ or $\frac{1}{d^2}$ relationship (or set to scale equally along the path). Results from TESSA provide data for a 3D anisotropy inversion 'average' starting model, varying from the method of Abt and Fischer [2008] where average starting models are calculated in a simpler way by considering an average delay per distance (i.e. s/km) parameter for finding the weighted fast direction average for each block, rather than delays determined through tomography. It must be remembered, however, that to use the TESSA results as input models, they must be identically replicated at each depth level (as they are only 2D), which may result in underestimating vertical variations in anisotropy.

For the purposes of ray tracing and various estimations of elastic parameters, we use the New Zealand wide velocity model of Eberhart-Phillips et al. [2010]. In order to adapt the velocity model to the 1D velocity model required as an input to the inversion, we find all velocity entries that lie within the volume of interest and average them over each available depth layer, before interpolating these results to the modelled depth layers. For the dataset used in this study, we take velocity model values that lie between -43.88° to -43.21° latitude and 171.36° to 173.14° longitude, down to a depth of 20 km (see table 3.1).

Depth (km)	V_p	V_s	Density (g/cm^3)
-1.0000	3.6065	2.0874	2.3937
3.0000	4.8996	2.8526	2.5883
8.0000	5.9713	3.4804	2.7437
15.0000	6.2391	3.6480	2.8139
23.0000	6.8339	3.9743	3.0113

Table 3.1: Velocities (in km/s) used in all Canterbury models.

3.3 Model Parameterisation and Forward Modelling

The aim of this inversion method is, for each model element, to find a solution for strength of anisotropy (henceforth to be referred to as α) and either 1, 2 or 3 angles (θ, ψ, γ) that describe the orientation of the elastic coefficient and by extension the anisotropy (figure 3.2). Specifically, in the case of modelling anisotropy with hexagonal symmetry, only two

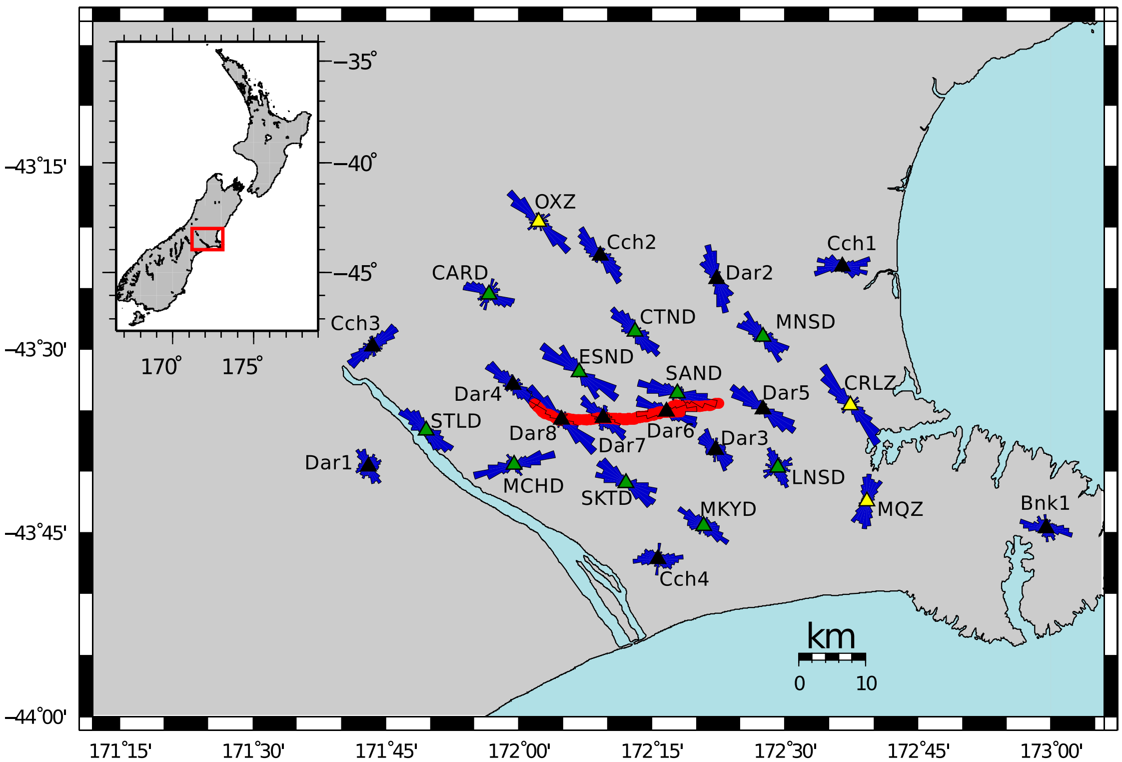

Figure 3.1: Circular histograms (rose diagrams) showing fast direction results, ϕ, for the data used for the anisotropy inversion. Coloured triangles represent GeoNet permanent stations (yellow), GNS Science temporary short period stations (green) and Victoria University, University of Wisconsin-Madison and University of Auckland temporary broadband stations (black). The main trace of the Greendale fault, as mapped by [Quigley et al., 2010a], is shown in red.

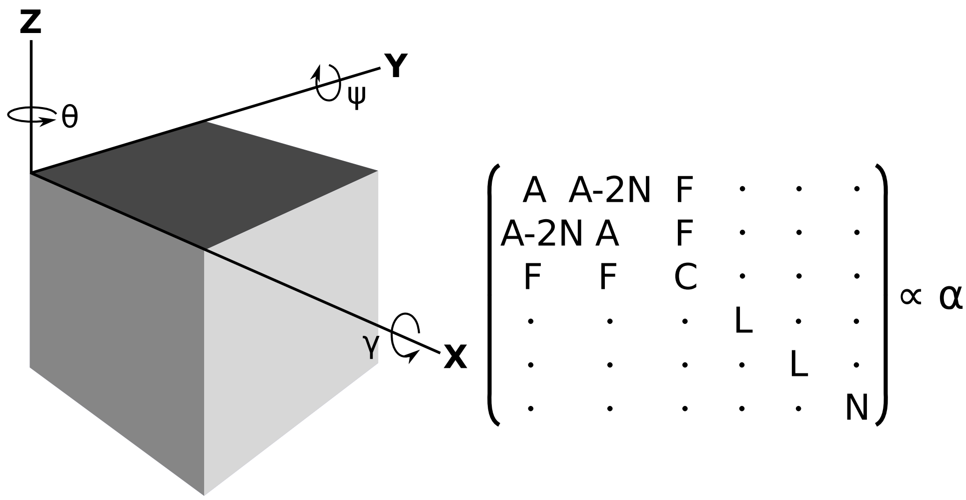

Figure 3.2: The four definable inversion parameters, α, θ, γ, and ψ and how they relate to a model element. The elastic tensor, in this case defined by the Love parameters A, C, F, N, L, has a degree of anisotropy proportional to the value of α, and is hexagonally symmetric. It is oriented using the angular parameters θ, γ, and ψ, or a subset of the three.

angles are required to orient the symmetry axis (θ and ψ). If the assumption is made that the symmetry axis is horizontally aligned (i.e. for the case of vertically aligned microcracks) only θ, or the rotation of the symmetry axis around the vertical axis is needed. The modelling technique is geared towards minimising the need for extensive manual configuration as well as being as versatile as possible for further analysis of SWS data, specifically MFAST formatted summary files. The geophysical focus of the method has been broadened from crystallographic mantle-derived anisotropy, as in Abt and Fischer [2008], to attempt to encompass the problem of crustal anisotropy.

At first, all earthquake/station locations, splitting parameters (ϕ and δt), *S*-wave frequency, initial *S*-wave polarisations and associated errors determined by MFAST are read into memory. The model domain is automatically extended to contain all events and divided into cubic elements at a resolution determined for the problem. A number of different block resolutions were tested, and results for cubes with sides of 5 km are shown. Changing the block resolution requires a compromise as smaller block sizes would lower the average parameter constraint for each model element and increase computation time, however better model fitting can be achieved with a denser and therefore potentially more heterogeneous model. All coordinates are transposed to a reference coordinate system relative to a user-specified origin or another location, such as the centre of the model domain. Ray paths are traced using Snell's law to calculate changes to ray incidence at each depth level using a 1D velocity model. This method of ray tracing adds an additional consideration to the selection of the block resolution as the shallow distribution of crustal earthquakes with depth is often small compared to their lateral distribution (e.g. events studied here are typically between 5-20 km deep) and a lack of depth horizons for the rays during ray tracing may introduce a significant error both in ray propagation direction and, more importantly, path length. The final consideration to account for with the ray tracing is the common raypath approximation between paths initially traced through the model and paths that reflect the modelled anisotropy, which will produce a small effect on the ray propagation direction and path length. Overall, this effect is expected to be small [e.g. Johnston and Christensen 1995] and not change what blocks are sampled by the raypath [Abt and Fischer, 2008], unless the block size is very small in comparison to total raypath length.

The anisotropy strength and direction parameters are used to produce an elastic tensor, C_{ijkl}, for each model element. Previous modelling approaches use the strength parameter either as a direct multiplication factor applied to the calculated velocity shift for raypath segments in the block (i.e. Abt and Fischer 2008, who use elastic constants representing an olivine-orthopyroxene blend typical in the mantle) or as a dilution of a base anisotropic elastic tensor with its isotropic equivalent achieved by Voigt-Reuss-Hill averaging [Wookey, 2012]. Any formulation of C_{ijkl} used should reflect the expected nature of the anisotropy in the model domain (i.e. lattice-preferred orientation, crystal-preferred orientation, stress-aligned crack anisotropy, etc.), however there is a limit at which the complexity of the model renders it over-parameterised. Here we look at the formulation of hexagonally symmetric elastic anisotropy using the Love coefficients A, C, F, L and N [Love 2013, Anderson 1989, Babuška and Cara 1991] defined as:

$$\frac{C}{\rho} = (V_p + \frac{dV_p}{2})^2, \quad \frac{A}{\rho} = (V_p - \frac{dV_p}{2})^2, \tag{3.3.1}$$

$$\frac{L}{\rho} = (V_s + \frac{dV_s}{2})^2, \quad \frac{N}{\rho} = (V_s - \frac{dV_s}{2})^2, \quad F = \eta(A - 2L) \tag{3.3.2}$$

Where ρ, V_p and V_s are, respectively, density, *P*-wave and *S*-wave velocity, as defined by the input velocity model. Values for dV_p and dV_s are calculated directly using the strength parameter as percent anisotropy. A limit for percent anisotropy is imposed to constrain results within those considered reasonable for the model domain. In the case of this study we use a limit of 20% due to measurements of equally strong anisotropy in the Haast schist terrane outcropping to the south-west of Canterbury, in which direction the metamorphic grade of outcropping rocks steadily increases due to the collision of the Pacific and Australian plates [Wellman, 1979, Godfrey et al. 2000]. The shape factor, η, defines the seismic velocity dependence of the hexagonal elasticity tensor between the orthogonal fast and slow axes [Babuška and Cara, 1991], and has a value of ~ 1 for mantle materials [Farra et al., 1991] and lower values of between 0.4-0.9 for various crustal materials [e.g. Godfrey et al. 2000, Ji and Salisbury 1993, Schulte-Pelkum and Mahan 2014]. Unfortunately, both η and the scaling relationship between dV_s (which has been sampled with SWS and is being indirectly solved for in this inversion) and dV_p are difficult to define without direct measurement. Here a value of unity for the scaling factor between *P*- and *S*-wave velocities is used.

ve that setting η to a value lower than 1 produces a non-linear behaviour between the model-ascribed anisotropy strength parameter and the amount of delay accrued along the raypath as determined by the Christoffel equation, so we set $\eta = 1$. Xie et al. [2013], studying surface wave anisotropy, comment that simply setting $dV_p = 0$ and $\eta = 1$ made little impact on their models despite their solving for shear wave anisotropy in a similar way. There are a number of studies that propose empirical relationships that parametise η and scaling factor between *P*- and *S*-wave anisotropy [e.g. Montagner and Anderson 1989, Becker et al. 2008, Takeo et al. 2013] which are generally applicable to mantle lithology. Unfortunately, due to their relative complexity there is no comparable set of relationships for crustal rocks, so we approximate the relationships. Once the C_{ijkl} matrix has been determined (see appendix A) for a model block it is rotated into position as determined by the available orientation parameters.

From the C_{ijkl} matrices of each block along a raypath a shear wave operator, $\Gamma(\phi, \delta t)$, is calculated by computing the Christoffel tensor:

$$m_{il} = \frac{1}{\rho}(C_{ijkl}n_j n_k) \tag{3.3.3}$$

Where n is the ray propagation vector. The eigenvalues and eigenvectors of the Christoffel matrix correspond to *P*-wave, fast *S*-wave and slow *S*-wave phase velocities and their polarisations, respectively [Babuška and Cara, 1991]. The time shift accrued for each ray segment, δt_n, is equal to $L(V_{ss}^{-1} - V_{sf}^{-1})$, where L is the segment length, and the fast direction, ϕ_n, is the fast polarisation direction eigenvector orthogonal to the raypath, and V_{ss} and V_{sf} are the slow and fast shear wave velocities, respectively. A simple synthetic wavelet at some predetermined frequency is successively delayed using the calculated Γ for each segment in propagation order, using the method of Fischer et al. [2000]. In this approach the frequency of the synthetic wavelet is determined by finding the mean of the frequency windows used by MFAST to calculate SWS measurements. Once the wavelet has been fully propagated along a raypath and each splitting operator applied, the final SWS parameters are found for the ray using the methodology of Silver and Chan [1991]. The process of wavelet perturbation and SWS measurement determination is fully detailed in Chapters 2 and 1, respectively.

One limitation of this approach is that each ray path is approximate in that it is affected by only one zone of anisotropy at a time. This neglects the effect of ray sensitivity 'Fresnel zones' which, depending on the shear wave frequency of interest and the block resolution, may span several model elements [Rümpker and Ryberg 2000, Hammond et al. 2010]. For crustal events with high frequencies ($\sim 1 - 10$ Hz) relative to longer period ($\sim 2 - 16$ s)

SKS phase splitting measurements (typical for studying mantle anisotropy), the problem presented by this is much less of an issue. Comparisons by Abt and Fischer [2008] between full-waveform modelling and the simple wavelet method outlined here find that errors due to this effect are most pronounced near element boundaries with a high anisotropy contrast.

This forward modelling process is functionally similar to, and described in more detail in, the previous chapter. The main differences between that initial approach and the method used here is the formulation of the elastic tensor and the nature of the *a priori* information used to produce the initial parameters. With regards to the elastic tensor formulation, someone attempting to invert for anisotropy using this technique may wish to use a specific method if there is evidence to suggest that the anisotropy present has a particular nature. For example one may wish to use formulation based on crack anisotropy [see e.g. Hudson 1981]. Introducing extra parameters to define the state of anisotropy (such as a parameter for the contribution of layering) may be problematic, especially with respect to the linearised inversion process, and ultimately we may have to be content with having only a broad and poorly defined estimate of anisotropy in the subsurface. Initial parameters in this study comprise the inversion starting model, which can have a profound effect on the end result [Aster et al., 2013].

Starting Models

Starting models can be defined by available *a priori* information about the expected state of anisotropy, or defined by the data itself. Here we look at three well defined starting models and a random starting model for comparison.

The first is an average model based on finding weighted parameter averages for α (the strength parameter) and θ (how the anisotropy is oriented as a rotation around the vertical, see figure 3.2) for each block dependent on the raypaths that exist within it. The average model is determined in a similar way to that in Abt and Fischer [2008]. The rotation parameters around the two horizontal components are set to zero regardless of whether or not they are being solved for in the inversion, due to the difficulty in determining information about them, considering that available ϕ measurements are virtually always measured in the horizontal plane. α is found by calculating a mean maximum delay accrual rate (in s/km) in order to determine an equivalence between observed delay and anisotropy strength. This is done by first deriving the C_{ijkl} for the highest degree of anisotropy defined in the model (i.e. the 'upper limit' of anisotropy) using the whole-model mean values for V_p, V_s, and ρ, and then solving the Christoffel equation for a ray traveling orthogonal to its symmetry axis. For each ray segment passing through a particular block, a value for α_{ray} is estimated by dividing the observed delay by the predicted maximum delay based on the ray length and this mean maximum delay accrual rate. The overall value for α in a block is found by taking the mean of all individual α_{ray} weighted by the ray segment lengths within that block. For any particular block containing a set of n rays with segment lengths L, this can be written as:

$$\alpha_{block} = \frac{\sum_{i=1}^{n} \left(\frac{\delta t_i^{obs}}{\overline{\delta t_i^{max}}} \right) \cdot L_{i,block}}{\sum_{i=1}^{n} L_{i,block}} \tag{3.3.4}$$

The value for θ is found simply by taking the circular mean of all observed fast directions for rays passing through a particular block. This time, the data are weighted by how close to vertical the angle of incidence of the ray segment is, because in the case of HTI (i.e. vertically aligned cracks and fractures) measured ϕ of vertical raypaths contain no ambiguity about the orientation of the anisotropy that may be imparted by its relative propagation through it. Again, this can be written as:

$$\theta_{block} = \angle \sum_{i=1}^{n} w_{i,block} e^{i\theta_i} \tag{3.3.5}$$

where $w_{i,block} = 1 - incidence/90$.

The second starting model uses results from TESSA [Johnson et al., 2011], as discussed earlier. This approach uses the spatial distribution of anisotropy strength as determined by iterative delay time tomography, which is then used to influence a weighted average for fast polarisation. The method of fast polarisation determination is very similar to the average model detailed above, with the weighting parameter being defined by Johnson et al. [2011] as:

$$w_{i,block} = \frac{\alpha_{block}}{\delta t_i} \cdot \frac{1}{D} \tag{3.3.6}$$

Where D controls weighting due to distance (d) from the receiver and can be set to 1 (i.e. no influence), d or d^2. The 2D TESSA results are interpolated onto the model grid and extended down into the vertical dimension, making them depth invariant.

Finally, we look at uniform and random starting models. A uniform starting model is simply defined using a single orientation and strength parameter that is applied to every model element. These parameters may be a global average taken from all the available data or another parameter set based on external results and considerations, with the assumption that the occurrence of shear wave splitting indicates that the model volume is not isotropic. For example, for modelling a stress controlled, preferential crack-closure anisotropy source, a uniform orientation could be set using the predetermined maximum compressive stress direction in the region of interest and a laterally uniform anisotropy strength that decreases with depth (due to increasing ambient pressure; see e.g. Ji and Salisbury 1993, Weiss et al. 1999) could be used. A random starting model uses randomly assigned values for α and θ.

3.4 Inversion

The inversion itself is an iterative, linearised least-squares (Newton-Raphson) approach [Tarantola and Valette 1982, Tarantola 2005] like that used by Abt and Fischer [2008] (figure 3.3). The problem is linearised in the sense that there is an assumed relationship between data (d) and model (**m**):

$$d = \mathbf{Gm} \tag{3.4.1}$$

Where **G** is a linear operator. The objective of the inversion is to design a method to

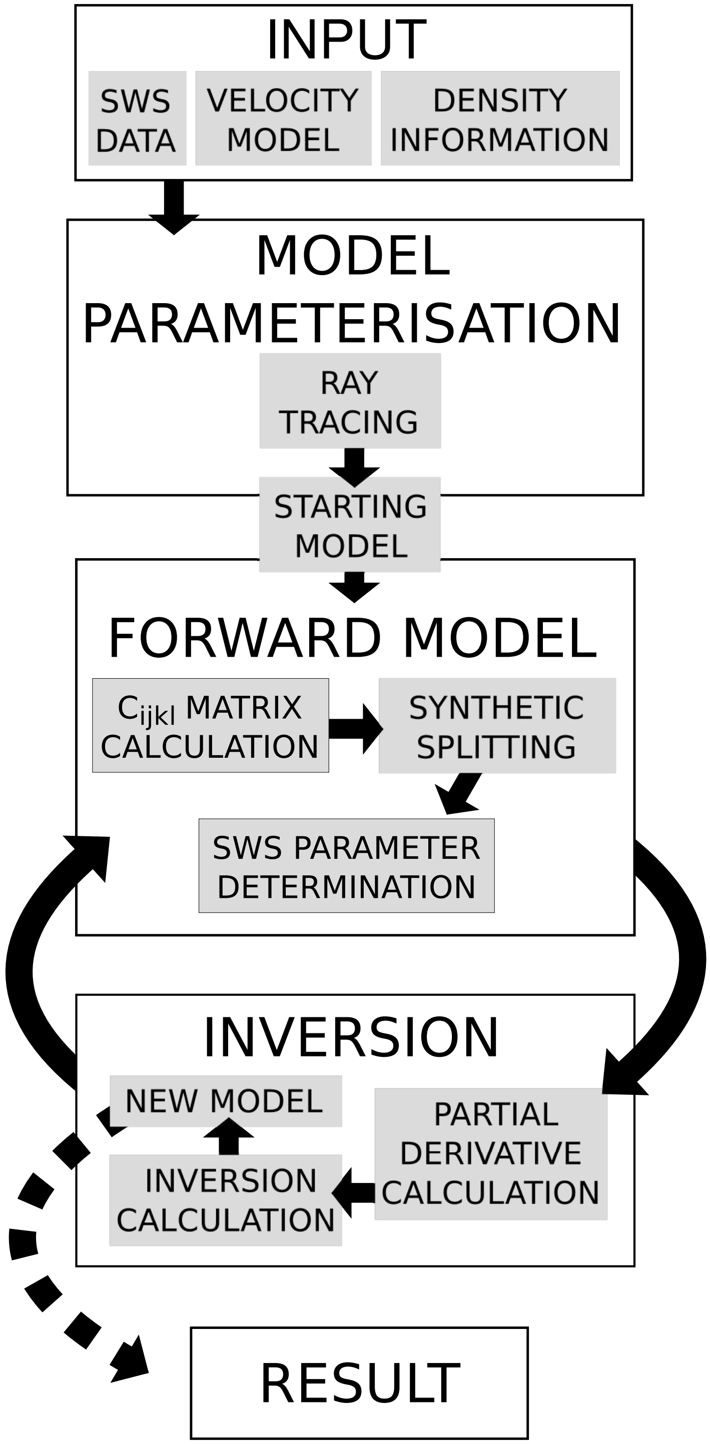

Figure 3.3: Schematic illustration showing the workflow of the inversion procedure.

solve for **m** for a given set of data. As is described in Tarantola [2005] (page 69), the least-squares, or Newton-Raphson, method achieves this iteratively with the equation:

$$\mathbf{m} = \mathbf{m}_{prior} - \mathbf{C}_M \mathbf{G}^t \left(\mathbf{C}_D + \mathbf{G}\mathbf{C}_M \mathbf{G}^t \right)^{-1} \left(\mathbf{G}\mathbf{m}_{prior} - d_{obs} \right) \tag{3.4.2}$$

Where $\mathbf{C}_M$ is the *a priori* model covariance operator and $\mathbf{C}_D$ is the data covariance operator. d_{obs} is the observed data vector, making the term $(\mathbf{G}\mathbf{m}_{prior} - d_{obs})$ the data misfit (elements of the objective function) for the model determined during the prior iteration.

The design matrix **G** is populated with finite difference partial derivatives and takes the form [Abt and Fischer, 2008]:

$$\mathbf{G} = \begin{bmatrix} \frac{\partial \phi_1}{\partial \alpha_1} & \frac{\partial \phi_1}{\partial \theta_1} & \cdots & \frac{\partial \phi_1}{\partial \alpha_m} & \frac{\partial \phi_1}{\partial \theta_m} \\ \frac{\partial \delta t_1}{\partial \alpha_1} & \frac{\partial \delta t_1}{\partial \theta_1} & \cdots & \frac{\partial \delta t_1}{\partial \alpha_m} & \frac{\partial \delta t_1}{\partial \theta_m} \\ \vdots & \vdots & \ddots & \vdots & \vdots \\ \frac{\partial \phi_n}{\partial \alpha_1} & \frac{\partial \phi_n}{\partial \theta_1} & \cdots & \frac{\partial \phi_n}{\partial \alpha_m} & \frac{\partial \phi_n}{\partial \theta_m} \\ \frac{\partial \delta t_n}{\partial \alpha_1} & \frac{\partial \delta t_n}{\partial \theta_1} & \cdots & \frac{\partial \delta t_n}{\partial \alpha_m} & \frac{\partial \delta t_n}{\partial \theta_m} \end{bmatrix} \tag{3.4.3}$$

Where there are n observations and m model blocks. The case above details the method for solving for two parameters (α and θ), which assumes that anisotropy in the entire domain exhibits horizontal transverse isotropic (HTI) conditions. It can be expanded to include more parameters when such an assumption cannot be made, specifically the two extra parameters that describe elastic tensor rotation around the two horizontal axes. The partial derivatives themselves are determined by applying the forward modelling technique to test the dependence of the synthetic δt and ϕ measurements on perturbations of the model parameters. Here we use perturbations of 5% of the maximum defined anisotropy for α and 5° for θ, or equivalent angular parameter. Partial derivatives are recalculated for each independent model parameter when the parameter deviation due to **G** (i.e. equation 3.3.2) for any particular iteration is greater than 1% of the maximum defined anisotropy for α, or greater than 1° for angular parameters.

As identified by Abt and Fischer [2008], the behaviour of shear wave polarisation becomes highly non-linear over a relatively small portion of the parameter space and is most likely to occur where the raypath is linearly polarised, i.e. at the onset of the shear wave. Once the raypath has been propagated through the first block it travels through, it becomes very unlikely that particle motion will be linear and parallel to a fast or slow polarisation axis, significantly reducing the chance of non-linear behaviour. An outcome of this type of non-linearity is that the starting model plays a significant role in the outcome of the inversion. Non-linear approaches, such as the 'nearest neighbour' method developed in Sambridge [1999] and applied to inverting anisotropy data by Wookey [2012], or other well-known methods (Monte Carlo, simulated annealing etc.), generally trade off this dependence on initial conditions with an increased computational requirement, which is already significant for the anisotropy problem.

The model covariance operator, $\mathbf{C}_M$, specifically the *a priori* model covariance (i.e. obtained independently of the results of measurements), generally describes confidence in m_{prior}. Non-zero values on the matrix diagonal are used as a means to damp changes from iteration to iteration so that the linear partial derivatives remain valid, and represent the allowed variance, σ^2, between the prior and subsequent model. Diagonal values of the $\mathbf{C}_M$ matrix are identical and are provided as an input parameter, referred to as the damping factor, designed to damp models between iterations whilst still allowing it to converge on the global minimum in the objective function. In this method, new models are strongly damped (i.e. have a low variance) until a particular iteration, after which damping is relaxed. The motivation for this is that if the inversion has converged on a global minimum, damping reduction will not result in a large change in the model, given that minima in the objective function tend to be narrow and deep [Wookey, 2012]. However if the model has been overly damped and is not able to converge on the global minimum, damping reduction may result in large variations to the model. Thus it is important to test damping values to examine the model for these types of behaviours.

Smoothing can also be incorporated into the model by including non-zero, off-diagonal elements into $\mathbf{C}_M$. The smoothing forces changes to model parameters to be reflected as similar changes to surrounding blocks. The off-diagonal values used for smoothing are determined by assuming a Gaussian distribution in the variance parameter and elements of $\mathbf{C}_M$ are populated so that only blocks adjacent to one another influence one another. In any particular block (b_0), smoothing elements of $\mathbf{C}_M$ for blocks (b) with centres at a distance of d from the block centre in question are defined as:

$$\mathbf{C}_{b,b0} = \sigma_{b0}^2 \cdot \exp(-d^2/2d_0^2) \tag{3.4.4}$$

Where σ_{b0}^2 is the same *a priori* variance defined for damping, and d_0 is the typical length scale of permitted parameter undulations. This equation describes the entire $\mathbf{C}_M$ operator for any arbitrarily defined value of d_0, with $d_0 = 0$ being a special case with no smoothing. Smoothing with directly adjacent blocks was applied to the model, however the results showed that the smoothing itself greatly decreased the overall resolution of the model. As such, we use non-smoothed results in this study.

The data covariance operator, $\mathbf{C}_D$, is a diagonal matrix with elements equal to the sum of the squared variances for the observed and predicted splitting measurements. The synthetic data errors are estimated using the [Silver and Chan, 1991] method with corrections as detailed by Walsh et al. [2013]. For each measurement (n), values for $\mathbf{C}_D$ can be written thus:

$$\mathbf{C}_{2n-\delta_i} = \sigma^2_{\Gamma_i obs} + \sigma^2_{\Gamma_i synth} \tag{3.4.5}$$

Where δ_i is the Kronecker delta, $\Gamma_i(\delta t, \phi)$ are splitting measurements, and $i = 0$ for δt measurements and $i = 1$ for ϕ measurements. Both $\mathbf{C}_M$ and $\mathbf{C}_D$ are positive definite and have a defined inverse.

The final step for each model iteration is to find the misfit function of the newly defined model. This is done simply by forward modelling the shear wave splitting of each raypath using the new model parameters and calculating the residual error between each modelled result (d_{synth}) and it's corresponding measured datum (d_{obs}) as such:

$$e_{residual} = |d_{obs} - d_{synth}| \tag{3.4.6}$$

Weighted misfit parameters are also calculated by multiplying the calculated residuals by a weighting factor, defined for a particular measurement as:

$$w_{residual} = \frac{1}{\sigma_{obs} + \sigma_{synth}} \tag{3.4.7}$$

Where σ_{obs} and σ_{synth} are the observed and predicted variances for the splitting parameter in question.

Model parameter resolution is determined using the resolution matrix [Tarantola, 2005], $\mathbf{R}_M$, defined as:

$$\mathbf{R}_M = \mathbf{C}_M \mathbf{G}^t (\mathbf{C}_D + \mathbf{G}\mathbf{C}_M \mathbf{G}^t)^{-1} \mathbf{G} \tag{3.4.8}$$

The resolution matrix is mapped to the model domain in order to assess the spatial properties of how well resolved the model parameters are. Once the model reaches its final iteration, the resultant anisotropy model, synthetic data and misfit function are output as results.

In this inversion approach, errors in the two input parameters (δt and ϕ) are treated as both Gaussian and independent, as the *a priori* data covariance matrix, $\mathbf{C}_D$ has no off-diagonal elements. This is a necessary assumption in order to treat the inversion procedure as linear, as well as to combine experimental and theoretical uncertainties [Tarantola, 2005]. The solution for the minimum eigenvalue (λ_2^{min}) in ϕ and δt parameter space, as can be seen in figures 1.5f, 1.6f and 1.7f, graphically represents data uncertainties. For the data uncertainties to be considered Gaussian, the 95% confidence interval contour should be symmetrical around the final parameter pick. For high quality MFAST results (e.g. figure 1.5), it is generally observed that this is the case, and uncertainties in ϕ and δt can be considered Gaussian. However, low quality results (e.g. figure 1.7) tend to have uncertainties that are asymmetrically distributed. Shear wave splitting measurements used in this modelling analysis all have a grade of "B" or higher, limiting the data to results where the assumption that the parameters are Gaussian and independent has a stronger basis. However, the assumption is still considered a simplification of the actual data uncertainties.

3.4.1 The Darfield earthquake

The initial $M_W 7.1$ Darfield mainshock occurred on the morning of 4 September 2010 (local time) roughly 10 km southeast of the town of Darfield, situated 40 km from Christchurch in the Canterbury region of New Zealand's South Island. The damage caused by the earthquake was widespread, and aftershocks distributed around the region extended across the fault system, including the destructive and fatal $M_W 6.3$ event that struck Christchurch on 22 February 2011 [Sibson et al. 2012, Bannister and Gledhill 2012]. The earthquake occurred in the tectonic setting of the Pacific-Australian plate boundary, which transitions from oblique subduction of the Pacific plate underneath the Australian plate at the Hikurangi trough in the north, to reversed subduction of the Australian plate at the Puysegur trench, situated near Fiordland to the south. Between these areas of subduction lies the 600 km long Alpine fault, the surface expression of a zone of right-lateral transpressive continental convergence. The relative motion of the Australian and Pacific plates in this region, averaging 37 ± 2 mm/year at a bearing of $071 \pm 2°$ [Norris and Cooper, 2001], has resulted in the uplift of the Southern Alps and is responsible for the major topographic features of the South Island. The fault system on which the Darfield earthquake occurred was previously unmapped [Quigley et al., 2010b], being in a region with low relative strain rates [Beavan and Haines, 2001] and having no pre-existing surface expression amongst the gravel alluvium that makes up the Canterbury plains [Forsyth et al., 2008]. Seismological and geodetic analysis of the earthquake sequence revealed the fault system that ruptured during the mainshock may have occurred on between four and seven separate fault segments over multiple subevents. The majority of this slip appears to have been concentrated along a ~ 40 km long section of the roughly E-W trending strike-slip Greendale fault [Beavan et al. 2010, Holden et al. 2011, Duffy et al. 2013, Syracuse et al. 2013]. Near-source seismological and geodetic analysis of the Darfield mainshock produce focal mechanisms that indicate that the initial rupture was reverse-slip. Conversely, teleseismic moment tensor analysis produces a near-vertical right lateral strike-slip focal mechanism [Gledhill et al., 2011]. Due to the good instrumental coverage and availability of data, the response of the scientific community to the earthquake sequence has been thorough, giving a strong bearing on which to analyse the results from the methods described here.

3.4.2 Geology and crustal stress in the Canterbury Plains

The Canterbury plains are made up of Quaternary alluvial gravels and muds with horizontal stratigraphy overlying Late Cretaceous-Tertiary sediments, volcanics and basement

Permian-Triassic greywacke [Forsyth et al. 2008, Dorn et al. 2010]. To the east, Banks Peninsula extends into the Pacific. It consists of Late Miocene alkaline volcanics presenting a marked topographic and structural transition from the surrounding sedimentary stratigraphy [Sewell, 1988]. To the west and north, the uplift of the Southern Alps represents lithospheric thickening due to the transpressive convergence of the Australian and Pacific plates, and metamorphic terranes associated with the orogen (such as the Haast schist and Alpine Fault mylonites) exhibit strong foliation anisotropy [Okaya et al., 1995]. The Canterbury plains are rimmed by surface outcropping Torlesse greywacke, samples of which were found to be relatively isotropic compared to the Haast schist at 2.1% anisotropy (using the formula $(V_{max} - V_{min})/V_{ave}$) [Okaya et al., 1995].

Crustal stress in the Canterbury region has been constrained in a number of ways, including earthquake focal mechanism inversions, borehole breakout measurements, geodetic techniques, and inferences from anisotropy measurements. Focal mechanism inversions made in the Marlborough area by McGinty et al. [2000] gave σ_{Hmax} bearings of 120° and 118° for the northern and southern regions, respectively. Similarly, Balfour et al. [2005] determined a relatively consistent σ_{Hmax} of $115 \pm 16°$ for the northern South Island, including the Marlborough fault system. Focal mechanism inversions of Darfield earthquake aftershocks in the Canterbury region by Holt et al. [2013] provide an average σ_{Hmax} direction of $116 \pm 18°$, consistent with the northern South Island [Townend et al., 2012], with evidence that σ_{Hmax} rotated to be more parallel to the Greendale fault (i.e. towards the east-west direction) in its central segment (see figure 3.4). It is suggested by the authors that this rotation may either be caused by low shear stresses in the locality, or by a co-seismic stress drop equivalent to $\sim 40\%$ of the ambient differential stress. For simplicity in this discussion, σ_{Hmax}, or maximum compressive horizontal stress, is assumed to be the same as σ_1, or maximum compressive stress, unless otherwise stated. The stress configuration in the Canterbury region is considered to be mostly strike-slip (i.e. $\sigma_v = \sigma_2$), while some faults exhibit reverse slip behaviour, indicating that σ_2 and σ_3 may be near equilibrium or reversed in particular areas [e.g. Sibson et al. 2012, Holt et al. 2013].

As discussed in Sibson et al. [2012], stress orientation has also been determined in the vicinity of the Canterbury region by analysing borehole breakouts (see Zoback [2010] for discussion on the method involved). Only one borehole exists, a near vertical hydrocarbon production well drilled 26 km offshore from the south Canterbury coast in 1985, with an average breakout orientation of $024 \pm 9°$, which implies a σ_{Hmax} orientation of $114 \pm 9°$ between the depths of 1900-2700 m.

Assuming parallel σ_{Hmax} and maximum compressive strain directions, strain estimations determined through consideration of the Hikurangi Margin [Reilly, 1990], global plate models [Pearson, 1993], and regional elastic models [Wallace et al., 2007], provide a σ_1 orientation between 110-118° in or near the Canterbury area [Sibson et al., 2012]. Local geodetic strain studies in the Central North Island [Pearson, 1994], the NW Canterbury plains [Pearson et al., 1995], and Southland [Walcott 1984, Moore et al. 2000, give maximum compressive strain bearings within the same 100-117° range. Also shown on figure 3.4 is the NE-SW Charing Cross blind thrust fault, one of the parasitic fault planes as-

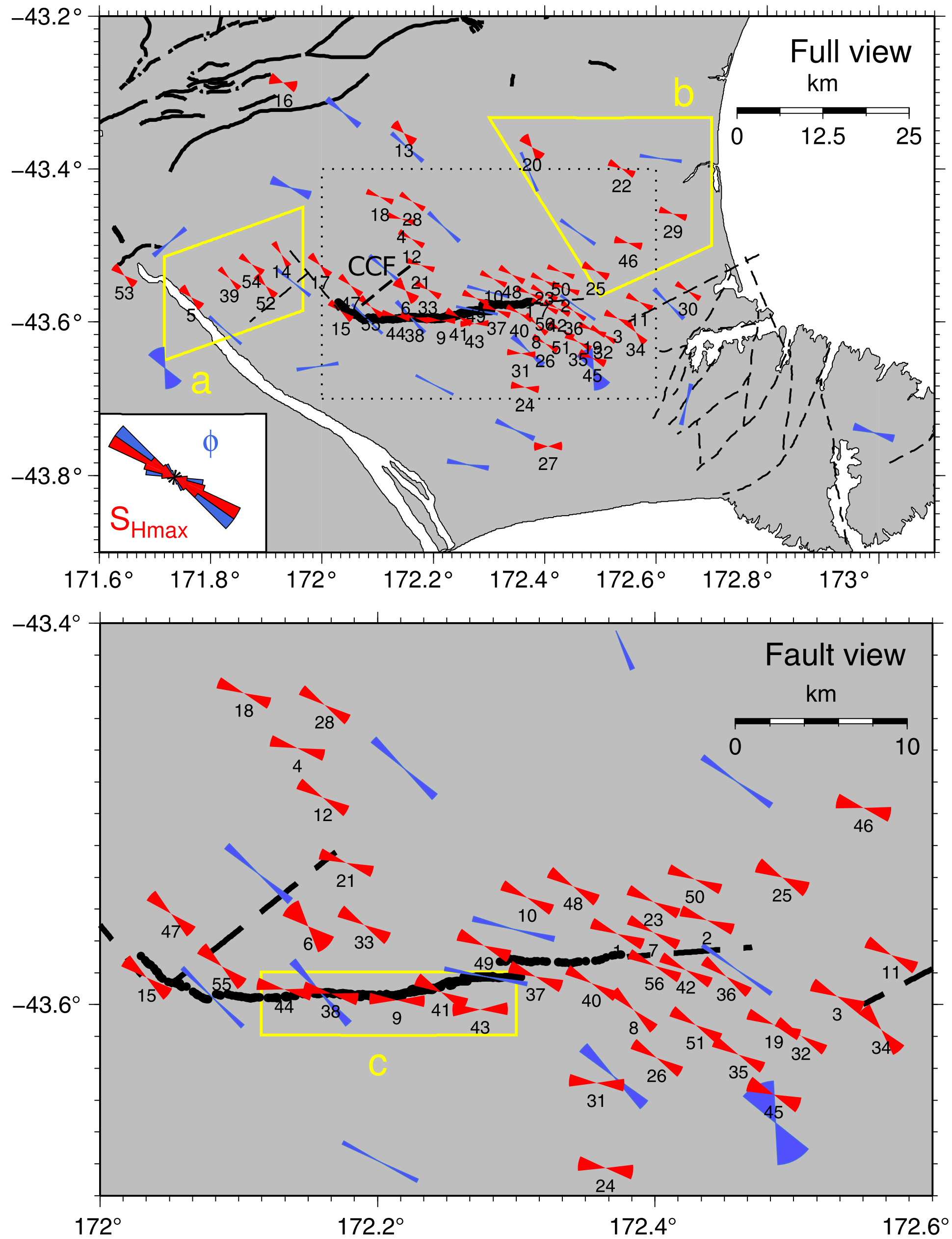

Figure 3.4: σ_{Hmax} and shear-wave splitting fast directions (ϕ) reproduced from Holt et al. [2013]. Red bow ties represent σ_{Hmax} with 90% confidence intervals located at the centre of the earthquake cluster used for focal mechanism inversion. Blue bow ties represent average ϕ located at the point of measurement, with 95% confidence intervals. Also shown is the Greendale fault (thick black line) and the inferred blind reverse Charing Cross fault (labeled CCF), as well as other inferred (dotted lines) and known (solid lines) faulting. Yellow boxes **a** and **b** (top figure) show regions of possible reverse faulting/stress reorientation. Yellow box **c** (bottom figure) shows region of possible stress rotation.

sociated with the Darfield earthquake. Geophysical studies of the Canterbury region have indicated the predominant presence of E-W faults that continue eastwards offshore along the Chatham Rise [e.g. Mortimer et al. 2002, Davy et al. 2012, Gladczenko et al. 1997]. These faults indicate an historic E-W strain orientation, possibly associated with the partial subduction of the Hikurangi Plateau, itself a fragment of the Ontong-Java Plateau large igneous province, underneath the Chatham Rise [Davy et al., 2008]. To the northwest of the the study region are NE-SW trending bounding faults that demarcate the transition into the Southern Alps.

Shear wave splitting (SWS) fast direction measurements (ϕ) from Holt et al. [2013], made using the MFAST automatic shear wave analysis software, are broadly aligned with the various σ_{Hmax} measurements in and around the region (see figure 3.4), indicating that the anisotropy is generally controlled by stress. Some atypical behaviour in ϕ is exhibited at a number of stations, which is interpreted as structurally controlled anisotropy (i.e. fault and macro-scale fracture planes that do not align perpendicularly to maximum compressive stress) with the exception of one seismometer, LNSD, where a satisfactory explanation of the anisotropy characteristics was not forthcoming. Another characteristic of the anisotropy outlined by Holt et al. [2013] was a possible near-isotropic zone around station MCHD (see figure 3.4 for reference). The shear wave splitting results from Holt et al. [2013], the technical details of which are discussed in a later section, are the data used for inversion in this study.

Fry et al. [2014] studied depth-variable anisotropy in the Canterbury region (broadly the same area as was studied in Holt et al. [2013]), as exhibited in surface waves measured using noise cross-correlation techniques. Rayleigh waves exhibit anisotropy in the subsurface to a depth proportionate to their period [Fry et al., 2010]. Fry et al. [2014] invert dispersion curves calculated from noise cross-correlations to determine the anisotropic parameters of the fundamental Rayleigh mode, known as the 2Ψ and 4Ψ anisotropic anomalies [Smith and Dahlen, 1973]. They find E-W trending horizontal fast axes with an apparent 15° anticlockwise rotation to the southwest for the 'upper-lower' crust (0-10/15 km depth, Rayleigh wave periods of 8 s). For the lower crust/mantle lithosphere depth range (0-20/30 km depth, Rayleigh wave periods of 15 s), 2Ψ axes are aligned NE-SW in the centre and east of the region, with an anticlockwise rotation of up to 40°, as well as a reduction of magnitude, towards the southwest (see figure 3.5). Rayleigh wave anisotropy in the upper crust appears to be controlled by E-W faulting patterns and historic strain, in comparison to the observed stress-controlled SWS. Deeper Rayleigh wave anisotropy is rotated further out of alignment from the predominant SWS orientation, closely resembling SKS wave anisotropy measurements in the region [e.g. Savage et al. 2007], which is hypothesised to be controlled by accumulated strain, or flow, in the upper mantle. One component of the 4Ψ axes is well aligned with σ_{Hmax} in the region, suggesting that a degree of surface wave anisotropy is stress-controlled, however no detailed physical interpretation for the 4Ψ axes is given.

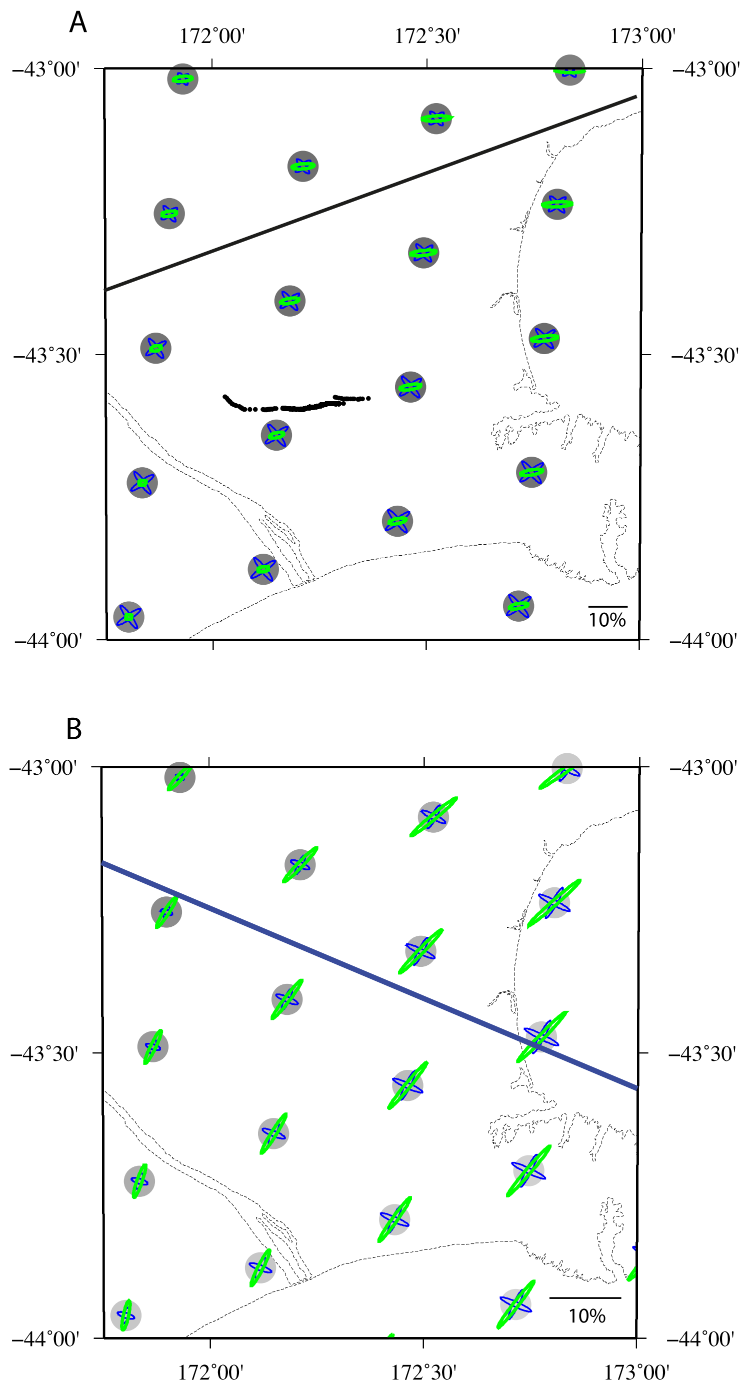

Figure 3.5: Rayleigh wave anisotropy inversion results reproduced from Fry et al. [2014]. (A) Anisotropy from the surface to 10-15 km, derived from surface waves with 8 s periods. Green and blue ellipses represent 2Ψ and 4Ψ anisotropy, respectively. The black line represents the direction of relative plate motion. (B) 2Ψ (green) and 4Ψ (blue) anisotropy from the surface to 25-30 km, derived from surface waves with 15 s periods. The solid blue line represents the axis of maximum compressional stress.

3.5 Results

3.5.1 Synthetic Modelling

In order to test how well the inversion method works in ideal cases, we produce a known test model of anisotropy and synthetic dataset, use them to forward model shear wave splitting parameters, and then use those splitting parameters to run an inversion. The final model can then be compared to the known input model for a measure of how successful the inversion was. Here, we look at how well the inversion method can resolve two features in this way; a vertical strip of high anisotropy within a low anisotropy region, and a horizontally layered system with two layers of distinct anisotropy direction and strength. In all cases, we use a synthetic dataset of 500 events and 15 stations over a model space with an area of 60 km^2 and a thickness of 25 km, which is of similar size to the model space encompassing the Darfield data. The velocity model used (Table 3.1) is, again, taken from Eberhart-Phillips et al. [2010], using the same reference coordinates as those used for the Darfield data. The synthetic testing itself is testing the inversion processes' ability to recover known structures, however the results are not directly applicable to the inversion results from the Darfield data. Each synthetic model solves for two parameters; strength of anisotropy, α, and the horizontal azimuth of anisotropy orientation, θ.

The distribution of events and stations in the synthetic modelling can be set to be spaced out either in a grid or randomly. Here, we choose a minimum depth of 10 km for events due to the fact that shallower events will likely be excluded from the model anyway due to the high incidence angle of the raypaths they trace to each station. Random event and station distributions are generated using MATLAB's '`rand`' function, which draws pseudorandom values from a standard uniform distribution. Uniform event distributions are created by finding a number of locations (as close to the specified number as possible whilst still having each 'event layer' contain the same number of events) over a number of layers separated by the depth increment multiplied by a fraction ($\frac{6}{11}$), in order to avoid layers being close to element boundaries. The lateral distribution of the event grid is similarly treated, using a spacing proportionate to the block size in x- and y-dimension multiplied by a fraction ($\frac{2}{11}$). Here we show results from models made with both uniform and random event and station distributions. Constructing a model with random events and uniform stations and vice-versa is also possible. Finally, we defined the event-station pairs between which raypaths are traced. Instead of simply tracing raypaths from each event to every available station, event-station pairings are determined psuedorandomly. First, the number of links for each event (i.e. raypaths that emanate from the event) is determined using the MATLAB function '`normrand`' which draws pseudorandom values from a normal distribution with a mean equal to half the number of stations and a standard deviation equal to a quarter of the number of stations (values found this way are rounded to the nearest integer). Initial shear-wave polarisations for each event can be set as uniform or random.

All synthetic models shown here have the same inversion parameters. A 2.5 Hz synthetic wavelet with 10% white noise with a random initial polarisation was subject to splitting as it propagated through layers with anisotropic elastic tensors derived using Love coefficients. 80 iterations of the inversion procedure were carried out, with initial damping factors of 2 until iteration 40, after which it is relaxed to 10, after Abt and Fischer [2008]. The upper limit for anisotropy strength was 20%. The synthetic models shown here solve for α and θ, however testing was also performed with models solving for three parameters, including ψ (in this case, the angle describing the dip of the plane of symmetry with respect to the vertical). Results from these models were significantly less accurate than those solving for two parameters, which is an expected result as the anisotropy in the original synthetic models have no ψ component. Judging by the results, solving for three parameters creates an inversion process that is far more underdetermined than solving for two parameters. The degree to which this affects model results is compounded by the fact that SWS data are measured in the horizontal plane (i.e. on the horizontal components of a seismometer), meaning that obtaining information about the dip of anisotropy is difficult, especially without some *a priori* assumption about the nature of the anisotropy in the model space. Currently, as the starting models used in this method assign a ψ and γ of 0 to all blocks, we approach the inversion as a two-parameter problem, with the implicit assumption that the anisotropy in the region is caused by vertically aligned cracks or fractures.

First, we will discuss the results from the 'strip' anisotropy model (figure 3.6), an ideal scenario that may be analogous to any vertical feature that may contribute to anisotropy, such as a zone of fault damage. For all model plots, anisotropy orientation information is only shown for a model element if there are data available in that block (i.e. a raypath exists within the block) and the anisotropy of the block is greater than 0% (since a block with 0% anisotropy has no meaningful orientation). To display the model resolution, the resolution matrix is mapped with a checkerboard that has cells alternating between values of 1 and -1. If the model is well resolved, the checkerboard is reproduced faithfully, and if the model is poorly resolved checkerboard values deviate from the 1/-1 cell characteristic.

The most faithful recreation of the initial model is made by the model in figure 3.7, with a uniform event and station distribution and the use of an average starting model, with a good consistency within the resolved model over all depth slices. Final weighted average data misfits (see table 3.2) for this model are smaller than the other two 'strip' models shown, one of which uses random event and station locations (figures 3.8 and 3.9) and the other of which uses a randomly determined starting model (figure 3.10). Unsurprisingly, using a uniform distribution of events and stations gives a more evenly resolved model domain than the model using a random distribution of events and stations (compare figures 3.7 and 3.9), where the best resolutions were in the half of the model where the stations were concentrated. The comparison between average and random starting models (compare figures 3.7 and 3.10) show a clear advantage in using the average starting model in terms of the accuracy of the final model. In particular, the strength of resolution at depth is lower when using the random starting model, and the form of the high anisotropy strip feature is much less discernible, especially at greater depths.

Next, random noise was added to the initial forward model to ascertain how the modelling process deals with non-ideal input data. Random noise was added to synthetic shear

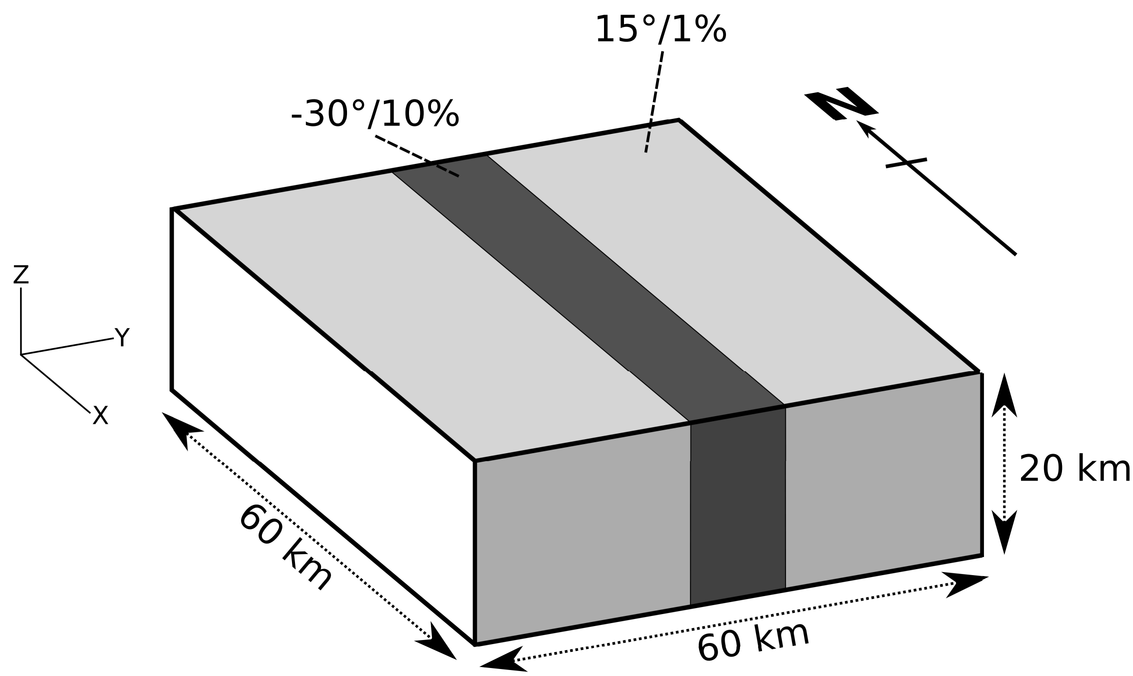

Figure 3.6: Schematic diagram showing the model domain used for the 'strip' synthetic model test. The anisotropy values shown refer to model θ and α, respectively. γ and ψ values are set to zero and are not solved for in the inversion.

wave splitting input data (as determined by the forward model) by multiplying a constant with a normally distributed random number (with a mean of 0 and a standard deviation of 1), found using MATLAB's '`randn`' function. The constants used were 0.05 s for delay times and 5° for fast directions, in order to realise standard uncertainties in the synthetic shear wave splitting parameters. Model parameters in figure 3.11 show results using the 'strip' model shown in figure 3.6, at 5 km resolution, with a uniform event and station distribution. It is evident that, in this case, the structure can still resolved, although not as well as in figure 3.7, and with more error.

The second model has two 'layers' of differing anisotropy (figure 3.12), which may, for the crust, represent the horizontal layering of lithologies with different anisotropy (or

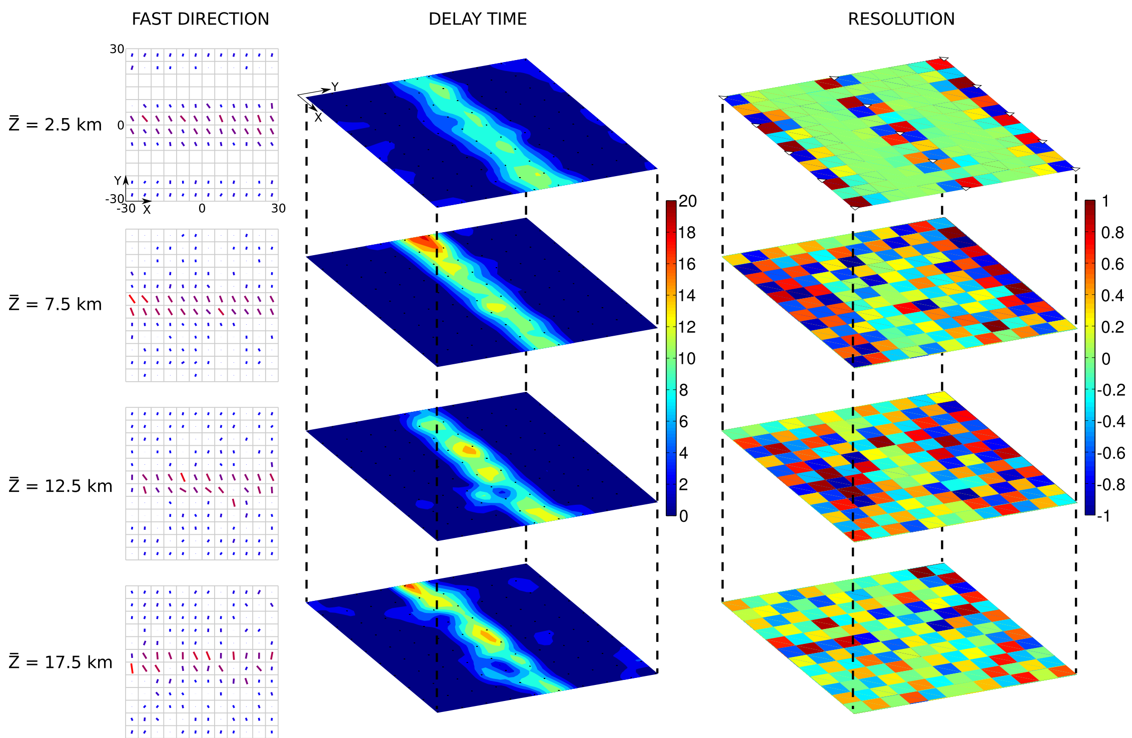

Figure 3.7: Inversion results from the 'strip' synthetic model test at 5 km resolution with a uniform event and station distribution. Fast direction plots show θ angles as bearings for each model element, with longer bars and warmer colours indicating stronger anisotropy. Empty cells indicate either no data available or no anisotropy strength for that particular block. Delay time plots show α values for each block (smoothed for plotting), scaled by percent anisotropy (0-20%). Triangles on the upper layer show the location of synthetic stations. Resolution plots show the results from checkerboard testing. Results close to a checkered arrangement of 1/-1 for adjacent blocks are well resolved. Generally, the model is well resolved, with areas of low resolution in the upper layer due to the nature of the station arrangement and in the bottom layer due to there being fewer raypaths passing through it.

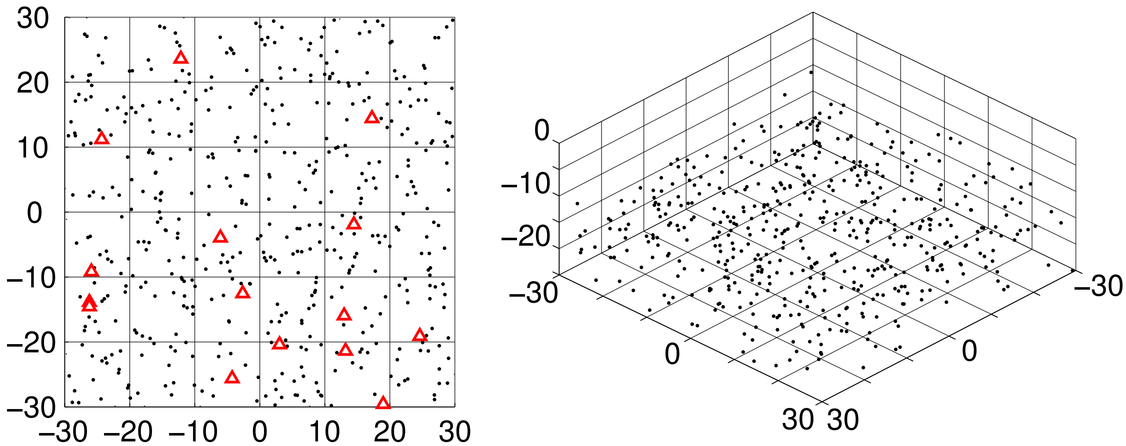

Figure 3.8: Event and station distribution for the 'strip' synthetic model with random event and station locations. Black dots represent the earthquake events and red triangles represent stations.

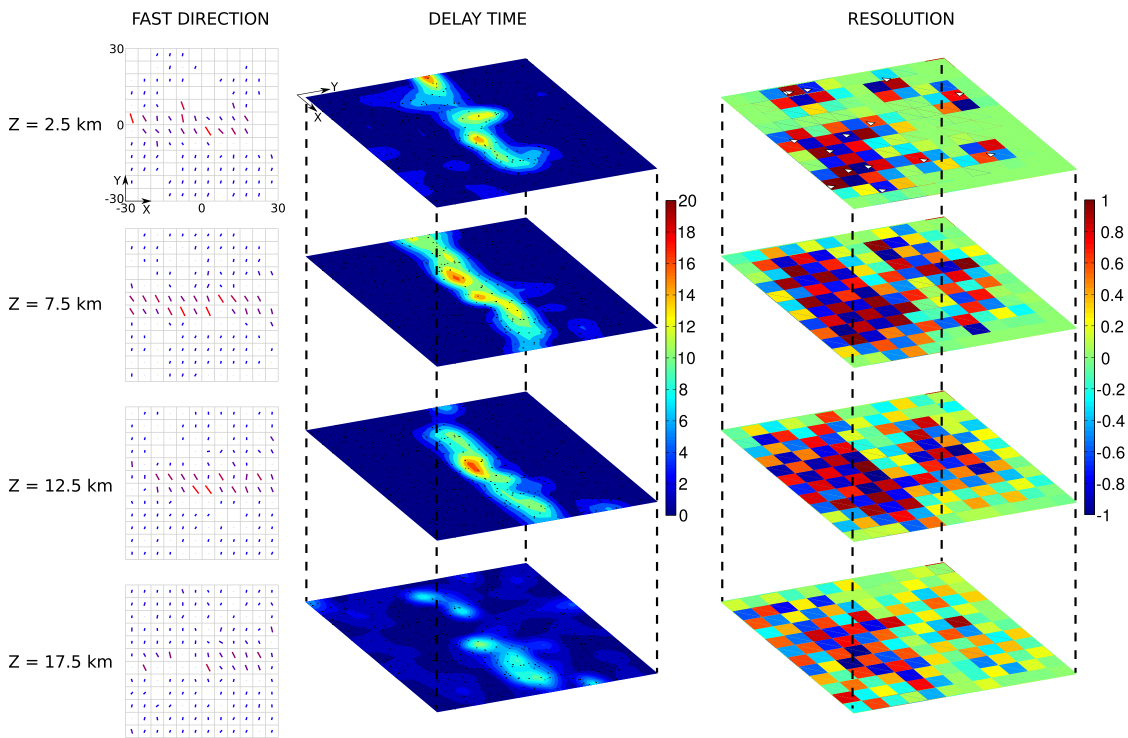

Figure 3.9: Inversion results from the 'strip' synthetic model test at 5 km resolution with a random event and station distribution. Fast direction plots show θ angles as bearings for each model element, with longer bars and warmer colours indicating stronger anisotropy. Empty cells indicate either no data available or no anisotropy strength for that particular block. Delay time plots show α values for each block (smoothed for plotting), scaled for percent anisotropy (0-20%). Triangles on the upper layer show the location of synthetic stations. Resolution plots show the results from checkerboard testing. Results close to a checkered arrangement of 1/-1 for adjacent blocks are well resolved. In comparison to the model using a uniform event and station distribution, the best resolved parts of the model are concentrated in the southern half ($0 < y < -30$) of the model where the stations are clustered.

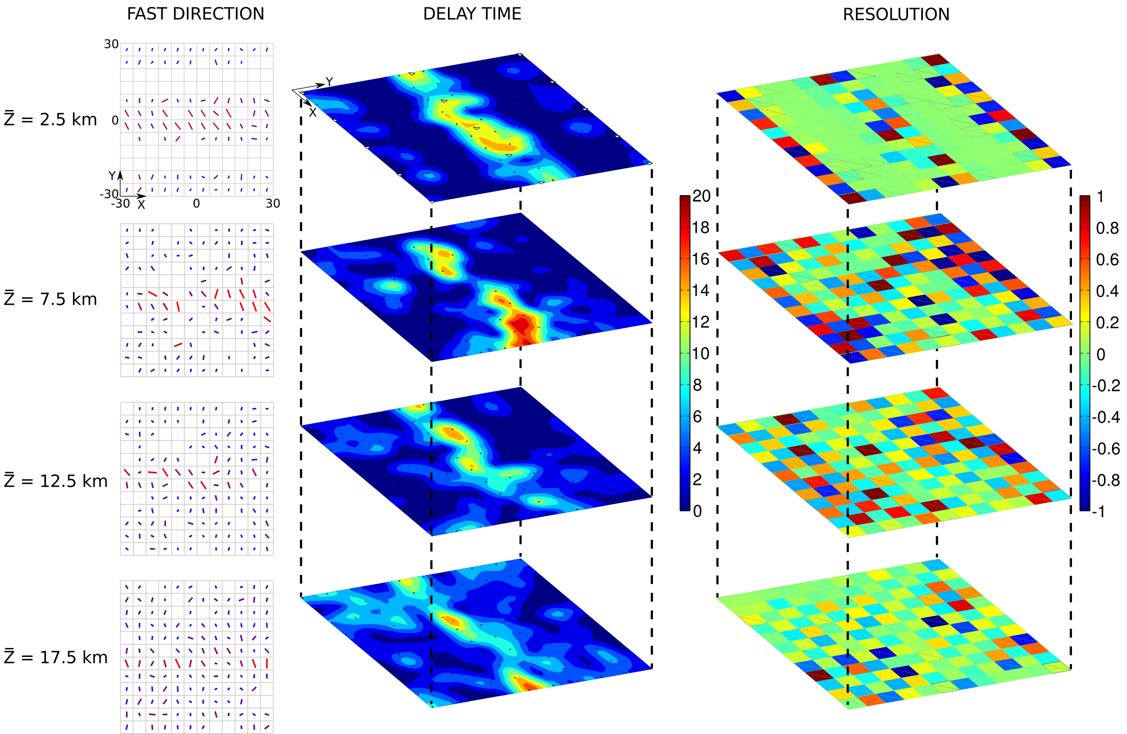

Figure 3.10: Inversion results from the 'strip' synthetic model test at 5 km resolution with a uniform event and station distribution. For this model, a 'random' starting model was used, where all initial model parameters (α and θ) were randomly assigned. Fast direction plots show θ angles as bearings for each model element, with longer bars and warmer colours indicating stronger anisotropy. Empty cells indicate either no data available or no anisotropy strength for that particular block. Delay time plots show α values for each block (smoothed for plotting), scaled for percent anisotropy (0-20%). Triangles on the upper layer show the location of synthetic stations. Resolution plots show the results from checkerboard testing. The high anisotropy 'strip' of the synthetic model is somewhat less evident in these results than both of the models that employ the 'average' starting model.

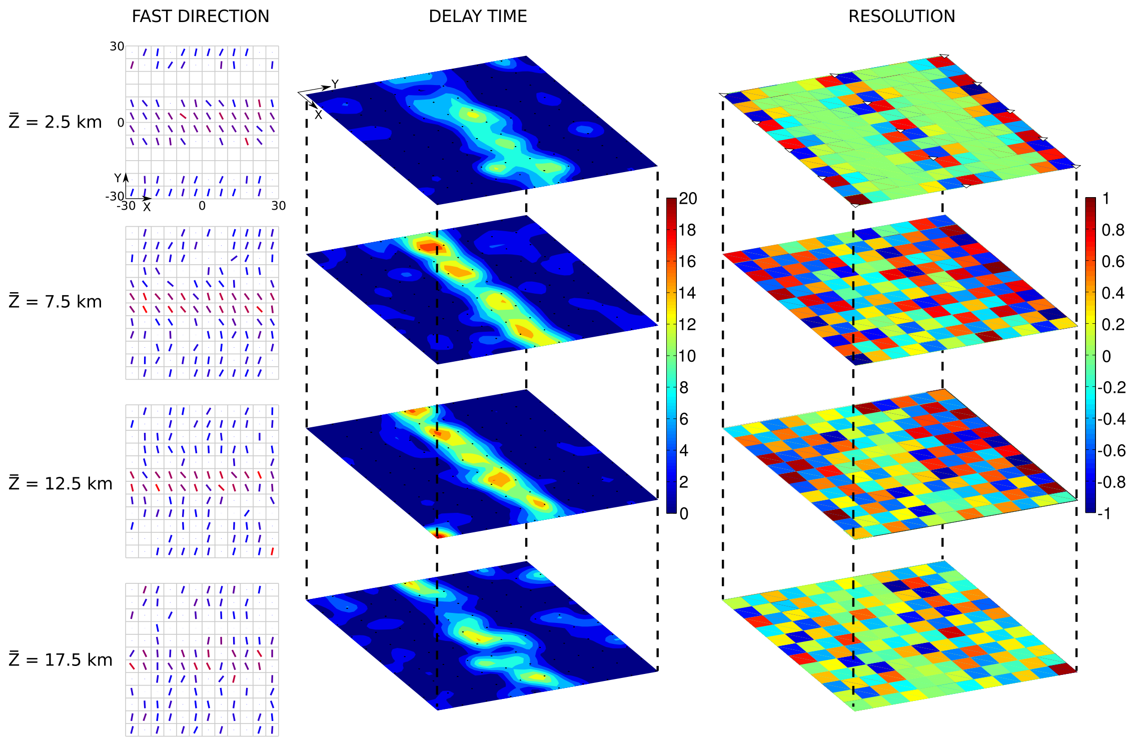

Figure 3.11: Inversion results from the 'strip' synthetic model test at 5 km resolution with a uniform event and station distribution, and additional noise added to the results of the initial forward model. Fast direction plots show θ angles as bearings for each model element, with longer bars and warmer colours indicating stronger anisotropy. Empty cells indicate either no data available or no anisotropy strength for that particular block. Delay time plots show α values for each block (smoothed for plotting), scaled by percent anisotropy (0-20%). Triangles on the upper layer show the location of synthetic stations. Resolution plots show the results from checkerboard mapping of the resolution matrix.

Inversion Parameter (universal)	Value	Model	Number of Measurements	Starting Model	Final delay misfit (s)	Final fast direction misfit (°)
Wavelet Frequency (Hz)	2.5	‘Strip’ model 1 (figure 3.7)	2502	Average	0.0140	2.8081
Wavelet whitening	10%	‘Strip’ model 2 (figure 3.9)	2930	Average	0.0105	3.1312
Iteration number	80	‘Strip’ model 3 (figure 3.10)	2543	Random	0.0382	6.5736
Initial damping	2	‘Strip’ model 4 (figure 3.11)	2476	Average	0.0328	4.5625
Subsequent damping	10	‘Layer’ model 2 (figure 3.15)	2861	Average	0.0508	13.6214
Damping iteration threshold	40	‘Layer’ model 3 (figure 3.17)	2555	Average	0.0322	4.1832
		‘Layer’ model 1 (figures 3.13 & 3.16)	2498	Average	0.0570	14.4432

Table 3.2: Inversion parameters and model summaries for the synthetic models shown in figures 3.6-3.17. Misfit values represent an average of all data misfits, weighted by measurement error.

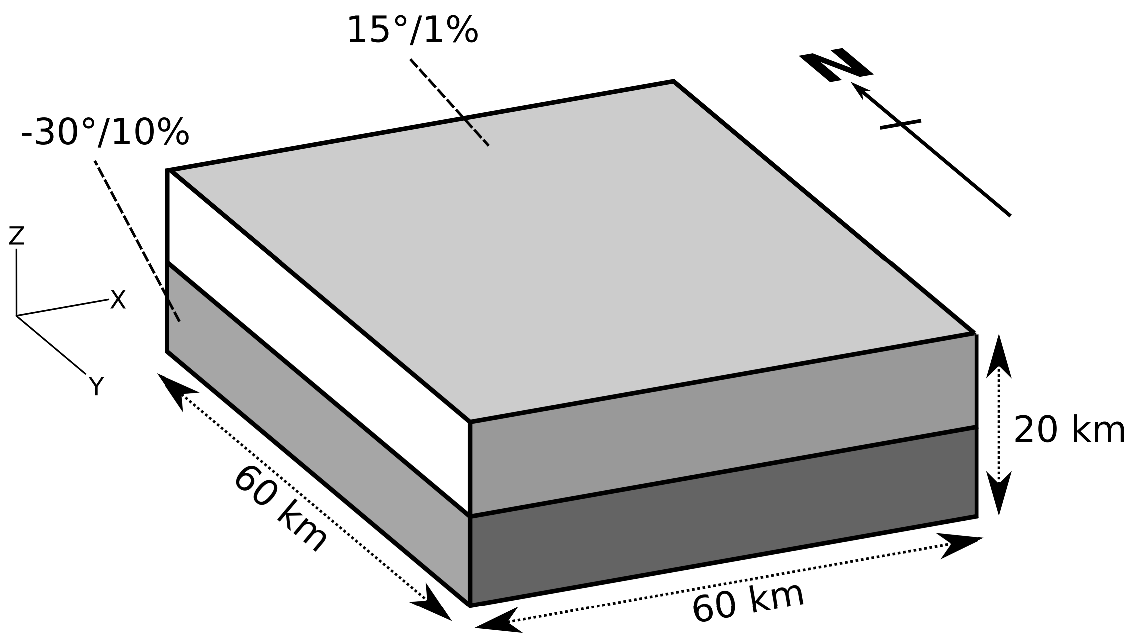

Figure 3.12: Schematic diagram showing the model domain used for the 'layer' synthetic model test. The anisotropy values shown refer to model θ and α, respectively. γ and ψ values are set to zero and are not solved for in the inversion.

susceptibility to induced anisotropy). Similarly to the 'strip' model, the 'layer' model, using uniform event and station locations (figure 3.13), produces lower weighted average final misfits and more accurate models than the model that uses random event and station location (figures 3.14 and 3.15). Results from the 'layer' models show a distinct two layer system, with a reasonably well determined upper layer despite its relatively low anisotropy. There is a degree of 'smearing' between the layers, as can be in figures 3.13 and 3.15 as the anisotropy parameters seem to gradually transition from one regime to another. This is demonstrated by looking at the distribution of θ values by depth level (figure 3.16) for the layer model shown in figure 3.13. Although the distribution peak coincides well with the actual layer θ value for each depth level, a broad distribution tail towards the other layer's θ value can be seen for each depth level.

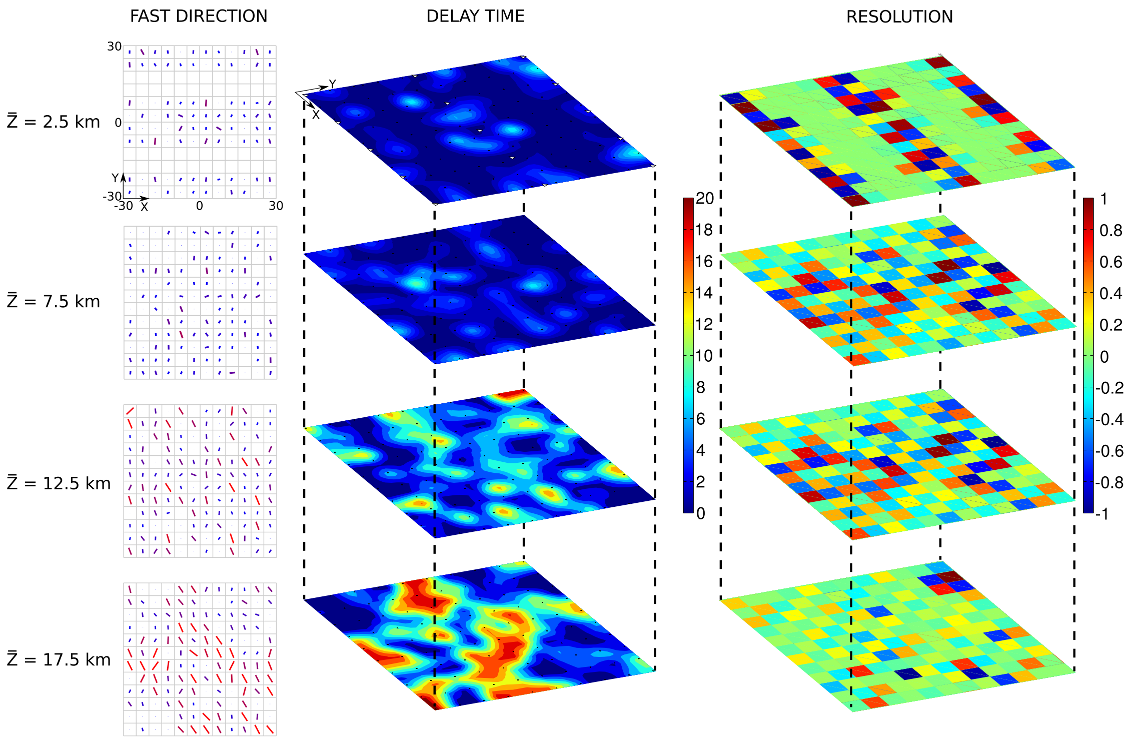

Figure 3.13: Inversion results from the 'layer' synthetic model test at 5 km resolution. Fast direction plots show θ angles as bearings for each model element, with longer bars and warmer colours indicating stronger anisotropy. Empty cells indicate either no data available or no anisotropy strength for that particular block. Delay time plots show α values for each block (smoothed for plotting), scaled for percent anisotropy. Triangles on the upper layer show the location of synthetic stations. Resolution plots show the results from checkerboard testing. Results close to a checkered arrangement of 1/-1 for adjacent blocks are well resolved.

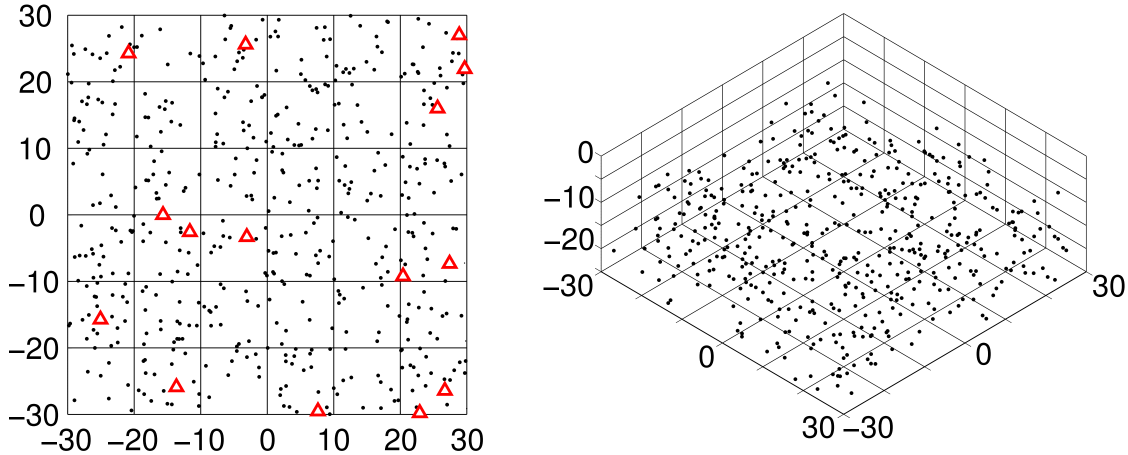

Figure 3.14: Event and station distribution for the 'layer' synthetic model with randomly derived event and station locations. Black dots represent the earthquake events and red triangles represent stations.

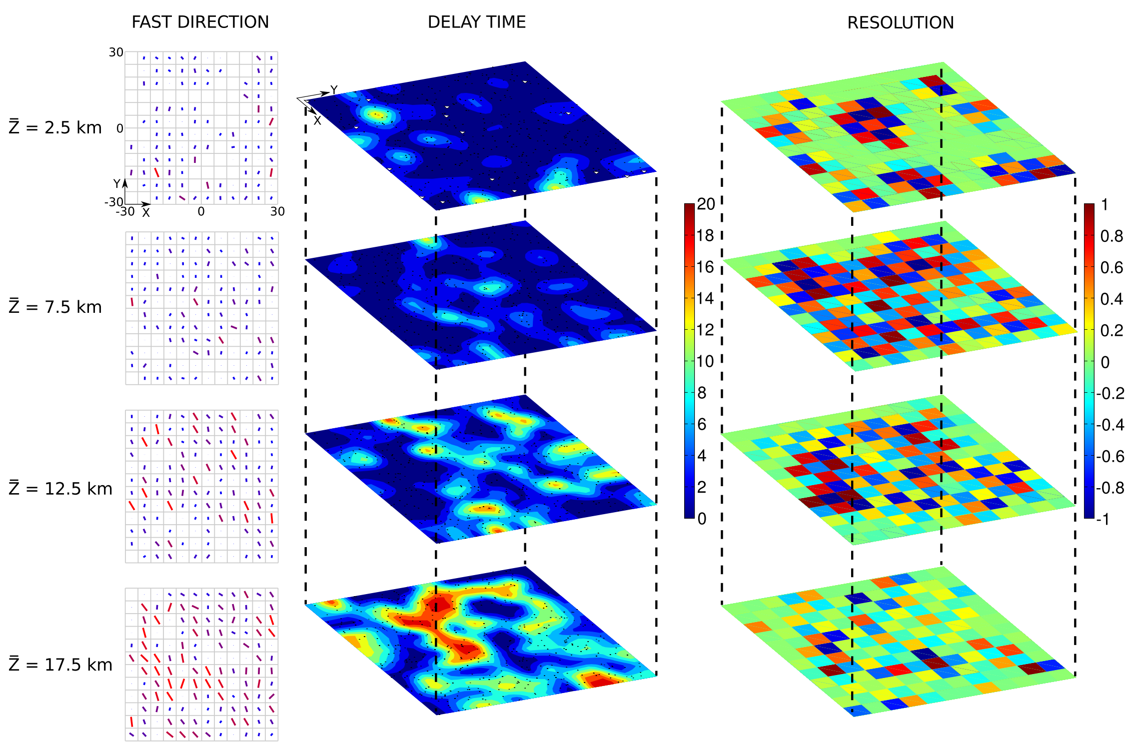

Figure 3.15: Inversion results from the 'layer' synthetic model test at 5 km resolution with a random event and station distribution. Fast direction plots show θ angles as bearings for each model element, with longer bars and warmer colours indicating stronger anisotropy. Triangles on the upper layer show the location of synthetic stations. Resolution plots show the results from checkerboard testing. Results close to a checkered arrangement of 1/-1 for adjacent blocks are well resolved.

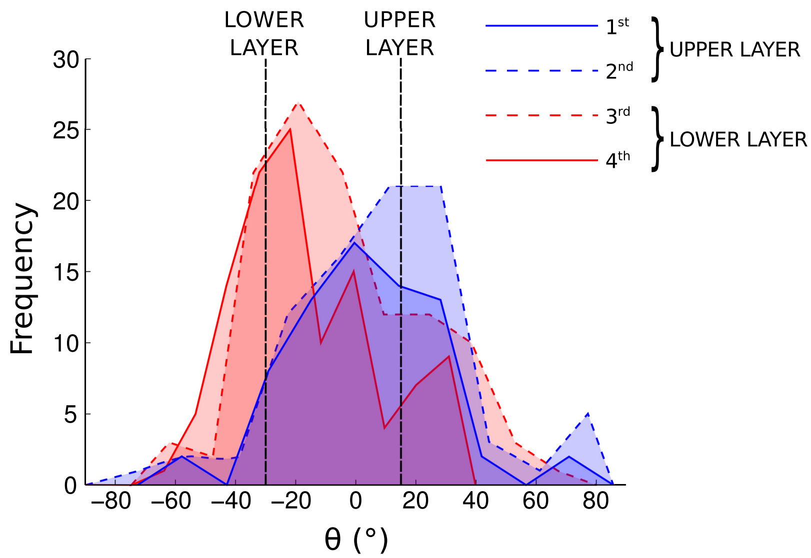

Figure 3.16: Histogram of anisotropy orientation, θ, frequencies per depth slice for 'layer' synthetic model 1, shown in figure 3.13. The 1^{st} depth slice is the one nearest the surface (at 2.5 km). The true synthetic model values for the upper and lower layers are also shown

Another model with more subtle layering was tested in order to test how the method deals with layers with more similar anisotropic properties. The model is a two layer system with the same geometry as that shown in figure 3.12, with an upper layer α of 5% and θ of 60° and a lower layer α of 5% and θ of 30°. Data misfits, shown in table 3.2 under the 'layer' model 3 entry, are relatively low. θ value frequency by depth slice is shown in figure 3.17, showing that anisotropy orientation in the top layer is very well constrained in comparison to the bottom layer. The general tendency for the upper layer of a layer model such as this to be better constrained was also observed in Özalaybey and Savage [1994] and Wookey [2012], who also investigated the layered anisotropy problem. A summary of all synthetic model measurements can be found in table 3.2.

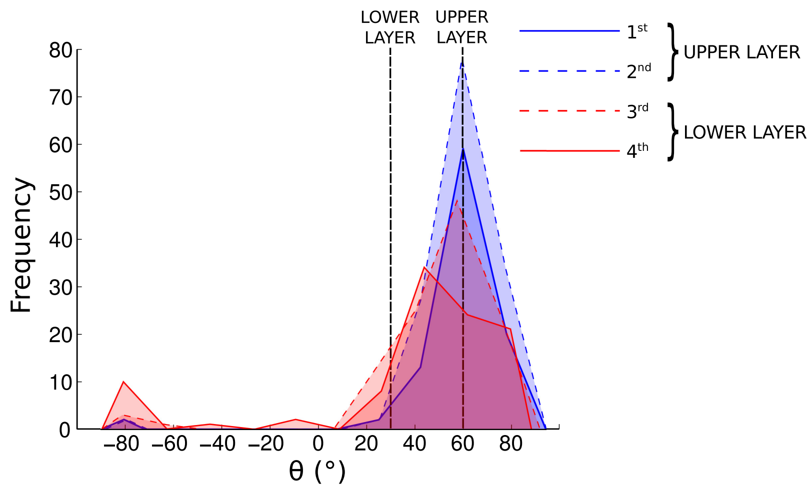

Figure 3.17: Anisotropy orientation, θ, frequencies per depth slice for 'layer' synthetic model 3, with an upper layer θ of 60° and a lower layer θ of 30°. Both layers in the model had an α value of 5%. The 1^{st} depth slice is the one nearest the surface (at 2.5 km).

3.5.2 Darfield data inversion

All models in this section use a block size of 5 km^3 and a maximum depth of 20 km. Recorded events outside a defined straight-line incidence are excluded from models in order to restrict events with large offset/depth ratios. A 60° straight-line incidence angle threshold was applied, leaving 2406 event-station paths from 1550 events. A wavelet frequency of 3.27 Hz was found from averaging MFAST filter windows for all results utilised. The upper limit of anisotropy was set at 20%. Final models for the Canterbury region are well resolved near the Darfield fault trace down to 10 km depth, beneath which resolution drops off until the lowest level, where resolution is poor. We investigate model dependence on the starting model, various model damping parameters, and model smoothing. The reader should note that in figures showing model α (anisotropy strength), areas in which there are no data are shown as having 0% anisotropy, however in reality the anisotropy is unconstrained. Areas of resolution are marked in each figure, but cross-referencing figures displaying α with figures showing anisotropy orientation will make it clear where data constraints exist in the model space.

Figures 3.18 and 3.19 show results from a standard model solving for two model parameters (α and θ). In this case, events outside of a 60° straight-line incidence were excluded and an 'average' starting model was used (see appendix B). An initial damping value of 1 was used between each iteration until the 40^{th} iteration, when the damping value was increased to 10. The results show that anisotropy is concentrated in the top 0-5 km layer where it is relatively evenly distributed, constituting a layer of around 9-14% anisotropy. The layer beneath this, at 5-10 km, shows a layer that is virtually isotropic in the vicinity of the Greendale fault. The strongly anisotropic top layer appears to extend to the 5-10 km depth towards the north of the model space at the edge of the resolved area. Beneath this, anisotropy is similarly small with an apparent patch of moderate (5-10%) anisotropy near the trace of the Charing Cross blind thrust offshoot (see figure 3.4).

Interpretation of the anisotropy orientation must be carefully considered, as anisotropy orientations for model elements with a very low α value are poorly defined within the model due to the small contribution to the shear wave splitting of rays passing through. Results shown in figure 3.19 show that anisotropy is somewhat aligned with the ~110-120° σ_{Hmax} direction found through other means. At the eastern section of the Greendale fault there is a distinct E-W rotation in anisotropy orientation, most evident in the uppermost layer, bringing it into alignment with the fault trace. At the western section, fast directions are

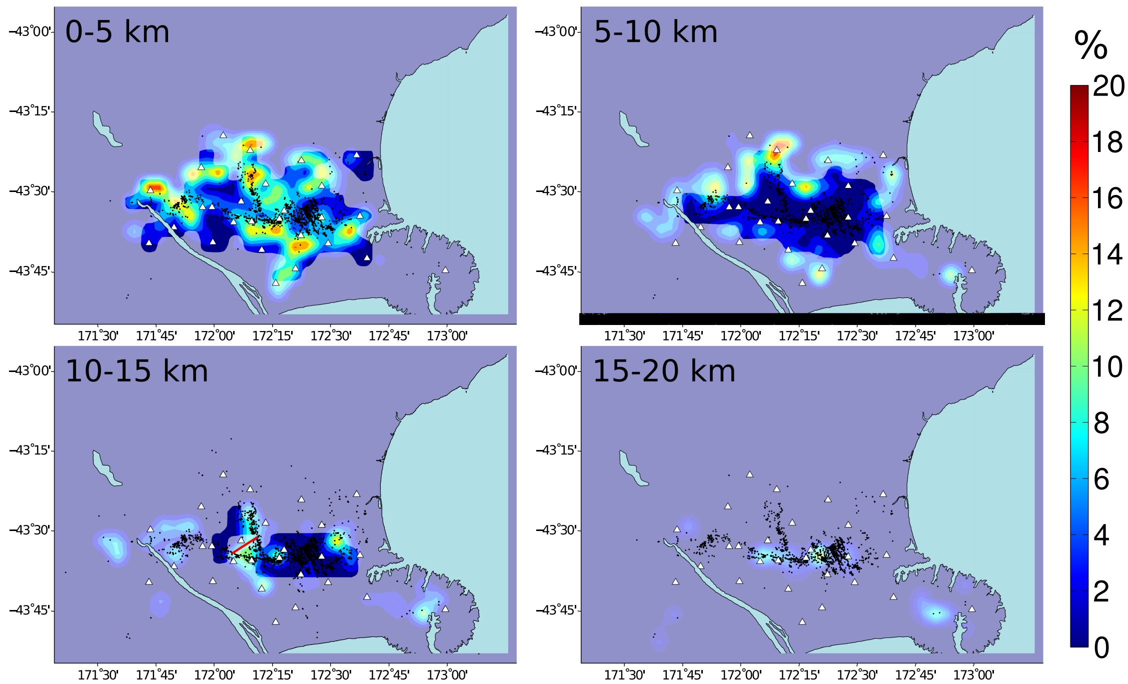

Figure 3.18: Inversion results using an average starting model, for the Canterbury region showing strength of anisotropy (α) shown as a percentage. Also shown are available event locations (black circles), and station locations (white triangles). Areas of the plot that are not well resolved by the model have been greyed out. This model solved for α and θ and was produced using 80 total model iterations, an initial damping value of 1 and a subsequent damping value of 10 after the 40^{th} iteration.

aligned both with σ_{Hmax} and the Greendale fault, due to the rotation of the fault trace. Anisotropy orientation at the periphery of the resolved model area, notably towards Bank's Peninsula to the southeast, as well as to the west and the north of the Greendale fault, undergoes further rotation from σ_{Hmax} and E-W.

Final data average misfit values for the model, weighted by the individual synthetic measurement error, were 0.065 s and 26.9° for delay times and fast directions, respectively. A visual comparison between the observed and synthetic SWS fast direction measurements can be seen in figure 3.20. The most noticeable difference between the measured and synthetic data, in terms of fast direction, is that, for all seismic stations, the variance in

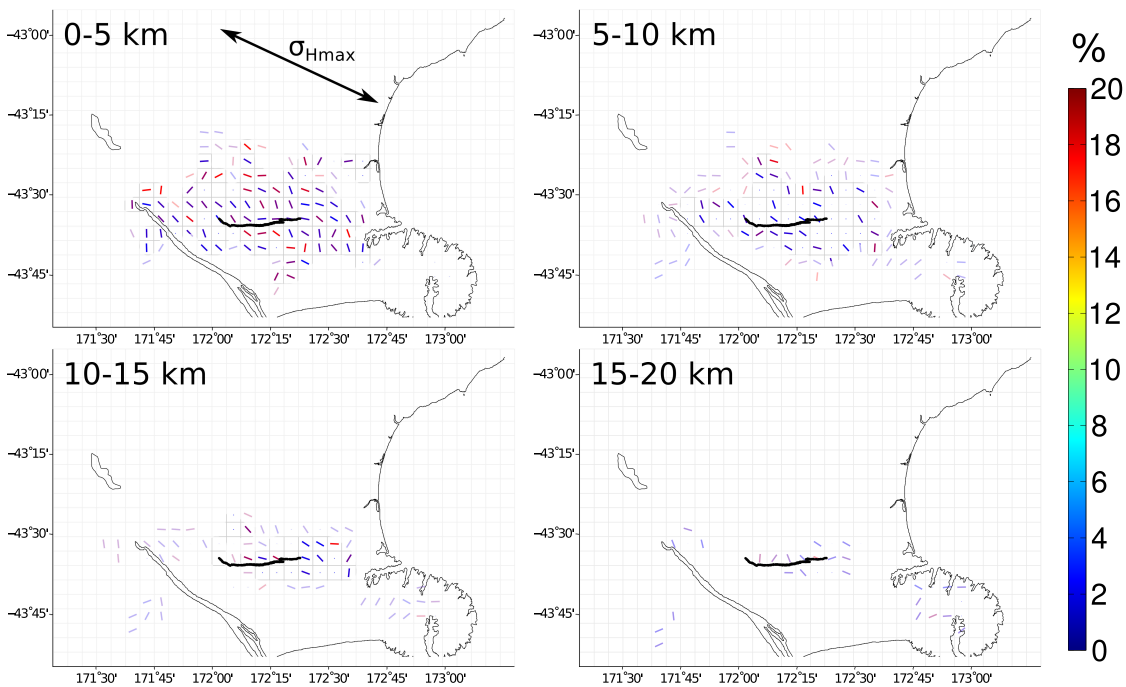

Figure 3.19: Inversion results using an average starting model, for the Canterbury region showing anisotropy orientation, represented by the fast shear wave axis (θ) projected onto the horizontal plane. Also shown is the surface trace of the main Darfield fault rupture. Areas of the plot that are not well resolved by the model have been greyed out. Model parameters are those described in figure 3.18.

results is greater for the observed values than it is for the synthetic values. The standard deviation of the distribution of observed fast directions (i.e. the SWS measurements) is 44.9°, in comparison to 40.3° for the synthetic fast directions (i.e. those derived from the model). This difference in measurement variance between observed and synthetic results is seen to a greater extent in delay times, with observed measurements giving a standard deviation of 0.10 s and synthetic measurements giving 0.058 s. The relatively low variance of synthetic SWS measurements in comparison to the observed ones is common throughout all models studied.

3.5.3 Testing other Starting Models

The TESSA results, given in Holt [2013], are shown in figure 3.21. These results were interpolated onto the model grid and used as starting parameters for an inversion, the results of which are shown in figures 3.22 and 3.23. There are certain incongruencies between the TESSA grid and the model grid that are dealt with simply by finding the nearest available measurement to the centre of each model element (but only in the lateral sense, as TESSA results are two dimensional). As TESSA employs quadtree gridding, with element sizes dependent on data availability, swaths of the derived inversion starting model may have identical anisotropy parameters. This is most evident in the southeastern part of the model, beneath Banks Peninsula. Other inversion parameters were set identically to those used with the average starting model, the results of which are shown in figures 3.18 and 3.19.

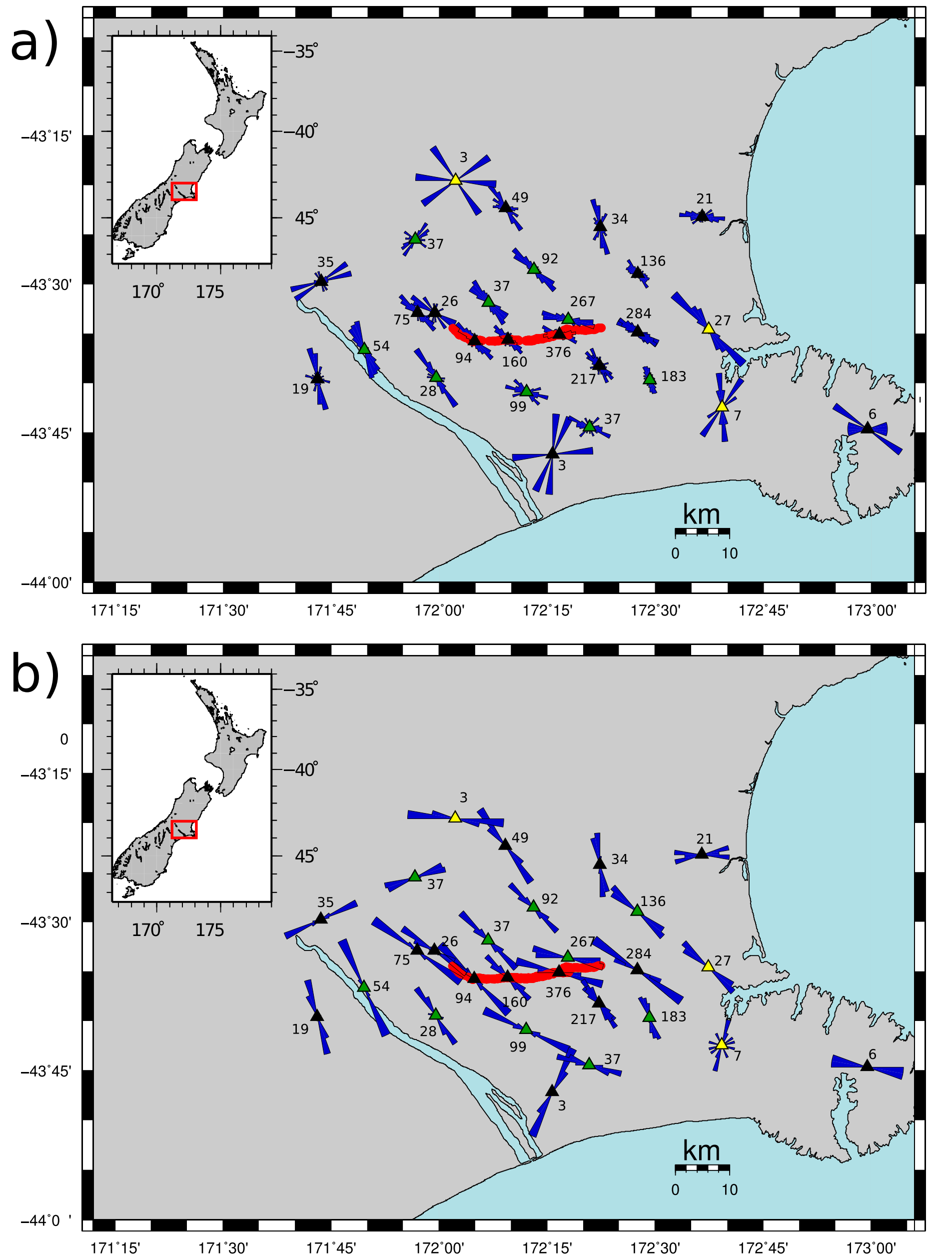

Figure 3.20: Map with circular histograms showing fast direction results across the seismic network. (A) shows the measured data used in the inversion. It differs from figure 3.1 in that events with a straight-line incidence angle greater than 60° are excluded, as per model specifications. (B) shows synthetic data produced using the inverted model. Inversion parameters are those described in figure 3.18. As in figure 3.1, black triangles represent temporary broadband stations, yellow represent GeoNet permanent stations and green represent GeoNet temporary short period stations. Numbers indicate the number of measurements at each station. The size of the circular histograms in A and B are scaled individually for display purposes.

The main similarity between inversion results using a TESSA derived starting model and those using an average starting model (compare figures 3.22 and 3.18) is the strongly anisotropic upper layer (< 5 km) overlying a weakly anisotropic volume in the vicinity of the Greendale fault. This feature is notable, especially as the TESSA starting model is depth-invariant on the outset of the inversion. Another feature which is somewhat preserved between the two results is a volume of strong anisotropy in the vicinity of the Charing Cross blind thrust at depths of between 10-15 km (shown in figure 3.18). A major feature found in the results taken from the inversion using the TESSA starting model inversion that is not found in those using an average starting model is a region of high anisotropy in the southeast beneath Banks Peninsula. This feature is a holdover from the TESSA input and is clearly evident in figure 3.21, however it is not well resolved in the TESSA delay time tomography, and the general lack of data in the vicinity of Banks Peninsula means that it similarly cannot be resolved by the method in this study. Results for the θ parameter are very similar between the two approaches (compare figures 3.23 and 3.19). We expect these particular results to be comparable due to the fact that a similar spatial averaging of fast directions was employed in both TESSA and the average starting model calculation. Final average weighted data misfit values are comparable to those obtained using the average starting model.

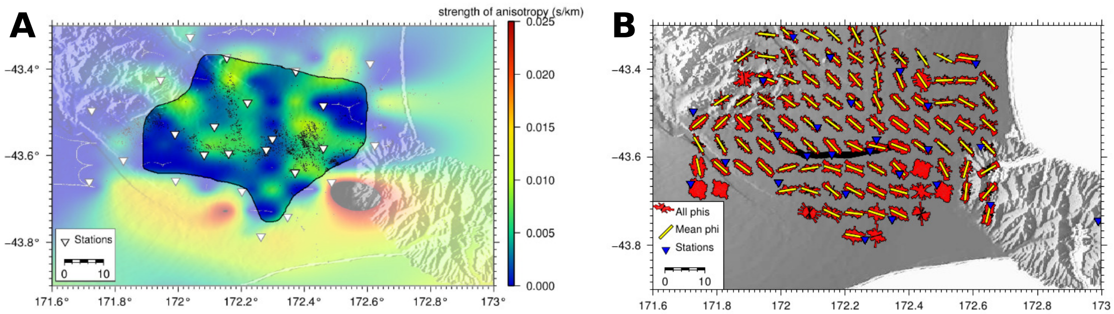

Figure 3.21: TESSA delay time tomography and fast direction spatial averaging of the entire Darfield dataset taken from Holt [2013]. (A) delay time tomography with resolved area highlighted. Note that anisotropy strength is displayed as s/km in this plot. (B) spatial averaging of ϕ measurements. Black dots represent seismicity, white/blue triangles are station locations. The thick black line in (B) represents the main trace of the Greendale fault.

Figures 3.23 and 3.25 show results from an inversion using a uniform starting model, where all elements were ascribed an α value of 5% and a θ value of 115°, thereby simulating a homogeneous anisotropic regime which is oriented parallel to σ_{Hmax} in the region. Again, inversion parameters were identical to those used to create the results from the average starting model shown in figures 3.18 and 3.19. Model α results (figure 3.23) contain many similar aspects to the previously shown average and TESSA derived results (figure 3.22); an upper layer of strong anisotropy between 0-5 km depth overlying a near-isotropic volume surrounding the Greendale fault. A volume of higher anisotropy near the Charing Cross thrust between 10-15 km depth is also present, however it lies further to the south than in the average model results and may be interpreted to be located at the confluence of the Charing Cross and Greendale faults or even on the Greendale fault only. Values for α are generally lower than those determined in the average model. Model θ results (figure 3.25) are, predictably, well aligned with the direction of σ_{Hmax}. As in the average model results, there are noticeable θ rotations in the uppermost layer, towards E-W at the eastern edge

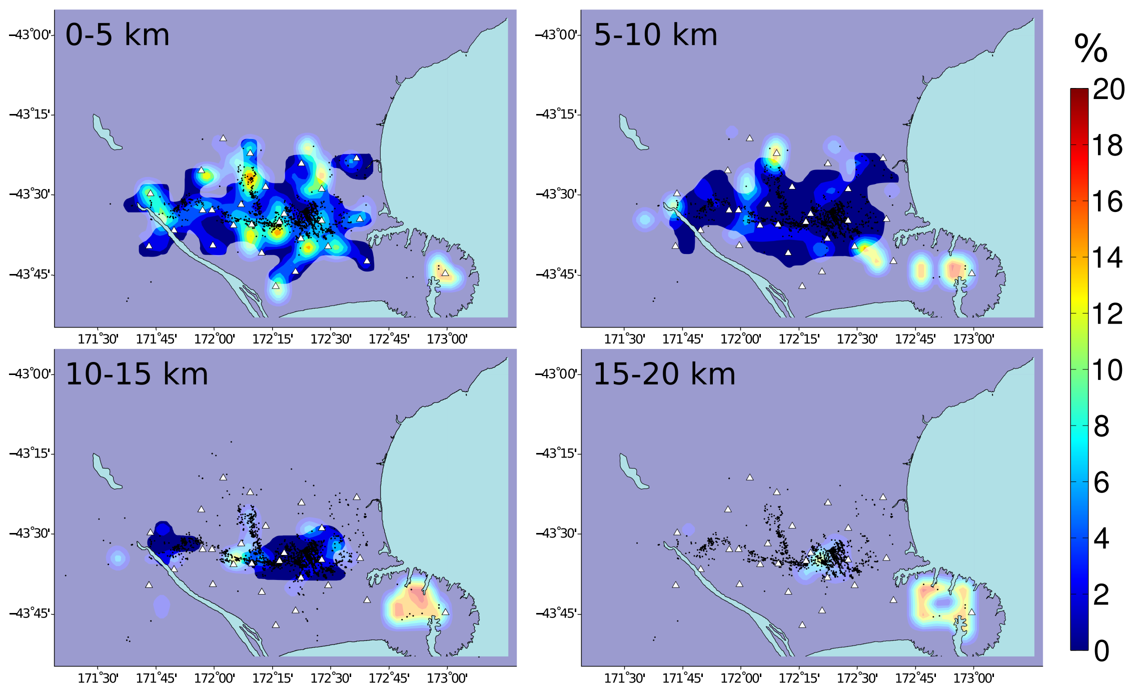

Figure 3.22: Inversion results using TESSA results as a starting model, for the Canterbury region showing strength of anisotropy shown as a percentage. Also shown are available event locations (black circles), and station locations (white triangles). Areas of the plot that are not well resolved by the model have been greyed out. This model was produced using 80 total model iterations, an initial damping value of 1 and a subsequent damping value of 10 after the 40th iteration.

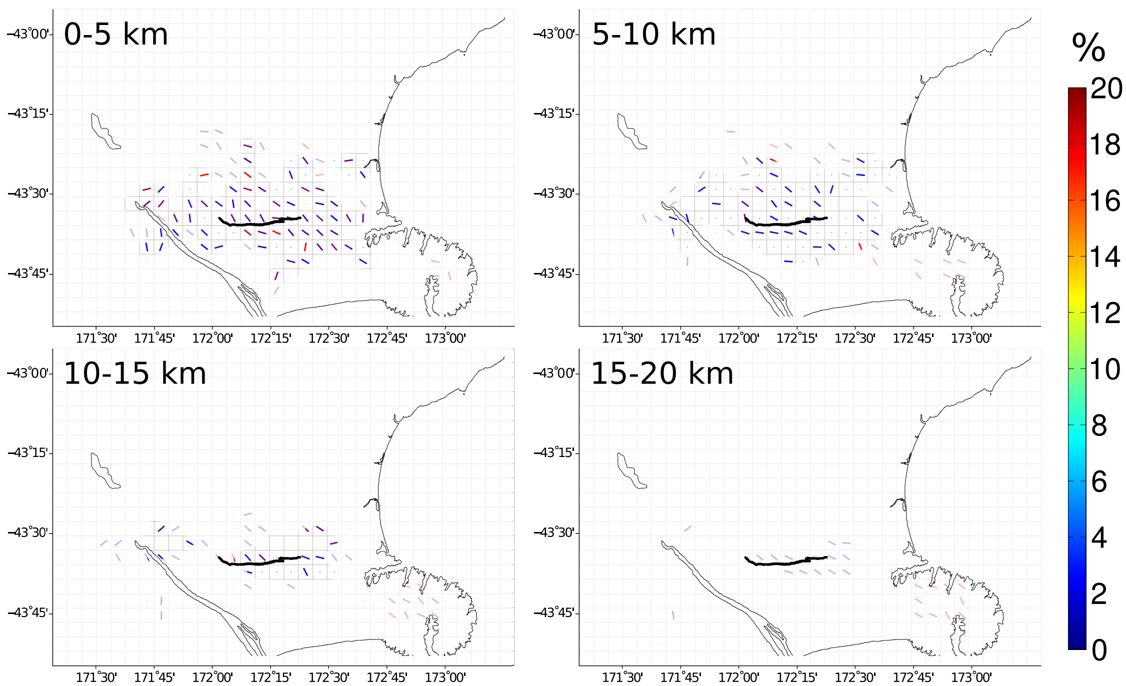

Figure 3.23: Inversion results using TESSA results as a starting model, for the Canterbury region showing anisotropy orientation, θ. Also shown is the surface trace of the main Darfield fault rupture. Areas of the plot that are not well resolved by the model have been greyed out. Model parameters are those in figure 3.22.

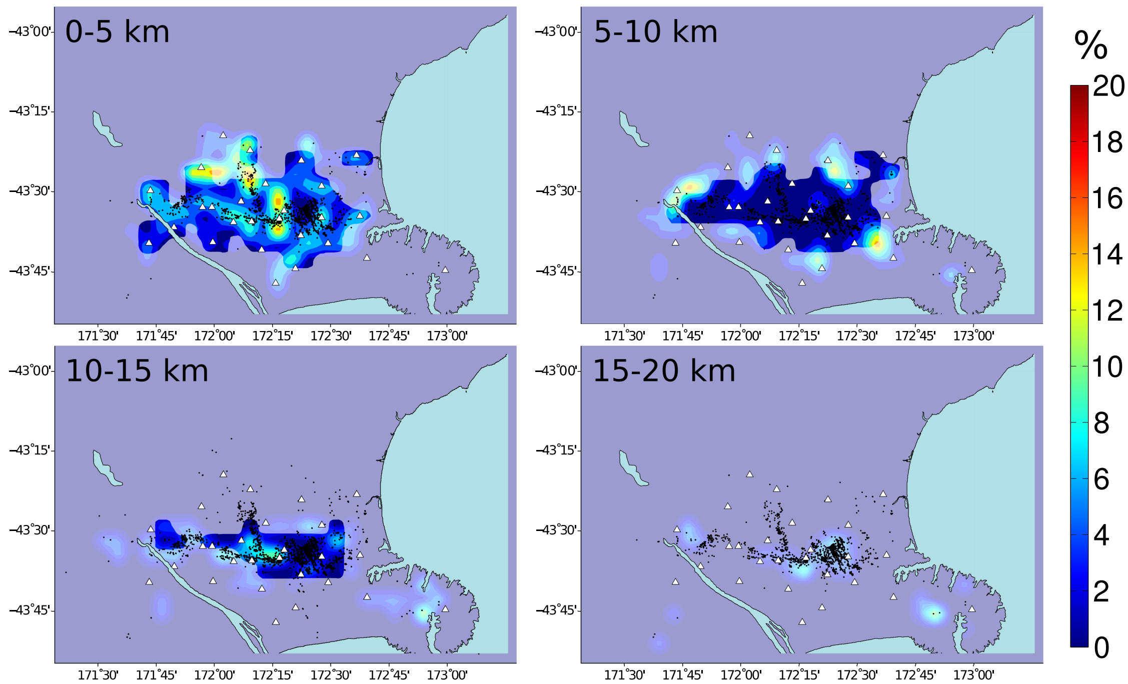

Figure 3.24: Inversion results from a uniform starting model for the Canterbury region showing strength of anisotropy shown as a percentage. Uniform starting model parameters were set θ to 115° and α to 5%. Also shown are available event locations (black circles), and station locations (white triangles). Areas of the plot that are not well resolved by the model have been greyed out. This model was produced using 80 total model iterations, an initial damping value of 1 and a subsequent damping value of 10 after the 40th iteration.

of the Greendale fault, as well as towards N-S elsewhere around the edge of the resolved area. Final average weighted misfit values for the model are 26.9° and 0.068 s for ϕ and δt measurements, respectively (table 3.3).

We also produced a model using a random starting model where all initial model parameters are randomly assigned. The inversion method was run in the same way as the average model inversion shown in figures 3.18 and 3.19. Splitting parameter average misfits (weighted by measurement error) after forward modelling the initial random model were 43.1° and 0.088 s for fast directions and delay times, respectively. These misfit values

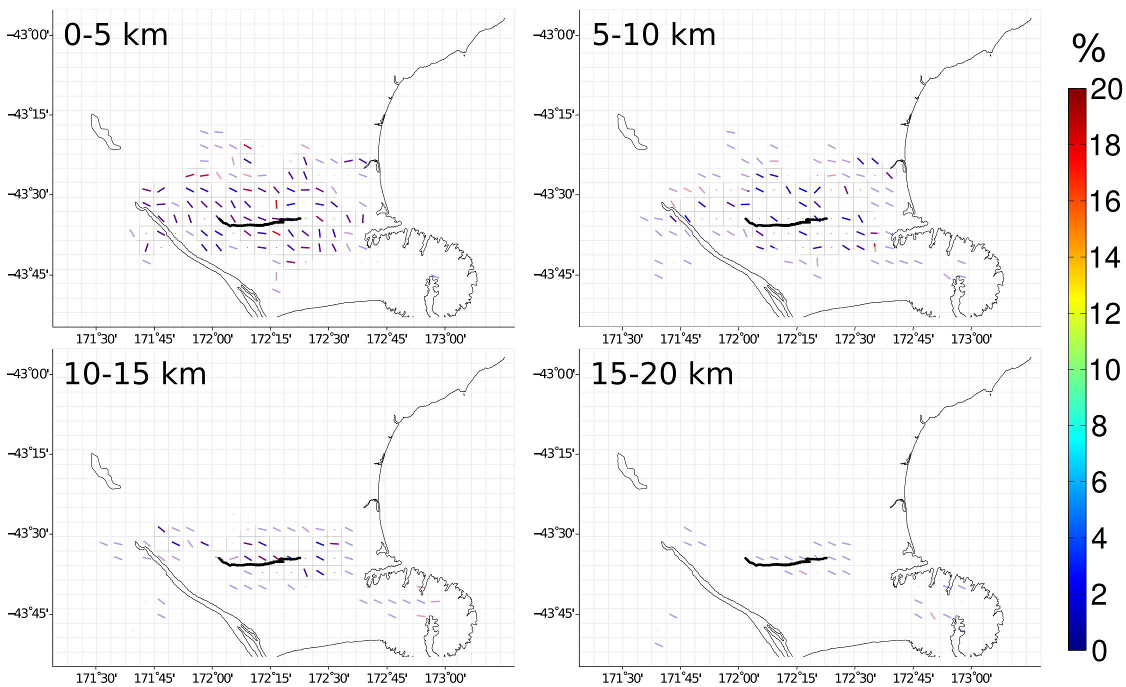

Figure 3.25: Inversion results from a uniform starting model for the Canterbury region showing anisotropy orientation, θ. Uniform starting model parameters were set θ to 115° and α to 5%. Also shown is the surface trace of the main Darfield fault rupture. Areas of the plot that are not well resolved by the model have been greyed out. Model parameters are those in figure 3.23.

represent a baseline accuracy that can be achieved using no prior consideration of the input data, although strictly speaking the delay time average misfit, and to a lesser extent the fast direction misfit, are controlled by the range of anisotropy strength allowed by the model (in this case, 0-20%). Final misfits after 80 iterations were 29.4° and 0.0724 s for ϕ and δt, respectively.

Figure 3.26 shows both the starting model and inversion results for the top two layers (0-5 km and 5-10 km). Again, the top layer is characterised by strong anisotropy overlaying a low anisotropy volume surrounding the Greendale fault, however the second layer (5-10 km) has a more significant component of anisotropy than the other models. The resulting area of good resolution is smaller than for the other starting models. Anisotropy orientation resolved from the random starting model is generally more scattered than the average model, but still somewhat resembles the average model in areas that are well constrained by data (i.e. near the Greendale fault).

3.5.4 Damping Parameters

In all, three sets of damping parameters were analysed to determine their effect on model variance between iterations. Each set of damping parameters consists of a small value to restrict variance until the 40^{th} iteration, in which the damping parameter is increased in order to test the stability of the solution that the inversion is converging towards. The damping factors for each set of damping parameters studied is 1-10 (i.e. a variance of 1 until iteration 40, at which it is increased to 10), 2-15, and 3-20. Each set of parameters

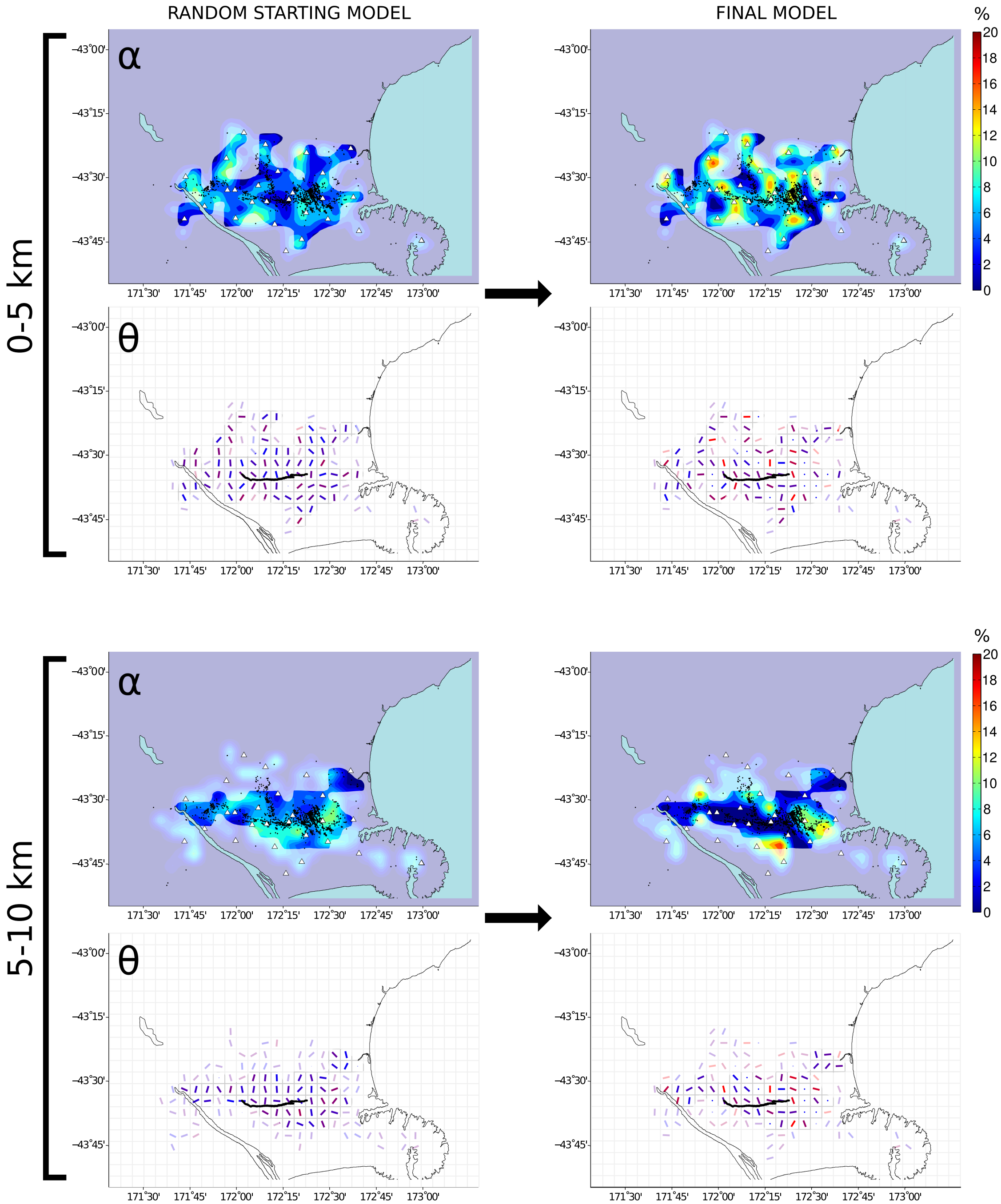

Figure 3.26: Diagram showing a random starting model (left column) and the associated inversion results (right column) showing both anisotropy strength, α, and orientation, θ. Only the top two layers (of four) are displayed. The resolved area (within the greyed out area) for both the starting model and the final results is based on the final model resolution. Anisotropy strength plots (α) show event and station distribution (white triangles and black dots, respectively) and orientation plots (θ) shows the main Darfield fault rupture in black. This model was produced using 80 total model iterations, an initial damping value of 1 and a subsequent damping value of 10 after the 40th iteration.

produced broadly similar results, the visual inspection of which unveiled no potential major points of difference that would indicate that the models are converging towards substantially different results.

A further comparison between average weighted data misfit and synthetic data variance can be seen in figure 3.27. Data misfit is not significantly reduced over the 80 iterations of each model, especially for fast directions where average misfits were consistently stable. Overall delay misfits were generally stable after around iteration 5. Misfits increasing over iterations are believed to be due to the process of solving for two parameters simultaneously, and generally indicative of the complexity of the data. The average misfit conflates all aspects of the real and synthetic data relationship to one value. In order to separate out another indicator of model progression, we also show the standard deviation of the distribution of synthetic measurements. Real data standard deviations are significantly higher than those shown in figure 3.27, at 0.10s and 44.9° for δt and ϕ, respectively. Due to this, we prefer damping parameters that increase synthetic data variance without sacrificing overall misfit. Lower damping values are also preferred as it is understood that applying the Newton-Raphson numerical technique to the relatively poorly constrained problem of SWS anisotropy (as compared to travel-time tomography, for example) imparts a strong dependence on the starting model [Abt and Fischer, 2008]. It is therefore expedient to limit model variance in an effort to maintain any integrity the starting model may have (although the quality of the starting model may be debated). Therefore the final models shown in this study use the 1-10 damping parameter set as it appears to best satisfy these theoretical ideals.

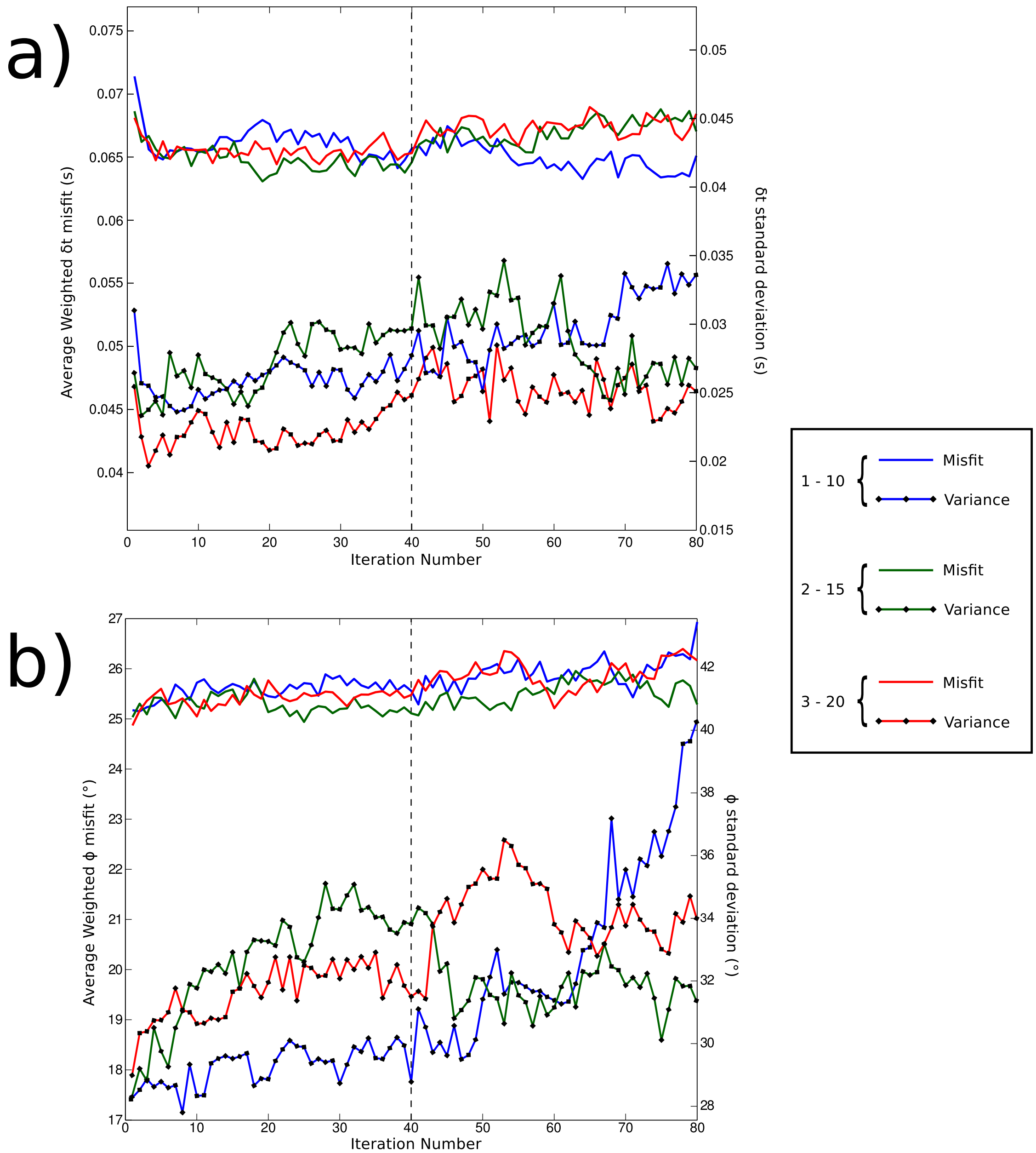

Figure 3.27: Result comparison between different damping parameter sets. (A) shows delay time (δt) average weighted data misfit (solid lines) and the standard deviation of synthetic δt values (solid lines with diamonds at vertices) for each iteration. (B) similarly shows fast direction (ϕ) average weighted data misfit and synthetic measurement standard deviation for each iteration. Vertical dashed lines indicate the iteration at which damping was relaxed (40). The damping parameter sets, 1-10, 2-15 and 3-20, are initial and subsequent inter-model variance values for each iteration.

3.5.5 Number of iterations

Models presented in this analysis have all undergone a total of 80 iterations, with a change of damping parameter at the 40^{th} iteration. The decision to perform this number of iterations is based on the precedent set in the similar approach used by Abt and Fischer [2008]. In setting the number of iterations used by the model, it is hoped that the model can converge on a stable solution in the number of iterations available, whilst maintaining a reasonable computation time for the process. As can be seen in figure 3.27, no significant decrease in the average weighted misfit is observed beyond iteration 5 or thereabouts. Close inspection of the model results in figures 3.18 and 3.19 show that the model parameters at the 5^{th} iteration are different in detail to the final model parameters, while still showing the same fundamental two-layer structure. Other than the synthetic data variance discussed earlier, the major difference between model parameters at the 5^{th} and the final iteration is that the resolution of the model as determined by the resolution matrix, $\mathbf{R}_M$, is extremely poor at the 5^{th} iteration. This lack of resolution is observed at all iterations until the damping parameter is relaxed from 1 to 10 at the 40^{th} iteration, at which point resolution rapidly improves over the subsequent 10 or so iterations. This result is, in a large part, due to the relationship between the resolution matrix and the model covariance matrix, $\mathbf{C}_M$ (see equation 3.4.8), which is defined by the damping parameter.

In light of these observations, a model was constructed with identical model parameters to those used to determine the results in figures 3.18 and 3.19, beginning with an average starting model, with the exception that only 10 model iterations were performed, and the model damping parameter is 10 for all iterations. The model parameter results, shown in figure 3.28 and 3.29 are very similar to those shown in figures 3.18 and 3.19 using the full 80 iterations, with a similar degree and area of resolution as determined using the resolution matrix. Final average data misfits were similar to those shown in figure 3.27, with an average weighted delay time misfit of 0.066 s and an average weighted fast direction misfit of 25.5° (compared with 0.065 s and 26.9° for the comparative inversion shown in figures 3.18 and 3.19). Therefore, it is apparent that the inversion process is capable of finding a stable solution within the objective function with significantly less iterations than were performed in the analysis. Given the potential for greatly reducing the overall computational time for individual models in this sense, employing models with fewer (10 or less) iterations may open avenues of approaching the exploration of parameter space in a increasingly stochastic manner.

3.5.6 Model block size

All models discussed up until now have had block elements with a 5 km^3 volume. We also performed an inversion using block elements with a 3 km^3 volume, again solving for α and θ, with an average starting model and 1-10 damping parameter values (see figure 3.30 and 3.31). Having smaller elements means that each model element has proportionately less data, and less of the model is well resolved. The ideal solution to this is to use an adaptive gridding technique, such as quad-tree gridding [e.g. Johnson et al. 2011,Townend and Zoback 2001], however this has not been implemented in this method. Conversely,

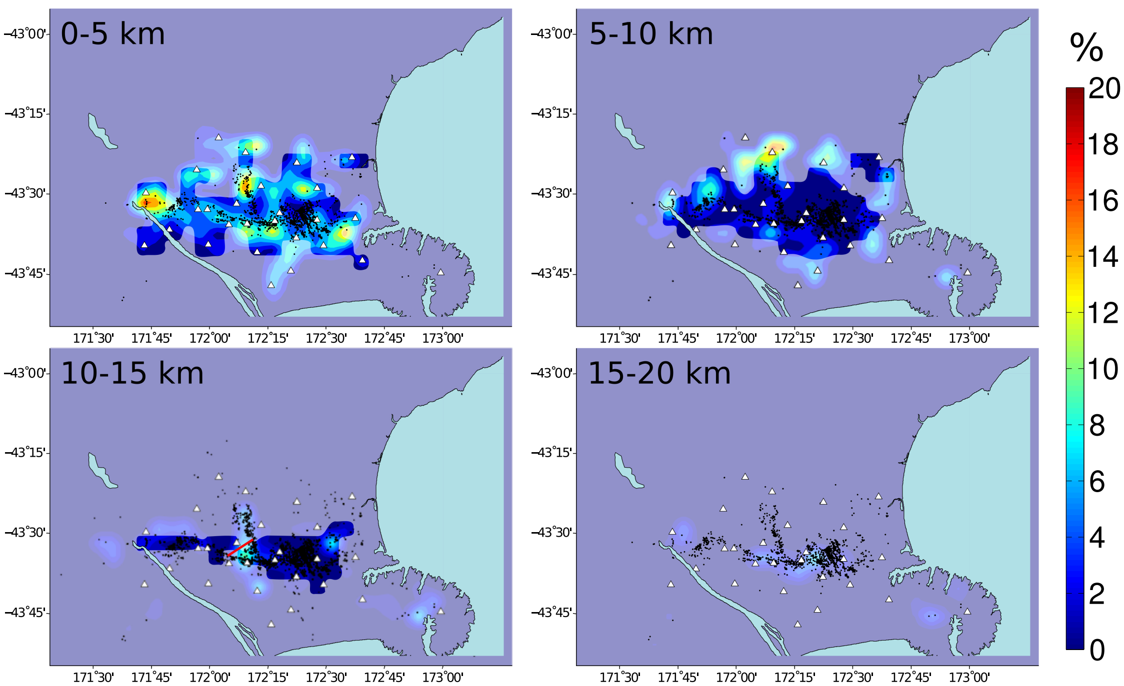

Figure 3.28: Inversion results using an average starting model, for the Canterbury region showing strength of anisotropy (α) shown as a percentage. Also shown are available event locations (black circles), and station locations (white triangles). Areas of the plot that are not well resolved by the model have been greyed out. This model solved for α and θ and was produced using 10 total model iterations, with a damping value of 10.

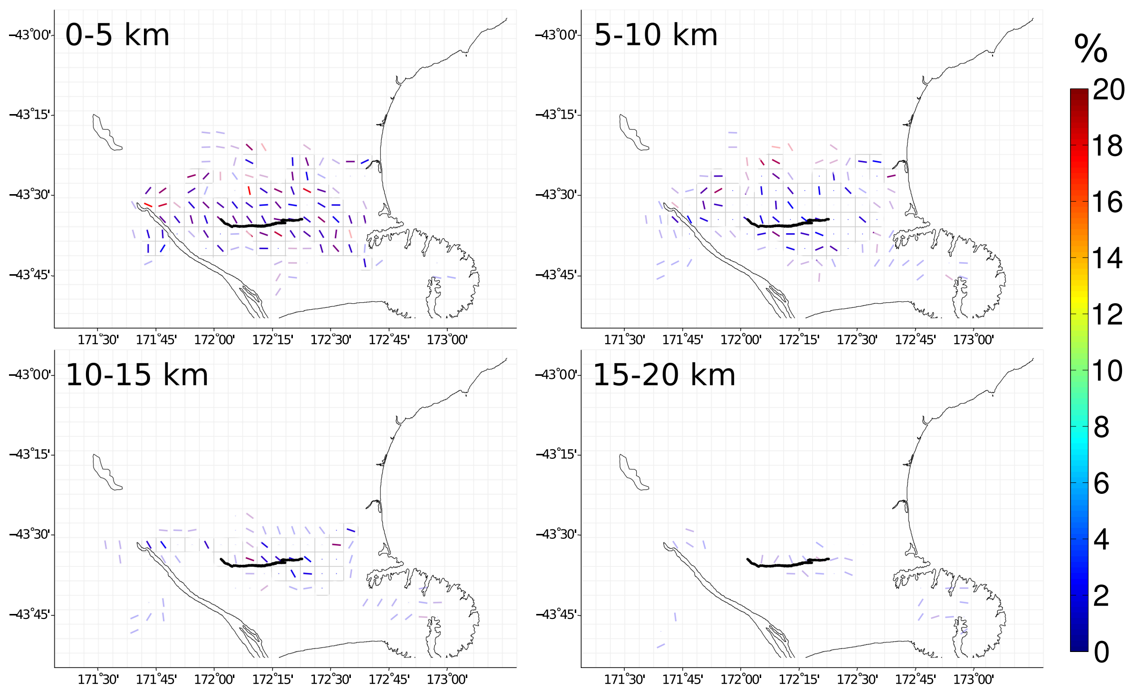

Figure 3.29: Inversion results using an average starting model, for the Canterbury region showing anisotropy orientation, represented by the fast shear wave axis (θ) projected onto the horizontal plane. Also shown is the surface trace of the main Darfield fault rupture. Areas of the plot that are not well resolved by the model have been greyed out. Model parameters are those described in figure 3.30.

a denser array of model elements allows for more fidelity in solving the inversion for the dataset. This is reflected in the final average weighted misfits which, at 0.057 s and 23.5° for δt and ϕ respectively, were lower than the methods using 5 km^3 model elements (see table 3.3).

Model α results (figure 3.30) show that the top layer, especially near the Greendale fault, has a strong degree of anisotropy. This layer is only resolved well near the seismic receivers due to the straight-line incidence restriction ($< 60°$) imposed on the data. The next layer, at 3-6 km depth, appears to differ from other models in that there is very low anisotropy towards the east of the resolved area, but still remains high towards the west. This indicates that there is a lateral variation in the depth of the upper high-anisotropy layer previously identified that is not evident at the 5 km block resolution.

Model θ results (figure 3.31) take a similar form to those obtained using 5 km^3 model elements, with the majority of the anisotropy oriented roughly parallel to σ_{Hmax}. E-W orientations, roughly parallel to the strike of the Greendale fault, are common towards the east of the fault trace. Rotations in anisotropy orientation away from the dominant ~110-140° bearing exist, but are scattered throughout the model, with the possible exception of results to the northwest of the resolved area, which appear to be have significant E-W and NE-SW components.

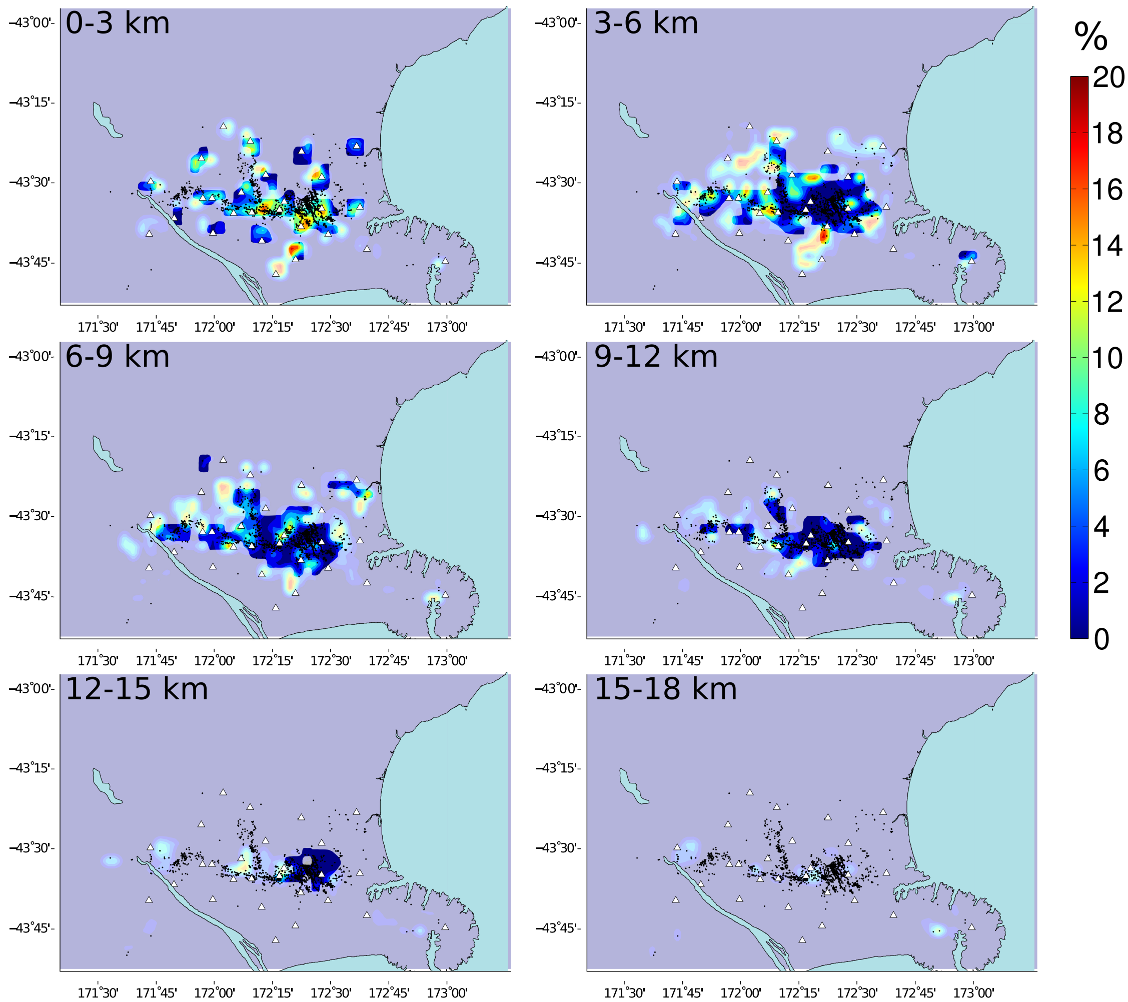

Figure 3.30: Inversion results using an average starting model with a block size of 3 km^3, for the Canterbury region showing strength of anisotropy (α) shown as a percentage. Also shown are available event locations (black circles), and station locations (white triangles). Areas of the plot that are not well resolved by the model have been greyed out. This model solved for α and θ and was produced using 80 total model iterations, an initial damping value of 1 and a subsequent damping value of 10 after the 40th iteration.

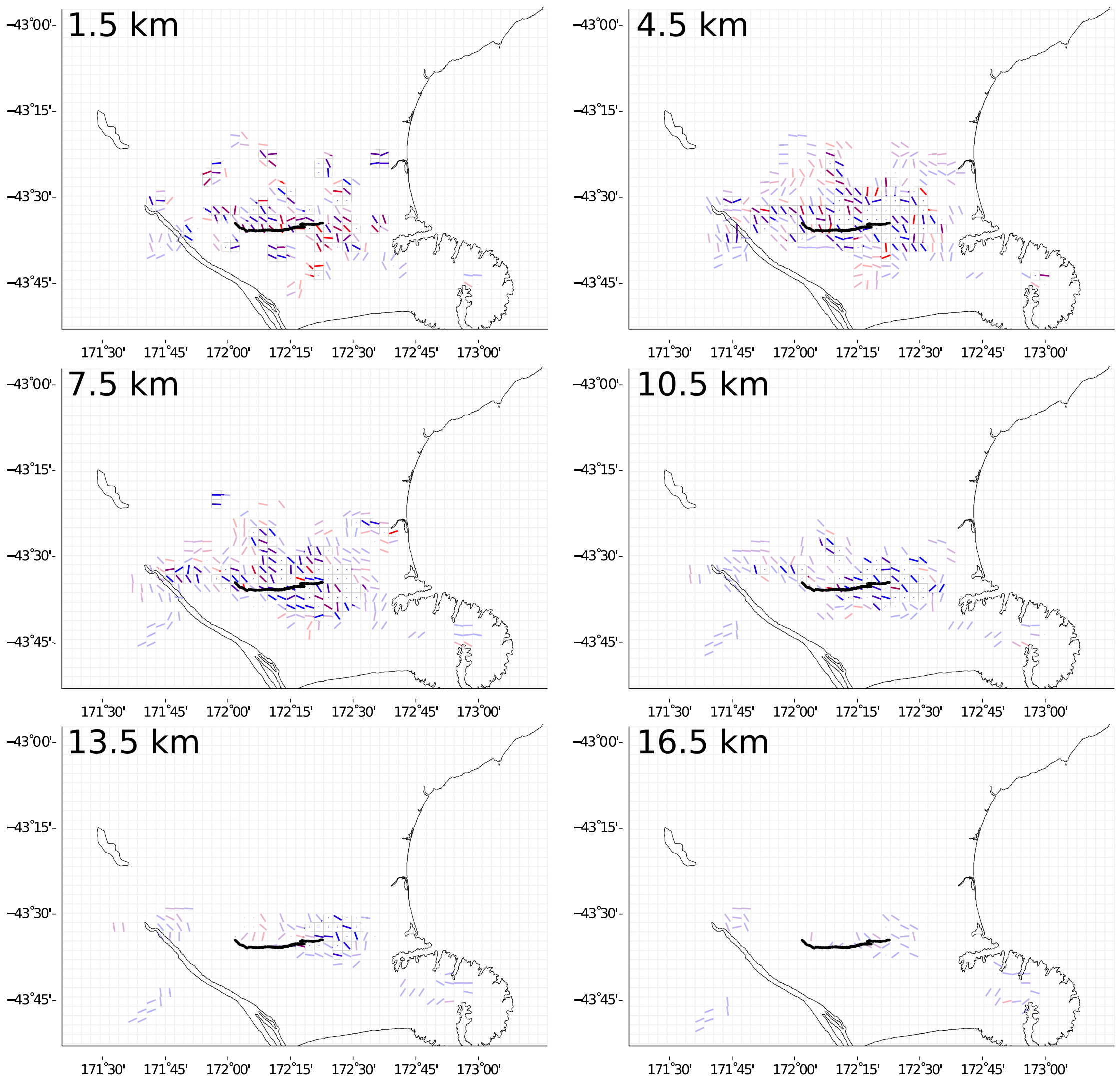

Figure 3.31: Inversion results using an average starting model with a block size of 3 km^3, for the Canterbury region showing anisotropy orientation, represented by the fast shear wave axis (θ) projected onto the horizontal plane. Also shown is the surface trace of the main Darfield fault rupture. Areas of the plot that are not well resolved by the model have been greyed out. Model parameters are those described in figure 1.27.

Starting Model	Block Size (km)	Initial Damping	Subsequent Damping	Damping Step Iteration	Final delay misfit (s)	Final fast direction misfit (°)	Figure
Average	5	1	10	40	0.0651	26.93	3.18/3.19
Average	5	2	15	40	0.0670	25.29	NA
Average	5	3	20	40	0.0684	26.16	NA
Average	5	10	-	-	0.0663	25.54	XXX/XXX
Average	3	1	10	40	0.0576	23.57	3.30/3.31
TESSA	5	1	10	40	0.0689	26.44	3.22/3.23
Uniform ($\alpha = 5\%$, $\theta = 115°$)	5	1	10	40	0.0684	26.87	3.23/3.25
Random	5	1	10	40	0.0724	29.42	3.26

Table 3.3: Damping parameters and final average weighted misfits for a variety of inversion models that incorporate the Darfield dataset. All models have a wavelet frequency of 3.2675 z and have a 10% whitening applied, and each one consisted of a total of 80 iterations

3.6 Interpretation of results

The iterative modelling approach presented here is influenced by the starting model [Tarantola and Valette, 1982] and thus it is important that starting models are designed carefully and investigated thoroughly. The average starting model shown here is a development of previous approaches [Abt and Fischer 2008, Johnson et al. 2011] and we find it works well when using the inversion to reproduce synthetic models. Models that employ the Darfield dataset show that the average starting model provides a significant improvement in reduction of the misfit function for fast directions and delay times over a random starting model. Use of TESSA and uniform starting models give similar misfit results to inversions employing the average starting model. The distribution of splitting results (as shown in figure 3.20) also show that real measurements tend to be more scattered than can be reproduced in the models. The result of this, especially when compared to simpler problems such as seismic velocity tomography, is that there can be a significant amount of leeway when solving for two or three non-independent parameters. Regardless, the approach of comparing and using carefully constructed starting models can provide insight into which anisotropic features resolved from the data are robust.

The most prevalent feature across all models was an upper layer of strong anisotropy overlying weak anisotropy. Comparison of models using 5 km^3 and 3 km^3 block sizes suggests that this upper layer does not extend much deeper than 5-6 km, and may be shallower to the east of the Greendale fault trace. The most straightforward explanation for this is that it marks the boundary between Cenozoic sediment and basement greywacke. The

P-wave velocity structure of the area [Syracuse et al. 2013, Reyners et al. 2014] (figure 3.32) indicates that this boundary lies at a depth around 1-4 km. The more recently deposited sediments are relatively poorly indurated compared to the basement greywacke, and thus we expect them to exhibit significantly greater porosity and compliance. Post-Darfield earthquake V_p/V_s [Reyners et al., 2014] are extremely low (< 1.60) to a depth of 5 km surrounding the Greendale fault, which is interpreted as being related to the widespread formation of open microcracks. This combination of compliant, porous sediment and microcrack rich basement greywacke is susceptible to stress-induced anisotropy. At depth, increasing lithostatic pressure is expected to reach a 'closing' pressure, determined by rock compliance and pore fluid pressure, at which the cracks can no longer contribute to anisotropy [Christensen 1996, Zatsepin and Crampin 1997, Gurevich et al. 2011]. Co- and post-seismic hydrologic analysis of the area surrounding the Greendale fault [Cox et al., 2012] find that groundwater levels underwent sustained rises and increased pressures, leading the authors to suggest that the damage zone from the Darfield earthquake and its aftershocks caused a sharp increase in fracture connectivity and permeability at depth. We suggest that the near-isotropic layer underlying the strongly anisotropic upper layer may be a result of pore fluid pressure decreasing due to fluid migration to shallower depths, resulting in a greater effective pressure and closed fracture networks.

The fact that the orientation of anisotropy is, for a large portion of the model space, well aligned with the direction of σ_{Hmax} indicates that stress-induced crack anisotropy is the prevalent source of anisotropy. Thus, any deviation away from this direction represents

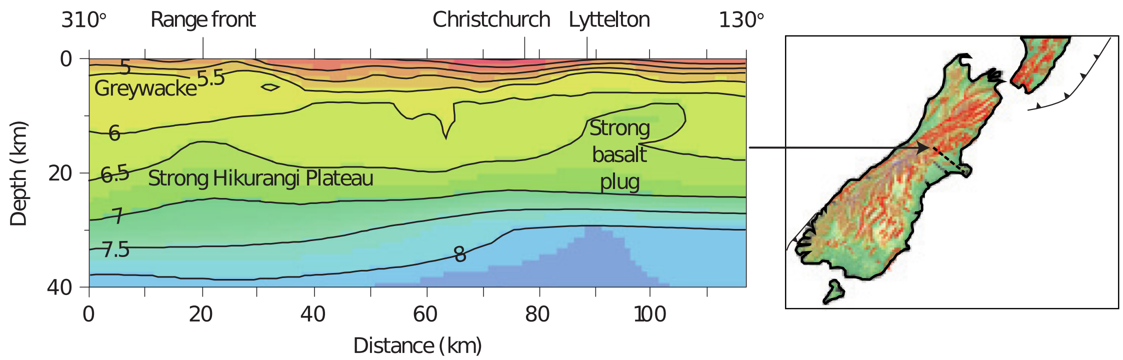

Figure 3.32: P-wave velocity structure underneath Canterbury, reproduced from Reyners et al. [2014]. Velocity contours are shown in km per second.

either a reorientation of the maximum compressive stress direction, or a strong contribution to anisotropy from other sources, such as fracture networks and fabrics formed under a strain regime that is not parallel to modern σ_{Hmax}. Anisotropy orientation at close proximity to the Greendale fault appears to be fault controlled in places, particularly at the western end of the fault where anisotropy is aligned E-W. The TESSA spatial average results of Holt [2013] (figure 3.21) also appear to show this, to a lesser extent. In contrast, stress inversions of focal mechanisms from Holt et al. [2013] give σ_{Hmax} orientations that are oriented E-W towards the centre of the Greendale fault trace, rather that to the western end.

Rayleigh wave anisotropy obtained from ambient noise analysis [Fry et al., 2014] at periods of 8 s and 15 s, as previously discussed in this chapter, is notably oriented ENE-WSW, a significant rotation from the predicted σ_{Hmax} orientation of 115° (see figure 3.5). This dominant ENE-WSW direction was attributed by the authors to arise from the direction of relative plate motion and historic strain. Depth sensitivity kernels for group velocity of fundamental mode Rayleigh waves used show that sensitivity is low in the upper ∼5 km (for 8 s periods) and upper ∼10 km (for 15 s periods) [Fry et al., 2014]. Thus the SWS data may be sampling this strongly anisotropic upper layer in the uppermost few kilometres of the crust, that is otherwise 'blind' to the surface waves used in the ambient noise technique.

A broader comparison between the 'cracked' low V_p/V_s zone surrounding the Greendale fault and the SWS data may serve to explain the rotation of anisotropy at distance from the Greendale fault (figure 3.33). SWS inversion models indicate that there is a significant rotation in anisotropy at distance from the Greendale fault (figure 3.33c), which may indicate a transition from stress-induced anisotropy to structure or fabric controlled anisotropy. Comparatively high V_p/V_s in these areas indicates that the extent of the damage (in the form of microcracks) caused by the Darfield earthquake has dropped off where we observe these rotations in anisotropy. The lack of microcracks will reduce the sensitivity of the rock to stress-induced anisotropy, thereby allowing structural anisotropy (in line with the Rayleigh wave anisotropy observed by Fry et al. [2014]) to dominate. The argument that the low V_p/V_s region surrounding the Darfield fault, indicative of crustal weakening and crack dilatation due to the earthquake sequence, is driving the stress sensitivity to SWS measurements, suggests that the state of anisotropy before the earthquake was not necessarily the same as it was for the period of study. Furthermore, SWS in the period after the February 2011 Christchurch earthquake may again be different to the period of study due to possible crustal weakening beneath Christchurch.

In order to test the hypothesis that the strongly anisotropic upper layer identified in this study is a result of stress-induced anisotropy centered around a zone of damage related to the Darfield earthquake and its aftershock sequence, a follow up study of anisotropy after some time has passed should be done. Post-seismic contraction and crack healing has been observed in the years following a large earthquake [e.g. Fielding et al. 2009]. Such a process may reduce anisotropic susceptibility to maximum compressive stress should it occur, as the crack compliance of the rock decreases with crack healing. There may also be other processes affecting the near surface such as a changes to pore fluid pressure and the overall stress state of the crust. According to GeoNet (*www.geonet.org.nz*, accessed 7/11/2014), there have been 9207 catalouged events since 12 January 2011, 667 of which occurred between 7 November 2013 and 7 November 2014. This provides a limited scope to perform a follow-up study of the evolution of anisotropy in the Canterbury plains.

We also consider the possibility that the models obtained are a result of the inversion process favouring high anisotropy near the surface due to there being additional effects on measured anisotropy that are not well quantified by the modelling process. The model using a 3 km^3 block size (figure 3.30) indicates that the base of the upper strongly anisotropic layer is shallower towards the eastern end of the Greendale fault. We notice that this correlates well with where the data density (i.e. earthquakes per model element) is greatest, meaning that the inversion may be favouring a near-isotropic state for these model elements in order to deal with the scatter of results once the raypaths reach their destination. Of course, this may well represent the state of anisotropy, however if there is a process

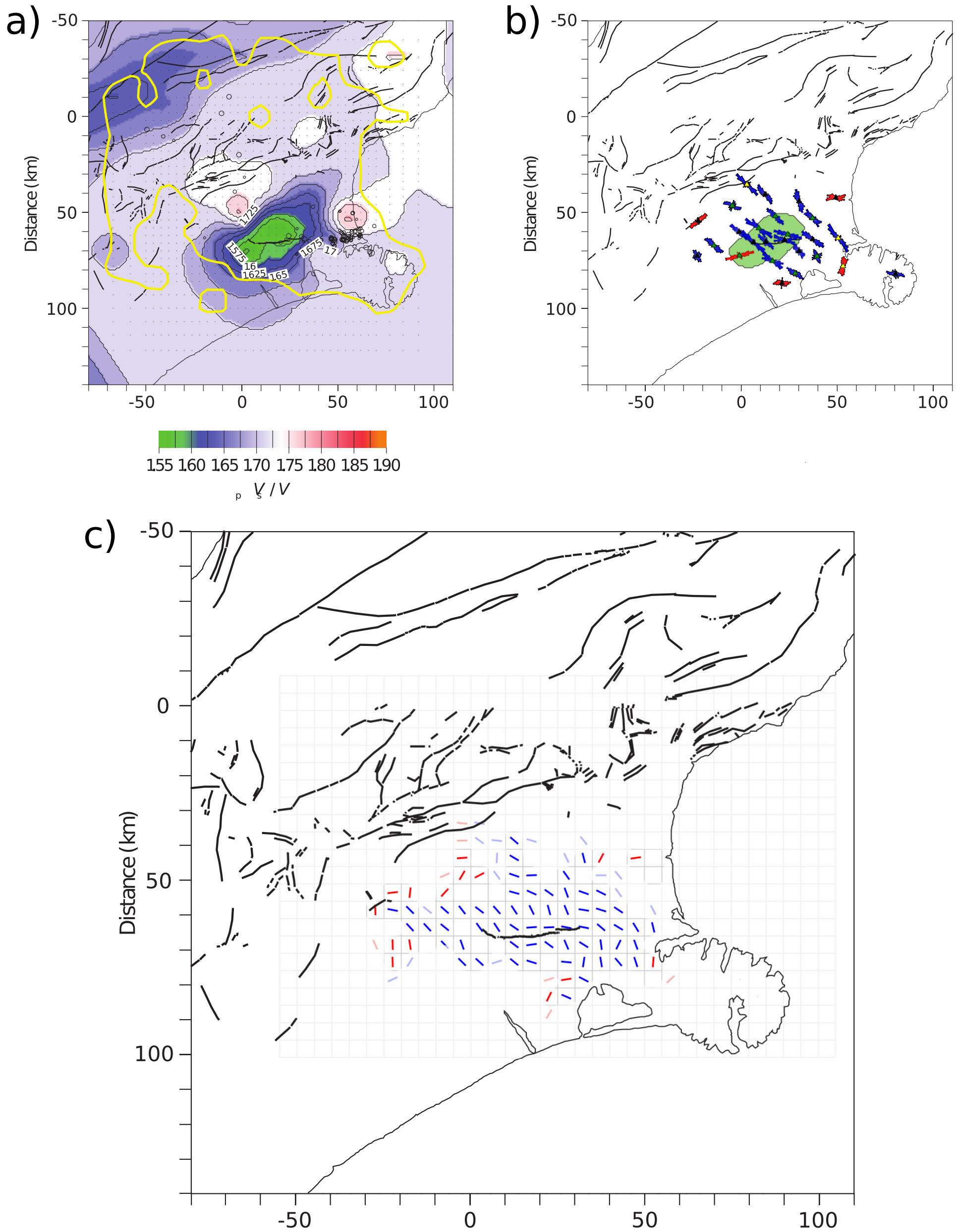

Figure 3.33: Comparison between V_p/V_s and SWS results. A) shows V_p/V_s inversion results for the Canterbury region at 5 km depth, reproduced from Reyners et al. [2014]. The yellow outline indicates the area where the inversion is well resolved. B) shows circular histograms representing SWS ϕ measurements where they are measured, as in figure 3.1. ϕ distributions with means between 100-170° are coloured blue, to indicate where anisotropy is expected to be stress controlled, and those with means outside that range are coloured red. The 1.60 V_p/V_s contour is also shown (shaded green). C) shows SWS inversion model orientation, as in figure 3.19, for the top 0-5 km. Orientations between 100-170° are coloured blue, to indicate where anisotropy is expected to be stress controlled, and those outside that range are coloured red.

obfuscating the element of anisotropy that may be present at this depth the technique may underestimate its strength. Also, we assume throughout the models shown that anisotropy is hexagonally symmetric with a plane of symmetry that is vertically aligned, i.e. it has a horizontal normal. We do this in order to maintain the linearity of the problem and to decrease the non-uniqueness of the solution. This assumption is made in Canterbury with the understanding that anisotropy will be closely associated with horizontal strain and stress that has a vertically aligned principal axis. There may be significant error in the models presented should this assumption be flawed.

The validity of the two-layer hypothesis can be tested by creating a synthetic inversion using the earthquake-station raypaths in the Darfield dataset and a simple two-layer model based on our interpretation of the inversion results, in a similar way to how the synthetic testing was performed in section 3.5.1. The two-layer model used has a 5 km thick layer with 10% anisotropy overlying a 15 km thick layer with 1% anisotropy, with a constant orientation of 115°. The inversion process was performed using the same parameters as those used to create the results shown in figures 3.18 and 3.19. The results, shown in figures 3.34 and 3.35, clearly show the two-layer input model in the well resolved areas. It can be seen that the anisotropy strength parameter for the top 5 km is somewhat more homogeneous than the range of results found by inverting the Darfield dataset (reference figures 3.18, 3.22 and 3.23), indicating that true anisotropy in the Canterbury region is more heterogeneous than the simple two-layer model being considered. Also interesting to note is the areas of higher anisotropy in the 5-10 km layer that are situated on or outside the

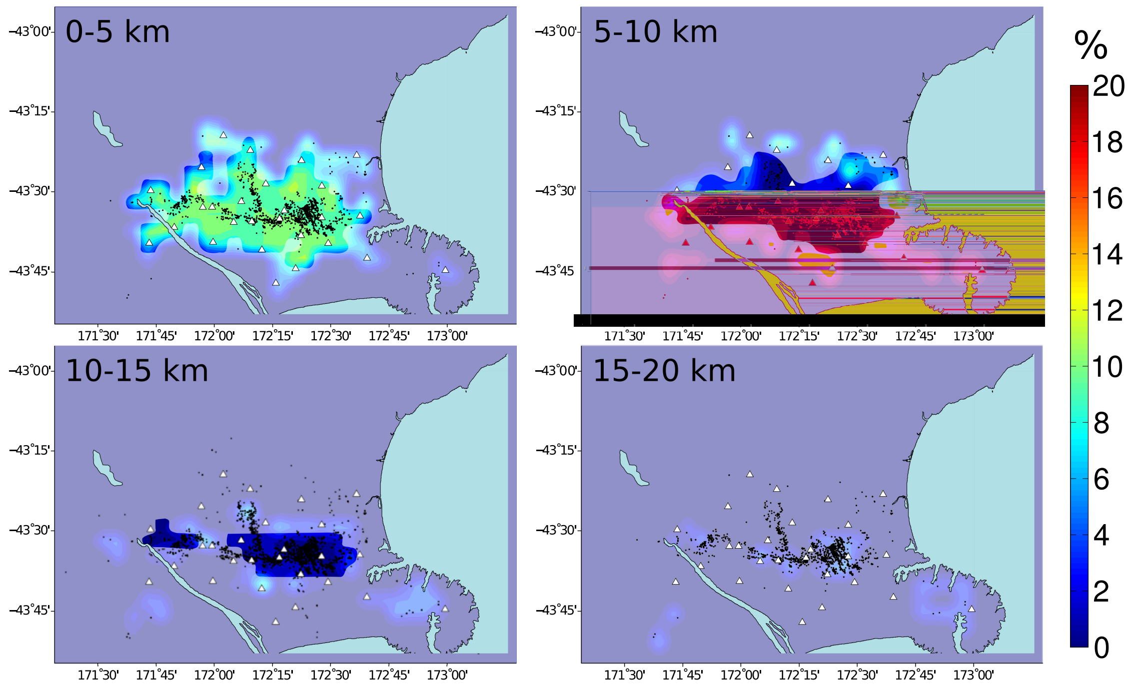

Figure 3.34: Inversion results using an average starting model with a block size of 5 km^3, for the Canterbury region showing strength of anisotropy (α) shown as a percentage. The results were created using synthetic input data created using real event-station locations from the Darfield dataset and a simple two-layer anisotropy model with a 5 km upper layer with 10% anisotropy overlying a 15 km thick layer with 1% anisotropy. Anisotropy orientation was constant at 115°. Also shown are available event locations (black circles), and station locations (white triangles). Areas of the plot that are not well resolved by the model have been greyed out. This model solved for α and θ and was produced using 80 total model iterations, an initial damping value of 1 and a subsequent damping value of 10 after the 40th iteration.

periphery of the resolved area. This pattern is also seen in the inversion results, particularly for those created using the average and uniform starting models (figures 3.18/3.19 and 3.25/3.26, respectively). This indicates that those areas of higher anisotropy at depth are more likely to be due to a lack of resolution rather than any actual structure.

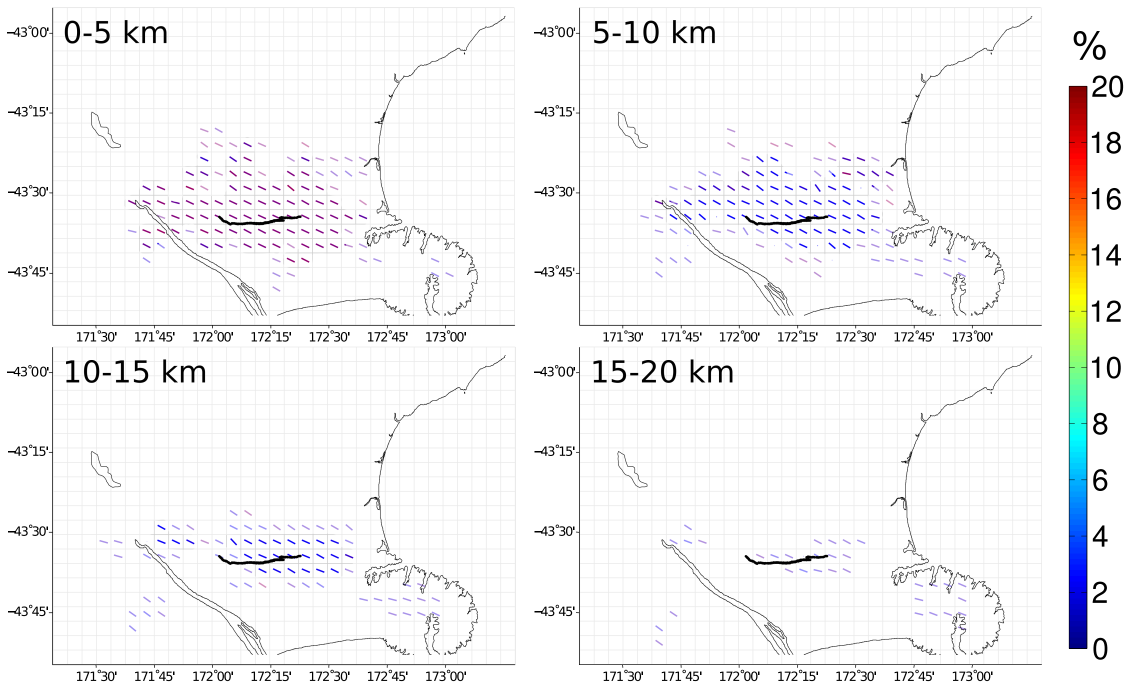

Figure 3.35: Inversion results using an average starting model with a block size of 5 km^3, for the Canterbury region showing anisotropy orientation, represented by the fast shear wave axis (θ) projected onto the horizontal plane. The results were created using synthetic input data created using real event-station locations from the Darfield dataset and a simple two-layer anisotropy model with a 5 km upper layer with 10% anisotropy overlying a 15 km thick layer with 1% anisotropy. Anisotropy orientation was constant at 115°. Also shown is the surface trace of the main Darfield fault rupture. Areas of the plot that are not well resolved by the model have been greyed out. Model parameters are those described in figure 1.27.

3.7 Conclusion

The modelling technique shown here is a damped linearised least-squares inversion to solve for anisotropy in the crust using shear-wave splitting measurements. It is designed to work directly with results taken from MFAST, an automatic technique for determining SWS parameters for earthquake data. Forward modelling is performed by first tracing seismic raypaths between source and receiver, then progressively splitting a sinusoidal wavelet by rotating and time shifting the orthogonal components of motion [Fischer et al., 2000] using polarisation orientation and phase velocities determined using the Christoffel matrix [Babuška and Cara, 1991]. This particle motion perturbation approximation, employed by Abt and Fischer [2008], has been previously shown to be accurate for models where lateral variations in anisotropy are not too extreme, and provides an efficient approach to the large number of calculations needed to determine partial derivatives. The anisotropy itself is assumed to be hexagonally symmetric, and is constructed using Love parameters [Love, 2013] as defined by the seismic velocity and density of the constituent rock, however other ways of determining elastic properties may be used. Non-linear aspects of shear wave splitting in anisotropic media are handled by the damped iterative inversion approach in which partial derivatives are recalculated after every iteration.

Synthetic models were used to test the method's ability to retrieve a known structure. Results show that strip and layer structures are well retrieved for both random and average starting models, however the best results are obtained using the average starting model, where each model element is assigned starting parameters that represent a weighted average of the raypaths travelling through it. Retrieval of the properties of a layered model suffer when the strength and orientation of each layer are very similar to one another. Synthetic modelling also shows that models solving for the rotation of anisotropy around the vertical and one horizontal axis suffer from a loss of accuracy when the anisotropy has no significant component of dip.

The technique was applied to a dataset of 8374 SWS measurements taken from the 2011 Darfield earthquake aftershock sequence in the Canterbury region. The data were trimmed to exclude events outside of a certain straight-line incidence angle in order to avoid ray tracing and SWS parameter measurement issues associated with rays that have large offsets in comparison to their depth. Models shown here use a 60° threshold as it provides a good compromise between reducing error and keeping as much data as possible. Final models, solving for α and θ, were well resolved near the Greendale fault down to a depth of 10 km. The models indicate that the Canterbury region consists of a near-surface layer of strong anisotropy (9-14%) overlying a near-isotropic layer that demonstrates the weakest anisotropy near the Greendale fault. The upper strong anisotropic layer is interpreted as being a zone of damage associated with the earthquake where open microcracks contribute to the overall susceptibility of the rock to stress-induced anisotropy, as the majority of the anisotropy is oriented near-parallel to the direction of σ_{Hmax}. At depth, high effective pressure, from a combination of large overburden pressures and possibly low pore fluid pressure, closes these microcracks making the basement greywacke significantly more isotropic. At distance to the Greendale fault, there is limited evidence that anisotropy orientations rotate towards the direction of plate motion and historic strain, as found by Fry et al. [2014], indicating that stress-induced anisotropy has less influence as earthquake related rock damage falls off.

The inversion method is effective in solving for crustal anisotropy when the plane of symmetry is assumed to be vertically aligned, providing a tool for determining anisotropic models of the Earth from shear-wave splitting data. Further work may be done to evaluate the method's effectiveness for different anisotropic structures, especially for those with dipping layers of anisotropy. Such work may benefit from employing a larger suite of models with fewer iterations (~ 10 rather than 80), taking advantage of reduced computation time. We also propose a follow-up study to investigate the hypothesis that stress-induced anisotropy near the Greendale fault is being compounded by earthquake related rock damage by modelling anisotropy measured several years after the Darfield earthquake. This may allow for a evaluation of possible time-dependent processes including crack healing, pore fluid pressure changes and stress relaxation.

Chapter 4

Active Source and Noise Interferometry: Investigating seismic velocity variation at Mount Ruapehu

4.1 Introduction

Understanding changes to elastic properties around volcanoes is a necessary step to routinely using these precursors to monitor volcanic hazards. Less ambiguous ways of detecting pre-eruptive volcanic activity such as recording precursory swarms of volcanic and long period earthquakes [Chouet et al. 1994, Aki and Ferrazzini 2000], or surface deformation [Voight, 1988] (mostly expressions of stress, magma and fluid processes) are not always present before an eruption and therefore it is unreliable to rely solely on them for hazard prediction.

Other ways of indirectly detecting changes in elastic properties around volcanoes, such as seismic anisotropy [Gerst and Savage, 2004], should be used to complement the tools available for early detection of volcanic hazards. In this chapter we look at a small study of seismic interferometry using active source and noise seismicity to determine the behaviour of seismic velocities the upper crust around Mount Ruapehu, New Zealand during a period of eruptive quiescence.

4.1.1 Mount Ruapehu Volcano

Mount Ruapehu is the largest and the southernmost volcano of the roughly NE-SW trending Taupo Volcanic Zone (TVZ), with a summit 2797m above sea level. The TVZ is the terrestrial section of the volcanic arc associated with the Hikurangi subduction margin between the Pacific and Australian plates. Ruapehu itself is an andesite-dacite stratovolcano that initiated around 300ka [Gamble et al., 2003]. Situated in a rifting system, Ruapehu is bounded by normal faulting to the east and west, with a somewhat more complicated faulting system to the south where the TVZ terminates [Villamor and Berryman, 2006].

Ruapehu presents volcanic hazards to the region, most commonly lahars created by crater lake collapse, notably in 1953 (causing the Tangiwai disaster) and in 2007, as well as volcanic atmospheric ejecta and debris avalanches [e.g. Lecointre et al. 2004, Keys and Green 2008]. Additionally, lava domes have been extruded in historic eruptions (1945 and possibly 1861) [Price et al., 2007]. The last significant volcanic eruption was in 1995-1996, where about 0.05 km^3 of material was ejected, triggering lahars down the flanks and a plume ∼12 km high, and occurring with little warning [Nakagawa et al., 1999]. There is also a history of minor phreatic and phreatomagmatic eruptions with the most recent occurring on 4 October 2006 and 25 September 2007. The latter of these was a small explosive hydrothermal eruption accompanied by a lahar that occurred with little warning [Jolly et al., 2010].

4.1.2 Active source coda-wave interferometry

Fundamental to the theory behind coda-wave interferometry is that coda waves represent energy that has been backscattered by heterogeneities present in a zone surrounding the direct wave path of a seismic source [Aki and Chouet, 1975]. As energy is scattered, waves take more circuitous routes to the receiver, being scattered more and more often. Due to this, later coda arrivals will be more sensitive to any perturbation to the scatterers in this zone than direct and early coda arrivals are, as they spend more time in the perturbed medium. One common geophysical application of this theory is to monitor temporal variations in crustal properties [e.g. Chouet 1979, Geller and Mueller 1980, Poupinet et al. 1984], including temporal variations near volcanoes [e.g. Aki and Ferrazzini 2000, Grêt et al. 2005, Pandolfi et al. 2006]. Generally this is done by identifying a highly correlated repeating source of seismic energy (i.e. an earthquake doublet or explosion) and either investigating coda decorrelations or time shifts.

More specifically, the crust near volcanoes is typically a highly inhomogeneous and scattering medium, something which has been shown to be true for the Taupo Volcanic

Zone [Bibby et al., 1995]. Thus, during periods of eruptive quiescence in which magmatic processes are still occurring, there may still be changes in scatterers that will manifest in the coda of seismic waves (either in terms of velocity properties or physical location). Detecting these changes, which may be caused by volcanic processes that cannot be directly observed with other methods, may serve as a tool to aid forecasting volcanic eruptions with proper classification. Volcanic mechanisms which can change the seismic velocity of rocks are broadly associated with magmatic activity that causes the opening or closing of small fractures or microcracks already present in the medium by means of increasing or decreasing the effective stress state, or alters the pressure or viscosity of the fluids present within crack and pore space.

4.1.3 Ambient seismic noise monitoring

Alongside active source methods of detecting changes in seismic velocity, a study was done using ambient noise recorded by the seismometers over the period of interest. It has been shown that ambient noise can be used to reconstruct the Green's function (i.e. the impulse response of the medium) between two seismometers by means of cross correlation [Shapiro and Campillo 2004, Sabra et al. 2005, Campillo 2006]. In a similar manner to active source coda-wave interferometry, small perturbations in the Green's function can be interpreted as velocity (or positional) changes to scatterers in the wavefield. The benefit of using ambient noise over active sources, multiplets, or any other repeated source of seismicity is that one is able to reconstruct a more-or-less continuous record of variations to arrivals in the wavefield, rather than having to resort to either costly active source experiments, or the temporal inconsistency of naturally repeating seismic sources. The temporal resolution of ambient noise interferometry is governed by the amount of time needed for the cross-correlations to become stable (convergence rate), effectively equivalent to the signal-to-noise ratio of the data [Larose et al., 2007]. For frequencies over which Rayleigh waves are sensitive to the top few kilometres of the crust (0.1-0.9 Hz, as used by Brenguier et al. [2008]) a record length between a couple of days to a week is needed [Hillers et al., 2014].

Ambient noise techniques have been employed to study volcanic regions and monitor hazards [e.g. Sens-Schönfelder and Wegler 2006, Clarke et al. 2013]. A study of ambient noise at Ruapehu by Mordret et al. [2010], focusing on the period encompassing the phreatic eruption on 4 October 2006, proposed the presence of velocity changes preceding an eruption caused by a small intrusion of magma beneath the volcano's NE flank. The study focused on many of the same GeoNet seismic stations used in this study, providing a useful reference for the results found in this study during a period of relative quiescence at Ruapehu. They looked at the Z-component cross correlation function for each seismometer pair and analysed velocity variations, following a similar process to that in the methods section below. Before the 2006 eruption of Ruapehu, a velocity drop up to a maximum of 0.8% was detected between four seismometers, in comparison to more consistent velocity variations occurring before the eruption of ~0.25%. In the week following the eruption, velocities were observed to return to the pre-eruption mean. There was no detected ground deformation associated with the eruption; Mordret *et al.* used this as a boundary condition alongside the observed velocity variations to model possible subsurface pressure sources that may have been responsible for the changes. It is significant that velocity variations recovered from the ambient noise were only seen in a subset of station pairs on the volcano, and similar measurements were not found for the later eruption on 25 September 2007.

Due to the continuous nature of recordings, another tool for a volcano seismologist using ambient noise interferometry is to study waveform decorrelation, or loss of coherence between cross-correlation functions [Brenguier et al. 2011, Grêt et al. 2005]. This method is unavailable to active source or earthquake interferometry due to the lack of temporal resolution these techniques typically possess. Decorrelation between cross-correlation functions was observed over the eruptive period of Piton de la Fournaise and linked to changes in the volcanic edifice by [Brenguier et al., 2011].

4.2 Method

In this section a description of the experimental technique, noise data, and processing techniques will be given, including how time domain Coda Wave Interferometry (CWI) [Snieder et al., 2002] and Moving Window Cross-Spectral (MWCS) analysis [Poupinet et al. 1984, Clarke et al. 2011] are used to determine velocity variations and decorrelations. Whereas MWCS analysis was done on the ambient noise cross-correlations, both techniques were used to analyse the active source experiment.

4.2.1 Active Source Experiment

The active source seismic experiment took place at Lake Moawhango, a small hydroelectric lake situated in the Waiouru region approximately 20 km south-east from the summit of Mount Ruapehu. The site was chosen to help ensure a repeatable environment to set off explosives, as it was reasoned that damage to the immediate area would be smaller at the lake bed rather than in a borehole. The water column above the explosion site, at roughly 30 m, serves to direct the energy into the Earth in a similar way to using boreholes on land. 100 kg of ammonium nitrate fuel oil (ANFO) was used for the main explosive agent. Each explosive was lowered through the water after locating the shot site on the lake surface using GPS (at 39.3904 S, 175.7593 E); this stage was the most prone to experimental error due to the difficulties in geolocation on water and ensuring that the explosives descended vertically. Experimental error in the final location of each shot is estimated to be $\sim 10-20$ m.

During the initial stage of the experiment, five explosions were set off over an 18 hour period on 12 February 2012 to encompass the diurnal variation in solid Earth tides. Solid Earth tidal loading typically contributes less than 0.1-1% of tectonic stress [De Fazio et al. 1973, Métivier et al. 2009]. However, lunar and solar tides have been attributed to observed variations in *P*-wave velocity and attenuation, with amplitudes of 0.3% and 4% respectively [Yamamura et al., 2003]. With this approach we are able to quantify the expected velocity variations that may be associated with solid Earth tides, or experimental error. Due to unforeseen circumstances, shots 4 and 5 were placed into the lake 10 m north of the shot location.

Another shot, planned to occur roughly six months after the initial five, was successfully detonated only after resting on the lake bed for two weeks. The resulting lack of efficacy in the explosives, as well as the uncertainty in the shot location, meant that the data recovered from this shot was unable to be used in this analysis. The last shot was successfully detonated on 30 April 2013, 14 months after the initial shots.

4.2.2 Data

Figure 4.1 shows the seismometer network used to record the explosions, encompassing sensors from the permanent GeoNet deployment in the area and temporary deployments. All sensors were short-period Sercel L4 3 component seismometers (1 s natural period) except for two GeoNet Guralp CMG-40T broadband 3 component borehole seismometers (60 s natural period), COVZ and WNVZ. Seismometers not part of the GeoNet deployment included three seismometers that were part of the 'Temporary Anisotropy Deployment At Ruapehu' (TADAR), recording for the entire duration of the study period, and two further seismometers that were deployed only to record the explosions. Of these two latter stations, NPFS was only deployed during the first set of explosions due to it recording a noisy signal, likely due to urban noise and near surface scattering in the area. All data were recorded continuously at a sampling rate of 100 Hz. The signal that was produced showed the source was well correlated (e.g. Figure 4.2), for stations surrounding Mount Ruapehu.

We used the bispectral cross-correlation algorithm (BCSEIS) from Du et al. [2004] to

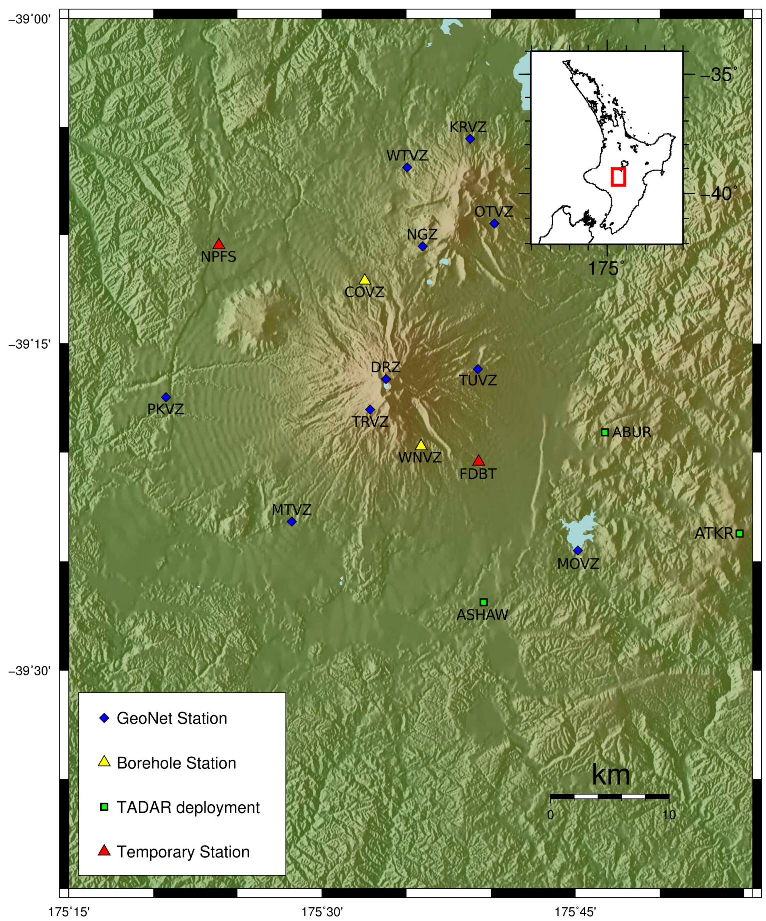

Figure 4.1: Seismometer locations around Mount Ruapehu. Station MOVZ is situated on the dam that holds Lake Moawhango.

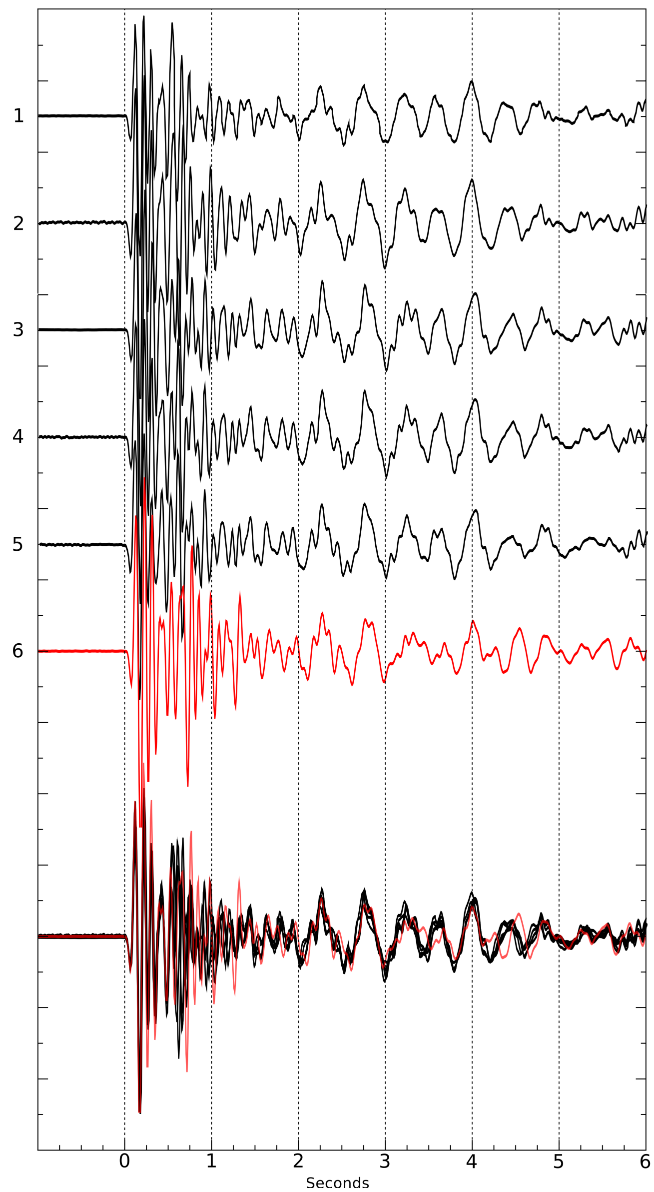

Figure 4.2: Shot recordings for all 6 shots at the temporary station ABUR, plotted individually then stacked on top of one another. The black seismograms are from the February 2012 explosions (shots 1-5), and the red seismogram is from the April 2013 explosion (shot 6).

provide differential arrival times for each shot arrival recorded. This allowed for refinement of the origin time of the final 30 April 2013 shot, which suffered from lack of a precise GPS timed detonation. Unfortunately station MOVZ, the GeoNet seismometer located on the dam at Lake Moawhango at a distance of ~ 2 km from the explosions, was not recording during the final shot. This, compounded with the possibility that velocities have changed in the intervening period, increases the uncertainty of the arrival time of the final shot to an estimated $\pm$0.04 s. Fortunately, coda-wave interferometry and the moving window cross-spectral method can be used to resolve clock errors in origin times as they manifest as a constant offset to window lag times, as will be explained later. Results from BCSEIS were used with the double difference relocation method, hypoDD [Waldhauser, 2001], to produce shot locations (constrained to the surface) from their recorded arrivals (Figure 4.3) using the velocity model of Hurst and McGinty [1999]. The calculated mean distance between the first three shots was 13$\pm$7 m, and between shots four and five was 6 m, giving a total mean separation of 29$\pm$13 m for all the February 2012 blasts. The distance between the back-calculated location of the April 2013 blast and the average location of the February 2012 blasts was $\sim 87 \pm 50$ m.

There were a total of 11 stations that provided a good signal for all shots; ABUR, ASHAW, COVZ, DRZ, MTVZ, NGZ, PKVZ, TRVZ, TUVZ, WNVZ and WTVZ. Both interferometry methods were applied to each pair of shot records for any particular station component, as well as all the February 2012 shots, stacked and averaged, with the April 2013 shot. Noise data were taken over the period spanning 1 January 2012 to 31 July

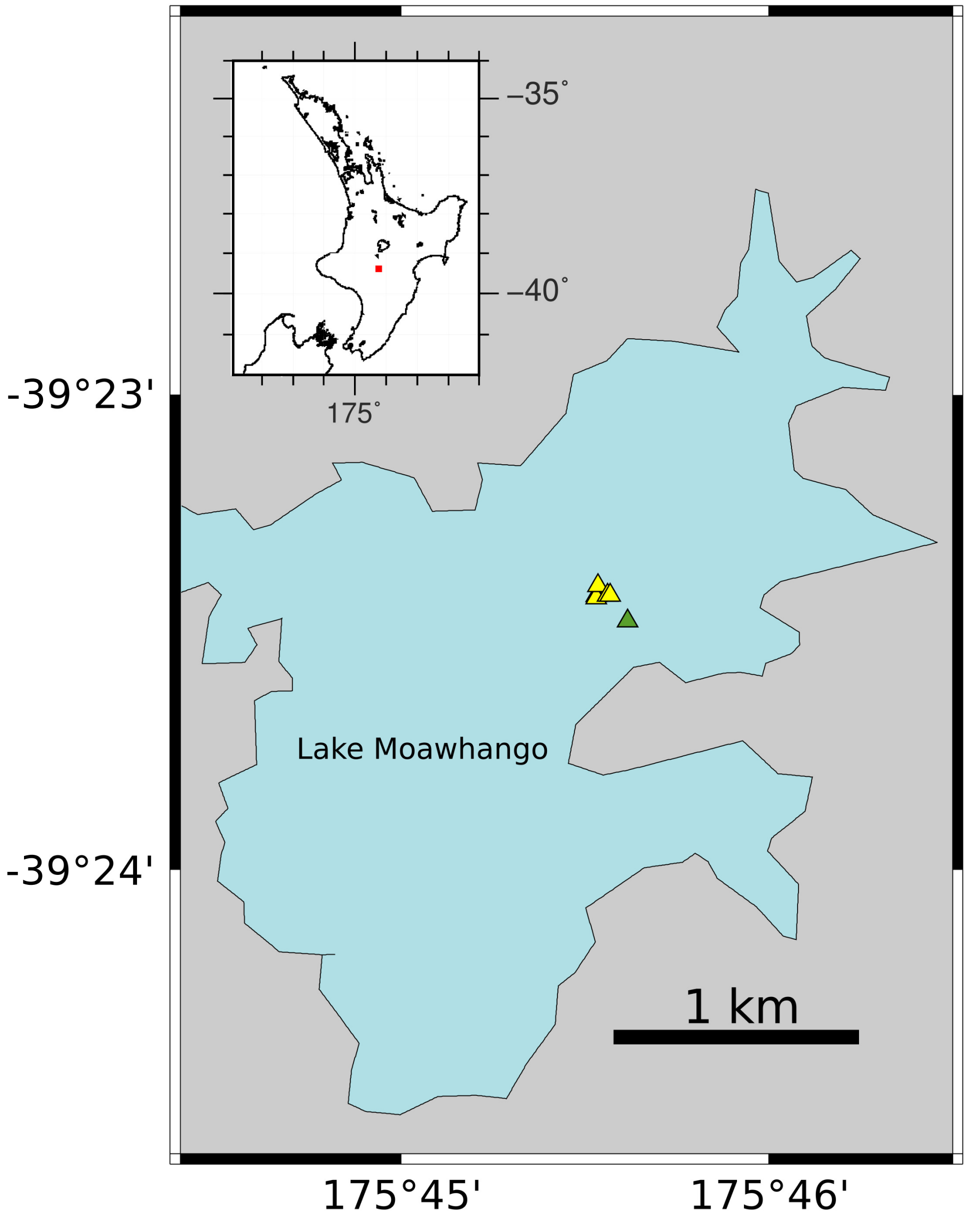

Figure 4.3: Back-projected shot locations according to double-difference relocation methods utilising BCSEIS and hypoDD. Initial explosions from 12-13 February 2012 are shown in yellow and subsequent explosions from 30 April 2013 in green.

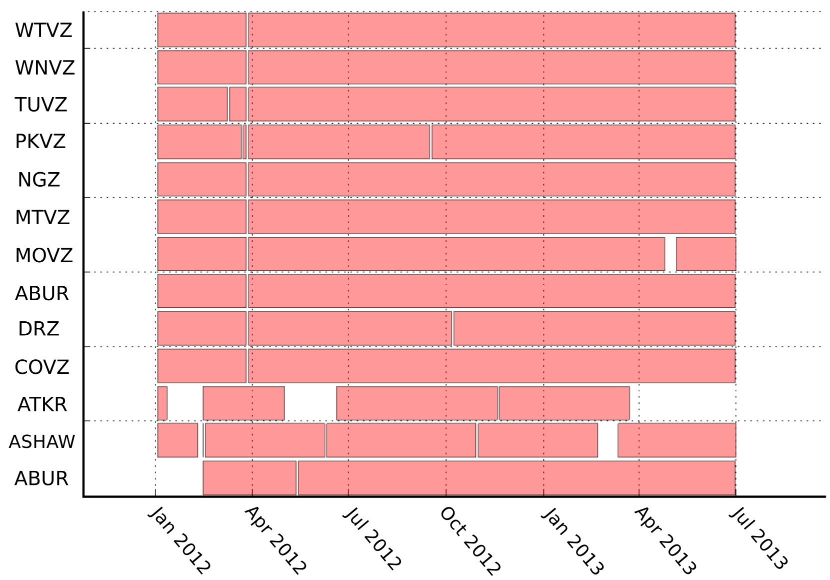

Figure 4.4: Seismic data availability for the period of interest. The data were used for the ambient noise analysis.

2013. Data availability over this time can be seen in figure 4.4.

4.2.3 Time Domain Coda Wave Interferometry

Time domain coda wave interferometry, as outlined in Snieder et al. [2002], is a method to find variations between two near-identical waveforms. It works by computing a time-shifted normalised cross-correlation between windowed sections of two waveforms (including the coda waves), u_{1i} and u_{2i}, for a given time window i. The size of the window, and by how much they overlap when the window is moved through the waveforms, is determined by the frequency content of the signal in the seismograms. The correlation coefficient function is defined as such:

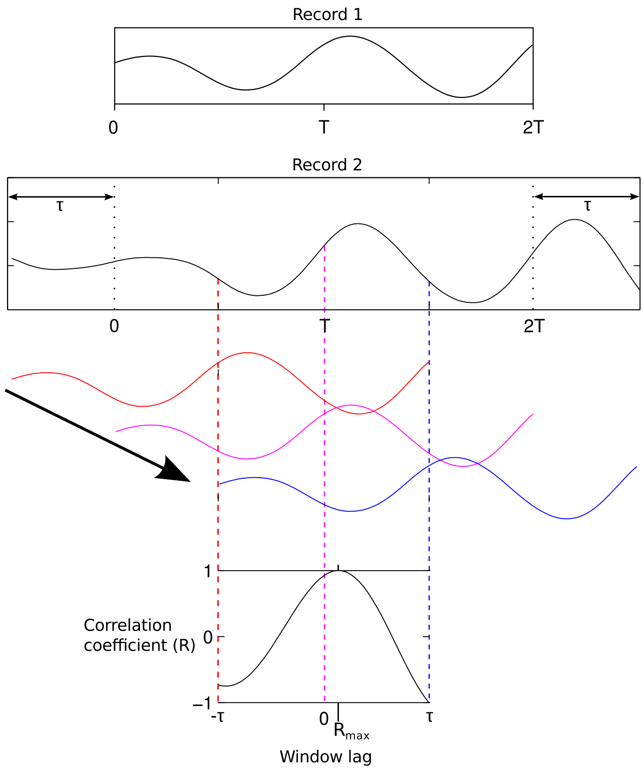

Figure 4.5: Example showing the time domain coda wave interferometry method. A window of length 2T is taken at some time t through the first shot recording, here labeled 'Record 1'. Record 1 is then correlated with windows of the same length taken from the second shot recording at some lag from t, denoted as τ, to find the correlation coefficient $R(\tau)$. R_{max} lies at the value of τ where Record 1 and Record 2 have the highest correlation coefficient.

$$R(\tau) = \frac{\displaystyle\int_{t-T}^{t+T} u_{1i}(t')u_{2i}(t'+\tau)dt'}{\sqrt{\displaystyle\int_{t-T}^{t+T} u_{1i}^2(t')dt' \int_{t-T}^{t-T} u_{2i}^2(t')dt'}} \tag{4.2.1}$$

Where the window i is defined with a length of $2T$ and a centre time of t. The cross correlation coefficient $R(\tau)$ returns its maximum value, R_{max}, at a value of $\tau = \delta t_i$ that is taken to be the lag between u_{1i} and u_{2i} at that part of the coda (see Figure 4.5). In a system in which the velocity, v is being perturbed homogeneously, it can be shown that the corresponding travel-time perturbation is given by Poupinet et al. [1984]:

$$\delta t_i = -\left(\frac{\delta v}{v}\right) t_i \tag{4.2.2}$$

It follows from this relationship that a velocity perturbation can be recovered from measuring the gradient of any correlation between window centre time, t, and δt. See Snieder [2006] for a more complete discussion of the mathematics of this technique. A 2 to 12 Hz bandpass filter was applied to the whole day long records. Subsequently, once a window of the record has been taken, a 50% cosine filter is applied to taper the signal, weighting the centre of the window in the correlation. Windows were taken to be 2 s long, with a window-to-window overlap of 1.75 s. The value of τ_{max} for each window was only used in subsequent analysis if $R_{max} > 0.975$ was satisfied.

Calculating values of ${}^{\delta v}/_{v}$ in this method requires some degree of data selection, as well correlated (i.e. high R_{max}) values can be obtained, by chance, between two records even where the signal-to-noise ratio is too low for the lag recovered to represent a true shift in arrival energy. In order to do this for the active source experiment data, calculated δt_i vs t_i data for the first five shots were smoothed over the data space using a Gaussian smoothing technique (see appendix C). The bin with the maximum data point density (after smoothing) is found at a location of $\delta t_{max}, t_{max}$ and a vector of data densities at each value of t summed for values between $\delta t_{max} \pm 0.004s$ is calculated. The time window for which data are chosen to calculate ${}^{\delta v}/_{v}$ is defined as the largest continuous set of t in which these data densities are at least 20% of the maximum. This ensures that the time window chosen has sufficient coherent energy between the two records for the analysis to work.

4.2.4 Moving Window Cross-Spectral Analysis

The moving window cross-spectral (MWCS) technique, as described first by Poupinet et al. [1984] for use with coda waves and assessed for application to noise data by Clarke et al. [2011], was applied both to the active source and the noise data. Here an overview of the method itself will be given (reference figure 4.6) before more detail about how it was applied to each set of data. In a similar manner to time domain coda wave interferometry, MWCS compares two waveforms to identify the position and magnitude of lagged arrivals, however it uses correlation in the frequency domain and derives the delay of lagged arrivals using phase information, providing a method that may resolve delays below the sampling interval of the data in question. Taking the same convention as in the last section, the centre time of the window is denoted as t and the recovered lag between two windows as δt. The windows are cosine tapered before being transformed into the frequency domain, so that $v_i(f) = \int_{-\infty}^{\infty} u_i(t)e^{-2\pi itf}dt$. From these the cross-spectrum, $S_i(f)$, between the two series is calculated with:

$$S_i(f) = v_{2i}(f)^* v_{1i}(f) \tag{4.2.3}$$

To evaluate the level of similarity between the two windows the coherence between their energy densities, $C_i(f)$, is calculated using the smoothed window spectra and cross-spectrum as such:

$$C_i(f) = \frac{\overline{|S_i(f)|}}{\sqrt{\overline{|v_{2i}(f)|} \cdot \overline{|v_{1i}(f)|}}} \tag{4.2.4}$$

In this study, smoothing was performed by filtering each time series through a Hanning (raised-cosine) function with a 0.1 Hz half-width. The coherence function will return values approaching 1 at frequencies where the spectral density is similar between the two windows. At higher frequencies (generally about ∼10 Hz, see figure 4.6), coherencies are lower due to shorter wavelengths with respect to the overall window length. The window delay, δt_i, is obtained from the gradient of the line described by the phase, $\phi(f) = \arg v(f)$, of the cross-spectrum, as described by the linear equation:

$$\phi(f) = 2\pi\delta t_i f \tag{4.2.5}$$

For each window, δt_i is found by a weighted linear regression using phase values at frequencies where the coherence is above a certain threshold. In the active source coda-wave analysis, this threshold was chosen to be 0.975. Phase values are weighted using the weighting relationship described by Clarke et al. [2011], defined for each sample j as:

$$w_j = \sqrt{\frac{C_j^2}{1 - C_j^2} \cdot \sqrt{|S_j|}} \tag{4.2.6}$$

Errors are estimated using the weights and the misfit to the modeled slope. For further details on this method and the process behind calculating the associated errors, please refer to Clarke et al. [2011]. For a true homogeneous velocity variation, the straight line defined by the above equation will necessarily go through the origin. In practice, it may not, either

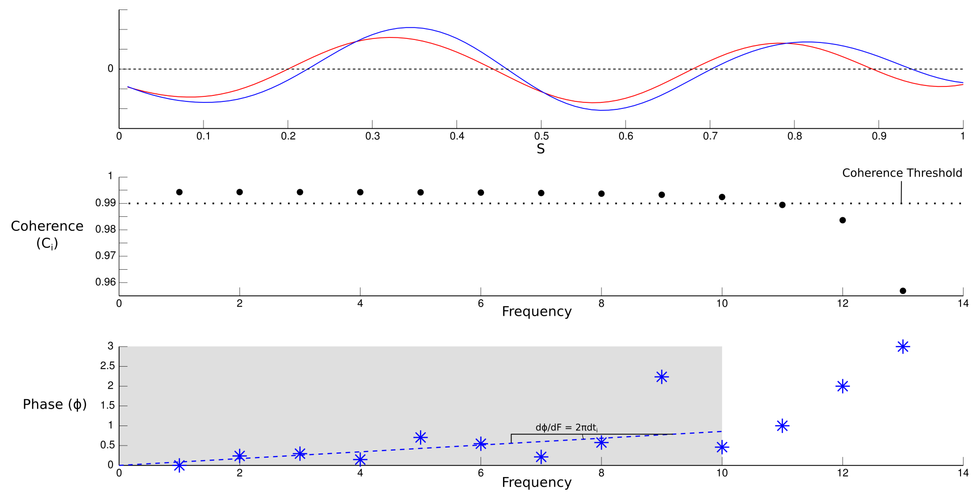

Figure 4.6: Example showing the moving window cross-spectral method. The coherence (centre plot) for the two windowed signals (upper plot) is calculated, and a line is fitted to phase values (bottom plot) where the coherence is above a certain threshold, show as 0.99 in this example. The gradient of this line is used to calculate the delay between the two records.

due to timing issues such as clock desynchronisation or errors in signal origin (relevant for the active source experiment) or due to coda variations being produced by inhomogeneous velocity or scatterer changes.

Once delays for each time window for a particular pair of records have been found, they are compiled and assessed for possible velocity variations in the same way as in the time domain method. Data selection for calculating velocity variations in the active source records was also carried out in the same way as described in the time domain method, including window length and overlap.

4.2.5 Noise analysis

Noise analysis was undertaken on data from all short-period seismometers (all previously documented seismometers not including WNVZ and COVZ, which were broadband instruments at the time) for the period between 1 January 2012 and 31 July 2013 (see figure 4.4). The noise analysis was performed using MSNoise, a python-based noise analysis package available on http://www.msnoise.org/ (last accessed May 2014) [Lecocq et al., 2014]. MSNoise applies the MWCS technique to two noise cross correlations functions (CCFs) computed over certain time windows. In the method, a reference CCF is produced and compared with subsequent 'current' CCFs to provide a series of velocity changes. Before the CCFs are computed, seismic traces are de-meaned, tapered and merged (or padded) into day long series. The data are then bandpass filtered between 0.01-8 Hz before being downsampled to 20 Hz (from 100 Hz).

For each station pair, computation of each CCF involves rotating the north and east components of the two seismic traces into radial and transverse components using the angle of azimuth between the two sensors. A Windsorizing (clipping) of three times the signal RMS and whitening is applied in order to reduce parasitic noise from seismic events. Then, both 5 and 10 day CCF stacks are produced using cross correlations between 30 minute periods for each station. In this study, signal components were correlated like for like with their counterparts from the other station (ZZ, RR and TT for the vertical, radial and transverse components, respectively), however computing correlations for cross-components may be desirable in certain circumstances.

Upon analysis of the cross correlation functions, the period between 28 April 2012 and 10 June 2012 was used to calculate the fixed reference function, due to the high stability of the cross correlation functions during this time. Analysis is carried out on the causal and acausal parts of the CCFs (representing wave energy going from station A to station B and from station B to station A, respectively) separately, unlike Mordret et al. [2010] who elect to normalise and average the causal and acausal parts together. Reference CCFs calculated for the 28 April-10 June 2012 period are shown in figure 4.7. Inspection of the CCFs used in this study revealed a prevalent asymmetry that indicates an uneven distribution in noise scatterers in the region of interest [Stehly et al., 2006]. The MWCS technique is applied to each reference-current CCF pair within the 10-30 s (and its negative counterpart) of the functions in order to ensure only coherent scattered coda waves were kept. A bandpass filter of 0.1-1 Hz is applied to the data, similarly to Clarke et al. [2013], to isolate secondary microseism noise (5-10 s) [Stehly et al., 2006] and exclude possible transient seismic sources such as 2 Hz tremor characteristic to Ruapehu [Hurst and Sherburn, 1993]. Due to the lower frequencies of the data in question (in comparison to the active source CWI), a window length of 6 s and an overlap of 3 s was used. This approach uses no coherence threshold but accounts for low cross-signal coherence using the weighting function given in the previous section.

4.3 Synthetic testing

In order to test the parameters used and the general effectiveness of each method, synthetic testing was carried out in which a real waveform was compared with a resampled version of itself at a known percentage of the original sampling rate. The resampled waveform preserves the sampling rate, simulating an arrival of the same source energy travelling

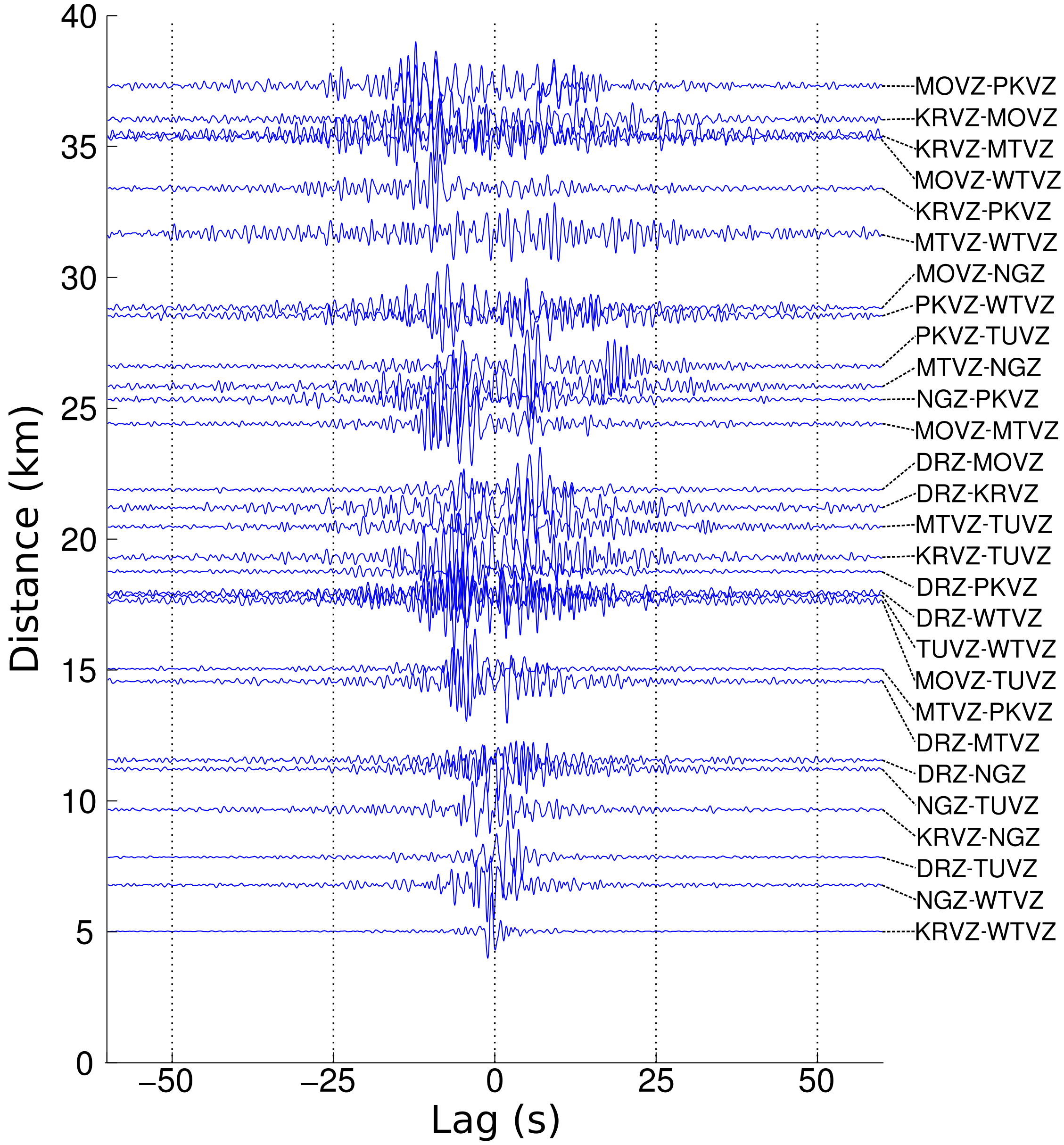

Figure 4.7: Average ZZ cross correlation functions calculated for the 28 April-10 June 2012 reference period, plotted with respect to station pair separation. See figure 4.1 for relative station locations.

through a medium with a different velocity. In this case a range between 0.005% and 0.1% ${}^{\delta v}/_{v}$ was used. To begin with, comparisons were made between the time domain and MWCS methods for each shot recording with various resampled versions of themselves, testing a number of different window lengths and overlaps with the final window length value of 2 s and overlap value of 1.75 s being chosen because they returned velocity variation solutions with the best fit over the largest degree of perturbation. All seismograms were filtered between 2 and 12 Hz. The only difference between the method used for the synthetic testing and the shot analysis is that no adaptive method for selecting the time period in the seismogram over which to choose window delays in order to make the ${}^{\delta t}/_{t}$ calculation could be used, and instead the fixed time period of 5-30 s along the record was used. Also, due to the results from the testing, it was found that limiting the delays used to calculate ${}^{\delta t}/_{t}$ to ± 0.1 s significantly increased accuracy due to the exclusion of outliers that arise when the window under analysis undergoes a cycle skipping-like phenomena, where the best correlation is found at a lag one wave cycle of the dominant period away from the true lag value.

As can be seen in figure 4.8, particular characteristics of each method can be discerned from the testing. Time domain coda wave interferometry provides more reliable results at higher velocity variations and has a large error-to-value ratio at lower velocity variations. Conversely, MWCS provides more precise results at low velocity variations ($\leq -0.08\%$), becoming unreliable at larger variations. This is a somewhat expected result, as delay results from cross correlation in the time domain is quantized to the sampling rate, creating

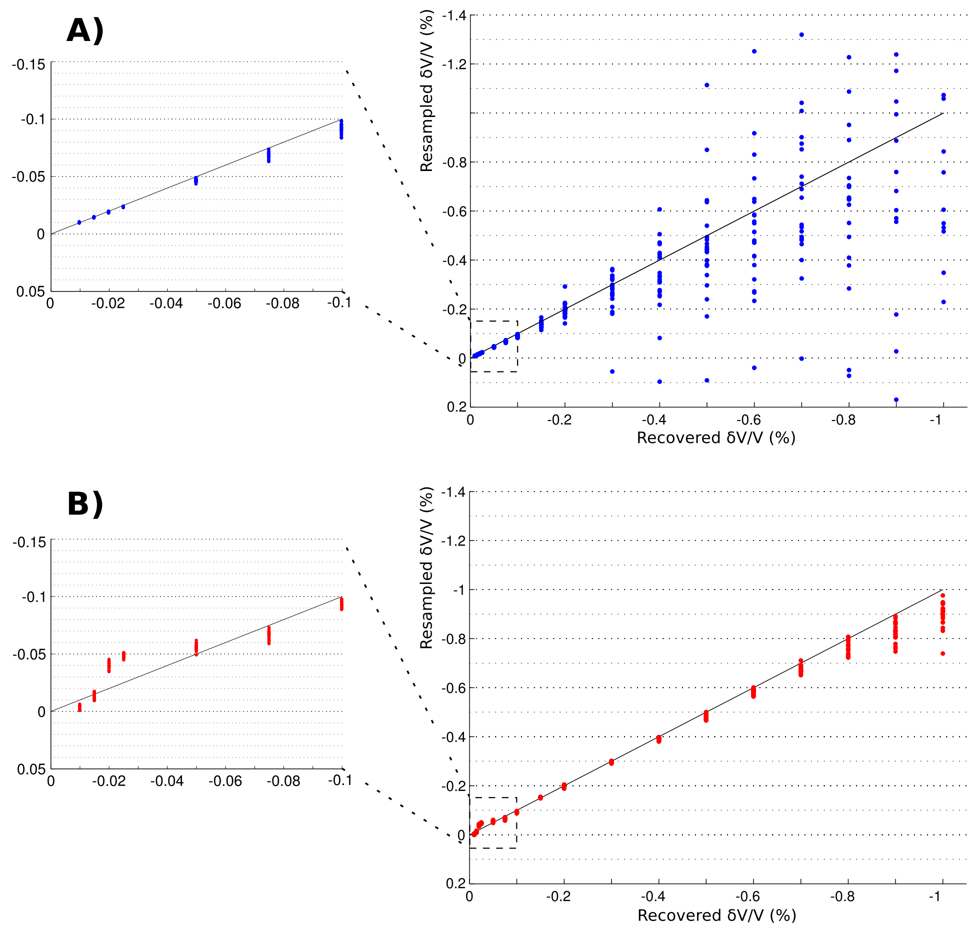

Figure 4.8: Velocity variation results from synthetic testing of the moving window cross-spectral method (A) and the time domain coda wave interferometry method (B). For this analysis, the time domain method is the most precise for velocity variations greater than $\sim -0.02\%$, below which the MWCS method is more precise.

a lower limit to the resolution of velocity variations that can be discerned, whereas using frequency domain cross correlation and calculating delay from the ensuing function's phase spectrum allows for resolution below the sampling rate [Poupinet et al., 1984].

This synthetic testing also outlined the significance of the parameters used to calculate the velocity changes, especially the choice of time period over which lag times are taken for the calculation (figure 4.9). An adaptive method such as the one used with the shot

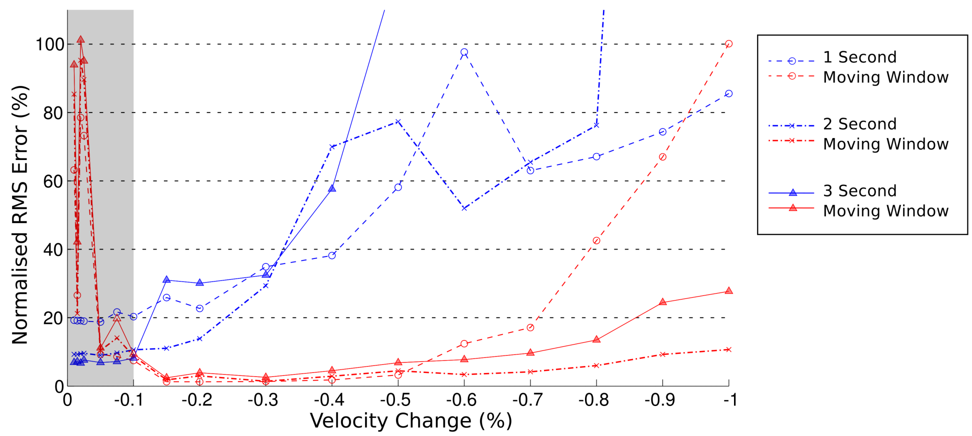

Figure 4.9: Direct comparisons of synthetic testing between the time domain (shown in red) and MWCS (shown in blue) methods for different moving window length sizes. RMS errors were calculated for each stretching factor and then normalised by the true velocity change. A normalised RMS error of 100% at a velocity change of -0.1% means a RMS error of 0.1% between true and recovered values. The shaded area shows velocity changes at which the MWCS was generally more accurate than the time domain method. In all cases, a window overlap of 0.25s was used. For the shot analysis, a window length of 2 seconds was chosen on the basis of this testing.

correlation here works well to restrict the choice of data in order to reduce the influence of outliers, however it is not always a viable approach as it requires that you have repeated events that do not express a significant change in their coda.

4.4 Results

For the period of study, recovered velocity variations ($^{\delta v}/_{v}$) from both these techniques were, overwhelmingly, below $\pm 0.5\%$. Velocity variations highlighted no significant variations that were consistent amongst a group of station pairs over a particular period.

The initial five shots of the active source experiment encompassed roughly 20 hours, sampling almost one whole period of the diurnal and almost two periods of the semi-diurnal components of the solid Earth tide. Figure 4.10 shows how these blasts relate in time with gravity readings made at Lake Moawhango during these shots, as well as a modelled synthetic solid Earth tide calculated using TSOFT [Van Camp and Vauterin, 2005]. Maximum variation in gravitational attraction at Lake Moawhango during the period was ~ 0.2 mGal. The time between shots 3 and 5 has the largest overall change in gravity at 0.13 mGal. Analysis of ocean tides at Lake Moawhango using the GOT4.7 ocean tide model shows that the maximum variation of the gravitational field due to ocean loading between tides is ~ 0.012 mGal. Studying continuous active source *P*-wave velocity measurements, Yamamura et al. [2003] found that strain from ocean loading effects fell off significantly with distance from the shore. As Lake Moawhango is more than 100 km from the Pacific Ocean, ocean tides are considered to be of secondary importance in this area. A robust fit between the measured gravity and synthetic gravity is displayed in figure 4.10, however a more useful metric to consider for isotropic variations in velocity would be areal strain, as it has been demonstrated [e.g. Nur and Simmons 1969b] that seismic velocity is dependent on loading, due to the closure of small discontinuities (i.e. cracks).

To look for possible indications of velocity changes between February 2012 and April 2013 when shot data were available, interferometry was carried out between the five February 2012 shots stacked into a single seismogram and the one April 2013 shot seismogram. All stations that returned results showed velocity decreases between 0.031–0.170%, except for station DRZ which showed a slight velocity increase of 0.013%. Velocities for both the time domain and MWCS method were generally in agreement. Velocity analysis of the first

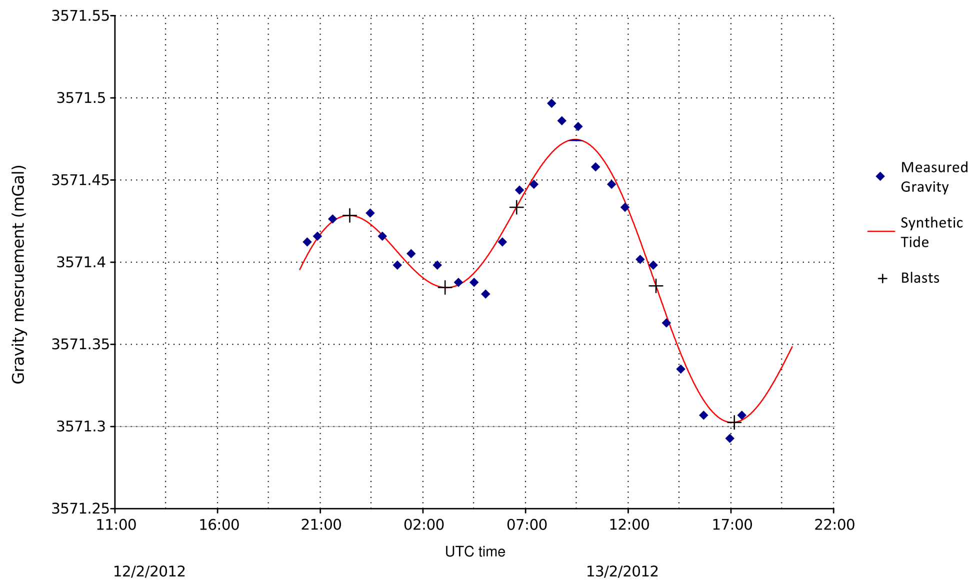

Figure 4.10: Gravity measurements and synthetic tide calculations over the course of the first five active source explosions showing the variation in gravitational acceleration. Gravity readings are given on a relative scale.

five shots, shown in figure 4.11, display variations using the first shot as the reference waveform. It can be seen that there is some degree of correlation between the mean progressive velocity change and the gravitational Earth tide. From the first to the fifth shot, there was a mean decrease of $\sim 0.05\%$ corresponding to a 0.11 mGal decrease in gravitational attraction. The progression and magnitude of velocity variations between shots calculated between successive shots (i.e. shot 1 with respect to shot 2, shot 2 with respect to shot 3, etc.) return similar results (after correction) to those shown in figure 4.11.

Velocity variations recovered from noise cross-correlations showed velocity fluctuations of $\sim \pm 0.2\%$ with respect to the reference correlation function throughout the studied period. Velocity variations of this magnitude were consistent across all station pairs and components, but it is noteworthy that results from the ZZ, RR and TT components were not well correlated. There are points at which either the ZZ, RR or TT components

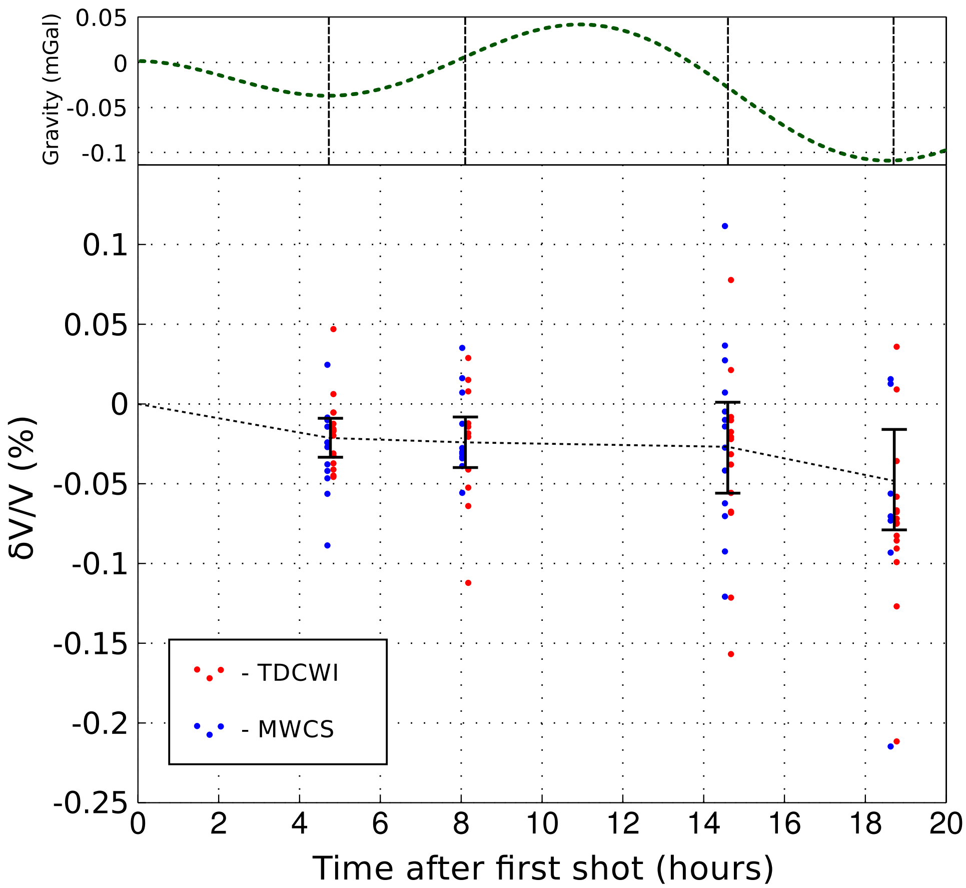

Figure 4.11: Velocity variation results from the first five shots at Lake Moawhango for all stations studied. Variations are calculated using the first shot (at time 0) as a reference. Time domain coda wave interferometry results are shown in red and moving window cross-spectral interferometry results in blue. The black dotted line shows the weighted average variation for both methods. Also shown is the synthetically derived gravity variation as displayed in figure 4.9. Each measurement represents the velocity variation for one station pair, calculated using data from all three components.

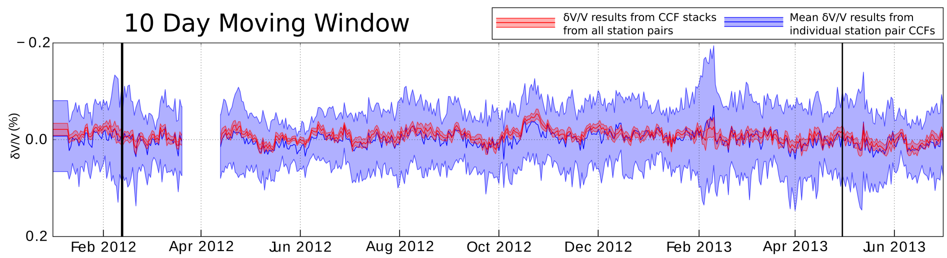

Figure 4.12: Velocity variations during the 2012-2013 period over which the active source experiment was conducted. The results show two averages- red represents velocity variations determined using stacked cross-correlation functions using all station pairs. Blue represents the mean velocity variation using CCFs for each station pair. The period around April 2012 is blank due to a network-wide omission of data for the GeoNet sensors used (refer to figure 4.4). Vertical black lines show the dates of the shots at Lake Moawhango.

show a velocity variation of $> 0.2\%$, however these are not similarly reflected in the other component correlations. This is illustrated in figure 4.12, which shows both the mean velocity variation for all station pairs and components, and velocity variations recovered from stacking all available CCFs. Velocity fluctuations in figure 4.12 are consistently smaller than those found for individual station pairs as no variations are consistent enough across the network to constructively stack.

Results for station pair NGZ and DRZ, whose bisector passes directly between Ruapehu and Ngauruhoe, are shown in figure 4.13. The station pair represents a typical dataset for the entire network, with no long-term velocity changes or significant ($> 0.5\%$) short-term departure from the mean velocity. The plot shows both velocity variations calculated from linear regression of phase data where there are no restrictions, and results that are forced through the origin. The lack of consistent departures between these two datasets indicates that there were no clock desynchronisations between the two stations. Also included in figure 4.13 are normalised correlation coefficients calculated between the reference and current CCFs used for each day (see appendix D). There are periodic decorrelations between CCFs that do not appear to be directly related to wind conditions or rainfall, however the wind and rainfall data available are taken from Chateau Tongariro, in the vicinity of COVZ (see figure 4.1), which may vary significantly to the sampled region due to the topographic effects of Ruapehu (and the Tongariro massif) on wind and precipitation.

2006 Ruapehu Eruption

In light of the results found from looking at noise correlations during the 2012/2013 period of relative quiescence at Ruapehu, particularly the poor correlation for results from different component pairs, we decided to apply the MWCS technique to the period containing the 4 October 2006 Ruapehu eruption. Specifically, we aim to recreate the study done by Mordret et al. [2010] as faithfully as possible in order to expand their analysis and see how volcanism affects changes on each of the ZZ, RR and TT component pairs. Mordret et al. [2010] studied noise correlations for two periods in 2006 and 2007, using the period between 01 April 2007 and 31 August 2007 for computing the average reference CCF to compare velocity variations with. They look at the frequency range between 0.2-0.7 Hz, and preprocess the data with spectral whitening and one-bit normalisation. They compute daily CCFs from stacking 2 minute long CCFs. 10 day long stacks are then used in the coda-wave interferometry, with the same 10-30 s time window as the MWCS technique applied earlier in order to find delays from parts of the coda wave that represent coherent

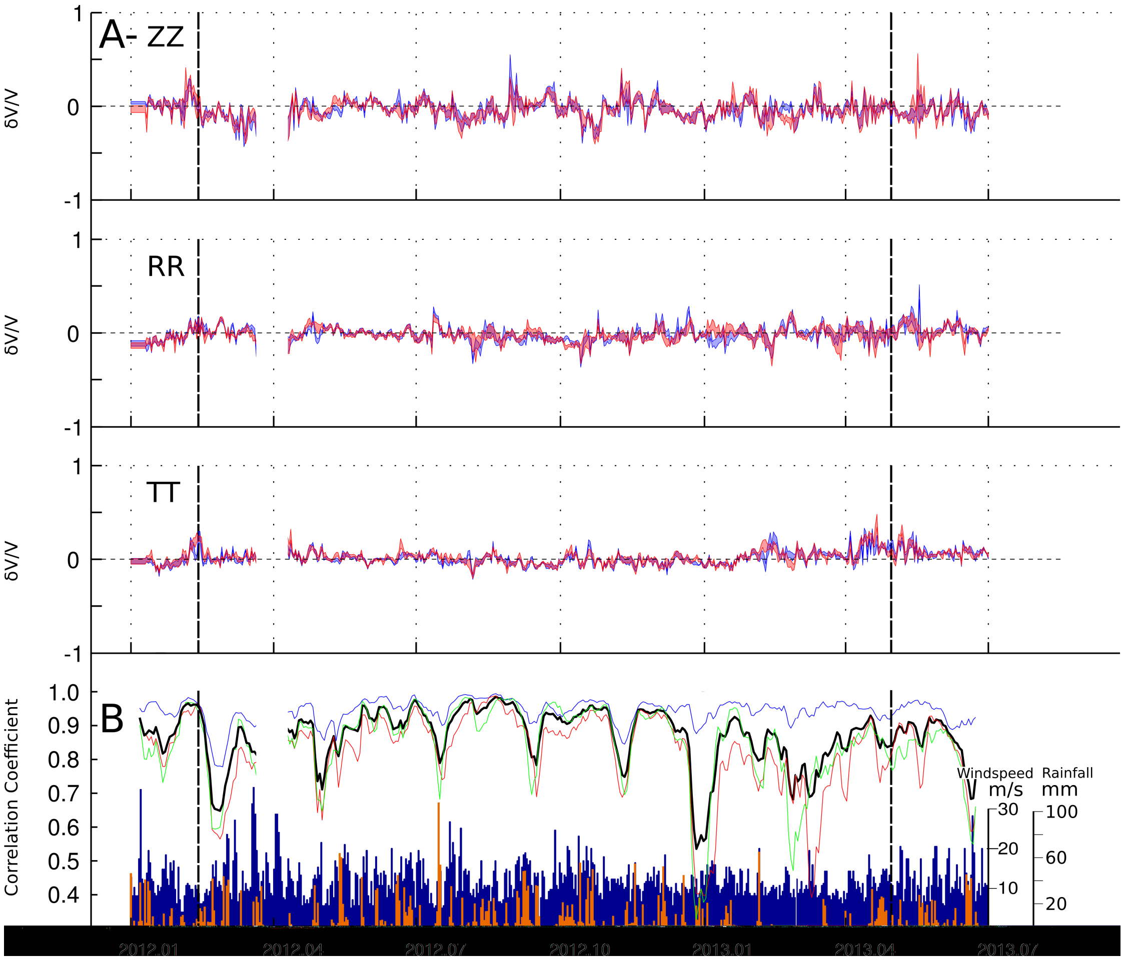

Figure 4.13: Noise interferometry results from station pair DRZ-NGZ during the 2012-2013 period of study. A) shows velocity variations (in %) recovered for ZZ, RR and TT component pairs, respectively. The data represents velocity variations determined using stacked cross-correlation functions using all station pairs. Blue represents velocity variations from linear regression calculations forced through the origin, while data shown in red were calculated without such a requirement. B) shows the maximum correlation coefficient between the reference CCF and the current CCF for each component pair (black- average, red- ZZ, green- RR, blue- TT). Also plotted are daily rainfall (orange bars) and daily maximum wind speed (blue bars) measured at Chateau Tongariro, co-located by station COVZ shown in figure 4.1. Vertical dashed black lines show the dates of the shots at Lake Moawhango.

scattered energy.

The method that Mordret et al. [2010] use to calculate ${}^{\delta v}/_{v}$ is the 'stretching' technique of Sens-Schönfelder and Wegler [2006], which they apply to the time series obtained by stacking the causal and acausal parts of the CCFs used for the interferometry, resulting in a 1 minute long stacked CCF. This stretching technique performs multiple cross correlations between a reference CCF and a current CCF that is stretched and resampled progressively. In simple terms, the stretched current CCF that is best correlated with the reference CCF represents the most likely velocity variation that has occurred between the current and reference CCF. The MWCS technique, in comparison, is applied to the causal and acausal parts of the CCFs separately. Studies comparing the two methods [e.g. Duputel et al. 2009 and Hadziioannou et al. 2009] find that the methods provide similar results, but highlight that the stretching technique may be more stable (Duputel et al. [2009] conclude that the stretching technique provides more stable results only during an eruptive period at Piton La Fournaise Volcano).

Other differences between the Mordret et al. [2010] method and approach performed above on the 2012-2013 period are found in the way the data are preprocessed. The study by Mordret et al. [2010] retains the original 100 Hz sampling rate (rather than downsampling to 20 Hz) and perform one-bit normalisation of the data (rather than Windsorizing). In the comparisons shown here between the MWCS method and the results of Mordret et al. [2010], we use the preprocessing steps employed by the Mordret approach. The data were whitened in the 0.2-0.7 Hz band before one-bit normalisation was implemented.

We performed noise interferometry analysis on four stations, NGZ, OTVZ, TUVZ, and WNVZ (a short period seismometer in 2006/7), as they were specifically mentioned in Mordret et al. [2010] as containing significant velocity variation signals between a number of the available station pairs (as well as having their results presented within the paper). Our results (figure 4.14) clearly show very little similarity in recovered velocity variations between each component pair, as in the previous section. More interestingly, however, the approach employed in this study was unable to discern any velocity signal from the 2006 eruption. Mordret et al. [2010] indicate that they only see a significant velocity variation coinciding with the eruption at specific station pairs. Figure 4.14 shows results from both methods for the station pair NGZ-TUVZ, which was identified by Mordret et al. [2010] as a station pair with the best resolved eruptive signal in the velocity variations. Nothing resembling the $\sim 0.8\%$ reduction in velocities is present in the new analysis.

Furthermore, correlation coefficients between reference and current CCFs do not correlate well between the two analysis (compare figures 4.14B and 4.14D), despite there being a common decorrelation around the eruption. Although both methods appear to have generally good (> 0.9) correlations between the CCFs, the extent of decorrelation during the eruption for the original analysis is, generally, greater than the new one. The trend in CCF correlation also displays differences to that of Mordret et al. [2010] during the rest of the study period, despite the expectation that they should be the same. Thus, although the differences between the MWCS technique and the stretching technique may be influencing the final results, it is clear that the CCFs used are likely to be fundamentally different. There is a certain ambiguity when calculating the correlation coefficient between the two CCFs, as there are different approaches that can be employed in the calculation method that are rarely explicitly stated and indeed are not explained thoroughly in Mordret et al. [2010] (for a more in depth analysis of the technique used here, see appendix D). However, correlation coefficient results calculated here are always different to the Mordret et al. [2010] analysis regardless of the correlation determination method employed. There was a broad agreement between correlation coefficients between CCFs for each component pair for the new analysis (at least in the overall shape of the data series), although absolute values often show a consistent offset between two component pairs e.g. ZZ and RR in figure 4.14B. This result contrasts with recovered velocity variations, which do not show a good agreement across the component pairs.

A comparison between stacking 2 minute long CCFs and 30 minute long CCFs can be seen in figure 4.15, where the case example of station pair NGZ-TUVZ is shown. The 2 minute long CCF stacks show durations of significant variation from the reference CCF with the introduction of a high amplitude, higher frequency signal (two durations of which are clearly visible in figure 4.15B). This signal is present during 5 distinct periods between August-December 2006, with the two episodes during October having the greatest amplitudes. The signal appears at different times in the CCF depending on the station pair being analysed (refer to figure 4.1), however as can be seen in figure 4.16, there is no clear Rayleigh wave move out from energy propagating between the station pairs, suggesting that the evident noise source may be highly inhomogeneous. For station pair NGZ-TUVZ

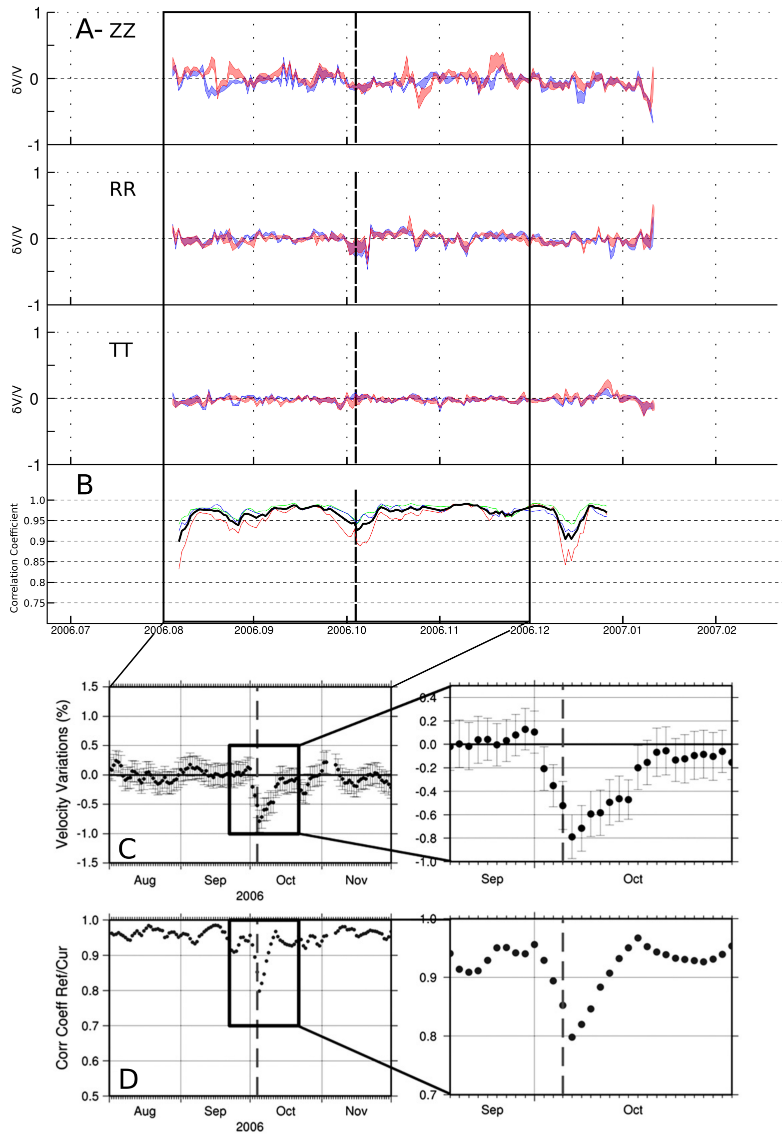

Figure 4.14: Noise interferometry results from station pair NGZ-TUVZ duing the 2006 period encompassing the 4 October eruption at Ruapehu. A) shows velocity variations (in %) recovered for ZZ, RR and TT component pairs, respectively. The data represents velocity variations determined using stacked cross-correlation functions using all station pairs. Blue represents velocity variations from linear regression calculations forced through the origin, while data shown in red were calculated without such a requirement. B) shows the maximum correlation coefficient between the reference CCF and the current CCF for each component pair (black- average, red- ZZ, green- RR, blue- TT). Parts C) and D) were reproduced from Mordret et al. [2010], with C) showing velocity variations in the ZZ component and D) showing the correlation coefficient between the reference and current CCF, as determined by their method/.

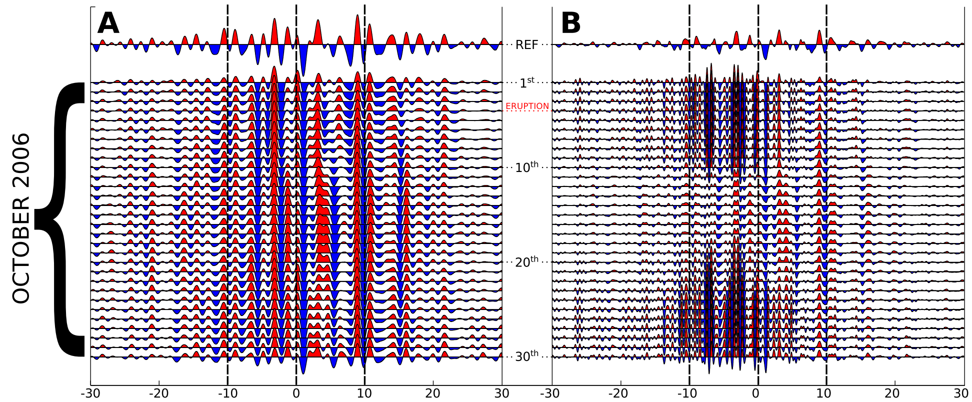

Figure 4.15: 10 day stacked cross correlation functions during October 2006 for station pair NGZ-TUVZ on the Z components, showing the comparison between using 30 minute long correlation periods (A) and 2 minute long correlation periods (B), both after applying 1-bit normalisation. Patches of higher frequency signal in the CCFs can be seen at the start and end of the month in B, but not in A. The reference CCFs, calculated from stacking data from April-August 2007, is shown at the top. Vertical dotted lines mark the 0-lag and -10/10 second points. Velocity variations are only calculated with coda waves outside the -10 to 10 second period.

it is contained in the acausal part of the CCF, indicating that energy from the signal is arriving at TUVZ before NGZ. Similarly for NGZ-WNVZ, OTVZ-TUVZ and OTVZ-WNVZ the signal exists mostly in the acausal section of the CCF with increasing lag and decreasing amplitude with increasing station pair separation. For station pair TUVZ-WNVZ, the most proximal of the station pairs, more higher frequency energy is focused around the 0 s lag mark in both the causal and acausal parts of the signal. These relationships, shown in figure 4.16, are consistent over every period during which the transient signal is present.

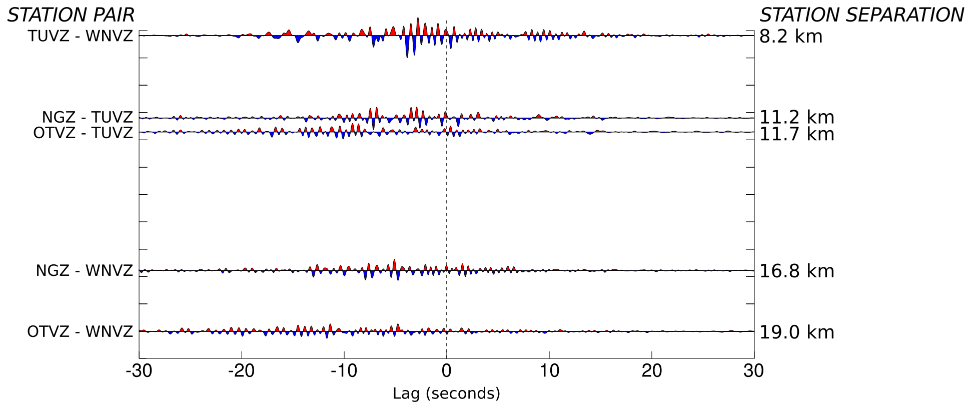

Figure 4.16: Cumulative 2-minute CCFs for the period 1-10th October 2006. Functions were produced by summing all 10-day CCF stacks for each day in the period. See figure 4.1 for relative station locations.

4.5 Discussion

4.5.1 Active source experiment: synthetic testing

The simple synthetic testing carried out here on recorded active source seismic signals demonstrates a marked difference between performing windowed coda wave interferometry in the time and frequency domain. Stretching and resampling the waveform in order to simulate velocity variations seeks to represent an ideal case in which velocity variations are homogeneous in magnitude and distribution, an assumption that is necessary for the interferometry methods described here. For larger changes in velocity (0.1-1%), the accuracy of the MWCS technique rapidly decreases as phase offset measurements become more unreliable and coherence between each windowed section of signal decreases. Coda wave interferometry in the time domain, conversely, stays relatively accurate at these velocity changes. At smaller velocity changes ($< 0.1\%$) the MWCS technique becomes more accurate, because quantization of δt results in the time domain due to the sampling interval start to introduce large errors relative to the velocity change. Evidence that the MWCS technique becomes unstable at larger velocity changes, where decorrelation between the two signals subject to comparison is subsequently high, is consistent with the findings of other noise studies [Duputel et al. 2009, Hadziioannou et al. 2009] that seek to compare the MWCS technique to the stretching method of Sens-Schönfelder and Wegler [2006]. The results of the synthetic testing suggest that large velocity changes determined using the MWCS technique ought to be well corroborated by a number of independent measurements in order to account for this lack of accuracy.

4.5.2 Active source experiment: velocity results

Velocity variations derived from the initial February 2012 shots generally display a positive correlation with gravitational acceleration, with an approximate velocity decrease of $\sim 0.05\%$ across the seismic network accompanying a 0.11 mGal decrease in gravitational acceleration (figure 4.11). Short-term changes in seismic velocity related to gravitational tides are generally attributed to changes in the compressional state of rocks affecting the aperture of small cracks and discontinuities that contribute to the rock's overall stiffness [Nur and Simmons, 1969b] with increased compression resulting in closed cracks, stiffer mechanical properties, and increased velocities. Differences in velocity change across the seismic network may be explained by the variable strain response of the crust to gravitational tides due to local geology, topography [Levine and Harrison, 1976] and cavity effects [Harrison, 1976]. Yamamura et al. [2003] measure differential travel time variations (and therefore velocity variations) of up to 0.3% for the largest tidal amplitudes. In order to estimate the strains associated with the gravitational tides around the Moawhango region, we calculate horizontal strains using the ERTID modelling package [Agnew, 2012]. The vertical strain can be derived assuming a free surface boundary condition, giving the relationship $\epsilon_{zz} = -\frac{\nu}{1-\nu}(\epsilon_{xx} + \epsilon_{yy})$, where ν is Poisson's ratio and ϵ_{xx} and ϵ_{yy} are the orthogonal components of the strain tensor in the horizontal plane [Melchior, 1983]. Given this relationship, the volumetric strain can then be expressed as a function of areal strain:

$$\Delta = \frac{1-2\nu}{1-\nu}(\epsilon_{xx} + \epsilon_{yy}) \tag{4.5.1}$$

Results from this modelling are shown in figure 4.17, with volumetric strain calculated assuming a Poisson's ratio of 0.2. From the first to the fifth shot, there is a modelled areal extension of approximately 40×10^{-9} and a calculated volumetric extension of approximately 30×10^{-9} (see figure 4.17). Note that these strains are around two orders of magnitude less than those measured by Yamamura et al. [2003] due to the added contribution from variable water loading caused by ocean tides. Assuming a static Young's modulus (E) of 30 GPa, typical for nearby Rotokawa andesites [Siratovich et al., 2014], we can express the bulk modulus (K) as:

$$K = \frac{E}{3(1-2\nu)} \tag{4.5.2}$$

Giving a bulk modulus of the order 16 GPa. In this case, the pressure change causing the volumetric strain is, therefore, on the order of 5×10^2 Pa, corresponding to a $\sim 0.05\%$

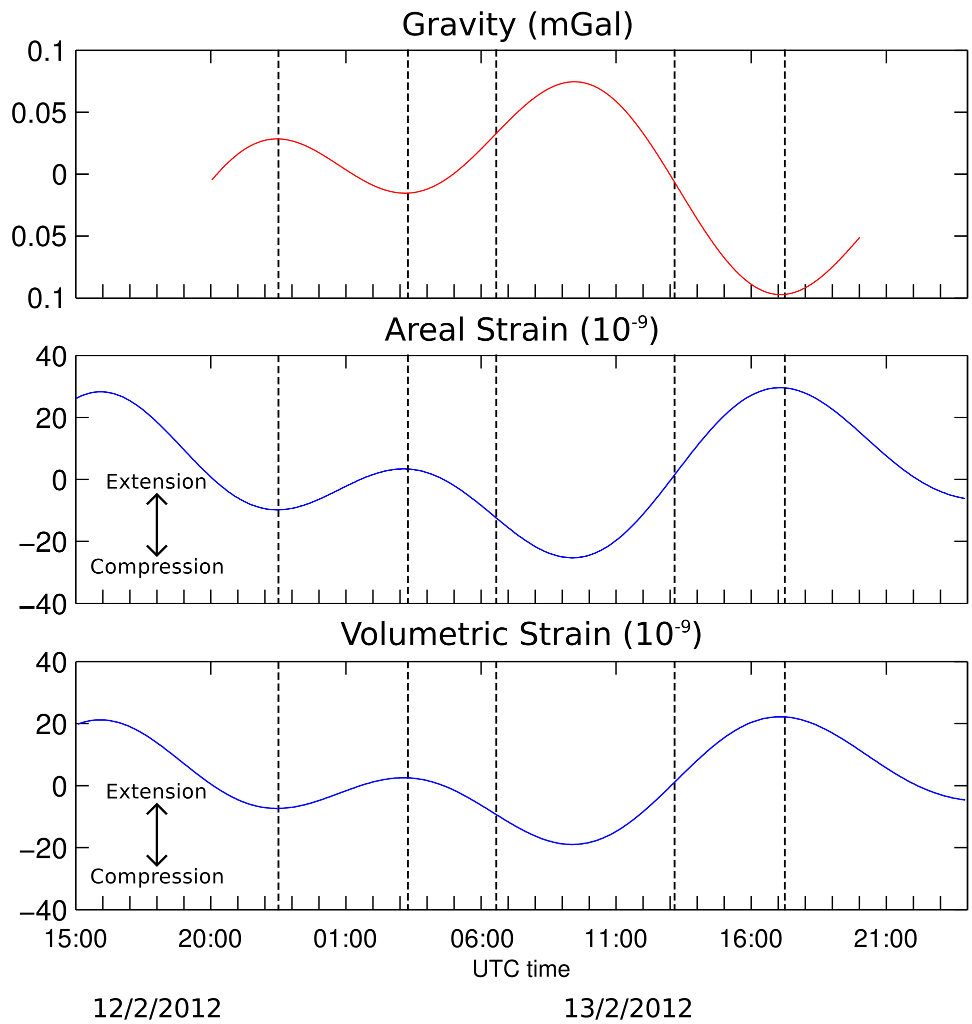

Figure 4.17: Modelled gravity, areal strain, and volumetric strain due to Earth body tides at Moawhango during the time period of the first five shots. Gravity and strain were modelled using the TSOFT [Van Camp and Vauterin, 2005] and ERTID [Agnew, 2012] software packages, respectively. Volumetric strain is calculated assuming a Poisson's ratio of 0.25.

velocity change (should the observed velocity change be caused gravitational strain). This pressure change should be considered a minimum, as strain is likely to be underestimated due to the omission of ocean loading effects. Nevertheless, bearing in mind that atmospheric pressure at the Earth's surface is, on average, 1×10^5 Pa, the calculated pressure change is extremely small. It is difficult to assess whether the observed velocity changes are indeed caused by Earth tides (or some other effect, be it atmospheric or experimental) without extending the experiment to cover several tidal cycles. The findings suggest that in situ velocity variations of around this magnitude, i.e. $< 0.1\%$ may be expected to exhibit cyclical behaviour corresponding to Earth tides, if the method of resolving such variations has sufficient resolution. Thus the range of velocity variations determined between the stacked average of the February 2012 shots and the subsequent April 2013 shot, with velocity decreases of between 0.031 and 0.17% with the exception of one station, likely represents a small overall decrease in velocities around Ruapehu, as the decrease was calculated after averaging of the tidal effects calculated over the initial 1-day experimental period, but may indeed be within the natural variation of velocity due to tidal processes (in both cases, given the validity of the velocity variations due to gravitational tides resolved here).

Nur and Simmons [1969b] found compressional wave velocity increases of 1.06–3.96% in Barre Granite samples (the range of velocity increase representing the rock's inherent anisotropy) when a uniaxial stress of 25×10^5 Pa was applied to a previously unstressed sample. Linearly extrapolating these changes down to a uniaxial stress of 5×10^2 Pa would result in velocity increases of 0.00021-0.00079%, several orders of magnitude below the velocity changes observed. In reality, the relationship between applied stress and seismic velocity is non-linear due to effects related to crack and pore closure (at a certain stress magnitude available cracks and pores are elastically closed and can provide no significant influence on the rock's overall stiffness). This non-linearity will act to lower the rock's pressure sensitivity when in situ due to confining pressures at depth. Barre Granite is stiffer than the andesites in the TVZ, with a Young's modulus of $\sim 46 - 53$ GPa [Santi et al., 2000], making seismic velocity in the granite less sensitive overall to pressure changes. On balance, however, it is clear that if the velocity changes we observe are caused by tides, the pressure sensitivity of the Barre Granites as found experimentally by Nur and Simmons [1969b] is significantly lower than the crust at Ruapehu.

4.5.3 Noise interferometry

Noise interferometry analysis during the 2012-2013 study period did not resolve any consistent seismic velocity changes at Ruapehu. Inconsistent velocity results from component pairs ZZ, RR and TT indicate that the method we use is not returning accurate velocity variation results. It has been shown that cross-correlation functions produced from different component pairs will possess energy propagating in various types of wave. The noise field consists of fundamental and higher order Rayleigh and body waves that are recorded variably depending on the azimuth and inclination of the respective component pairs being analysed [Bonnefoy-Claudet et al., 2006]. The presence of higher order surface wave modes that become apparent on particular component pairs, such as the first order Rayleigh mode on

RR [Savage et al., 2013], is important to consider when determining velocities from seismic noise. Regardless, they can not explain the discrepancies observed between velocity variations determined here, which often and inconsistently reverse sign across component pairs. Changes in the location and nature of noise sources, and their relative amplitudes, may explain the seemingly random velocity variation signals. The relative proportion of body and surface waves present in the noise field is linked to noise source and receiver distribution, as well as site conditions [e.g. Bonnefoy-Claudet et al. 2006, Bonnefoy-Claudet et al. 2008]. This means that interferometry analysis may detect an apparent velocity change when variations amongst CCFs are caused by noise source variation. The combination of these effects with the limited range of precision identified in the synthetic testing discussed in section 5.1 means that use of the MWCS technique should be carefully parameterised when applied to specific problems.

Applying the MWCS technique to the period encompassing the 2006 eruption of Mount Ruapehu, where velocity drops of up to $\sim 0.8\%$ were measured over the eruptive period by Mordret et al. [2010], failed to recover similar velocity variations and produced inconsistencies across component pairs like those initially found during the 2012-2013 period. Again, considering a 0.8% change is greater than the theoretical 0.1% limit of stability as determined by synthetic testing, it is possible that the MWCS method is unable to resolve this relatively large velocity variation. For the parameter sets investigated in this study, therefore, it is not recommended to use the MWCS technique as a means to monitor velocity changes at volcanoes. Below is a summary of the parameters applied to the investigation of the 2006 data period

Cross-Correlation Function reference periods	Cross-Correlation Function length	Band-pass filter frequencies	MWCS window length	MWCS window overlap	Coda analysis period	Minimum Coherence
1/4/2007–31/8/2007	1 s	0.1–1 Hz	6 s	50%	10-30 s	0.7
	2 s	0.2–0.7 Hz	3 s	33%		0.9
Entire period						
	30 s					

These parameters were tested for every permutation apart from the 0.1–1 Hz band-pass filter frequencies, which was only tested with 2 s cross-correlation length, with a 6 s/50% MWCS window length/overlap and 0.7 minimum coherence. Although only selected data are shown here, results for different parameters were such that no significant stable velocity variations could be found either across component pairs or parameter choices.

In order to improve the robustness of the noise interferometry method with the view to develop its usefulness for volcano forecasting, there are a number of approaches that can be further investigated in future studies. Clearly, the two major difficulties in the process are, first, the question of choosing method parameters that will resolve an eruption related velocity change without the benefit of hindsight, and second, being able to identify real results from false positives caused by non-volcanic processes (ideally, quality parameterisation design would go some way to mitigate the presence of false positives in velocity variation results). Parameterisation may be improved by incorporating techniques that use analysis of existing data to objectively define certain parameters. For example, the upper lag threshold for the coda analysis period (i.e. how far into the coda interferometry is performed) can be determined from preceding cross correlation functions by analysing their coherency using the Gaussian smoothing method used here for the active source experiment and outlined in appendix D.

Choice of period for producing the reference CCF is also important, as the reference CCF needs to represent (as closely as possible) the stable noise field and thus the constituent CCFs require a good degree of self-coherency. The problem facing good choice of reference is twofold; firstly, it is difficult to know whether your choice of reference is indeed representative of the stable noise field without intimate knowledge of the study area and the relevant noise sources, and secondly, the choice may be moot if a stable noise field doesn't exist. In order to mitigate against these problems, a more dynamic approach to formulating the reference CCF from which velocity variations are assessed can be adopted. One such example of this is demonstrated in Brenguier et al. [2014], who perform a Bayesian inversion of the linear equation $d = \mathbf{G}m$ where the data vector, d, contains each velocity variation calculated using the MWCS technique between the 'current' CCF in question and all other daily CCFs for a station pair, and the model vector, m, describes the daily velocity changes for that particular pair. In doing this, the subjectivity of choosing a reference CCF is superseded by a probabilistic assessment of all recoverable velocity changes available in the data. Using this technique, Brenguier et al. [2014] were able to resolve velocity variations of the order of 10^{-2}%, up to a maximum of -0.12%, small enough to be accurate as determined by the synthetic testing shown here. A logical and relatively trivial expansion of this technique would see its application to multiple component configurations in order to test their relative responses to velocity variation.

The high-frequency signals evident during the 2006 eruptive period, shown in figures 4.15B and 4.16, display a transient departure from the more consistent, longer period signals generally evident in the CCFs. The transient signal, having a frequency of roughly 1.2 Hz in the CCFs, exists predominantly in the acausal part of the CCFs in which it exists. It is unclear what causes this signal, which appear in the 2 minute CCFs but not in the 30 minute CCFs. One hypothesis is that it is a source of volcanic tremor originating from Ruapehu, as there is evidence that the source of the signal lies towards the summit of Ruapehu. Analysis of the station locations (see figure 4.1) indicate that the acausal part of the CCFs all contain energy arriving at western and southern stations first. Also, the lag of the signal for station pairs NGZ-WNVZ and OTVZ-TUVZ, at between roughly -15 – 0 s (see Figure 4.16), are similar depsite NGZ-WNVZ having a greater station separation. The relative proximity to the summit of Ruapehu could be controlling the lag time of the signal in the CCFs. On the other hand, comparing the times at which the signal exists and when volcanic tremor was recorded over the same period (as shown in Mordret et al. [2010]), there does not seem to be any correlation between the two.

4.6 Conclusion

The results here do not show any significant long or short term velocity variations in the Ruapehu region over the 2012-2013 period of study, suggesting that no detectable build up of volcanic pressure occurred over this time. However, the study also highlighted potential issues with using the moving-window cross spectral method to perform noise interferometry at Ruapehu. We also indicate that forces associated with the solid Earth tides may be responsible for diurnal and semi-diurnal variations up to approximately $\sim 0.07\%$, however this number may vary significantly depending on local geology and topography.

Combining active source and noise interferometry provides a certain degree of mutual mitigation of the limitations of each approach. The active source experiment is a particularly involved undertaking, as detonation of such volumes of explosives carries with it a cost and difficulty which makes it unfeasible for truly consistent monitoring. Environmental damage, a concern in terms of both natural conservation as well as the degradation of the shot site that will ultimately affect seismic energy propagation and render interferometry pointless, should also be considered. It is due to this that noise interferometry is such an attractive option for continuous velocity monitoring, given that storing and processing the required data is becoming increasingly easy to do with relatively modest computation (in modern terms). However, the temporal resolution of noise interferometry is limited by the necessity to stack data, 10 days worth in this case, in order to increase the signal-to-noise ratio and produce stable CCFs. The temporal resolution of active source interferometry is limited by the experimental procedure.

Measurements from the active source experiment repeated over the course of a day show a weak correlation with the solid Earth tide, however conducting the experiment over several periods of the diurnal and semi-diurnal Earth tide is recommended in order to ascertain whether the measurements represent true velocity variations or unquantified experimental error. A comparison with theoretical tidal calculations and results from Yamamura et al. [2003] show that the measured changes are within what would be expected for gravitational forces, estimated to be caused by a pressure change of approximately 5×10^2 Pa assuming that pressure changes due to ocean loading are negligible at Ruapehu. From the first set of shots in February 2012 to the final shot performed in April 2013, there were velocity decreases of 0.031–0.170% across the network (with one exception) after performing interferometry on the final shot and the stacked average of the first five shots.

This study used two similar moving window techniques to calculate velocity variations from coda wave interferometry. Synthetic testing of both techniques explored in this study showed that there is a shift in effectiveness at around a 0.1% velocity change of performing analysis in the frequency domain (i.e. MWCS) or the time domain, with the MWCS technique being more accurate at smaller velocity changes and less stable at higher velocity changes.

Applying the MWCS interferometry technique on noise cross-correlations produced velocity variations of $\pm <$0.5%, however the variations lacked consistency across station pairs and across the components analysed. This indicates that the velocity variations recovered by the method are not true velocity variations but in fact reflect changes to CCFs that are most likely caused by changes to the noise field or localised non-homogeneous changes to scatterers or velocities. This occurred in a similar manner for analysis during both the 2012-2013 period of eruptive quiescence and the period encompassing the 2006 eruption at Ruapehu. The implications of this study are that the standard moving window cross-spectral method is not suitable for resolving true velocity changes associated with volcanism at Ruapehu, and instead either another method (such as the stretching method employed by Mordret et al. [2010], or the Bayesian method employed by Brenguier et al. [2014]) or a somewhat different approach to the parametisation of the MWCS technique should be taken. From the results found in this study, it is also recommended that velocity variations are calculated for each of the ZZ, RR and TT components, and a comparison between their relative magnitudes made. If it can be shown that there is a correlation across component pairs, it may act as a way to identify true velocity variations from false positives.

Chapter 5

Conclusions and Synthesis

Here, the conclusions of each previous chapter will be briefly recapped, and there will be a discussion about the potential for developing techniques in future work. Moreover, since the studies in each chapter were performed independently, some of the broader implications of each topic's conclusions when synthesised will be discussed. Chapters 2 and 3, both being concerned with numerical modelling of seismic anisotropy, are intimately related, and taken together they give an interesting perspective on the benefits and limitations of approaching shear wave splitting using computational methods. With chapters 2 and 4, which focus on seismic detection of volcanic processes at Asama and Ruapehu, respectively, we hope to inform the development of the suite of eruption forecasting tools available to geophysicists. The conclusions in this thesis, especially those formed using computational modelling, are predicated on the assumption that the input data are valid and that their errors are well defined. This is especially worth bearing in mind as the SWS data that was used in chapters

2 and 3 were determined in previous studies.

5.1 Chapter 2: Review

Modelling shear wave splitting due to stress-induced anisotropy; with an application to Mount Asama Volcano, Japan

The study of shear wave splitting at Mount Asama by Savage et al. [2010b] identified a close correlation between delay time and GPS measurements during its 2004 eruption, suggesting a causative relationship between the volcanic processes that produced the surface deformation measured using GPS and the measured anisotropy. This relationship has been suggested in a number of studies at other volcanoes [e.g. Bianco et al. 1998, Gerst and Savage 2004, Johnson et al. 2010, Roman et al. 2011] and is virtually always attributed to changing stress conditions that result from the movement of magma within the volcano. The assertion of a link between volcanic deformation processes and seismic anisotropy at Mount Asama, combined with geodetic information of the magmatic processes [Takeo et al., 2006] (itself a part of a suite of work that make Asama a relatively comprehensively studied area), gives a good opportunity employ forward modelling in order to test the parameters that define such a link.

The modelling results themselves indicate a number of things. Foremost is the evidence suggesting that the change in stress state caused by an inflating dyke, the process that was determined to be the major contributor to the GPS measurements during the 2004 eruption, is by itself too small to produce the variation in shear wave splitting measurements made by Savage et al. [2010b]. This does not exclude stress-induced anisotropy as a mechanism for temporally-varying anisotropy at Asama, however, due to the prescriptive nature of the forward modelling and the assumptions needed to perform it. Deciding how to formulate the anisotropic elastic properties of the model space is the step that bears the most profound assumptions. Results show that using crack anisotropy elastic tensor values determined by Hudson [1981] gives synthetic measurements that best approximate the data, however a constant crack density was assumed for the entire model space, overlooking any heterogeneity in anisotropic parameters (except for its orientation). Significantly, using the analytic relationship between elastic anisotropy and stress of Gurevich et al. [2011] shows that the overall stress conditions are far too high for dry crack conditions similar to those used to formulate the relationship. This leads to the conclusion that crack induced anisotropy must be influenced by pore fluids, as high pore fluid pressure serves to reduce effective stress at depth. Also, it seems apparent from stress modelling that dyke stresses at distances of a few kilometres away from the source are small compared to the general pressure expected from the rock overburden. This implies a number of things; firstly that changes to the strength of anisotropy along a raypath (which affects the overall delay of a shear wave) must have some other, perhaps secondary, source than just changes in stress magnitude, or at the very least is sensitive to relatively small stress perturbations. Secondly, that the background regional stress may be close to isotropic in order for the dyke stresses to have a noticeable effect on anisotropy at the distances that the events and stations were situated. We suggest, therefore, that the crustal rocks surrounding Asama may have significant pore fluid pressures and that the fracture networks are locally connected, in order for there to be low effective pressure conditions that are sensitive to small stress changes. With the approach used in this chapter, however, it is impossible to constrain these parameters and truly understand what the sensitivity to stress change may be.

5.2 Chapter 3: Review

Inversion of Shear Wave Splitting Data: Imaging the subsurface of the Canterbury Plains

The 4 September, 2010 $M_W 7.1$ Darfield earthquake was followed by a significant aftershock sequence in a region of New Zealand that previously saw little seismicity in recent history. SWS measurements from these events were made by Holt et al. [2013] between 4 September 2010 and 11 January 2011, giving a large dataset of 8374 δt and ϕ pairs. After inverting these data for two anisotropy parameters; strength of anisotropy in %, α, and its orientation relative to the vertical axis, θ, a distinct layered pattern of anisotropy was determined using a number of different starting models. Inverting for only one angular parameter means the inversion solution is significantly better resolved, and the assumption is made with the understanding that near-vertical cracks and fracture sets constitute the majority of the anisotropy sampled by the SWS data. Model features exhibited across inversions that employ a range of starting models are considered robust.

The proposed anisotropy structure of the region consists of an upper layer, between 3-6 km thick, of highly anisotropic material overlaying a near-isotropic volume surrounding the Greendale fault. Some evidence for relatively anisotropic material below this upper layer exists at depths of ~ 12.5 km near the Charing Cross blind thrust fault, and the region to the northwest and south of the resolved model space. Anisotropy is oriented broadly parallel with σ_{Hmax} ($\sim 115°$) across the model space, with rotations towards E-W evident on the eastern end of the Greendale fault. Further rotations exist at distance (> 10 km) to the Greendale fault, and are most evident towards the NW of the resolved model space. With reference to V_p/V_s and hydrological studies in the region by Reyners et al. [2014] and Cox et al. [2012], respectively, we propose that this pattern of anisotropy is brought about by rock damage caused by the earthquake and aftershock sequences, resulting in the dilatation of microcracks and the mobilisation of pore fluids. Increased microcrack density near the surface, where rock overburden is small, increases the sensitivity of the rock to stress-induced anisotropy. At depth, low anisotropy close to the Greendale fault may be explained by high overburden pressure, and perhaps increased effective stress due to decreased pore fluid pressures as pore fluid migrates towards the surface. This model also presents a convenient explanation for the discrepancies between surface wave anisotropy as determined by Fry et al. [2014], who find broadly E-W and NE-SW fast directions, and the SWS data of Holt et al. [2013]. The ambient noise method employed by Fry et al. [2014]

has a low sensitivity to the top ~ 5 km of the crust, and samples a much wider region due to the low frequencies used, in comparison to the higher frequency S-waves used for SWS.

5.3 Chapter 4: Review

Active Source and Noise Interferometry: Investigating seismic velocity variation at Mount Ruapehu

The final topic of this thesis is a study that combines active source and ambient noise interferometry in an effort to investigate the nature of seismic velocity changes at Mount Ruapehu. The study began with the explosion of eight 100 km ANFO charges (although only six were usable) on the bed of Lake Moawhango, situated approximately 20 km south-east from the summit of Ruapehu. Although the use of repeated events to monitor volcanoes is not new [e.g. Pandolfi et al. 2006], it became quickly apparent that on-site issues affecting the precision of the experiment's repeatability and the prohibitively high cost of material and logistics makes such an active source approach inappropriate as a useful volcanic monitoring tool. It does, however, offer a relatively controlled experiment (in comparison to using naturally repeating sources) to constrain and contrast with the ambient noise methods that are presented in tandem with it. We apply two methods of interferometry on the explosions; moving window cross-spectral and time domain coda wave interferometry.

As the period of interest, between 1 January 2012 and 31 July 2013, was not marked by any detected eruptive events at Ruapehu, the analysis aimed to resolve the range of velocity variation that the two methods produce. Synthetic testing of both interferometry techniques shows that the accuracy of the MWCS method is best at small velocity changes ($< 0.1\%$), and the time domain method is most accurate at higher velocity changes ($0.1 - 1\%$). Applying the interferometry to the active source experiment, we show limited evidence of velocity changes of a magnitude of up to $\sim 0.07\%$ over the period of approximately 19 hours, covering just over one period of the solid Earth tide. These changes are smaller than the $\sim 0.2\%$ changes measured by Yamamura et al. [2003], possibly due to the lessened effect of tidal loading in the central North Island compared to the coast of Japan. When comparing ambient noise interferometry with active source interferometry over the entire period, we show that MWCS velocity change results derived from ambient noise cross correlations continuously vary by $\sim 0.5\%$, notably outside the accurate region found using synthetic testing, with no significant velocity change occurring consistently over the network. When expanded to use three component cross correlation pairs, ZZ, RR, and TT (out of a total of nine possible pairs), results show that velocity variations between each station pair are also internally inconsistent depending on the choice of component pair. In order to see whether the results were indicating that the MWCS method was noisy below a certain velocity change threshold, we apply it to an eruptive period at Ruapehu in 2006. Ambient noise interferometry using a different technique (the 'stretching' technique) was already applied to this period by Mordret et al. [2010], who found a number of significant velocity changes during the eruption which they attributed to magmatic processes. The comparison between the methods show that the same velocity change found by Mordret et al. [2010]

cannot be resolved using the MWCS technique, and moreover that there are still internal inconsistencies across station component pairs. In light of these results, we suggest that the MWCS interferometry technique be used with care at Ruapehu or, ideally, a more robust technique be employed.

5.4 Numerical modelling of Shear Wave Splitting

The following suggestions of follow-on work on the topic of SWS modelling and anisotropy are made:

1. The forward modelling method suffers from limitations due to its prescriptive nature, restricting our conclusions so that we can only reliably exclude specific causes of anisotropy at Mount Asama. As many assumptions about the state of the model region and the interaction between volcanic processes and anisotropy are necessary, the resulting method works for testing those various assumptions in hindsight, but offers little by way of providing a tool for eruption forecasting. In performing the forward modelling applied in this thesis, various questions about time-varying anisotropy at volcanoes arose that could not be fully addressed. Some of these are long standing questions: To what extent does measured variance in SWS reflect path effects (i.e. the nature of anisotropy changing), or source effects (e.g. changing focal mechanisms, source location changing in a heterogeneously anisotropic medium, etc.)? Are SWS measurements truly reflective of bulk anisotropy properties, as is assumed, or do various factors such as near-surface structure, topography, receiver site effects, and

interfering phase conversions make the majority of them inscrutable? Others arise directly from the results of the study: What is the spatial extent to which volcanic processes affect anisotropy along nearby raypaths? What controls this extent? Is pore fluid transmission the mechanism behind varying anisotropy strength near some volcanoes?

Regardless of this, a future step that may increase the predictive power of SWS in terms of volcanic eruptions may be to apply an inversion method similar to that developed in chapter 3 to a volcanic region. As eruptive periods are often limited to months, weeks, or days, the small amount of data occurring during it may be restrictive for modelling purposes (as was found during the Asama study). To overcome this, a larger dataset of SWS data from periods of eruptive quiescence should be used to produce a model of anisotropy while volcanic processes are dormant. Using such a reference model, the existence of time-varying anisotropy, hopefully indicative of magmatic processes, would manifest as misfits when forward modelled. Of course, this relies on there being no general variation of anisotropy over time other than that related directly to the eruption itself. Therefore any investigation that seeks to create a reference model of anisotropy at a volcano should use 4D tomography if possible in order to assess the possibility that the nature of anisotropy is changing during periods of quiescence.

2. The inversion processes itself may be improved in a number of ways. The linearised least squares approach may not be optimal for solving anisotropy from SWS, and

a non-linear approach such as that used by Wookey [2012] may prove to be more suitable. Another addition to the method that may increase resolution in regions with little data, which was implemented by Abt and Fischer [2008] but not used here, is the use of correlated volumes which homogenise anisotropy parameters over a number of blocks. This works in a similar way to quad-tree gridding, and serves to stabilise parts of the model that are otherwise poorly constrained.

On a more technical note, opportunities for parallelisation of the modelling code were taken when possible, which greatly reduces the processing time needed to produce inversions. Alongside this, using MFAST results means that the method would need less computation than methods such as that of Wookey [2012], where the raw seismograms are manipulated in the code rather than abstracted to SWS measurements. There are two ways in which these aspects could be improved. Firstly, MFAST input data can be expanded to include null measurements (i.e. those with no splitting), provided that the null measurements are evaluated to be representative of truly non-split waves, rather than poor-quality measurements. This is helpful as null measurements of this nature provide information about the state of anisotropy the raypath travelled through, indicating either an isotropic medium, or a case where the *S*-wave polarisation is parallel to either the fast or slow direction of an anisotropic medium. The second of these is to execute the modelling code in an environment other than MATLAB, in which it is currently written, as MATLAB places a restriction on the number of parallel cores a code is allowed to exploit.

3. Improvements to the inversion process may be made by including anisotropy data from means other than SWS. For example, anisotropy in the Canterbury region was also studied by Fry et al. [2014] using surface waves detected in ambient noise. Producing a modelling technique that is able to solve for both S- and surface wave anisotropy simultaneously will provide a better understanding of what controls them. Differences between the SWS measurements of Holt et al. [2013] and the surface wave anisotropy tomography of Fry et al. [2014] are intriguing, and the models presented in Chapter 3 provide one explanation for the disparity. Producing a model that is able to reproduce both datasets, for example, taking into account the Fresnel zones of each wave type, would be extremely useful for increasing model resolution and overall understanding about the source of the anisotropy being measured. Furthermore, a more robust understanding of SWS measurements and anisotropy models created using them may open the technique up for use as a tool to determine a range of geophysical parameters. For example, SWS in well determined sedimentary basins may provide detailed information about rock and crack compliances through empirical relationships such as those introduced in Chapter 2.

5.5 Volcanic eruption-related seismic velocity variations

As discussed in sections 2.5.1 and 5.4, there is some potential for developing numerical modelling of anisotropy for use in volcano monitoring. The other focus of this thesis was to study velocity variations in volcanic areas, both in terms of changes to seismic anisotropy and absolute seismic velocity. Again, the results shown here pose a number of questions suitable for further study:

1. The ambient noise study in chapter 4 highlights an issue with the reliability of using the moving window cross-spectral technique to monitor velocity variations. Further investigation into the effect of certain parameters of the method, such as cross-correlation function duration, stack length, and filter frequencies, would be useful to test the approach more thoroughly. One significant result from the ambient noise derived velocity variations presented in this thesis is the lack of consistency across component pairs. For a particular station pair, should a true increase or decrease in velocity manifest itself any differently on the ZZ component than on the RR or TT component? What about the other 6 (RZ, RT, TZ, etc.) possible component combinations? Expanding the study to cover an actual eruptive period at Ruapehu in 2006, for which the previous noise study by Mordret et al. [2010] had tentatively (as it was only seen on select station pairs) identified co-eruptive velocity variations, found that component pairs were similarly inconsistent during this period, and that the method itself could not resolve the same velocity variations as found by Mordret et al. [2010]. As the vast majority of ambient noise studies looking at velocity variations use the ZZ component solely, there is an opportunity to study results from the entire component pair matrix in an effort to improve the reliability of ambient noise results. Provided we can expect to see similar results across component pairs in the case of true, homogeneous velocity variations, a simple stack of results would

help increase the measurement signal-to-noise ratio. A true recreation of the Mordret et al. [2010] using the 'stretching' method (described in chapter 4), whilst looking at all component pairs, may be a good starting point to reassess the method given the fact that previous studies have deemed it more stable than the MWCS technique (e.g. Duputel et al. 2009).

2. While the research in chapter 4 was being written up, a study by Brenguier et al. [2014] was published that uses the MWCS technique to resolve regional scale velocity variations of $< 0.12\%$ in Japan following the 2011 Tohoku-Oki earthquake. The method they use is novel in the sense that they eschew the use of a reference cross correlation function in favour of a process in which they use a Bayesian least-squares inversion [Tarantola, 2005] to produce a model of velocity change given an input dataset containing measured velocity changes for every day (and station) pair in the study period. Therefore, the solution is based on the differences of all elemental CCFs (in this case, day long CCFs) rather than the difference between an elemental CCF and a reference CCF chosen from some arbitrary set. Given that this method was applied by Brenguier et al. [2014] in order to improve the reliability and objectivity of the MWCS technique, something that the study of ambient noise in this thesis suffered from, a similar study at Ruapehu in the future may look to employ such an inversion approach. The major drawback of this method is that it is more computationally intensive than simply using a reference CCF for determining velocity changes.

   There is also an opportunity to incorporate the inversion technique into a monitoring tool for volcanoes, in which CCFs are added to the data vector and inverted daily. Again, the computational needs of such a method will be significantly higher than MSNoise method of using a predetermined reference CCF. However, it may potentially be able to detect ongoing velocity variations in a reliable manner.

3. The active source experiment performed in chapter 4 gives results that suggest that velocities in the Ruapehu region may be susceptibility to the solid Earth tide. This was found over five explosions encompassing approximately 19 hours. Unfortunately, the fact that the duration of the study period does not last for longer than one tidal period means that it is difficult to ascertain whether the velocity trend is due to the solid Earth tide, some broader process, or just noise. Designing an experiment to investigate how solid Earth tides manifest in seismic velocity variations on a regional scale like this would need to occur over two or more tidal periods, as a cyclical variation in velocity conforming with tidal strain would be good evidence that the detected variations are indeed caused by tides. As we have shown, this may provide empirical evidence for the relationship between pressure and velocity changes, which in turn may be useful for future studies relating to velocity variations in the study area.

5.6 Summary

This thesis has explored a number of different ways to image and monitor earth processes using seismic data. In this chapter, we consider a number of questions and future avenues of research that arise from the work in this thesis. There is great potential in both seismic anisotropy and ambient noise methods to contribute to volcanic monitoring, however it seems clear from the conclusions here that further groundwork in necessary to establish them. Each method has one aspect in particular that we believe is of immediate interest to those wishing to employ these approaches. Seismic anisotropy, and especially shear wave splitting in the crust, still suffers from a lack of certainty with respect to both the measurements themselves and what is contributing to the anisotropy measured. Results in Chapter 3 indicate that anisotropy in Canterbury is concentrated in the upper 3-5 or so kilometres of crust, but the question of how that anisotropy is distributed within that layer still remains. There are also other considerations to make, such as topography and near surface scattering, which are especially important when considering volcanic regions. In terms of ambient noise monitoring, developing methods to increase the stability of interferometry techniques is essential to ensure that those methods can be used reliably, and must be considered a priority in future work.

Appendix A

Constructing the C_{ijkl} matrix from Love Parameters A, C, F, L and N

The parameters A, C, F, L and N, as described in the main body of text above, define an anisotropic elastic tensor with hexagonal symmetry. For the case of a symmetry axis aligned with the vertical, they can be written in 6×6 matrix notation as such [e.g. Babuška and Cara 1991]:

$$C_{ij} = \begin{bmatrix} A & A-2N & F & 0 & 0 & 0 \\ A-2N & A & F & 0 & 0 & 0 \\ F & F & C & 0 & 0 & 0 \\ 0 & 0 & 0 & L & 0 & 0 \\ 0 & 0 & 0 & 0 & L & 0 \\ 0 & 0 & 0 & 0 & 0 & N \end{bmatrix} \tag{A.0.1}$$

The C_{ij} matrix represents the independent coefficients of the forth-rank C_{ijkl} tensor and the two can be freely exchanged using the relationships outlined in Chapter 1.

Appendix B

Average Starting Model

Shown below are the α and θ parameters that constitute the average starting model for the Darfield data. All event-station pairs outside a 60° straight-line incidence angle were removed before the model was created.

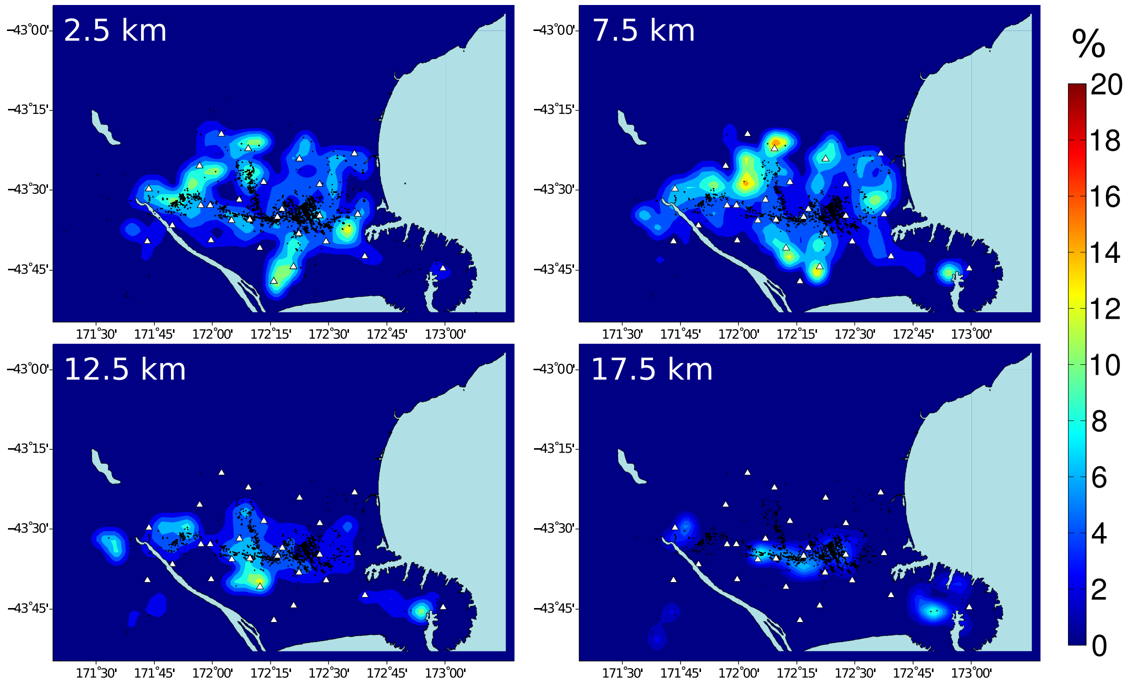

Figure B.1: Plot of α values for the average starting model, before any inversion has been undertaken.

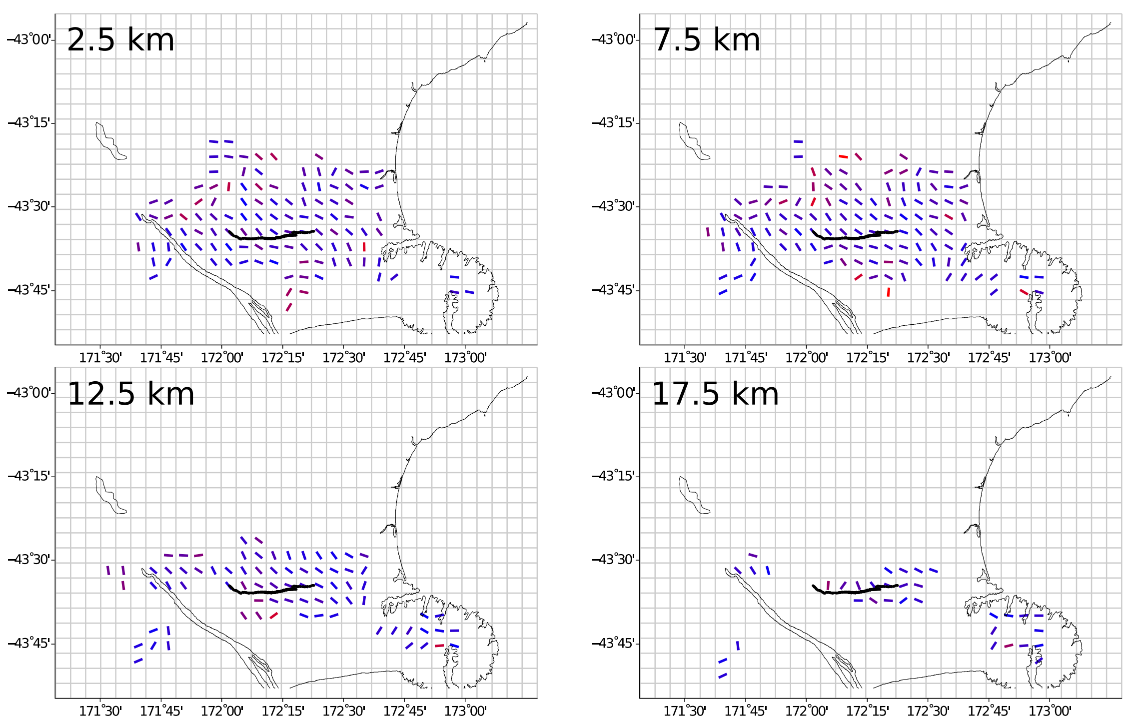

Figure B.2: Plot of θ values for the average starting model, before any inversion has been undertaken. All other angular parameters are set to zero in the formulation of the starting model.

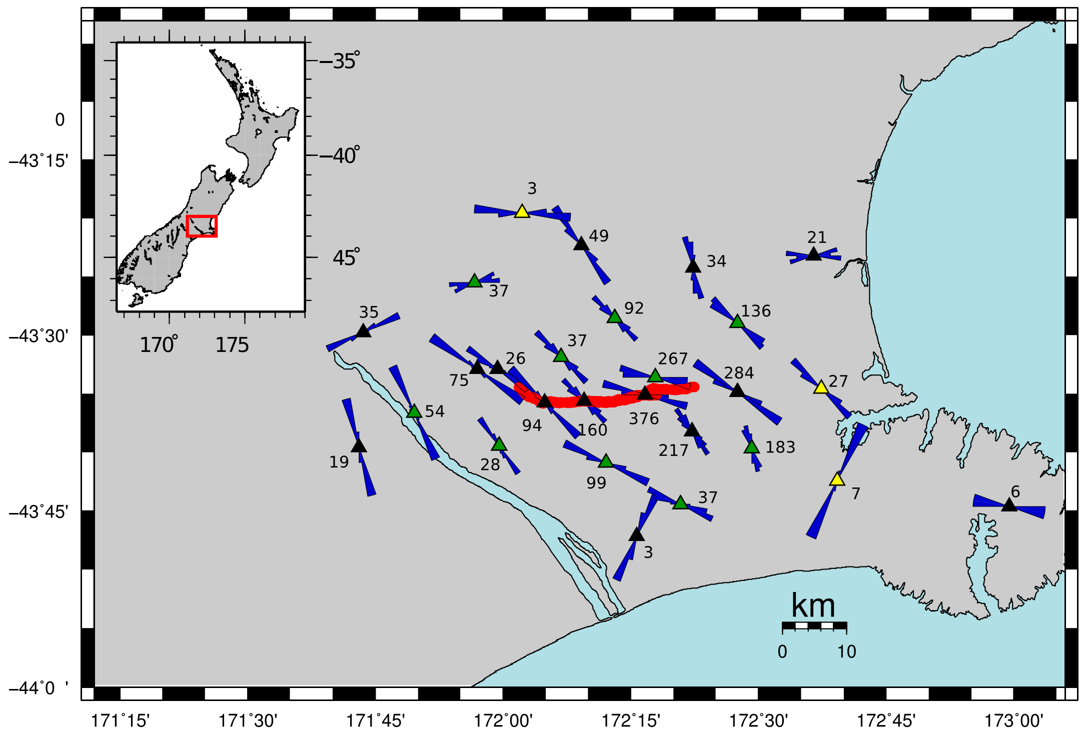

Figure B.3: Circular histograms of synthetic fast direction measurements taken using the inital starting model. As in figure 3.1, black triangles represent temporary broadband stations, yellow represent GeoNet permanent stations and green represent GeoNet temporary short period stations. Numbers indicate the number of measurements at each station. The size of the circular histograms in A and B are scaled individually for display purposes.

Appendix C

Gaussian data smoothing

Gaussian data smoothing is a 2-D convolution operator applied to the window delay times recovered using both the time domain and MWCS techniques in order to evaluate the time window of coherent energy over which delays are chosen for each station. Once each window analysed in a dataset is binned according to the calculated delay time associated with it, the smoothed value of a bin at position (x, y) is calculated using the following operator for all data point i:

$$G(x, y) = \frac{1}{2\pi N\sigma^2} . \sum_i e^{-\frac{L_i}{2\sigma^2}} \tag{C.0.1}$$

With

$$L_i = \sqrt{(x^2 - x_i^2) + (y^2 - y_i^2)} \tag{C.0.2}$$

Where σ is the operator bandwidth and N is the number of data points. Once this is achieved the maximum value of G is located and a new data vector D is calculated like so

$$D(y) = \sum_X G(X, y), \text{ for } X = (x_{max} - dx) \leq x \leq (x_{max} + dx) \tag{C.0.3}$$

Where x_{max} is the x location of the maximum G value and dx defines the horizontal swathe across which values of G, which is a 2-D array, will be summed across the x dimension. The vector D can now be used to find the time window where the collapsed data density reaches a certain threshold. In this study a value of $dx = 4$ ms was used and the threshold was taken to be 20% of the maximum data density.

Using the smoothed function G allows for a more robust estimation of where two signals are coherent using both interferometry techniques, however it can only be used when the two signals being compared are assumed to have a good degree of similarity. As an adaptive technique it is useful because each station will have first arrivals at a time dependent on their distance from the source and a coda wave train with a length dependent on many other factors regarding the seismic scatters between the source and receiver.

Appendix D

Determining correlation coefficients for Cross-Correlation Functions

The calculation of the correlation coefficient between two cross-correlation functions is a useful measure of similarity between the two series. In noise analyses, knowing the similarity between the CCFs serves to bring attention to periods that may show decorrelation due to effects pertinent to the analysis (i.e. the source of noise has changed). Correlation values can be computed using the single correlation value defined as Pearson's r [Buda and Jarynowski, 2010], defined between signals x and y over each sample, n, as:

$$r = \frac{\sum_{n}(x_n - \bar{x})(y_n - \bar{y})}{\sqrt{\sum_{n}(x_n - \bar{x})^2}\sqrt{\sum_{n}(y_n - \bar{y})^2}} \tag{D.0.1}$$

Here, n, the number of samples in the CCFs, is a property that is defined by the input data. However, when it comes to calculating velocity variations only part of the CCF coda is used (i.e. in this study it is generally between 10 to 30 s and the negative equivalent), meaning that signal outside these brackets does not factor into the final analysis. Therefore, when calculating correlation coefficients, it may be more convenient to consider only the signal within the analysis brackets rather than the entire signal. In this study, correlation coefficients are generally used to determine the relationship between the decorrelation of the reference and current CCF and the velocity variations derived from them, so correlation coefficients are calculated using only the signal coda of interest in the velocity variation calculation (unless otherwise stated). However, it may be the case that one wants to investigate (in a general sense) the introduction of transient signals that are affecting the CCFs, in which case it may be more convenient to find the correlation of the two CCFs in their entirety.

Appendix E

Using the SWS anisotropy inversion code

The inversion code used to produce the results in Chapter 3 is written and executed in MATLAB. The directory structure, including the required scripts, is shown in figure E.1.

Main Directory

The main directory contains the velocity models and the configuration file. The velocity model files have a .vel extension. This can be formatted any way, but changes must be made to the script *make_modelVsD.m* (in Command_Files) in order to handle custom formats. Currently, the script is designed to deal with the formats in *ak135.vel* (global 1D velocity model) and *eberhart-phillips.NZ.vel* [Eberhart-Phillips et al., 2010] (New Zealand-wide 3D velocity model). The *ak135.vel* format has the columns;

Depth (km), density (Mg/km^3), V_p (km/s), V_s (km/s)

The *eberhart-phillips.NZ.vel* format has the columns;

V_p (km/s), V_p/V_s (km/s), V_s (km/s), density (Mg/km^3), (σV_p (km/s)), ($\sigma V_p/V_s$ (km/s)), (x (km)), (y (km)), Depth (km), Latitude, Longitude, (Northing (NZMG)), (East-

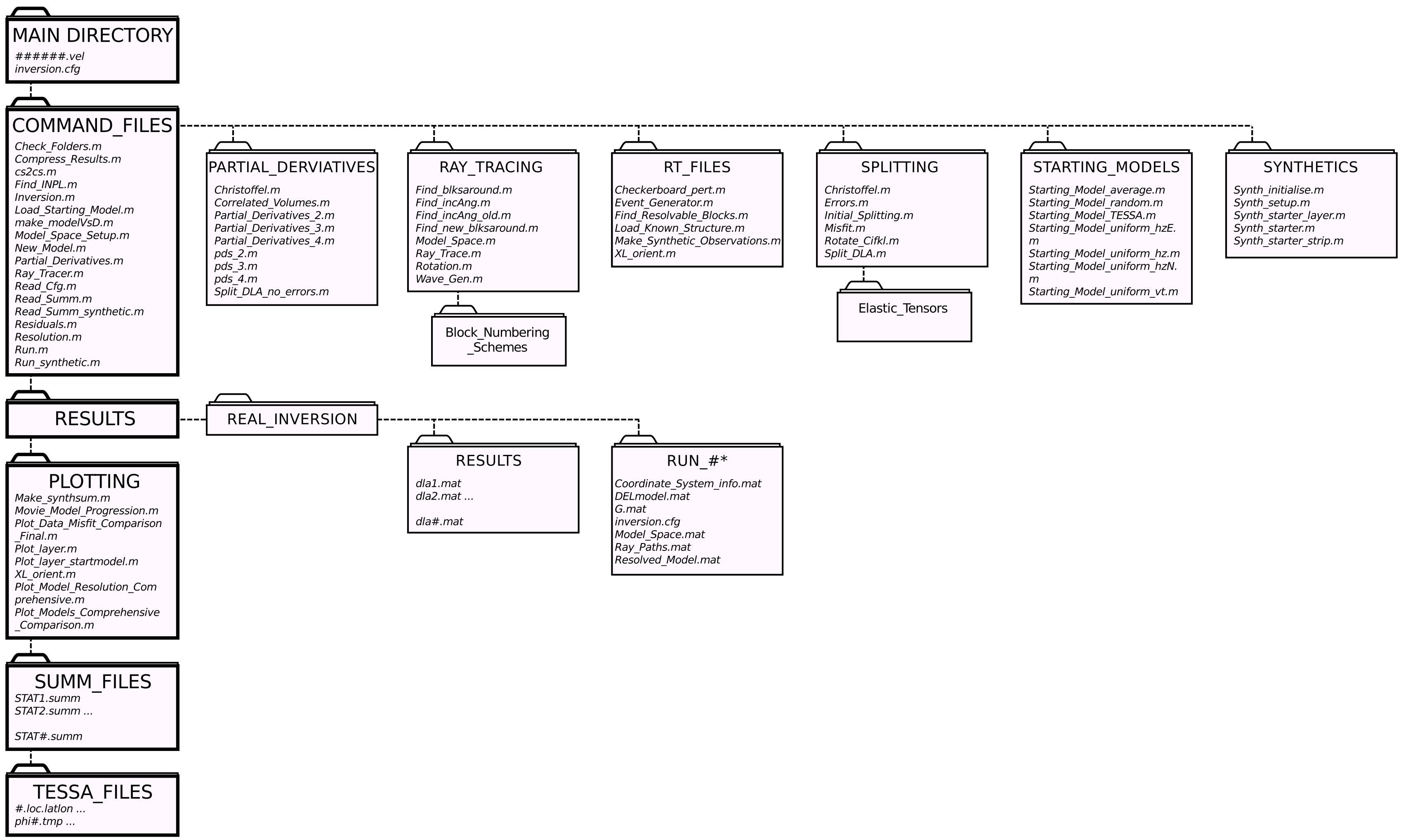

Figure E.1: Anisotropy inversion code directory structures. Files with a # denotes its index number (individual file designation in the case of the velocity .vel file). * = a Run_# directory is created for each attempted model run.

ing (NZMG))

where bracketed entries are unused. The configuration file, *inversion.cfg*, contains input parameters that define how the model will run. They are as follows:

Coordsystem. Defines how the model produces the reference coordinate system. It can be set to *auto* to produce a coordinate system with the centre point of the earthquake epicentre distribution as a reference point, or can be given as 'LON, LAT' to produce a coordinate system with those particular coordinates as a reference point.

Resolution. Defines the side length of each model block, and is given in kilometres.

Max Depth. Defines the maximum model depth. To select the lowest data point, set it to *auto*. Sometimes you may want to define a higher depth to exclude parts of the model that will not be well defined, to increase processing speed. To do this, enter the desired maximum model depth in kilometres.

Number of iterations. Defines the number of iterations taken by the model.

Real events. Currently unimplemented. Leave at 'yes'.

Velocity Model. Set this to the name of the .vel velocity model file you wish to use.

Whiten. Set to 'yes' or 'no' depending on whether or not you want to add 10% noise to the synthetic *S*-wave.

Frequency. Set to the frequency of the synthetic *S*-wave in Hz. If set to 'data', the frequency will be set as the average of the best frequency windows for each measurement as given in the .summ file.

Starting Model. Set to 'average', 'random', 'uniform', or 'tadar'. Determines which starting model the inversion uses.

Elastic module. Set to the name of the file (without the .m extension) that creates the elastic tensor. The elastic tensor can be defined using any relationship. Scripts that produce the elastic tensor are found in in Command_Files/Splitting/Elastic_Tensors/.

Model parameters. Set to the number of parameters you would like to solve for. Can be 2 for α and θ, 3 to add ψ and 4 to add γ. Your choice depends on your assumptions and the symmetry of your elastic tensor.

Smoothing. Smoothing as described in Chapter 3 of this thesis. Currently, smoothing vastly reduces model resolution, so try with the default 'no' to begin with.

Iteration for correlation. Currently not implemented. Intended for volume parameter correlation.

Synthetic variance matrix. Currently not implemented. Intended for use with synthetic input parameters.

Damping value (initial). Defines the factor of damping for the iterations up to the 'Damping iteration threshold'.

Damping value (subsequent). Defines the factor of damping for the iterations after the 'Damping iteration threshold'.

Damping iteration threshold. The iteration number at which the model switches from the 'initial' damping value to the 'subsequent' damping value.

Data variance. Currently not implemented. Controls variance in correlated volumes.

Conic angle. Defines the straight-line incidence angle that earthquakes must lie within to be counted in the inversion.

max anisotropy. Defines the maximum possible anisotropy value in percent.

Command Files

The Command_Files directory contains all the scripts that govern the inversion process. There are two 'master' scripts that manage all the other scripts, *Run.m* and *Run_synthetic.m*. *Run_synthetic.m* does a synthetic run with a known input model, which is defined in-script under the 'CREATE MODEL' heading. Currently there is a strip model (defined in *Synthetics/Synth_starter_strip.m*) and a layer model (defined in *Synthetics/Synth_starter_layer.m*). Otherwise, *Run_synthetic.m* is used in the same way as *Run.m*.

Executing *Run.m*, the user is prompted to provide a run index number and instruct the program to run in parallel or serial. If the run index number has already been used, the user will have the option of re-starting a run from the last completed iteration for that run index number. IF NO ITERATION WAS COMPLETED THEN THIS WILL NOT WORK. The script will then attempt to complete an inversion using the settings currently defined in *inversion.cfg*, contained within Command_Files.

Possible Bugs: The velocity and density model used in the program may become buggy depending on the input velocity model and the block resolution. The function *make_modelVsD.m*, found in Command_Files, outputs a matrix ('*VDM*') containing all the velocity and density information. It has four columns; columns 1, 2 and 4 contain the V_p, V_s and density information, respectively. Column 3 should have just two non-zero elements; block size in the first row and number of layers in the third row. If there are problems with the ray tracing or infinite value errors in the inversion, please check this matrix.

Results

The Results directory contains information on completed and partially completed model runs. For any model run, a directory is created containing a number of MATLAB files and a copy of the *inversion.cfg* file used to create that particular run. *Coordinate_System_info.mat* contains information on what latitude and longitudes were used to create the reference coordinate system of the model. Other MATLAB files are used to store variables during the inversion run. Final state variables that summarise the model results are found in Results/Real_Inversion/Results/ in the file dla#.mat (where # is the run index number).

Plotting

The plotting directory contains various scripts that facilitate the plotting of inversion results. *Plot_layer.m* and *Plot_layer_startmodel.m* are used to plot model α, θ, resolution, and θ distribution for a particular depth layer. The script, *Make_synthsum.m*, outputs model results as .summ files (the MFAST output format). This is useful if you wish to plot the synthetic results the same way you plot the input .summ files. All other scripts in the Plotting directory are not maintained and may not work properly.

Summ Files

The Summ_Files directory should contain all the .summ files that you wish the inversion to use as input data. These files can be placed in this directory straight away after being output by MFAST.

TESSA Files

The TESSA_Files directory is where TESSA files, if used for the TESSA starting model, should be placed. There are two types of TESSA files; #.tmp.latlon files that contain information about the strength of anisotropy and phi#.tmp files that contain information about the orientation of anisotropy.

Bibliography

Aagaard, B., S. Kientz, M. Knepley, L. Strand, and C. Williams (2007), Pylith User Manual Version 1.0, *www.geodynamics.org*.

Aagaard, B., M. Knepley, and C. Williams (2013), A domain decomposition approach to implementing fault slip in finite-element models of quasi-static and dynamic crustal deformation, *Journal of Geophysical Research: Solid Earth*.

Abt, D. L., and K. M. Fischer (2008), Resolving three-dimensional anisotropic structure with shear wave splitting tomography, *Geophysical Journal International*, *173*(3), 859–886.

Agnew, D. C. (2012), SPOTL: Some programs for ocean-tide loading.

Aizawa, K., Y. Ogawa, T. Hashimoto, T. Koyama, W. Kanda, Y. Yamaya, M. Mishina, and T. Kagiyama (2008), Shallow resistivity structure of Asama Volcano and its implications for magma ascent process in the 2004 eruption, *Journal of Volcanology and Geothermal Research*, *173*(3), 165–177.

Aki, K., and B. Chouet (1975), Origin of coda waves: source, attenuation, and scattering effects, *Journal of geophysical research*, *80*(23), 3322–3342.

Aki, K., and V. Ferrazzini (2000), Seismic monitoring and modeling of an active volcano for prediction, *Journal of Geophysical Research: Solid Earth (1978–2012)*, *105*(B7), 16,617–16,640.

Anderson, D. L. (1989), Theory of the Earth.

Anderson, E. (1951), The dynamics of faulting, 206, *Oliver and Boyd, Edinburgh*.

Angerer, E., S. Crampin, X.-Y. Li, and T. L. Davis (2002), Processing, modelling and predicting time-lapse effects of overpressured fluid-injection in a fractured reservoir, *Geophysical Journal International*, *149*(2), 267–280.

Angus, D. A., J. P. Verdon, Q. J. Fisher, and J.-M. Kendall (2009), Exploring trends in microcrack properties of sedimentary rocks: An audit of dry-core velocity-stress measurements, *Geophysics*, *74*(5), E193–E203.

Angus, D. A., Q. J. Fisher, and J. P. Verdon (2012), Exploring Trends in Microcrack Properties of Sedimentary Rocks: An Audit of Dry and Water Saturated Sandstone Core Velocity–Stress Measurements, *International Journal of Geosciences*, *3*, 822–833.

Aoki, Y., et al. (2009), P-wave velocity structure beneath Asama Volcano, Japan, inferred from active source seismic experiment, *Journal of Volcanology and Geothermal Research*, *187*(3), 272–277.

Aoki, Y., M. Takeo, T. Ohminato, Y. Nagaoka, and K. Nishida (2013), Magma pathway and its structural controls of Asama Volcano, Japan, *Geological Society, London, Special Publications*, *380*(1), 67–84.

Aster, R. C., P. M. Shearer, and J. Berger (1990), Quantitative measurements of shear wave polarizations at the Anza seismic network, southern California: Implications for shear wave splitting and earthquake prediction, *Journal of Geophysical Research: Solid Earth (1978–2012)*, *95*(B8), 12,449–12,473.

Aster, R. C., B. Borchers, and C. H. Thurber (2013), *Parameter estimation and inverse problems*, Academic Press.

Audoine, E., M. K. Savage, and K. Gledhill (2004), Anisotropic structure under a back arc spreading region, the Taupo Volcanic Zone, New Zealand, *Journal of Geophysical Research: Solid Earth (1978–2012)*, *109*(B11).

Babuska, V., and M. Cara (1991), *Seismic anisotropy in the Earth*, vol. 10, Springer.

Babuška, V., and M. Cara (1991), *Seismic anisotropy in the Earth*, vol. 10, Springer.

Balfour, N., M. Savage, and J. Townend (2005), Stress and crustal anisotropy in Marlborough, New Zealand: evidence for low fault strength and structure-controlled anisotropy, *Geophysical Journal International*, *163*(3), 1073–1086.

Bannister, S., and K. Gledhill (2012), Evolution of the 2010–2012 Canterbury earthquake sequence, *New Zealand Journal of Geology and Geophysics*, *55*(3), 295–304.

Beavan, J., and J. Haines (2001), Contemporary horizontal velocity and strain rate fields of the Pacific-Australian plate boundary zone through New Zealand, *Journal of Geophysical Research: Solid Earth (1978–2012)*, *106*(B1), 741–770.

Beavan, J., L. Wallace, S. Samsonov, S. Ellis, M. Motagh, and N. Palmer (2010), The Darfield (Canterbury) earthquake: geodetic observations and preliminary source model, *Bulletin of the New Zealand Society for Earthquake Engineering*, *43*(4), 228.

Becker, T. W., B. Kustowski, and G. Ekström (2008), Radial seismic anisotropy as a constraint for upper mantle rheology, *Earth and Planetary Science Letters*, *267*(1), 213–227.

Bensen, G., M. Ritzwoller, and Y. Yang (2009), A 3-D shear velocity model of the crust and uppermost mantle beneath the United States from ambient seismic noise, *Geophysical Journal International*, *177*(3), 1177–1196.

Bianco, F., M. Castellano, G. Milano, G. Ventura, and G. Vilardo (1998), The Somma–Vesuvius stress field induced by regional tectonics: evidences from seismological and mesostructural data, *Journal of volcanology and geothermal research*, *82*(1), 199–218.

Bibby, H., T. Caldwell, F. Davey, and T. Webb (1995), Geophysical evidence on the structure of the Taupo Volcanic Zone and its hydrothermal circulation, *Journal of Volcanology and Geothermal Research*, *68*(1–3), 29 – 58, doi:http://dx.doi.org/10.1016/0377-0273(95)00007-H, taupo Volcanic Zone, New Zealand.

Biot, M. A. (1955), Theory of elasticity and consolidation for a porous anisotropic solid, *Journal of Applied Physics*, *26*(2), 182–185.

Biot, M. A. (1956), Theory of propagation of elastic waves in a fluid-saturated porous solid. I. Low-frequency range, *The Journal of the Acoustical Society of America*, *28*(2), 168–178.

Birch, F. (1960), The velocity of compressional waves in rocks to 10 kilobars: 1., *Journal of Geophysical Research*, *65*(4), 1083–1102.

Boness, N. L., and M. D. Zoback (2006), A multiscale study of the mechanisms controlling shear velocity anisotropy in the San Andreas Fault Observatory at Depth, *Geophysics*, *71*(5), F131–F146.

Bonnefoy-Claudet, S., F. Cotton, and P.-Y. Bard (2006), The nature of noise wavefield and its applications for site effects studies: a literature review, *Earth-Science Reviews*, *79*(3), 205–227.

Bonnefoy-Claudet, S., A. Köhler, C. Cornou, M. Wathelet, and P.-Y. Bard (2008), Effects of Love waves on microtremor H/V ratio, *Bulletin of the Seismological Society of America*, *98*(1), 288–300.

Booth, D. C., and S. Crampin (1985), Shear-wave polarizations on a curved wavefront at an isotropic free surface, *Geophysical Journal International*, *83*(1), 31–45.

Brenguier, F., N. M. Shapiro, M. Campillo, V. Ferrazzini, Z. Duputel, O. Coutant, and

A. Nercessian (2008), Towards forecasting volcanic eruptions using seismic noise, *Nature Geoscience*, *1*(2), 126–130.

Brenguier, F., D. Clarke, Y. Aoki, N. M. Shapiro, M. Campillo, and V. Ferrazzini (2011), Monitoring volcanoes using seismic noise correlations, *Comptes Rendus Geoscience*, *343*(8–9), 633 – 638.

Brenguier, F., M. Campillo, T. Takeda, Y. Aoki, N. Shapiro, X. Briand, K. Emoto, and H. Miyake (2014), Mapping pressurized volcanic fluids from induced crustal seismic velocity drops, *Science*, *345*(6192), 80–82.

Buda, A., and A. Jarynowski (2010), *Life Time of Correlations and its Applications*, Andrzej Buda Wydawnictwo NiezaleĹĽne.

Campillo, M. (2006), Phase and Correlation in Random Seismic Fields and the Reconstruction of the Green Function, *Pure and Applied Geophysics*, *163*(2-3), 475–502.

Chapman, M., S. V. Zatsepin, and S. Crampin (2002), Derivation of a microstructural poroelastic model, *Geophysical Journal International*, *151*(2), 427–451.

Chouet, B. (1979), Temporal variation in the attenuation of earthquake coda near Stone Canyon, California, *Geophysical Research Letters*, *6*(3), 143–146.

Chouet, B. A., R. A. Page, C. D. Stephens, J. C. Lahr, and J. A. Power (1994), Precursory swarms of long-period events at Redoubt Volcano (1989–1990), Alaska: Their origin and use as a forecasting tool, *Journal of Volcanology and Geothermal Research*, *62*(1), 95–135.

Christensen, N., and R. Crosson (1968), Seismic anisotropy in the upper mantle, *Tectonophysics*, *6*(2), 93–107.

Christensen, N. I. (1996), Poisson's ratio and crustal seismology, *Journal of Geophysical Research: Solid Earth (1978–2012)*, *101*(B2), 3139–3156.

Clarke, D., L. Zaccarelli, N. Shapiro, and F. Brenguier (2011), Assessment of resolution and accuracy of the Moving Window Cross Spectral technique for monitoring crustal temporal variations using ambient seismic noise, *Geophysical Journal International*, *186*(2), 867–882.

Clarke, D., F. Brenguier, J.-L. Froger, N. M. Shapiro, A. Peltier, and T. Staudacher (2013), Timing of a large volcanic flank movement at Piton de la Fournaise Volcano using noise-based seismic monitoring and ground deformation measurements, *Geophysical Journal International*, doi:10.1093/gji/ggt276.

Collet, O., and B. Gurevich (2013), Fluid dependence of anisotropy parameters in weakly anisotropic porous media, *Geophysics*, *78*(5), WC137–WC145.

Cox, S., H. Rutter, A. Sims, M. Manga, J. Weir, T. Ezzy, P. White, T. Horton, and D. Scott (2012), Hydrological effects of the Mw 7.1 Darfield (Canterbury) earthquake, 4 September 2010, New Zealand, *New Zealand Journal of Geology and Geophysics*, *55*(3), 231–247.

Crampin, S. (1985), Evaluation of anisotropy by shear-wave splitting, *Geophysics*, *50*(1), 142–152.

Crampin, S. (1987), Geological and industrial implications of extensive-dilatancy anisotropy, *Nature*, *328*, 491–496.

Crampin, S. (1994), The fracture criticality of crustal rocks, *Geophysical Journal International*, *118*(2), 428–438.

Crampin, S., and J. H. Lovell (1991), A decade of shear-wave splitting in the Earth's crust: what does it mean? what use can we make of it? and what should we do next?, *Geophysical Journal International*, *107*(3), 387–407.

Crampin, S., and S. Peacock (2008), A review of the current understanding of seismic shear-wave splitting in the Earth's crust and common fallacies in interpretation, *Wave Motion*, *45*(6), 675–722.

Crampin, S., Y. Gao, and S. Peacock (2008), Stress-forecasting (not predicting) earthquakes: A paradigm shift?, *Geology*, *36*(5), 427–430.

Crotwell, H. P., T. J. Owens, and J. Ritsema (1999), The taup toolkit: Flexible seismic travel-time and ray-path utilities, *Seismological Research Letters*, *70*(2), 154–160.

Dahlen, F. (1972), Elastic velocity anisotropy in the presence of an anisotropic initial stress, *Bulletin of the Seismological Society of America*, *62*(5), 1183–1193.

Davy, B., K. Hoernle, and R. Werner (2008), Hikurangi Plateau: Crustal structure, rifted formation, and Gondwana subduction history, *Geochemistry, Geophysics, Geosystems*, *9*(7).

Davy, B., V. Stagpoole, D. Barker, and J. Yu (2012), Subsurface structure of the Canterbury region interpreted from gravity and aeromagnetic data, *New Zealand Journal of Geology and Geophysics*, *55*(3), 185–191.

De Fazio, T. L., K. Aki, and J. Alba (1973), Solid earth tide and observed change in the in situ seismic velocity, *Journal of Geophysical Research*, *78*(8), 1319–1322.

Debayle, E., , and B. Kennett (2000), The Australian continental upper mantle: structure and deformation inferred from surface waves, *Journal of Geophysical Research: Solid Earth (1978–2012)*, *105*(B11), 25,423–25,450.

Del Negro, C., G. Currenti, and D. Scandura (2009), Temperature-dependent viscoelastic modeling of ground deformation: Application to Etna volcano during the 1993–1997 inflation period, *Physics of the Earth and Planetary Interiors*, *172*(3), 299–309.

Dorn, C., et al. (2010), High-resolution seismic images of potentially seismogenic structures beneath the northwest Canterbury Plains, New Zealand, *Journal of Geophysical Research: Solid Earth (1978–2012)*, *115*(B11).

Du, W.-X., C. H. Thurber, and D. Eberhart-Phillips (2004), Earthquake Relocation using Cross-Correlation Time Delay Estimates Verified with the Bispectrum Method, *Bulletin of the Seismological Society of America*, *94*(3), 856–866, doi:10.1785/0120030084.

Duffy, B., M. Quigley, D. J. Barrell, R. Van Dissen, T. Stahl, S. Leprince, C. McInnes, and E. Bilderback (2013), Fault kinematics and surface deformation across a releasing bend during the 2010 Mw 7.1 Darfield, New Zealand, earthquake revealed by differential LiDAR and cadastral surveying, *Geological Society of America Bulletin*, *125*(3-4), 420–431.

Duputel, Z., V. Ferrazzini, F. Brenguier, N. Shapiro, M. Campillo, and A. Nercessian (2009), Real time monitoring of relative velocity changes using ambient seismic noise at the Piton de la Fournaise volcano (La Réunion) from January 2006 to June 2007, *Journal of Volcanology and Geothermal Research*, *184*(1), 164–173.

Dvorkin, J., G. Mavko, and A. Nur (1995), Squirt flow in fully saturated rocks, *Geophysics*, *60*(1), 97–107.

Eberhart-Phillips, D., M. Reyners, S. Bannister, M. Chadwick, and S. Ellis (2010), Establishing a versatile 3-D seismic velocity model for New Zealand, *Seismological Research Letters*, *81*(6), 992–1000.

Ekström, G., and A. M. Dziewonski (1998), The unique anisotropy of the Pacific upper mantle, *Nature*, *394*(6689), 168–172.

Farra, V., L. P. Vinnik, B. Romanowicz, G. L. Kosarev, and R. Kind (1991), Inversion of teleseismic S particle motion for azimuthal anisotropy in the upper mantle: a feasibility study, *Geophysical Journal International*, *106*(2), 421–431, doi:10.1111/j.1365-246X.1991.tb03905.x.

Fielding, E. J., P. R. Lundgren, R. Bürgmann, and G. J. Funning (2009), Shallow fault-zone dilatancy recovery after the 2003 Bam earthquake in Iran, *Nature*, *458*(7234), 64–68.

Fischer, K. M., E. Parmentier, A. R. Stine, and E. R. Wolf (2000), Modeling anisotropy and plate-driven flow in the Tonga subduction zone back arc, *Journal of Geophysical Research: Solid Earth (1978–2012)*, *105*(B7), 16,181–16,191.

Forsyth, P. J., R. Jongens, and D. J. A. Barrell (2008), *Geology of the Christchurch area*, GNS Science Lower Hutt.

Fry, B., F. Deschamps, E. Kissling, L. Stehly, and D. Giardini (2010), Layered azimuthal anisotropy of Rayleigh wave phase velocities in the European Alpine lithosphere inferred from ambient noise, *Earth and Planetary Science Letters*, *297*(1), 95–102.

Fry, B., F. Davey, D. Eberhart-Phillips, and S. Lebedev (2014), Depth variable crustal anisotropy, patterns of crustal weakness, and destructive earthquakes in Canterbury, New Zealand, *Earth and Planetary Science Letters*, *392*, 50–57.

Gamble, J. A., R. C. Price, I. E. Smith, W. C. McIntosh, and N. W. Dunbar (2003), ^{40}Ar/^{39}Ar geochronology of magmatic activity, magma flux and hazards at Ruapehu Volcano, Taupo volcanic zone, New Zealand, *Journal of Volcanology and Geothermal Research*, *120*(3), 271–287.

Gao, Y., and S. Crampin (2004), Observations of stress relaxation before earthquakes, *Geophysical Journal International*, *157*(2), 578–582.

Gardine, M., and D. Roman (2010), Investigating the pre-and post-eruptive stress regime at redoubt volcano, Alaska, from 2008-1010 using seismic anisotropy and stress-tensor inversions, in *AGU Fall Meeting Abstracts*, vol. 1, p. 06.

Geller, R. J., and C. S. Mueller (1980), Four similar earthquakes in central California, *Geophysical Research Letters*, *7*(10), 821–824.

Gerst, A., and M. K. Savage (2004), Seismic anisotropy beneath Ruapehu volcano: A possible eruption forecasting tool, *Science*, *306*(5701), 1543–1547.

Gladczenko, T. P., M. F. Coffin, and O. Eldholm (1997), Crustal structure of the Ontong Java Plateau: modeling of new gravity and existing seismic data, *Journal of Geophysical Research: Solid Earth (1978–2012)*, *102*(B10), 22,711–22,729.

Gledhill, K., J. Ristau, M. Reyners, B. Fry, and C. Holden (2011), The darfield (Canterbury, New Zealand) Mw 7.1 earthquake of September 2010: A preliminary seismological report, *Seismological Research Letters*, *82*(3), 378–386.

Godfrey, N. J., N. I. Christensen, and D. A. Okaya (2000), Anisotropy of schists: Contribution of crustal anisotropy to active source seismic experiments and shear wave splitting observations, *Journal of Geophysical Research: Solid Earth (1978–2012)*, *105*(B12), 27,991–28,007.

Gray, S. H., J. Etgen, J. Dellinger, and D. Whitmore (2001), Seismic migration problems and solutions, *Geophysics*, *66*(5), 1622–1640.

Grechka, V., and M. Kachanov (2006), Effective elasticity of fractured rocks: A snapshot of the work in progress, *Geophysics*, *71*(6), W45–W58.

Grêt, A., R. Snieder, R. C. Aster, and P. R. Kyle (2005), Monitoring rapid temporal change in a volcano with coda wave interferometry, *Geophysical Research Letters*, *32*(6).

Gurevich, B., D. Makarynska, O. B. de Paula, and M. Pervukhina (2010), A simple model for squirt-flow dispersion and attenuation in fluid-saturated granular rocks, *Geophysics*, *75*(6), N109–N120.

Gurevich, B., M. Pervukhina, and D. Makarynska (2011), An analytic model for the stress-induced anisotropy of dry rocks, *Geophysics*, *76*(3), WA125–WA133.

Hadziioannou, C., E. Larose, O. Coutant, P. Roux, and M. Campillo (2009), Stability of monitoring weak changes in multiply scattering media with ambient noise correlation: Laboratory experiments, *The Journal of the Acoustical Society of America*, *125*(6), 3688–3695.

Hammond, J., J.-M. Kendall, D. Angus, and J. Wookey (2010), Interpreting spatial variations in anisotropy: insights into the Main Ethiopian Rift from SKS waveform modelling, *Geophysical Journal International*, *181*(3), 1701–1712.

Harrison, J. (1976), Cavity and topographic effects in tilt and strain measurement, *Journal of Geophysical Research*, *81*(2), 319–328.

Hess, H. (1964), Seismic anisotropy of the uppermost mantle under oceans.

Hillers, G., M. Campillo, and K.-F. Ma (2014), Seismic velocity variations at TCDP are controlled by MJO driven precipitation pattern and high fluid discharge properties, *Earth and Planetary Science Letters*, *391*, 121–127.

Holden, C., J. Beavan, B. Fry, M. Reyners, J. Ristau, R. Van Dissen, P. Villamor, and M. Quigley (2011), Preliminary source model of the Mw 7.1 Darfield earthquake from geological, geodetic and seismic data, in *9th Pacific conference on earthquake engineering*, pp. 1063–1092.

Holt, R. (2013), Seismic Anisotropy and Stress of the Canterbury Plains, Master's thesis, Victoria University of Wellington.

Holt, R., M. Savage, J. Townend, E. Syracuse, and C. Thurber (2013), Crustal stress and fault strength in the Canterbury Plains, New Zealand, *Earth and Planetary Science Letters*, *383*, 173–181.

Horne, S., and C. MacBeth (1994), Inversion for seismic anisotropy using genetic algorithms1, *Geophysical prospecting*, *42*(8), 953–974.

Hudson, J. (1981), Wave speeds and attenuation of elastic waves in material containing cracks, *Geophysical Journal of the Royal Astronomical Society*, *64*(1), 133–150.

Hurst, A., and P. McGinty (1999), Earthquake swarms to the west of Mt Ruapehu preceding its 1995 eruption, *Journal of Volcanology and Geothermal Research*, *90*(1), 19–28.

Hurst, A., and S. Sherburn (1993), Volcanic tremor at Ruapehu: characteristics and implications for the resonant source, *New Zealand journal of geology and geophysics*, *36*(4), 475–485.

Ji, S., and M. H. Salisbury (1993), Shear-wave velocities, anisotropy and splitting in high-grade mylonites, *Tectonophysics*, *221*(3), 453–473.

Ji, S., A. Li, Q. Wang, C. Long, H. Wang, D. Marcotte, and M. Salisbury (2013), Seismic velocities, anisotropy, and shear-wave splitting of antigorite serpentinites and tectonic implications for subduction zones, *Journal of Geophysical Research: Solid Earth*.

Johnson, J. H., and M. P. Poland (2013), Seismic detection of increased degassing before Kīlauea's 2008 summit explosion, *Nature communications*, *4*, 1668.

Johnson, J. H., S. Prejean, M. K. Savage, and J. Townend (2010), Anisotropy, repeating earthquakes, and seismicity associated with the 2008 eruption of Okmok volcano, Alaska, *Journal of Geophysical Research: Solid Earth (1978–2012)*, *115*(B9).

Johnson, J. H., M. K. Savage, and J. Townend (2011), Distinguishing between stress-induced and structural anisotropy at Mount Ruapehu volcano, New Zealand, *Journal of Geophysical Research: Solid Earth (1978–2012)*, *116*(B12).

Johnston, D. H., M. Toksöz, and A. Timur (1979), Attenuation of seismic waves in dry and saturated rocks: II. Mechanisms, *Geophysics*, *44*(4), 691–711.

Johnston, J. E., and N. I. Christensen (1995), Seismic anisotropy of shales, *Journal of Geophysical Research: Solid Earth (1978–2012)*, *100*(B4), 5991–6003.

Jolly, A., S. Sherburn, P. Jousset, and G. Kilgour (2010), Eruption source processes derived from seismic and acoustic observations of the 25 september 2007 Ruapehu eruption—North Island, New Zealand, *Journal of Volcanology and Geothermal Research*, *191*(1), 33–45.

Jónsson, S. (2009), Stress interaction between magma accumulation and trapdoor faulting on Sierra Negra volcano, Galápagos, *Tectonophysics*, *471*(1), 36–44.

Karato, S.-i., and P. Wu (1993), Rheology of the upper mantle: A synthesis, *Science*, *260*(5109), 771–778.

Kazama, T., and S. Okubo (2009), Hydrological modeling of groundwater disturbances to observed gravity: Theory and application to Asama Volcano, Central Japan, *Journal of Geophysical Research: Solid Earth (1978–2012)*, *114*(B8).

Kennett, B., and E. Engdahl (1991), Traveltimes for global earthquake location and phase identification, *Geophysical Journal International*, *105*(2), 429–465.

Kennett, B., E. Engdahl, and R. Buland (1995), Constraints on seismic velocities in the earth from traveltimes, *Geophysical Journal International*, *122*(1), 108–124.

Keys, H. J., and P. M. Green (2008), Ruapehu lahar New Zealand 18 March 2007: Lessons for hazard assessment and risk mitigation 1995–2007, *Journal of Disaster Research*, *3*(4), 284–296.

Larose, E., P. Roux, and M. Campillo (2007), Reconstruction of Rayleigh–Lamb dispersion spectrum based on noise obtained from an air-jet forcing, *The Journal of the Acoustical Society of America*, *122*(6), 3437–3444.

Lay, T., and T. C. Wallace (1995), *Modern global seismology*, vol. 58, Academic press.

Lecocq, T., C. Caudron, and F. Brenguier (2014), MSNoise, a Python Package for Monitoring Seismic Velocity Changes Using Ambient Seismic Noise, *Seismological Research Letters*, *85*(3), 715–726.

Lecointre, J., K. Hodgson, V. Neall, and S. Cronin (2004), Lahar-triggering mechanisms and hazard at Ruapehu volcano, New Zealand, *Natural hazards*, *31*(1), 85–109.

Levin, V., and J. Park (1997), Crustal anisotropy in the Ural Mountains foredeep from teleseismic receiver functions, *Geophysical research letters*, *24*(11), 1283–1286.

Levine, J., and J. Harrison (1976), Earth tide strain measurements in the Poorman Mine near Boulder, Colorado, *Journal of Geophysical Research*, *81*(14), 2543–2555.

Lin, F.-C., M. H. Ritzwoller, Y. Yang, M. P. Moschetti, and M. J. Fouch (2011), Complex and variable crustal and uppermost mantle seismic anisotropy in the western United States, *Nature Geoscience*, *4*(1), 55–61.

Liu, Y., H. Zhang, C. Thurber, and S. Roecker (2008), Shear wave anisotropy in the crust around the San Andreas fault near Parkfield: spatial and temporal analysis, *Geophysical Journal International*, *172*(3), 957–970.

Lockner, D., J. Walsh, and J. Byerlee (1977), Changes in seismic velocity and attenuation during deformation of granite, *Journal of Geophysical Research*, *82*(33), 5374–5378.

Long, M. D., and T. W. Becker (2010), Mantle dynamics and seismic anisotropy, *Earth and Planetary Science Letters*, *297*(3), 341–354.

Love, A. E. H. (1927), *A treatise on the mathematical theory of elasticity*, Cambridge University Press.

Love, A. E. H. (2013), *A treatise on the mathematical theory of elasticity*, Cambridge University Press.

Marsden, J. E., and T. J. Hughes (1994), *Mathematical foundations of elasticity*, Courier Dover Publications.

McGinty, P., M. Reyners, and R. Robinson (2000), Stress directions in the shallow part of the Hikurangi subduction zone, New Zealand, from the inversion of earthquake first motions, *Geophysical Journal International*, *142*(2), 339–350.

McKenzie, D. P. (1969), The relation between fault plane solutions for earthquakes and the directions of the principal stresses, *Bulletin of the Seismological Society of America*, *59*(2), 591–601.

Melchior, P. (1983), The tides of the planet Earth, *Organic Photonics and Photovoltaics*, *1*.

Métivier, L., O. de Viron, C. P. Conrad, S. Renault, M. Diament, and G. Patau (2009), Evidence of earthquake triggering by the solid earth tides, *Earth and Planetary Science Letters*, *278*(3), 370–375.

Montagner, J.-P., and D. L. Anderson (1989), Petrological constraints on seismic anisotropy, *Physics of the earth and planetary interiors*, *54*(1), 82–105.

Montagner, J.-P., and H.-C. Nataf (1986), A simple method for inverting the azimuthal anisotropy of surface waves, *Journal of Geophysical Research: Solid Earth (1978–2012)*, *91*(B1), 511–520.

Moore, M., H. Anderson, and C. Pearson (2000), Seismic and geodetic constraints on plate boundary deformation across the northern Macquarie Ridge and southern South Island of New Zealand, *Geophysical Journal International*, *143*(3), 847–880.

Mordret, A., A. Jolly, Z. Duputel, and N. Fournier (2010), Monitoring of phreatic eruptions using Interferometry on Retrieved Cross-Correlation Function from Ambient Seismic Noise: Results from Mt. Ruapehu, New Zealand, *Journal of Volcanology and Geothermal Research*, *191*(1–2), 46 – 59, doi:http://dx.doi.org/10.1016/j.jvolgeores.2010.01.010.

Mortimer, N., F. Davey, A. Melhuish, J. Yu, and N. Godfrey (2002), Geological interpretation of a deep seismic reflection profile across the Eastern Province and Median Batholith, New Zealand: crustal architecture of an extended Phanerozoic convergent orogen, *New Zealand Journal of Geology and Geophysics*, *45*(3), 349–363.

Mueller, M. C. (1991), Prediction of lateral variability in fracture intensity using multi-component shear-wave surface seismic as a precursor to horizontal drilling in the Austin Chalk, *Geophysical Journal International*, *107*(3), 409–415.

Munson, C. G., C. H. Thurber, Y. Li, and P. G. Okubo (1995), Crustal shear wave anisotropy in southern Hawaii: spatial and temporal analysis, *Journal of geophysical research*, *100*(B10), 20,367–20.

Murase, M., et al. (2007), Time-dependent model for volume changes in pressure sources at Asama volcano, central Japan due to vertical deformations detected by precise leveling during 1902–2005, *Journal of volcanology and geothermal research*, *164*(1), 54–75.

Nagaoka, Y., K. Nishida, Y. Aoki, and M. Takeo (2010), Temporal change of phase velocity beneath Mt. Asama, Japan, inferred from coda wave interferometry, *Geophysical Research Letters*, *37*(22).

Nakagawa, M., K. Wada, T. Thordarson, C. Wood, and J. Gamble (1999), Petrologic investigations of the 1995 and 1996 eruptions of Ruapehu volcano, New Zealand: formation of discrete and small magma pockets and their intermittent discharge, *Bulletin of Volcanology*, *61*(1-2), 15–31.

Newman, A. V., T. H. Dixon, and N. Gourmelen (2006), A four-dimensional viscoelastic deformation model for Long Valley Caldera, California, between 1995 and 2000, *Journal of volcanology and geothermal research*, *150*(1), 244–269.

Nishimura, C. E., and D. W. Forsyth (1989), The anisotropic structure of the upper mantle in the pacific, *Geophysical Journal International*, *96*(2), 203–229.

Nistala, S., and G. A. McMechan (2005), 3D Modeling of fracture-induced shear-wave splitting in the Southern California basin, *Bulletin of the Seismological Society of America*, *95*(3), 1090–1100.

Norris, R. J., and A. F. Cooper (2001), Late Quaternary slip rates and slip partitioning on the Alpine Fault, New Zealand, *Journal of Structural Geology*, *23*(2), 507–520.

Nur, A., and G. Simmons (1969a), The effect of saturation on velocity in low porosity rocks, *Earth and Planetary Science Letters*, *7*(2), 183–193.

Nur, A., and G. Simmons (1969b), Stress-induced velocity anisotropy in rock: An experimental study, *Journal of Geophysical Research*, *74*(27), 6667–6674.

Nuttli, O. (1961), The effect of the Earth's surface on the S wave particle motion, *Bulletin of the Seismological Society of America*, *51*(2), 237–246.

Okaya, D., N. Christensen, D. Stanley, T. Stern, and S. I. G. Transect (1995), Crustal anisotropy in the vicinity of the Alpine fault zone, South Island, New Zealand, *New Zealand journal of geology and geophysics*, *38*(4), 579–583.

Özalaybey, S., and M. K. Savage (1994), Double-layer anisotropy resolved from S phases, *Geophysical Journal International*, *117*(3), 653–664.

Pandolfi, D., C. Bean, and G. Saccorotti (2006), Coda wave interferometric detection of seismic velocity changes associated with the 1999 M= 3.6 event at Mt. Vesuvius, *Geophysical research letters*, *33*(6).

Pearson, C. (1993), Rate of co-seismic strain release in the northern South Island, New Zealand, *New Zealand journal of geology and geophysics*, *36*(2), 161–166.

Pearson, C. (1994), Geodetic strain determinations from the Okarito and Godley-Tekapo regions, central South Island, New Zealand, *New Zealand journal of geology and geophysics*, *37*(3), 309–318.

Pearson, C., J. Beavan, D. Darby, G. Blick, and R. Walcott (1995), Strain distribution across the Australian-Pacific plate boundary in the central South Island, New Zealand, from 1992 gps and earlier terrestrial observations, *Journal of Geophysical Research: Solid Earth (1978–2012)*, *100*(B11), 22,071–22,081.

Petrini, K., and Y. Podladchikov (2000), Lithospheric pressure-depth relationship in compressive regions of thickned crust, *Journal of Metamorphic Geology*, *18*(1), 67–78.

Poupinet, G., W. Ellsworth, and J. Frechet (1984), Monitoring velocity variations in the crust using earthquake doublets: An application to the Calaveras Fault, California, *Journal of Geophysical Research: Solid Earth (1978–2012)*, *89*(B7), 5719–5731.

Price, R. C., R. George, J. A. Gamble, S. Turner, I. E. Smith, C. Cook, B. Hobden, and A. Dosseto (2007), U–Th–Ra fractionation during crustal-level andesite formation at Ruapehu volcano, New Zealand, *Chemical Geology*, *244*(3), 437–451.

Quigley, M., et al. (2010a), Surface rupture of the Greendale fault during the Darfield (Canterbury) earthquake, New Zealand: Initial findings, *Bulletin of the New Zealand Society for Earthquake Engineering*, *43*(4), 236–242, cited By (since 1996)31.

Quigley, M., et al. (2010b), Previously unknown fault shakes New Zealand's South Island, *EOS, Transactions American Geophysical Union*, *91*(49), 469–470.

Reilly, W. (1990), Horizontal crustal deformation on the Hikurangi Margin, *New Zealand journal of geology and geophysics*, *33*(2), 393–400.

Reyners, M., D. Eberhart-Phillips, and S. Martin (2014), Prolonged Canterbury earthquake sequence linked to widespread weakening of strong crust, *Nature Geoscience*, *7*(1), 34–37.

Rial, J. A., M. Elkibbi, and M. Yang (2005), Shear-wave splitting as a tool for the characterization of geothermal fractured reservoirs: lessons learned, *Geothermics*, *34*(3), 365–385.

Roman, D. C., and P. Heron (2007), Effect of regional tectonic setting on local fault response to episodes of volcanic activity, *Geophysical research letters*, *34*(13).

Roman, D. C., M. K. Savage, R. Arnold, J. L. Latchman, and S. De Angelis (2011), Analysis and forward modeling of seismic anisotropy during the ongoing eruption of the Soufrière Hills Volcano, Montserrat, 1996–2007, *Journal of Geophysical Research: Solid Earth (1978–2012)*, *116*(B3).

Rümpker, G., and T. Ryberg (2000), New "Fresnel-Zone" estimates for shear-wave splitting observations from finite-difference modeling, *Geophysical research letters*, *27*(13), 2005–2008.

Rümpker, G., and P. G. Silver (1998), Apparent shear-wave splitting parameters in the presence of vertically varying anisotropy, *Geophysical Journal International*, *135*(3), 790–800.

Sabra, K. G., P. Gerstoft, P. Roux, W. Kuperman, and M. C. Fehler (2005), Extracting time-domain Green's function estimates from ambient seismic noise, *Geophysical Research Letters*, *32*(3).

Sambridge, M. (1999), Geophysical inversion with a neighbourhood algorithm—I. Searching a parameter space, *Geophysical Journal International*, *138*(2), 479–494.

Santi, P. M., J. E. Holschen, and R. W. Stephenson (2000), Improving elastic modulus measurements for rock based on geology, *Environmental & Engineering Geoscience*, *6*(4), 333–346.

Savage, M. (1999), Seismic anisotropy and mantle deformation: what have we learned from shear wave splitting?, *Reviews of Geophysics*, *37*(1), 65–106.

Savage, M., W. Peppin, and U. Vetter (1990), Shear wave anisotropy and stress direction in and near Long Valley caldera, California, 1979–1988, *Journal of Geophysical Research: Solid Earth (1978–2012)*, *95*(B7), 11,165–11,177.

Savage, M., A. Wessel, N. Teanby, and A. Hurst (2010a), Automatic measurement of shear wave splitting and applications to time varying anisotropy at Mount Ruapehu volcano, New Zealand, *Journal of Geophysical Research: Solid Earth (1978–2012)*, *115*(B12).

Savage, M. K., M. Duclos, and K. Marson-Pidgeon (2007), Seismic anisotropy in south island, New Zealand, *A Continental Plate Boundary: Tectonics at South Island, New Zealand*, pp. 95–114.

Savage, M. K., T. Ohminato, Y. Aoki, H. Tsuji, and S. M. Greve (2010b), Stress magnitude and its temporal variation at Mt. Asama Volcano, Japan, from seismic anisotropy and gps, *Earth and Planetary Science Letters*, *290*(3), 403–414.

Savage, M. K., F.-C. Lin, and J. Townend (2013), Ambient noise cross-correlation observations of fundamental and higher-mode Rayleigh wave propagation governed by basement resonance, *Geophysical Research Letters*, *40*(14), 3556–3561.

Sayers, C., and M. Kachanov (1995), Microcrack-induced elastic wave anisotropy of brittle rocks, *Journal of Geophysical Research*, *100*(B3), 4149–4156.

Sayers, C. M., and D.-H. M. Han (2002), The effect of pore fluid on the stress-dependent elastic wave velocities in sandstones, in *2002 SEG Annual Meeting*.

Schlue, J., and L. Knopoff (1977), Shear-wave polarization anisotropy in the Pacific Basin, *Geophysical Journal International*, *49*(1), 145–165.

Schulte-Pelkum, V., and K. H. Mahan (2014), Imaging faults and shear zones using receiver functions, *Pure and Applied Geophysics*, pp. 1–25.

Sens-Schönfelder, C., and U. Wegler (2006), Passive image interferometry and seasonal variations of seismic velocities at Merapi Volcano, Indonesia, *Geophysical Research Letters*, *33*(21).

Sewell, R. (1988), Late Miocene volcanic stratigraphy of central Banks Peninsula, Canterbury, New Zealand, *New Zealand journal of geology and geophysics*, *31*(1), 41–64.

Shapiro, N. M., and M. Campillo (2004), Emergence of broadband Rayleigh waves from correlations of the ambient seismic noise, *Geophysical Research Letters*, *31*(L07614), doi:doi:10.1029/2004GL019491.

Shapiro, N. M., M. H. Ritzwoller, P. Molnar, and V. Levin (2004), Thinning and flow of Tibetan crust constrained by seismic anisotropy, *Science*, *305*(5681), 233–236.

Shearer, P. M. (2009), *Introduction to seismology*, Cambridge University Press.

Shelley, A., M. Savage, C. Williams, Y. Aoki, and B. Gurevich (2014), Modeling shear wave splitting due to stress-induced anisotropy, with an application to Mount Asama Volcano, Japan, *Journal of Geophysical Research: Solid Earth*.

Sibson, R., F. Ghisetti, and R. Crookbain (2012), Andersonian wrench faulting in a regional stress field during the 2010–2011 Canterbury, New Zealand, earthquake sequence, *Geological Society, London, Special Publications*, *367*(1), 7–18.

Silver, P. G., and W. W. Chan (1991), Shear wave splitting and subcontinental mantle deformation, *Journal of Geophysical Research: Solid Earth (1978–2012)*, *96*(B10), 16,429–16,454.

Silver, P. G., and M. K. Savage (1994), The interpretation of shear-wave splitting parameters in the presence of two anisotropic layers, *Geophysical Journal International*, *119*(3), 949–963.

Siratovich, P. A., M. J. Heap, M. C. Villenueve, J. W. Cole, and T. Reuschlé (2014), Physical property relationships of the Rotokawa Andesite, a significant geothermal reservoir rock in the Taupo Volcanic Zone, New Zealand, *Geothermal Energy*, *2*(1), 1–31.

Smith, M. L., and F. Dahlen (1973), The azimuthal dependence of love and rayleigh wave propagation in a slightly anisotropic medium, *Journal of Geophysical Research*, *78*(17), 3321–3333.

Snieder, R. (2006), The theory of coda wave interferometry, *Pure and Applied Geophysics*, *163*(2-3), 455–473.

Snieder, R., A. Grêt, H. Douma, and J. Scales (2002), Coda wave interferometry for estimating nonlinear behavior in seismic velocity, *Science*, *295*(5563), 2253–2255.

Stehly, L., M. Campillo, and N. Shapiro (2006), A study of the seismic noise from its long-range correlation properties, *Journal of Geophysical Research: Solid Earth (1978–2012)*, *111*(B10).

Syracuse, E., C. Thurber, C. Rawles, M. Savage, and S. Bannister (2013), High-resolution relocation of aftershocks of the Mw 7.1 Darfield, New Zealand, earthquake and implications for fault activity, *Journal of Geophysical Research: Solid Earth*, *118*(8), 4184–4195.

Taisne, B., S. Tait, and C. Jaupart (2011), Conditions for the arrest of a vertical propagating dyke, *Bulletin of Volcanology*, *73*(2), 191–204.

Takagi, A., K. Fukui, K. Fujiwara, Y. Ueda, S. Iijima, T. Yamamoto, T. Sakai, T. Kanno, and H. Katayama (2005), Magma supply system of the 2004 eruption at Asama Volcano estimated by crustal deformation data, *Kazan*, *50*(5), 363–375.

Takeo, A., K. Nishida, T. Isse, H. Kawakatsu, H. Shiobara, H. Sugioka, and T. Kanazawa (2013), Radially anisotropic structure beneath the Shikoku Basin from broadband surface wave analysis of ocean bottom seismometer records, *Journal of Geophysical Research: Solid Earth*, *118*(6), 2878–2892.

Takeo, M., Y. Aoki, T. Ohminato, and M. Yamamoto (2006), Magma supply path beneath Mt. Asama volcano, Japan, *Geophysical research letters*, *33*(15), L15,310.

Tanaka, H. K., et al. (2007), High resolution imaging in the inhomogeneous crust with cosmic-ray muon radiography: The density structure below the volcanic crater floor of Mt. Asama, Japan, *Earth and Planetary Science Letters*, *263*(1), 104–113.

Tarantola, A. (2005), *Inverse problem theory and methods for model parameter estimation*, siam.

Tarantola, A., and B. Valette (1982), Inverse problems= quest for information, *Journal of Geophysics*, *50*(3), 150–170.

Teanby, N., J.-M. Kendall, and M. Van der Baan (2004), Automation of shear-wave splitting measurements using cluster analysis, *Bulletin of the Seismological Society of America*, *94*(2), 453–463.

Todd, T., and G. Simmons (1972), Effect of pore pressure on the velocity of compressional waves in low-porosity rocks, *Journal of Geophysical Research*, *77*(20), 3731–3743.

Townend, J., and M. D. Zoback (2001), Implications of earthquake focal mechanisms for the frictional strength of the San Andreas fault system, *Geological Society, London, Special Publications*, *186*(1), 13–21.

Townend, J., and M. D. Zoback (2006), Stress, strain, and mountain building in central Japan, *Journal of Geophysical Research: Solid Earth (1978–2012)*, *111*(B3).

Townend, J., S. Sherburn, R. Arnold, C. Boese, and L. Woods (2012), Three-dimensional variations in present-day tectonic stress along the Australia–Pacific plate boundary in New Zealand, *Earth and Planetary Science Letters*, *353*, 47–59.

Tsvankin, I., J. Gaiser, V. Grechka, M. van der Baan, and L. Thomsen (2010), Seismic anisotropy in exploration and reservoir characterization: An overview, *Geophysics*, *75*(5), 75A15–75A29.

Turcotte, D. L., and G. Schubert (2002), *Geodynamics*, Cambridge University Press.

Van Camp, M., and P. Vauterin (2005), Tsoft: graphical and interactive software for the analysis of time series and Earth tides, *Computers & Geosciences*, *31*(5), 631–640.

Verdon, J., J.-M. Kendall, and A. Wüstefeld (2009), Imaging fractures and sedimentary fabrics using shear wave splitting measurements made on passive seismic data, *Geophysical Journal International*, *179*(2), 1245–1254.

Villamor, P., and K. Berryman (2006), Evolution of the southern termination of the Taupo Rift, New Zealand, *New Zealand Journal of Geology and Geophysics*, *49*(1), 23–37.

Voight, B. (1988), A method for prediction of volcanic eruptions, *Nature*, *332*(6160), 125–130.

Walcott, R. (1984), The kinematics of the plate boundary zone through New Zealand: a comparison of short-and long-term deformations, *Geophysical Journal International*, *79*(2), 613–633.

Waldhauser, F. (2001), hypoDD–A Program to Compute Double-Difference Hypocenter Locations (hypoDD version 1.0-03/2001), *US Geol. Surv. Open File Rep., 01*, *113*.

Wallace, L. M., J. Beavan, R. McCaffrey, K. Berryman, and P. Denys (2007), Balancing the plate motion budget in the South Island, New Zealand using GPS, geological and seismological data, *Geophysical Journal International*, *168*(1), 332–352.

Walsh, E., R. Arnold, and M. Savage (2013), Silver and Chan revisited, *Journal of Geophysical Research: Solid Earth*, *118*(10), 5500–5515.

Walsh, J. (1965), The effect of cracks on the compressibility of rock, *Journal of Geophysical Research*, *70*(2), 381–389.

Wang, X.-Q., A. Schubnel, J. Fortin, E. David, Y. Guéguen, and H.-K. Ge (2012), High Vp/Vs ratio: Saturated cracks or anisotropy effects?, *Geophysical Research Letters*, *39*(11).

Weiss, T., S. Siegesmund, W. Rabbel, T. Bohlen, and M. Pohl (1999), Seismic velocities and anisotropy of the lower continental crust: a review, in *Seismic Exploration of the Deep Continental Crust*, pp. 97–122, Springer.

Wookey, J. (2012), Direct probabilistic inversion of shear wave data for seismic anisotropy, *Geophysical Journal International*, *189*(2), 1025–1037.

Wüstefeld, A., G. Bokelmann, C. Zaroli, and G. Barruol (2008), SplitLab: A shear-wave splitting environment in Matlab, *Computers & Geosciences*, *34*(5), 515–528.

Xie, J., M. H. Ritzwoller, W. Shen, Y. Yang, Y. Zheng, and L. Zhou (2013), Crustal radial anisotropy across eastern Tibet and the western Yangtze craton, *Journal of Geophysical Research: Solid Earth*, *118*(8), 4226–4252.

Yamamura, K., O. Sano, H. Utada, Y. Takei, S. Nakao, and Y. Fukao (2003), Long-term observation of in situ seismic velocity and attenuation, *Journal of Geophysical Research: Solid Earth (1978–2012)*, *108*(B6).

Yang, M., M. Elkibbi, and J. Rial (2003), Modeling of 3D crack attributes and crack densities in geothermal reservoirs, *Proc. Geothermal Reservoir Engineering*, pp. 321–327.

Zatsepin, S. V., and S. Crampin (1997), Modelling the compliance of crustal rock—I. Response of shear-wave splitting to differential stress, *Geophysical Journal International*, *129*(3), 477–494.

Zhang, H., Y. Liu, C. Thurber, and S. Roecker (2007), Three-dimensional shear-wave splitting tomography in the Parkfield, California, region, *Geophysical Research Letters*, *34*(24).

Zinke, J. C., and M. D. Zoback (2000), Structure-related and stress-induced shear-wave velocity anisotropy: observations from microearthquakes near the Calaveras Fault in Central California, *Bulletin of the Seismological Society of America*, *90*(5), 1305–1312.

Zoback, M. D. (2010), *Reservoir geomechanics*, Cambridge University Press.